



HAL
open science

Theoretical and experimental study of tuned nonlinear energy sink : application to passive vibration control

Donghai Qiu

► **To cite this version:**

Donghai Qiu. Theoretical and experimental study of tuned nonlinear energy sink : application to passive vibration control. Mechanics of materials [physics.class-ph]. INSA de Toulouse, 2018. English. NNT : 2018ISAT0029 . tel-02083714

HAL Id: tel-02083714

<https://theses.hal.science/tel-02083714>

Submitted on 29 Mar 2019

HAL is a multi-disciplinary open access archive for the deposit and dissemination of scientific research documents, whether they are published or not. The documents may come from teaching and research institutions in France or abroad, or from public or private research centers.

L'archive ouverte pluridisciplinaire **HAL**, est destinée au dépôt et à la diffusion de documents scientifiques de niveau recherche, publiés ou non, émanant des établissements d'enseignement et de recherche français ou étrangers, des laboratoires publics ou privés.



THÈSE

En vue de l'obtention du

DOCTORAT DE L'UNIVERSITÉ DE TOULOUSE

Délivré par:

Institut National des Sciences Appliquées de Toulouse (INSA Toulouse)

Présentée et soutenue par :

Donghai QIU

le 29 Mars 2018

Titre :

Theoretical and experimental study of tuned nonlinear energy sink:
application to passive vibration control

École doctorale et discipline ou spécialité :

ED MEGEP : Génie mécanique

Unité de recherche :

Institut Clément Ader, CNRS UMR 5312

Directeur(s) de Thèse :

Sébastien SEGUY

Manuel PAREDES

MCF, INSA Toulouse

Professeur, INSA Toulouse

Co-Directeur

Directeur

Jury :

Claude-Henri LAMARQUE

Pierre-Alain YVARS

Régis DUFOUR

Alain BERLIOZ

Professeur, ENTPE Vaulx-en-Velin

Professeur, SUPMECA Paris

Professeur, INSA Lyon

Professeur, UPS Toulouse

Rapporteur

Rapporteur

Examineur

Examineur

Acknowledgment

I wish to express my sincere appreciation to those who have contributed to this thesis and supported me in one way or the other during this amazing journey.

First of all, I am extremely grateful to my two supervisors, Manuel Paredes and Sébastien Seguy, for their guidance and all the useful discussions and brainstorming sessions, especially during the difficult conceptual development stage. Their deep insights helped me at various stages of my research.

Secondly, I would like to thank my thesis committee: Prof. Régis Dufour, Prof. Claude-Henri Lamarque, Prof. Pierre-Alain Yvars and Prof. Alain Berlioz, for their insightful comments and encouragement, but also for the brilliant suggestions which incited me to widen my research from various perspectives.

Thirdly, I greatly appreciate the experimental help received through the collaborative work undertaken with Jean-Benoit Alibert and Guilhem Michon. Also I would like to thank the two technicians, Abdlali Khalfaoui and Bruno Simonigh, for their manufacturing support of my experimental setups.

Fourthly, I sincerely acknowledge the financial support of CSC and the working environment of laboratory ICA, as well as my colleagues and friends: Iman, Varun, Daniel, Irene, Florians (Neveu and Sanchez), Jim, Tommy, Montassa, Dominique, Francesco, Silvio, Simon, Adama, Landry, Alexandra, Julien, Guillermo, Georges, Yichang, Yanfeng, Tao, Carole. . . , who have accompanied me throughout those happy and unforgettable periods in our beautiful city: Toulouse – “La Ville Rose”.

Finally, I would like to say a heartfelt thank you to my mother and father for always believing in me and encouraging me to follow my dreams and for helping in whatever way they could during this challenging period.

Abstract

The work presented in this thesis deals with the passive control of dynamics systems subjected to harmonic and transient excitations using a Nonlinear Energy Sink (NES). Several research aspects have been developed: design theory and experimental study of a novel NES, efficient Targeted Energy Transfer (TET) of bistable NES and design criteria for optimally tuned Vibro-Impact (VI) NES.

Firstly, a design criterion intended to provide optimal nonlinear stiffness is proposed. Then a novel design of NES system yielding cubic nonlinearity with conical springs or variable pitch springs and negative stiffness mechanism is developed.

Secondly, the experimental procedures for static and dynamic test are presented and applied to validate the concept of NES system. Then a sensitivity analysis is performed with respect to the pre-compressed length of springs.

Thirdly, the optimal design of the above device with negative stiffness (termed as bistable NES) is studied. This type of NES is proved to work robustly for different types of excitation, and experimental study of semi-active control are explored.

Finally, design criteria for optimally tuned VI NES are studied. Detailed analytical calculations of clearance to control the vibration under different excitations are proposed. A good correspondence between theoretical and experimental results is observed.

Keywords: Nonlinear energy sink, Targeted energy transfer, Cubic nonlinearity, Vibro-impact, Conical spring, Variable pitch spring, Negative stiffness mechanism

Résumé

Les travaux présentés dans cette thèse traitent du contrôle de systèmes dynamiques soumis à des excitations harmoniques et transitoires en utilisant des absorbeurs de type Nonlinear Energy Sink (NES). Plusieurs aspects ont été développés : la conception et la réalisation d'un nouveau design pour le NES cubique, l'étude de la location et du transfert irréversible d'énergie sur un NES bistable et le développement d'un critère de conception pour un NES à Vibro-Impact (VI).

Dans un premier temps, un critère de conception est proposé pour le NES à raideur cubique. Le design proposé est basé sur des ressorts coniques ou des ressorts à pas variable. Un mécanisme à raideur négative est aussi introduit pour supprimer la partie linéaire et avoir une raideur cubique pure.

Dans un deuxième temps, le concept du NES est validé expérimentalement par des essais statiques et des essais dynamiques. Une analyse de sensibilité est aussi menée sur la longueur des ressorts précontraints, elle dénote parfois un état bistable de l'oscillateur.

Ensuite, le NES bistable ainsi obtenu est étudié plus en détail. Ce type d'absorbeur s'avère être très robuste pour différents types d'excitation. Des études expérimentales sont aussi menées afin d'explorer le comportement dynamique.

Enfin, un critère de conception est proposé pour le NES à Vibro-Impact. Des calculs analytiques détaillés sont proposés pour contrôler les vibrations sous différentes excitations. L'étude expérimentale montre une bonne cohérence avec les résultats théoriques.

Keywords: Dynamique non linéaire, Nonlinear Energy Sink NES, Raideur cubique, Vibro-impact, Ressort, Raideur négative

Contents

Acknowledgment	iii
Abstract	v
Résumé	vii
Table of Contents	xi
Figures	xvii
Notations	xvii
General Introduction	1
1 Literature Review	5
1.1 Vibration control method	6
1.1.1 Passive control	6
1.1.2 Semi-active control	7
1.1.3 Active control	7
1.2 Linear and nonlinear vibration absorber	8
1.2.1 Tuned mass damper	8
1.2.2 Nonlinear energy sink	9
1.3 Determination of nonlinear force characteristics	11
1.3.1 Linear spring	11
1.3.2 Nonlinear spring	16
1.3.3 Variable stiffness mechanism	18
1.4 Analysis tools of nonlinear dynamics	21
1.4.1 Perturbation methods	21
1.4.2 Stability and bifurcation analysis	23
1.4.3 Time-frequency analysis	23
1.5 Theoretical development of the NES	24
1.5.1 NES with smooth nonlinearity	24
1.5.2 Vibro-impact NES	26
1.5.3 Experiments and applications	27
1.6 Objective and work of this thesis	29
2 Tuned NES with nonlinear spring: design theory	33
2.1 Design criterion for cubic NES	33
2.1.1 Dynamic modeling	34
2.1.2 Analytical treatment	37

2.1.3	Criterion for efficient energy pumping	41
2.2	Design theory of NES system	43
2.2.1	Generalized methodology of NES	43
2.2.2	Eliminating linear stiffness by negative stiffness mechanism	44
2.2.3	Producing strong nonlinearity by nonlinear springs	47
2.3	Conclusion	55
3	Tuned NES with nonlinear spring: experimental study	57
3.1	Identification of the NES system	57
3.1.1	Static test	58
3.1.2	Effective mass	62
3.2	Dynamic test under periodic excitation	64
3.2.1	NES system with conical spring	64
3.2.2	NES system with variable pitch spring	65
3.3	Sensitivity analysis	69
3.4	Conclusion	72
4	Efficient targeted energy transfer of bistable NES	75
4.1	Theoretical Development	76
4.1.1	Modelling and analytical treatment	76
4.1.2	Response regimes	79
4.2	Study of threshold at different levels of energy	83
4.2.1	Asymptotic analysis for high energy level	83
4.2.2	Melnikov analysis for low energy level	85
4.3	Dynamical efficiency and design criterion	89
4.3.1	Efficiency of bistable NES and cubic NES	89
4.3.2	Detailed analysis of each regime	92
4.3.3	Optimal design criterion	98
4.4	Semi-active control of NES	100
4.5	Conclusion	105
5	Design criteria for optimally tuned vibro-impact NES	107
5.1	Asymptotic analysis of a single VI-NES	108
5.1.1	Dynamical modeling	108
5.1.2	Analytical treatment of Slow Invariant Manifold (SIM)	111
5.1.3	Bifurcation analysis	112
5.2	Criteria for efficient targeted energy transfer	114
5.2.1	Optimal design criterion for periodic excitation	114
5.2.2	Optimal design criterion for transient excitation	116
5.3	Optimal design of multiple VI-NESs	119
5.4	Experimental validation	121
5.4.1	Periodic excitation	122
5.4.2	Transient excitation	125
5.5	Conclusion	129
	Conclusion and Perspectives	131
	Bibliography	147

Publications

149

List of Figures

1.1	Schematic of three vibration control methods: (a) passive control; (b) semi-active control; (c) active control. Where f_e is the force of excitation, and f_a is the force of actuator.	6
1.2	Comparison of Frequency Response Function (FRF) between a TMD and a NES [Gourdon et al., 2007]	9
1.3	Schematic of representation of different types of NES.	10
1.4	Force characteristics of a linear spring	11
1.5	Schematic of a small spring segment with length dl . It is acted upon by an axial force F	12
1.6	The cut sections of the spring. Where the broken arrows show the shear stresses (τ_T), solid arrows show the shear stresses (τ_F).	13
1.7	Types of bearing with respective bearing coefficients for axially loaded compression springs.	15
1.8	Theoretical buckling limits of helical compression springs.	15
1.9	Deflection curve and successive coil arrangements according to compression phases [Rodriguez et al., 2006].	17
1.10	Distribution of active coils for nontelelescoping (left) and telescoping (right) conical spring, at any step of the nonlinear phase [Rodriguez et al., 2006].	18
1.11	Variable stiffness mechanism with horizontal compression spring type	19
1.12	Variable stiffness mechanism with oblique extension spring type	19
1.13	Variable stiffness device of semi-active TMD [Nagarajaiah and Varadarajan, 2005].	20
1.14	Frequency energy plot of (a) linear system and (b) nonlinear system by harmonic balance method [Kerschen et al., 2009].	22
1.15	Different types of the topological structure of SIM: (a) cubic NES [Gourc et al., 2014]; (b) piecewise NES [Lamarque et al., 2011]; (c) VI NES [Gourc et al., 2015a]; (d) rotational NES [Gendelman and Alloni, 2015].	25
1.16	Experimental setup for NES with cubic nonlinearity: (a) a single NES [Gourc et al., 2014]; (b) two parallel NESs [Savadkoobi et al., 2012].	27
1.17	Experimental setup for chatter control in turning: (a) global view; (b) detailed view of the VI NES [Gourc et al., 2015b].	28
1.18	Comparison of the behavior during unstable machining operation without and with VI NES [Gourc et al., 2015b].	29
2.1	Schematic of a harmonically excited LO coupled with a NES	34
2.2	SIM structure: two solide blue lines represent the stable branch and a blue dashed line means the unstable branch.	37

2.3	Cubic NES under periodic forcing with parameters $K = 2400$, $\lambda_1 = 0.8$, $\lambda_2 = 0.2$, $\epsilon = 0.015$, $G = 0.3\text{ mm}$ and initial conditions $x_0 = 0$, $\dot{x}_0 = 0$, $y_0 = 0$ and $\dot{y}_0 = 0$. (a) time-displacement of LO and NES; (b) wavelet transform of LO and NES. The states of 1, 2 and 3 represent the regime of nonlinear beating, transient resonance capture and escape from resonance capture, respectively.	37
2.4	SIM structure (blue line) and the transient projection motion of SMR (red line). The states 1, 2 and 3 represent the regime of nonlinear beating, transient resonance capture and escape from resonance capture, respectively.	38
2.5	Frequency response function (FRF) of LO with cubic NES (points) and without NES (thin line) in different types of excitation: (a) $G = 0.08\text{ mm}$; (b) $G = 0.13\text{ mm}$; (c) $G = 0.18\text{ mm}$; (d) $G = 0.23\text{ mm}$. The blue points and the red crosses represent stable and unstable fixed points respectively.	40
2.6	Maximum amplitude of LO with the variation of (a) nonlinear stiffness and excitation amplitude; (b) nonlinear stiffness; (c) excitation amplitude. Each point is extracted from the maximum amplitude of FRF.	41
2.7	Evolution of the multiplicity of periodic solutions for the system with parameters $K = 3000$, $\lambda_1 = 0.6$, $\lambda_2 = 0.3$, $\epsilon = 0.01$	42
2.8	Critical excitation amplitude as a function of the nonlinear stiffness, $\lambda_1 = 0.6$, $\lambda_2 = 0.3$, $\epsilon = 0.01$	42
2.9	(a) Schematic of NES system with negative stiffness mechanism and nonlinear spring; (b) restoring force with respect to the compressing length.	44
2.10	Schematic of the sub-system and the corresponding force-displacement curves, with respect to the compressing length: (a)(b) negative stiffness mechanism; (c)(d) nonlinear spring.	45
2.11	Detailed realization of NES system: (a) negative stiffness mechanism; (b) conical spring; (c) the composed system.	46
2.12	Force characteristics of two nonlinear springs (green and blue): (a) at original length; (b) pre-compressed at the transition point. The red curve represents the composed force.	46
2.13	Force characteristic of conical spring, T represents the transition point between linear and nonlinear phase.	47
2.14	State of two conical springs: (a) at original length; (b) pre-compressed at the transition point.	48
2.15	Polynomial components of the two optimized conical springs	50
2.16	Two types of shape for variable pitch spring: (a) each coil with a different pitch; (b) each group of coils with a different pitch.	50
2.17	Force characteristics of variable pitch spring: (a) each coil with a different pitch; (b) each group of coils with a different pitch.	51
2.18	Symmetrical type of pitch distribution for the spring	53
2.19	Compression spring for negative stiffness mechanism	54
2.20	Assembly of NES system. x and y correspond to the displacement of LO and NES respectively.	55
3.1	Details of the experimental setup and measuring system	58
3.2	First group of conical spring and the corresponding force characteristics	59

3.3	Second group of conical spring and the corresponding force characteristics .	59
3.4	NES system with linear springs of small mean diameter	60
3.5	NES system with linear springs of large mean diameter	60
3.6	Force-displacement relation of the designed NES	61
3.7	Manufactured variable pitch spring and measuring equipment	61
3.8	Details of the NES experimental setup and measuring system	62
3.9	Force-displacement relation of the designed spring (a) and NES system (b)	63
3.10	Experimental setup: (a) global view of the system and (b) detailed view of LO and NES	65
3.11	Frequency response curve of LO with (blue) and without (red) the designed NES	66
3.12	Strongly Modulated Response of LO (blue) and NES (green)	66
3.13	Experimental setup: (a) global scheme of the system and (b) detailed view of LO and NES.	67
3.14	Experimental results: (a) frequency response curve of LO with (blue) and without (red) designed NES, $G = 0.25$ mm; (b) frequency response curve of LO with (blue) and without (red) designed NES, $G = 0.40$ mm; (c) detailed view of response of LO under frequency sweep test with $G = 0.25$ mm; (d) Strongly Modulated Response of LO (blue) and NES (green) with $G = 0.25$ mm, $\sigma = 0$	68
3.15	Differences of the adjustment length for conical springs (γ_i) and linear springs (η_i)	70
3.16	The nonlinear NES force versus the response of LO and NES with $G =$ 0.205 mm, $\sigma = -0.2$: (a)(d) positive linear stiffness, $\gamma_1 = \gamma_2 = 1$, $\eta_1 =$ $\eta_2 = -1$; (b)(e) negative linear stiffness, $\gamma_1 = \gamma_2 = -1$, $\eta_1 = \eta_2 = 1$; (c)(f) unsymmetrical stiffness, $\gamma_1 = 1$, $\gamma_2 = -1$, $\eta_1 = \eta_2 = 0$	72
4.1	Schematic of the 2 DOF system comprising a LO and a bistable NES . . .	76
4.2	The SIM structure with different value of δ . The solid line represents the stable branch, and the dotted line the unstable branch.	79
4.3	The force displacement relation of a bistable NES: the two side points represent the two stable equilibria, and the middle point represents the unstable equilibrium	80
4.4	Responses at different levels of energy: a intra-well oscillation; b chaotic inter-well oscillation; c strongly modulated response; d stable periodic re- sponse	81
4.5	Time-displacement response of LO and bistable NES, and the motion of the system projected into SIM (a) intra-well oscillation with $G = 0.06$ mm (b) chaotic inter-well oscillation with $G = 0.1$ mm (c) strongly modulated response with $G = 0.42$ mm (d) stable periodic response with $G = 0.55$ mm	82
4.6	(a) Potential energy and (b) Hamilton phase plane: pseudo-separatrix . . .	87
4.7	The critical amplitude for the appearance of intra-well and chaotic oscilla- tions as a function of the excitation frequency, with the various values of (a) cubic nonlinearity and (b) negative stiffness.	89
4.8	Efficiency of cubic NES (a) energy dissipation ratio of NES and (b) ampli- tude of the LO. A_e represents the mean amplitude, and A_m the maximum amplitude	90

4.9	Efficiency of bistable NES (a) energy dissipation ratio of NES and (b) amplitude of the LO. Ae represents the mean amplitude, and Am the maximum amplitude	91
4.10	Response corresponding to point A (a) time-displacement response (b) projection in SIM structure (c) working range in the force-displacement relation (d) phase trajectory of NES	93
4.11	Response corresponding to point B (a) time-displacement response (b) projection in SIM structure (c) working range in the force-displacement relation (d) phase trajectory of NES	94
4.12	Response corresponding to point B_1 (a) time-displacement response (b) phase trajectory of NES (c) wavelet transform: 1:3 subharmonic resonance. Where the natural frequency of LO (f_0) is given by $f_0 = 2\pi/\omega_0$	95
4.13	SMR response in the first column, and the corresponding instantaneous amplitude and frequency in the second column, for different types of energy: (a) input $G = 0.21$ mm, corresponding to point C_1 ; (b) input $G = 0.25$ mm, corresponding to point C_2 ; (c) input $G = 0.42$ mm, corresponding to point C . Where the instantaneous amplitude of w is inferred from the leading (first) IMF, the instantaneous frequency of bistable NES is defined as f , and the natural frequency of LO is defined as f_0	96
4.14	Wavelet transform for different type of energy: (a) input $G = 0.21$ mm corresponding to point C_1 ; (b) input $G = 0.25$ mm corresponding to point C_2 ; (c) input $G = 0.42$ mm corresponding to point C	97
4.15	Controlling the optimal working point of NES by adjusting the nonlinear stiffness K and negative stiffness δ	99
4.16	NES with different kinds of linear stiffness, with respect to the state (compression or extension) of springs.	100
4.17	NES system with second group of conical springs: experiment for semi-active control	101
4.18	Force characteristics of NES system with respect to compressing length: (a) NES with positive stiffness, $\eta_1 = \eta_2 = -1.5$ mm; (b) NES with pure cubic nonlinearity $\eta_1 = \eta_2 = 0$ mm; (c) NES with negative stiffness $\eta_1 = \eta_2 = 3$ mm. The red dashed line is the objective curve of pure cubic nonlinearity, the blue solid line is the measured curve.	101
4.19	Time history of displacement of the LO with different kinds of NES, $G = 0.5$ mm.	102
4.20	(a) Frequency response curve of LO with semi-active control of the NES, at low energy excitation $G = 0.20$ mm, and detailed view of time displacement of LO under frequency sweep test for NES with positive stiffness (b), pure cubic nonlinearity (c) and negative stiffness (d).	103
4.21	(a) Frequency response curve of LO with semi-active control of the NES, at moderate energy excitation $G = 0.35$ mm, and detailed view of time displacement of LO under frequency sweep test for NES with positive stiffness (b), pure cubic nonlinearity (c) and negative stiffness (d).	104
4.22	(a) Frequency response curve of LO with semi-active control of the NES, at high energy excitation $G = 0.45$ mm, and detailed view of time displacement of LO under frequency sweep test for NES with positive stiffness (b), pure cubic nonlinearity (c) and negative stiffness (d).	104

5.1	Schematic of the dynamic system: a harmonically excited LO coupled with a VI NES	108
5.2	SIM of VI NES: on the stable branch in blue line and two unstable branches in green line with two transition point T_1 and T_2 . $\epsilon = 0.68\%$, $\lambda = 1.91$	111
5.3	Time-displacement response of LO and VI NES, and the motion of the system projected into the SIM: (a) SMR with $b > b_c$; (b) steady state response with $b < b_c$	115
5.4	TET efficiency explained by the amplitude of LO with the variation of clearance b : A_e represents the mean amplitude, and A_m the maximum amplitude.	116
5.5	Time-displacement response of LO and VI NES, and the motion of the system projected into the SIM: (a) four response regimes with $b < b_t$; (b) two response regimes with $b = b_t$	118
5.6	Four response regimes of VI NES: (a) three impacts per cycle; (b) two asymmetric impacts per cycle; (c) two symmetric impacts per cycle; (d) chaos with no duration of two impacts per cycle.	118
5.7	Schematic of the dynamic system: a harmonically excited LO coupled with two VI NESs in parallel	119
5.8	Experimental setup for periodic excitation:(a) global view of the configuration; (b) detailed view of the VI NES	122
5.9	Experimental results of single VI NES: response of the LO under periodic excitation $G = 0.25$ mm with (a) $b = 25$ mm ($< b_c$); (b) $b = 34$ mm ($= b_c$); (c) $b = 45$ mm ($> b_c$) and (d) optimal length of the cavity b_c under different types of excitation.	124
5.10	Experimental results of single VI NES: (a) frequency response curve of the LO with $G = 0.25$ mm and detailed view of response of the LO under sweep frequency test with (b) $b = 25$ mm ($< b_c$); (c) $b = 34$ mm ($= b_c$); (d) $b = 45$ mm ($> b_c$).	125
5.11	Experimental results of two VI NESs: (a) frequency response curve of the LO with $G = 0.25$ mm and detailed view of response of the LO under sweep frequency test with (b) $b_1 = 23$ mm, $b_2 = 23$ mm; (c) $b_1 = 23$ mm, $b_2 = 34$ mm; (d) $b_1 = 34$ mm, $b_2 = 34$ mm.	126
5.12	Experimental setup for transient excitation	126
5.13	Experimental results of single VI NES: (a) time history of the displacement; (b) time history of the acceleration; (c) comparison of the displacement envelope with different b	127
5.14	Experimental results of two VI NESs: (a) time history of the displacement; (b) time history of the acceleration; (c) comparison of the displacement envelope with different b	128

General Introduction

With the faster, lighter and more sophisticated mechanical products designed nowadays, vibration mitigation devices are required to be more rigorous than ever before. To ensure the performance of the designed system, different types of vibration control methods (e.g. smart structure, passive and active vibration absorber) have been exploited in the recent decades. Among them, the Tuned Mass Damper (TMD), a linear absorber with the passive control method, has been widely applied. When attached to a primary system, this absorber can be tuned to suppress the dynamic vibration of the structure and its amplitude at resonance condition. However, the combined system has two degrees of freedom, which means that there are two natural frequencies corresponding to two resonance peaks, making this absorber effective over only a narrow band of excitation frequencies.

To overcome this limitation, an innovative nonlinear absorber named Nonlinear Energy Sink (NES) has been proposed recently. This type of absorber is characterized by a secondary mass strongly coupled via a nonlinear stiffness to the primary system that needs to be protected. Because of the strong (non-linearizable) nonlinearity, irreversible Targeted Energy Transfer (TET) from the main structure to the secondary mass is achieved, enabling the NES to be effective in a broad band of frequencies. Mastering the nonlinearity is a key element for obtaining the optimum performance of a NES. Depending on the type of nonlinearity, a NES can be classified as a cubic NES, a vibro-impact NES, a piece-wise NES or a rotational NES. As far as the cubic NES is concerned, it has been shown that this configuration is most effective at moderate-energy regimes. However, this NES is sensitive to the excitation amplitude, and in practice, it is difficult to obtain cubic nonlinearity without a linear part. Implementing a cubic nonlinearity element and using some adaptive control methods (e.g. semi-active control) are still important issues if the applications of NES are to be broadened.

As for Vibro-Impact (VI) NES, it is also worth to explore the semi-active control method. This absorber is referred as a ball which is attached to a main structure and can freely move inside its clearance. With consecutive impacts, the excessive energy can be fast transferred and dissipated. In the context of TET, it is also found that the activation of a VI NES is limited to a range of excitation amplitude of primary system. To increase the range of effectiveness of vibration control, adopting multiples VI NESs with different

clearances is an alternative way, yet the detailed calculation to choose the clearance is still not clear. Thus, to obtain the optimal performance for a VI NES or multiple VI NESs and lay the foundation for semi-active control, analytical calculation for the clearance needs to be further studied.

From the above analysis, the following four questions are raised for the study of this thesis:

- Under a given primary system specification, how to calculate the optimally nonlinear stiffness for NES system and design this system with strongly cubic nonlinearity without any linear part?
- Since high efficiency of a NES system is achieved only in relatively narrow ranges of the external forcing amplitudes, is it possible to tune the designed NES work robustly over a range of excitation?
- Bistable NES seems perform better than cubic NES, whether it is possible to establish an optimal design criterion for this NES and improve its robustness by semi-active control method?
- Semi-active control may also be applied for VI NES, and its clearance is a key factor to influence the TET efficiency, whether possible and how to obtain the optimal clearance by analytical calculation?

As response to the above questions, the manuscript of this thesis is composed of five chapters.

In the first chapter, a general background about the development of NES system is presented. Firstly, the vibration control methods are introduced. Then, linear and nonlinear vibration absorber are presented and compared. Thirdly, the determination of nonlinear force characteristics is investigated. Fourthly, analysis tools of nonlinear dynamics are introduced. Finally, theoretical development of NES system is presented and examined from the view point of experiments and applications.

In the second chapter, a design criterion intended to provide the optimal nonlinear stiffness of NES is firstly proposed. Then a novel design of NES system yielding cubic nonlinearity without a linear part is developed. Key features of the system include: (i) specifically sizing two nonlinear springs to provide the force polynomial components with only linear and cubic terms; (ii) pre-compressing the two springs at the transition point to produce smooth nonlinear force characteristics; (iii) adding a negative stiffness mechanism to counterbalance the linear term. Finally, a small-sized NES system is developed.

The third chapter focuses on experimental studies, so as to validate the concept of NES. Firstly, identification of the NES system is performed, including static tests and

calculation of effective mass. Then dynamic experiments of the whole system embedded on an electrodynamic shaker are studied. The results show that this type of NES can not only output the expected nonlinear characteristics, but can also be tuned to work robustly over a range of excitation. Finally, a sensitivity analysis is performed with respect to the pre-compressed length of springs.

In the fourth chapter, efficient TET of bistable NES is studied. Firstly, an analytically obtained SIM is used to explain the different response regimes. Secondly, asymptotic analysis and Melnikov analysis are used to obtain the thresholds of different response regimes at different energy levels, respectively. Thirdly, dynamical efficiencies of different response regimes are compared, and design criterion for optimal response is proposed. Finally, experimental study of semi-active control for tuning this NES work robustly at different types of excitation, is explored.

The fifth chapter is devoted to propose the design criteria for optimally tuned VI NES. Firstly, dynamic modelling and bifurcation analysis around the SIM are studied. Secondly, detailed analytical calculations of clearance to control the vibration under periodic and transient excitation are proposed, respectively. Fourthly, the procedure extended in case of multiple VI NESs in parallel is studied. Finally, experiments involving the primary system with single VI NES and multiple VI NESs are performed, and the results confirm the design criteria and prove the feasibility of semi-active control.

Finally, a conclusion is addressed. Then, future researches based on the work of this thesis are presented.

Abstract

The first chapter is dedicated to the presentation of a general background about the development of NES system, and the framework of this thesis. Firstly, the vibration control methods, such as passive, semi-active and active method, are introduced. Then, linear and nonlinear vibration absorber (i.e., Tuned Mass Damper and Nonlinear Energy Sink) are presented and compared. Thirdly, the determination of nonlinear force characteristics is investigated, including nonlinear spring and variable stiffness mechanism. Fourthly, analysis tools of nonlinear dynamics are introduced. Fifthly, theoretical development of NES with smooth nonlinearity and vibro-impact is presented to understand the difficulties and unresolved issues. Finally, objective of this thesis is proposed.

Contents

1.1	Vibration control method	6
1.1.1	Passive control	6
1.1.2	Semi-active control	7
1.1.3	Active control	7
1.2	Linear and nonlinear vibration absorber	8
1.2.1	Tuned mass damper	8
1.2.2	Nonlinear energy sink	9
1.3	Determination of nonlinear force characteristics	11
1.3.1	Linear spring	11
1.3.2	Nonlinear spring	16
1.3.3	Variable stiffness mechanism	18
1.4	Analysis tools of nonlinear dynamics	21
1.4.1	Perturbation methods	21
1.4.2	Stability and bifurcation analysis	23
1.4.3	Time-frequency analysis	23
1.5	Theoretical development of the NES	24
1.5.1	NES with smooth nonlinearity	24
1.5.2	Vibro-impact NES	26
1.5.3	Experiments and applications	27
1.6	Objective and work of this thesis	29

1.1 Vibration control method

Mitigation of unwanted vibration has been an important issue in many fields of engineering. For civil structures, vibrating machinery, acoustical spaces or any other system that experiences vibration (or resonance), energy needs to be fast absorbed and dissipated by a vibration mitigation device, so as to avoid catastrophic failures. Different types of vibration control methods have been exploited in the recent decades [Soong and Costantinou, 2014 ; Fuller et al., 1996 ; Fisco and Adeli, 2011]. Among them, three main families of control methods can be categorized as: passive control, semi-active active control and active control (see Fig. 1.1). Detailed explanation is introduced as follows.

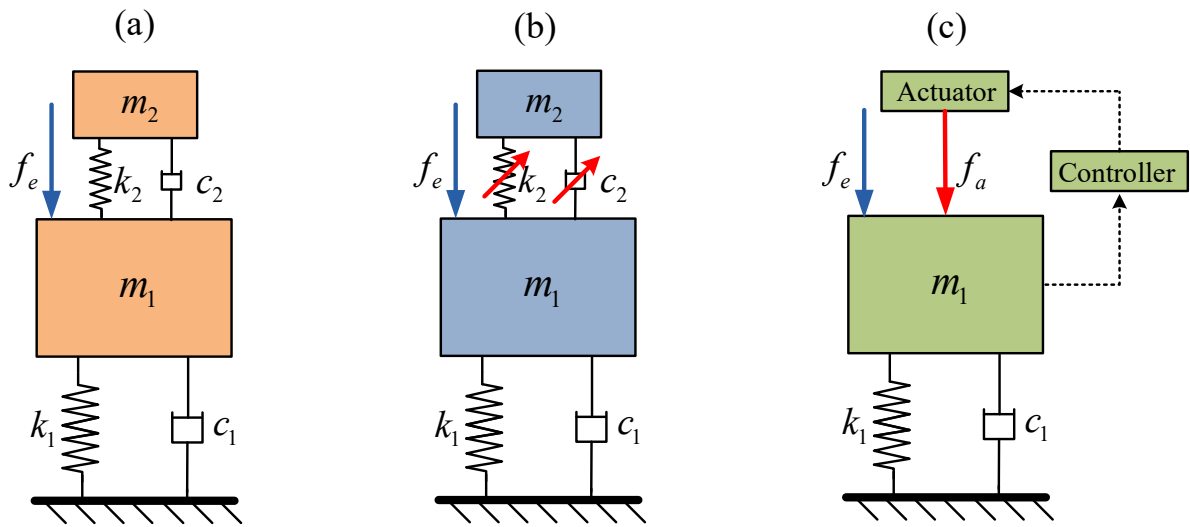


Figure 1.1: Schematic of three vibration control methods: (a) passive control; (b) semi-active control; (c) active control. Where f_e is the force of excitation, and f_a is the force of actuator.

1.1.1 Passive control

Passive control involves the use of reactive or resistive devices that either load the transmission path of the disturbing vibration or absorb vibration energy [Franchek et al., 1996 ; Mead, 1999]. The traditional passive devices include vibration damper, shock absorbers and base isolation. Fig. 1.1(a) shows a simple form of passive vibration absorber, where m_1 is a mass emulating the primary structure, k_1 is its mounting spring and c_1 is its viscous damping. The second mass m_2 and the coupling spring k_2 and damping c_2 constitute the absorber system. The new system consisting of the primary structure and absorber has two degrees of freedom and thus it has two natural frequency. If the natural frequency of the absorber is tuned to the frequency of the external forcing, the steady

state vibration amplitude of the main device can be controlled at a minimum value. In order to achieve the small motion of the primary system, the energy delivered to the system by the disturbing input must be absorbed by the absorber's mass and stiffness. Thus the resulting motion of absorber will be large [Mead, 1999]. From a control perspective, these absorber acts like a controller that has a internal model of the disturbance, which therefore cancels the effect of the disturbance. Owing to its economical cost and convenient maintenance, these kinds of absorbers (e.g. tuned mass damper) are commonly used in vibration mitigation of building and related structure.

1.1.2 Semi-active control

The advantage of passive control device is that it offers protection for a structure without the need to dramatically increase the size or complexity of the underlying structural system. However, this device is only effective in a particular range of frequency. Outside this frequency bandwidth, it can be ineffective and possibly make the structure's response worse. For example, the natural frequency of buildings can change with time. This is due to changes in building use/occupancy that result in a variation of live load distribution and in changes to non-structural elements [Alexander and Schilder, 2009]. To overcome this problem, semi-active control is an alternative way. By adjusting stiffness and/or damping properties in real-time (see Fig. 1.1(b)), correct tuning can be achieved, so as to obtain an optimal dynamic performance [Dyke et al., 1996a]. Various semi-active devices have been developed, such as variable orifice dampers [Kobori et al., 1993 ; Sack et al., 1994], controllable friction braces [Dowdell and Cherry, 1994 ; Xu et al., 2001], controllable friction isolators [Feng and Shinozuka, 1990 ; Feng et al., 1993], variable stiffness devices [Kobori et al., 1993 ; Liu et al., 2008], and electrorheological (ER) dampers [Kamath et al., 1996 ; Choi and Kim, 2000]. Another new device of magnetorheological (MR) dampers is recently proposed, which use MR fluids to provide controllable dampers [Dyke et al., 1998 ; Jansen and Dyke, 2000]. Compared with active and passive control systems, semi-active control devices can offer highly reliable operation at a modest cost and do not require hither-power supply, which are quite promising for the civil engineering and vehicle suspension systems [Dyke et al., 1996b ; Yao et al., 2002].

1.1.3 Active control

Active vibration control is the active application of force in an equal and opposite fashion to the forces imposed by external vibration. It achieves dynamic performance by adding degrees of freedom to the system and controlling actuator forces depending on feedback and feedforward real-time information of the system, which obtained from sen-

sor [Preumont, 2011]. The vibrating mechanical system is presented in Fig. 1.1(c), which consists of an actuator and a controller coupled to the primary system. Active actuators can be hydraulic, pneumatic and other styles. With this application, a precision industrial process can be maintained on a platform essentially vibration-free. Like the passive control method, it can loads the transmission path but achieves this loading through the use of force actuators requiring external energy. Thus, the use of added large power or energy can be distinguished for passive control and active control [Vasques and Rodrigues, 2006]. Active control of structure is also a multi-disciplinary field involving basic disciplines of structural dynamics, fluid-structure coupling, acoustics, automatic control, and material research, since it is increasing attempted to include the active control sensor and actuator functions in the material. This results in intelligent structures. However, active control systems require high-performance digital processors and bulky power amplifiers to drive actuators, which are not suitable for many practical applications.

1.2 Linear and nonlinear vibration absorber

Depending on the force characteristics, the vibration absorber can be classified as linear and nonlinear absorber. Among them, there exists two representative examples, as shown in the following part.

1.2.1 Tuned mass damper

Tuned Mass Dampers (TMD) are passive damping devices that consist of a mass which is connected to the primary system by a spring and a damper [Weber and Maślanka, 2012]. The classical design of a TMD is described by Den Hartog [Hartog, 1956] for minimum displacement response of the target mode of the main structure. Due to simplicity of TMD, these passive damping devices have been employed in huge variety of structures in field of civil and mechanical engineering [Matta, 2011 ; QIN et al., 2009]. As the primary system vibrates at the target resonance frequency to which the TMD was designed, the efficiency of vibration reduction can be optimal. However, the primary structure may also vibrate at other frequencies [Weber, 2014], due to:

- (1) Forced vibrations: the disturbing force excites the primary structure at a frequency that differs from the target resonance frequency;
- (2) Other resonance frequencies: another resonance frequency of the primary structure is excited than the resonance frequency that was used for the design of the TMD;
- (3) Time-varying target resonance frequency due to environmental impacts: the resonance frequency of the target mode differs from the resonance frequency that was used

for the design of the TMD due to temperature effects and/or life loads on the structure.

In all these cases de-tuning between the TMD properties and the modal parameters of the primary structure is present that ends up in deteriorated vibration reduction efficiency [Hazra et al., 2010 ; Occhiuzzi et al., 2008 ; Casado et al., 2007]. For this limitation, a vast variety of controllable tuned mass damper has been developed, such as active control [Chang and Soong, 1980] or semi-active control [Hrovat et al., 1983 ; Pinkaew and Fujino, 2001] of TMD, and multiple TMDs [Yamaguchi and Harnpornchai, 1993 ; Li, 2000].

1.2.2 Nonlinear energy sink

To overcome the drawback of TMD, an innovative nonlinear absorber named Nonlinear Energy Sink (NES) has been proposed recently [Vakakis and Gendelman, 2001]. This type of absorber is characterized by a secondary mass strongly coupled via a nonlinear stiffness to the primary system that needs to be protected. Because of the strong (non-linearizable) nonlinearity, irreversible Targeted Energy Transfer (TET) from the main structure to the secondary mass is achieved, enabling the NES to tune itself to the resonance frequency of different linear systems [Lee et al., 2008].

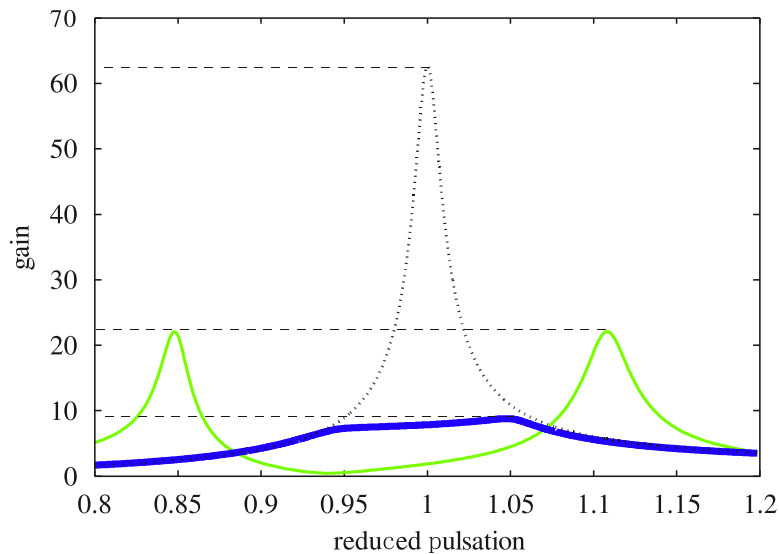


Figure 1.2: Comparison of Frequency Response Function (FRF) between a TMD and a NES [Gourdon et al., 2007]

Fig. 1.2 shows the comparison of Frequency Response Function (FRF) between a TMD and a NES. As can be seen, the dotted line is the response of linear oscillator without coupling any absorber. After attaching TMD, the large resonance peak is vanished, but it still has two small resonance peaks, making this absorber only effective in a narrow

band of natural frequency. By changing the absorber to NES, the resonance peak is disappeared, and it can be found that the NES can be effective over a much broader range of frequency than the TMD and does not suffer from the problem of amplification just outside the target bandwidth.

Mastering the nonlinearity is a key element for obtaining the optimum performance of a NES. Depending on the type of nonlinearity, a NES can be classified as a cubic NES [Gourdon et al., 2007 ; Gourc et al., 2014], a vibro-impact (VI) NES [Gourc et al., 2015a], a piecewise NES [Lamarque et al., 2011] or a rotational NES [Sigalov et al., 2012]. The detailed schematic for these types of NES is presented in Fig. 1.3.

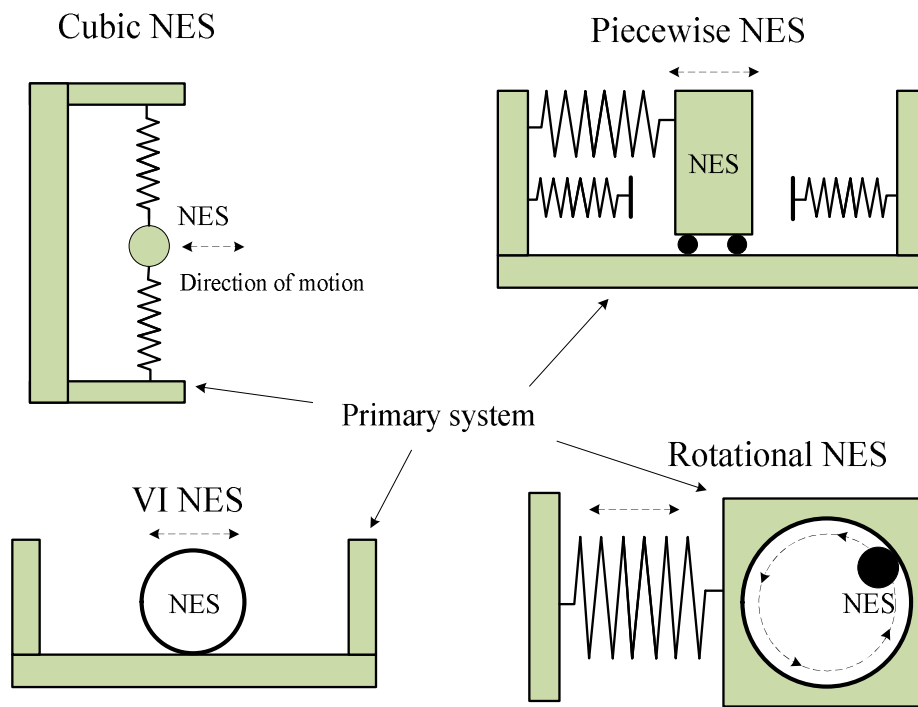


Figure 1.3: Schematic of representation of different types of NES.

As far as the cubic NES is concerned, it has been shown that this configuration is most effective at moderate-energy regimes [Vakakis et al., 2008]. This demonstration will be presented in our study. However, in practice, it is difficult to obtain cubic nonlinearity without a linear part. In our recent approaches, the essential cubic nonlinearity was mostly achieved by adopting the construction of two linear springs with no pretension. Due to self-geometric nonlinearity, the springs stretch in tension, thus creating the cubic force [Gourdon et al., 2007 ; Gourc et al., 2014]. However, this classical type of device cannot effectively profit from spring compression and extension, and the result is a large vertical structure attached to the main system. Addition of a relatively weak nonlinear stiffness existing at the beginning extension, leads to the whole cubic term being approximated to

a linear term. Therefore, implementing a cubic nonlinearity element in practice is still an important issue if the applications of NES are to be broadened.

1.3 Determination of nonlinear force characteristics

Nowadays, physical determination of the nonlinear force-displacement characteristics can be performed by two common methods. One is direct using nonlinear springs, the other method is to design a mechanism with variable stiffness. To understand the underlying mechanism of their force characteristics, the linear springs are firstly introduced.

1.3.1 Linear spring

A spring is a system whose function is to become deformed under the action of a force or a torque and then to restore the energy with the resumption of its initial form. A common reference book related to spring design was written several decades ago by [Wahl, 1944], in which the most common springs are cylindrical compression springs with constant pitch and cylindrical wire and closed and ground ends. The force characteristics of a linear spring is presented in Fig. 1.4, and detailed nomenclatures can be referred from [Paredes, 2013b]. Here, the design of a new spring involves the following considerations:

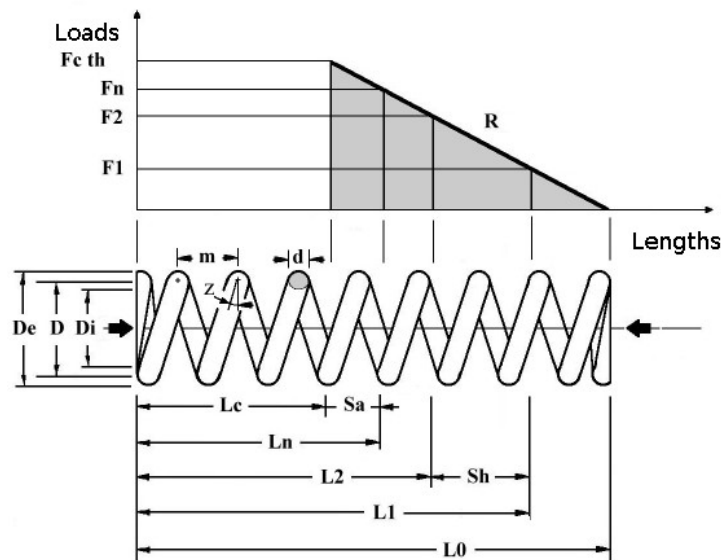


Figure 1.4: Force characteristics of a linear spring

- Space into which the spring must fit and operate.
- Values of working forces and deflections.
- Accuracy and reliability needed.
- Tolerances and permissible variations in specifications.

- Environmental conditions such as temperature, presence of a corrosive atmosphere.
- Cost and qualities needed.

The designers use these parameters to select a material and specify suitable values for the wire size, the number of coils, the coil diameter and the free length, type of ends and the spring rate needed to satisfy working force deflection requirements [Gopinath and Mayuram, 2006 ; Bentley et al., 2015]. The primary design constraints are that the wire size should be commercially available for the objective stiffness and that the stress at the solid length be no longer greater than the torsional yield strength [Trabelsi et al., 2015]. Further functioning of the spring should be stable. To explain this, several design procedures for helical cylindrical spring are introduced as follows.

1.3.1.1 Stiffness of helical spring

A small spring segment with length dl is presented in Fig. 1.5. As the spring is acted upon by a force F , the spring segment is consequently subjected by torsion with a torque $T = F \times \frac{D}{2}$. Where D is the mean diameter of spring.

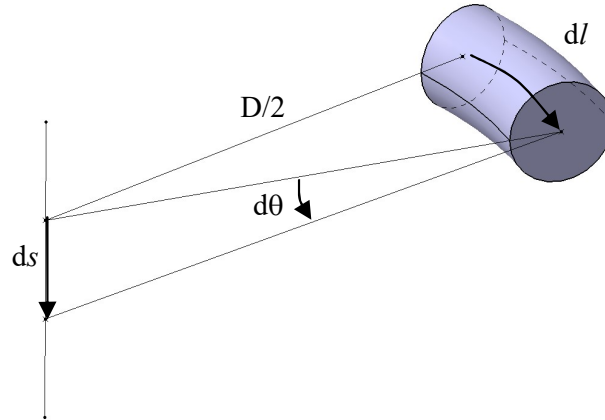


Figure 1.5: Schematic of a small spring segment with length dl . It is acted upon by an axial force F .

Then a small rotational angle $d\theta$ is produced, which is given by:

$$d\theta = \frac{T \times dl}{\bar{G}I_p} = \frac{\frac{FD}{2} \times dl}{\bar{G} \times \frac{\pi d^4}{32}} = \frac{16FDdl}{\bar{G}\pi d^4} \quad (1.1)$$

Where

$$\begin{aligned}
 I_p &= \text{the polar moment of inertia of the spring wire} \\
 &= \frac{\pi d^4}{32}, \quad d = \text{the diameter of spring wire}
 \end{aligned}
 \tag{1.2}$$

\bar{G} = torsion modulus for the material of spring wire

The axial deflection of spring segment is calculated by:

$$ds = d\theta \times \frac{D}{2} \tag{1.3}$$

The entire active length of the spring wire is

$$\begin{aligned}
 l &= \text{Length of one coil} \times \text{No. of active coils} = \pi D \times n_a \\
 n_a &= \text{the number of active coils}
 \end{aligned}
 \tag{1.4}$$

Substituting Eq. (1.1) to Eq. (1.3), and integrating Eq. (1.3) for the entire length of the spring wire, the total deflection of spring can be obtained.

$$s = \int_0^{n_a \pi D} \frac{D}{2} \times \frac{16FD}{\bar{G}\pi d^4} dl = F \times \frac{8n_a D^3}{\bar{G}d^4} \tag{1.5}$$

Thus the stiffness of helical spring is expressed as:

$$k = \frac{F}{s} = \frac{\bar{G}d^4}{8n_a D^3} \tag{1.6}$$

1.3.1.2 Stresses in the helical spring wire

The cut sections of the spring, subjected to the compressive load is presented in Fig. 1.6. The broken arrows show the shear stresses (τ_T) arising due to the torsion T and solid arrows show the shear stresses (τ_F) due to the force F .

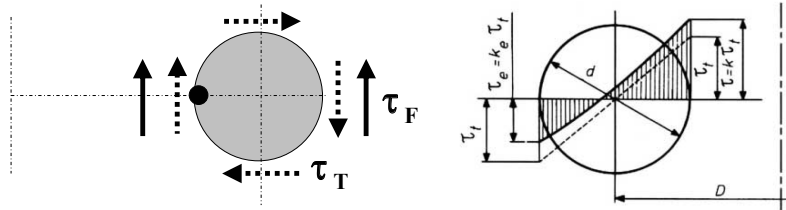


Figure 1.6: The cut sections of the spring. Where the broken arrows show the shear stresses (τ_T), solid arrows show the shear stresses (τ_F).

It is observed that for both tensile load as well as compressive load on the spring, maximum shear stress ($\tau_F + \tau_T$) always occurs at the inner side of the spring. Hence,

failure of the compression spring, in the form of crake, is always initiated from the inner radius of the spring.

The shear stress in the spring wire due to torsion (T) is

$$\tau_T = \frac{T \times r}{I_p} = \frac{\frac{FD}{2} \times \frac{d}{2}}{\frac{\pi d^4}{32}} = \frac{8FD}{\pi d^3} \quad (1.7)$$

Average shear stress in the spring wire due to force F is

$$\tau_F = \frac{F}{\frac{\pi d^2}{4}} = \frac{4F}{\pi d^2} \quad (1.8)$$

Therefore, maximum shear stress the spring wire is

$$\tau_{max} = \tau_T + \tau_F = \frac{8FD}{\pi d^3} + \frac{4F}{\pi d^2} = \frac{8FD}{\pi d^3} \left(1 + \frac{1}{2C}\right) \quad (1.9)$$

Where $C = \frac{D}{d}$ is called the spring index.

1.3.1.3 Stability of the spring (buckling)

In case of compression springs, it is always necessary to check its protection against side deflection (buckling) [Trabelsi, 2014]. The check is performed by comparison of the maximum working deformation of the spring with the permitted deformation. The length below which the phenomenon appears is called critical buckling length L_K .

A compression spring must be dimensioned so that it does not buckle laterally during its use. By using the spring with lengths higher than L_K , there is no problem of buckling. The length below which the phenomenon appears is called critical buckling length L_K . A compression spring must be dimensioned so that it does not buckle laterally during its use. The critical length of buckling L_K depends on the spring geometry (L_0/D) and of the type of supports of the spring. L_K is thus independent of the theoretically acceptable maximum stress in the spring body [Paredes, 2000]. European standards (NF EN13906-1) count 5 support cases (see Fig. 1.7). Each one of them is associated with a different value of the sitting factor ν . Here, types of bearing from left to right side show:

- 1 Fixed - free ends
- 2 Pinned - pinned ends
- 3 Clamped - clamped ends with lateral restraint
- 4 Clamped - pinned ends
- 5 Clamped - clamped ends without lateral restraint

Critical length L_K can be given starting from the abacus of Fig. 1.8 or starting from

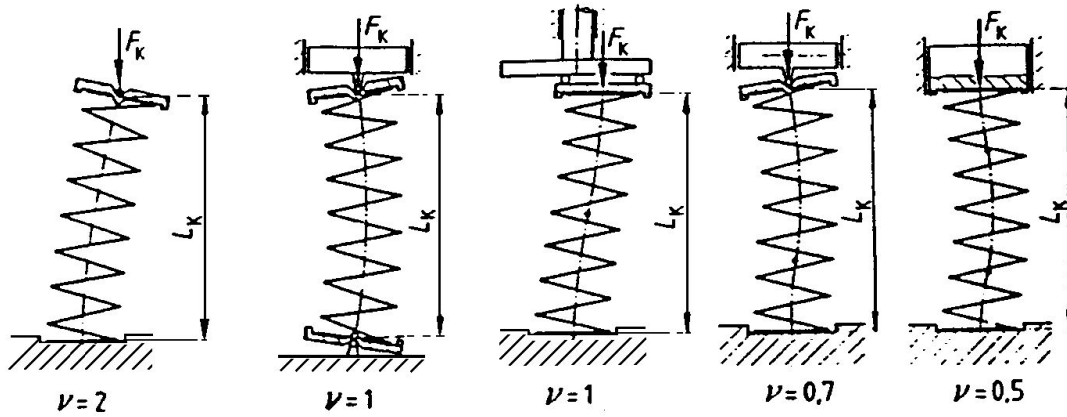


Figure 1.7: Types of bearing with respective bearing coefficients for axially loaded compression springs.

the following formulation (European standards):

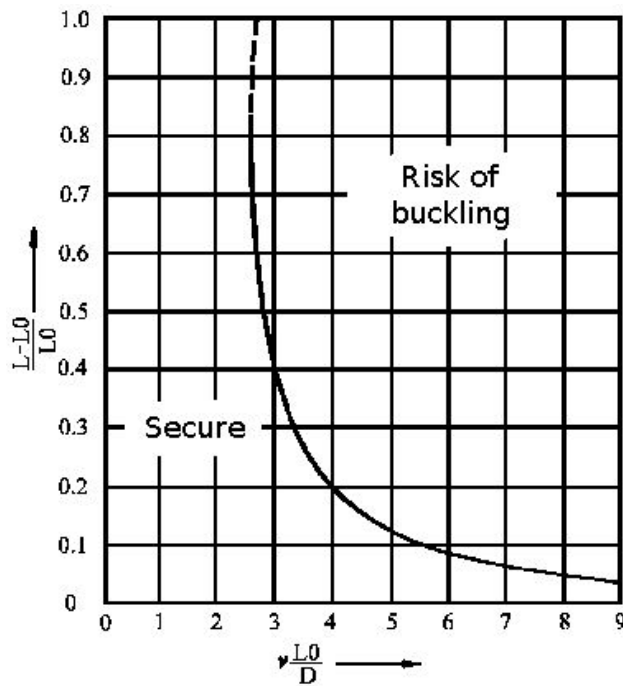


Figure 1.8: Theoretical buckling limits of helical compression springs.

$$\begin{aligned}
 &\text{If } \mu L_0/D < \pi \sqrt{\frac{2\mu + 1}{\mu + 2}}, \quad \text{then } L_K = 0 \text{ (no risk of buckling)} \\
 &\text{Else } L_K = L_0 \left(1 - \frac{\mu + 1}{2\mu + 1} \left(1 - \sqrt{1 - \frac{2\mu + 1}{\mu + 2} \left(\frac{\pi D}{\nu L_0} \right)^2} \right) \right) \quad (1.10) \\
 &\text{with } \mu = \frac{E}{2G} - 1 \text{ (Poisson's ratio)}
 \end{aligned}$$

From above equation, it can be observed that the value of the permitted deformation is determined empirically for the given slenderness ratio of the spring L_0/D and the type of seating of the spring. Generally, the risk of possible side deflection increases with an increasing value of the slenderness ratio and increasing value of the working compression of the spring [Hoff, 1954]. The manner of seating of the spring has a significant effect on its possible side deflection. The springs for which it is not possible to ensure buckling strength must be maintained in a boring or by an axis. But a friction then occurs and reduce the fatigue resistance.

1.3.2 Nonlinear spring

A nonlinear spring has a defined nonlinear load-displacement function, which is also equivalent to its strain energy absorption rate [Jutte and Kota, 2008]. As each nonlinear spring application requires a unique load-displacement function, spring configurations must be tailored for each application. The nonlinear behavior of a nonlinear spring occurs when the number of active coils decreases or increases with varying compression. It can be achieved by:

- 1 Varying the mean diameter
- 2 Varying the pitch
- 3 Varying the coil diameter

Among them, the third case is hard to realize by the current production process, thus engineers usually choose the first two methods in practice. Besides, there also exists piecewise springs [Chicurel-Uziel, 2001], special sized beam segments [Wang et al., 2017] and other type shapes [Touzé and Thomas, 2006], which can produce piecewise and nonlinear stiffness, respectively. Various applications of nonlinear springs can be found in vibration absorbers, robotic joints, bandpass filters, and crash-worthiness structures [Malher et al., 2017].

One common example of such nonlinear springs is conical spring. During the compression, the first biggest coil starts gradually to bottom, causing a gradually stiffening of the spring. Conical springs are cone shaped compression springs designed to provide a near constant spring rate and a solid height lower than a normal spring [Paredes and Rodriguez, 2009]. Fig. 1.9 shows the dynamical behavior of a conical spring with a constant pitch, which shows a two-phase compression in relation to their load length characteristics. The first phase is linear with a straight slope, as with a basic cylindrical spring, and the second phase is nonlinear at the end of compression. Detailed analytical law to fully describe the linear and nonlinear load length curve of this conical spring can be referred

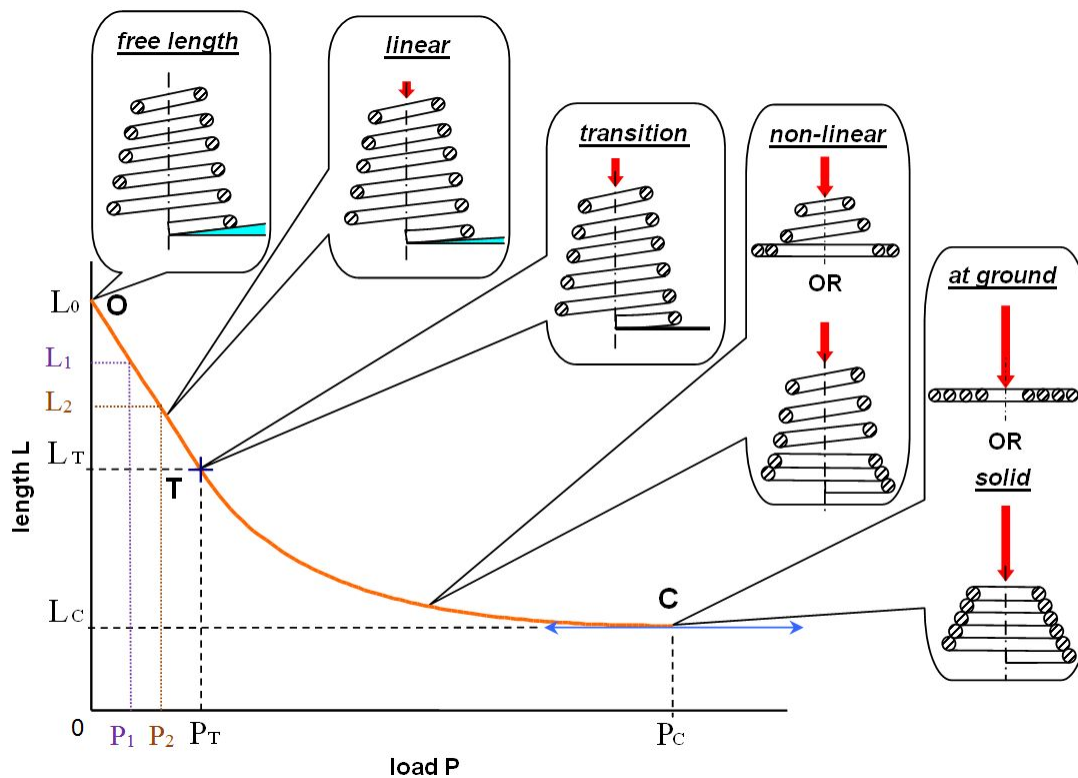


Figure 1.9: Deflection curve and successive coil arrangements according to compression phases [Rodriguez et al., 2006].

from [Rodriguez, 2006].

According to the initial geometry, the coil arrangements of conical spring can be classified as two types: nontelescoping and telescoping, as shown in Fig. 1.10. For the second geometry, the spring can be able to fully telescope, inducing a solid length equal to the wire diameter. It uses a very little space at maximum compression while storing as much energy as cylindrical springs, which make it be useful to lower a primary system (the center of mass is lowered) which improves its performance. Another advantage is that it offers more lateral stability and less tendency to buckle than cylindrical helical springs [Patil et al., 2014 ; Pati et al., 2015].

For a given conical shape and a given number of coils, the properties of the spring can evolve significantly depending on the way the coils are distributed along the conical profile. Recently, conical telescoping springs with nonconstant pitch was proposed, and the accuracy of its theoretical formulas was verified by experimental tests [Paredes, 2013a]. Different kinds of engineering applications with conical springs can be found, such as engine valves, railway and automotive suspension systems or as a buffer for an elevator [Den boer, 2009].

Another common example of nonlinear springs is variable pitch spring. Unlike the

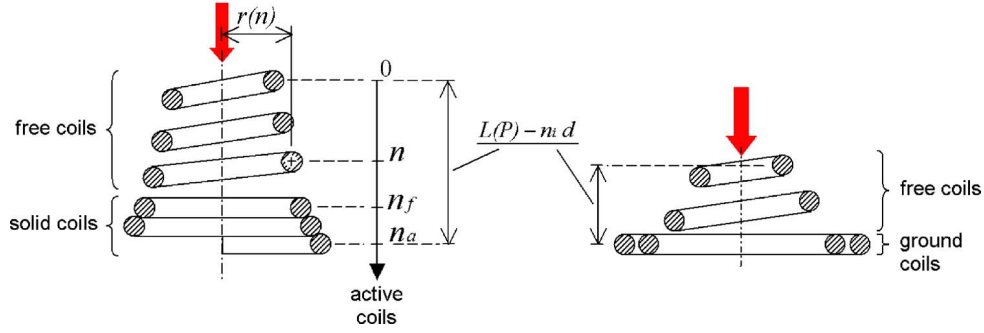


Figure 1.10: Distribution of active coils for nontelescoping (left) and telescoping (right) conical spring, at any step of the nonlinear phase [Rodriguez et al., 2006].

regular compression springs that are designed to have a linear spring rate, variable pitch spring can have multiple rates or, while the springs is compressing, they can have a progressively increasing or decreasing spring rate, by varying the pitch, or the center distance between the coils. By lessening the amount of active energy absorbing coils as they become inactive and no longer absorb energy during compression, because some of the coils close up faster than the others, the spring in turn becomes stiffer and the rate increase [Stanleyspring, 2011]. As the springs offer flexibility and will change based on the load balance, many race cars and motorcycles use variable pitch springs to allow for better handling as well as shock absorbers [Pullbarspring, 2017 ; Simcoespring, 2010].

However, these kinds of nonlinear springs (conical and variable pitch spring) have a linear phase for its force characteristics, and in its nonlinear phase, it also has the component of linear term. Thus it is difficult to directly use the conical springs or variable pitch springs to generate pure cubic nonlinearity for NES system.

1.3.3 Variable stiffness mechanism

To achieve the nonlinear force characteristics, a particular structure or mechanism whose stiffness can be varied was recently proposed. According to [Van Ham et al., 2009], variable-stiffness techniques can be classified as: (1) changing the elastic modulus of a structure; (2) altering the geometry of an elastic mechanism. The first approach can be realized by thermal or electromagnetic stimulation. This approach is scalable but limited to specific materials such as shape memory alloys, magneto-rheological fluids, elastomers, and piezoelectric materials [Wu and Lan, 2014]. Thus, the second approach is commonly adopted for engineering applications.

The structural type of second approach is based on altering the flexural rigidity, whereas the mechanical type is based on altering the moment arm length or force trans-

mission angle. The common method is to combine a positive-stiffness element and a negative-stiffness element to form variable stiffness. While the positive stiffness can be readily achieved using a compression spring, the negative stiffness may be achieved using magnets [Liu and Liu, 2006 ; Xu et al., 2013] or spring mechanisms [Kovacic et al., 2008 ; Huang et al., 2014]. Various types of negative-stiffness spring mechanisms can be found in [Alabuzhev and Rivin, 1989].

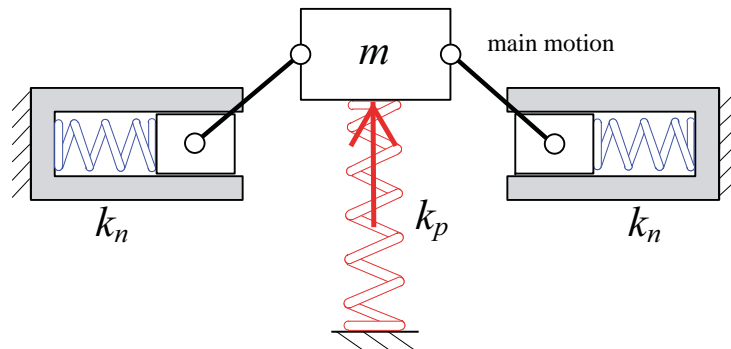


Figure 1.11: Variable stiffness mechanism with horizontal compression spring type

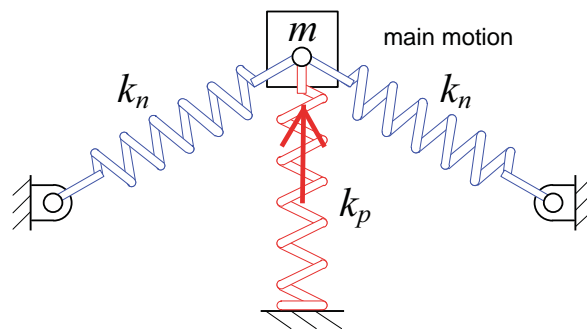


Figure 1.12: Variable stiffness mechanism with oblique extension spring type

Among them, there exists three representative mechanisms: (1) horizontal-spring type; (2) oblique-spring type; (3) buckled-beam type [Lan et al., 2014]. The first type adopts two horizontal springs (see Fig. 1.11), which are connected to the load through sliders and inclined links. This technique has been applied in designing vibration isolator to support a vehicle seat [Le and Ahn, 2011]. The second type shown in Fig. 1.12 directly uses two oblique springs connected to the load to obtain negative stiffness. This idea has been adopted to design the isolators with quasi-zero stiffness [Carrella et al., 2007].

The third types takes advantage of the snap-through behavior of beams or structures, so as to obtain the negative stiffness. For this method, Wu and Lan [Wu and Lan, 2014] proposed a linear variable stiffness mechanism with preloaded curved beams. Sönmez

and Tutum [Sönmez and Tutum, 2008] introduced a compliant bistable mechanism with flexible beams. Chen and Lan [Chen and Lan, 2012] designed an adjustable constant force mechanism for adaptive end effector operations. Stanton et al. [Stanton et al., 2010] developed a piezoelectric cantilever with a permanent magnet for the energy harvesting system.

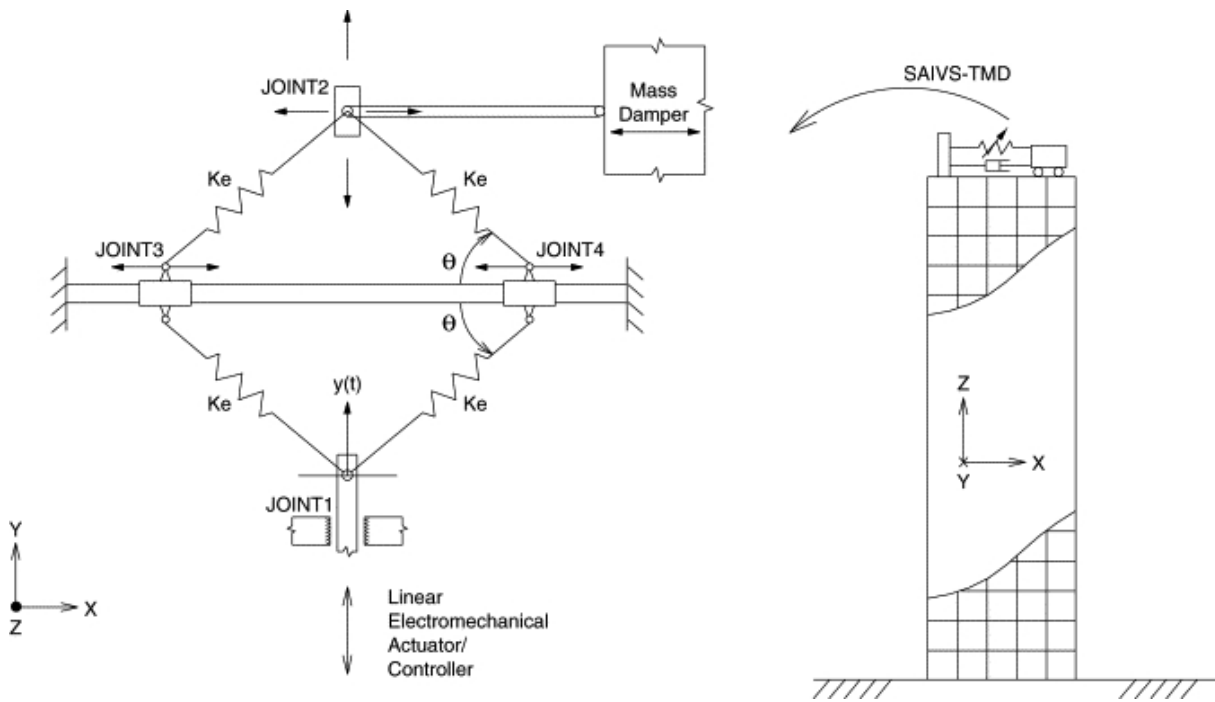


Figure 1.13: Variable stiffness device of semi-active TMD [Nagarajaiah and Varadarajan, 2005].

Nowadays, utilizing the variable stiffness mechanism to realize the semi-active control of vibration absorber has also been implemented. Fig. 1.13 shows a variable stiffness device of semi-active TMD. It consists of four spring elements arranged in a plane rhombus configuration, with pivot joints at the vertices [Nagarajaiah and Varadarajan, 2005]. A linear electromechanical actuator reconfigures the aspect ratio of the rhombus configuration. Where the aspect ratio can be changed between the fully closed and open configurations, so as to produce maximum and minimum stiffness, respectively.

As can be seen, the majority of previous work on variable stiffness focuses on techniques of altering the geometry of elastic mechanisms. For these mechanisms, a key issue to be satisfied for a NES is that the linear part of the force-displacement characteristics should be very small, so as to ensure that the NES can adapt itself to the frequency of any primary system.

1.4 Analysis tools of nonlinear dynamics

To understand the nonlinear behavior of NES, several analysis tools of nonlinear dynamics are presented here. These techniques will be further explored in this thesis, particularly around the efficiency of Targeted Energy Transfer (TET), so as to guide the design of NES system.

1.4.1 Perturbation methods

Perturbation methods are aimed at finding approximate analytic solutions to problems whose exact analytic solutions can not be found. There are many perturbation techniques to calculate periodic solutions of a nonlinear system, such as the methods of averaging, of harmonic balance and of multiple-scales [Nayfeh and Mook, 2008]. In essence, they are fundamentally equivalent to each other. Their application is restricted to the assumption of weak non-linearity. In this way, the derived analytical solutions of the non-linear system lie close to those of the corresponding linearized system. The method of averaging is the procedure of replacing a vector field by its average (over time or an angular variable) with the goal to obtain asymptotic approximations to the original system, so as to obtain periodic solutions.

The harmonic balance method is frequently used for the dynamic analysis of nonlinear systems as an efficient alternative to expensive time-marching techniques. This technique assumes that the response of nonlinear system is periodic and approximates it by means of a finite Fourier series. Compared to the other perturbation methods, it has the advantage of capable application to strongly nonlinear system [Lee et al., 2008]. Recently, harmonic balance method has also been applied to illustrate the frequency–energy dependence of the Nonlinear Normal Models (NNMs). Fig. 1.14 shows the Frequency Energy Plot (FEP) of a linear system and a nonlinear system by harmonic balance method. An NNM motion is represented by a point in the FEP, which is drawn at a frequency corresponding to the minimal period of the periodic motion and at an energy equal to the conserved total energy during the motion. A branch, represented by a solid line, is a family of NNM motions possessing the same qualitative features (e.g. the in-phase NNM motions of a 2DOF system). The backbone of the plot is formed by two branched, which represent in-phase (S_{11+}) and out-of-phase (S_{11-}) synchronous NNMs. The letter S refers to symmetric periodic solutions for which the displacements and velocities of the system at half period are equal but with an opposite sign to those at time $t = 0$. Unlike the linear normal mode, the FEP of Fig. 1.14 (b) clearly shows that the nonlinear modal parameters have a strong dependence on the total energy in the system [Kerschen et al., 2009].

The methods of multiple-scales (MMS) is realized by introducing fast-scale and slow-

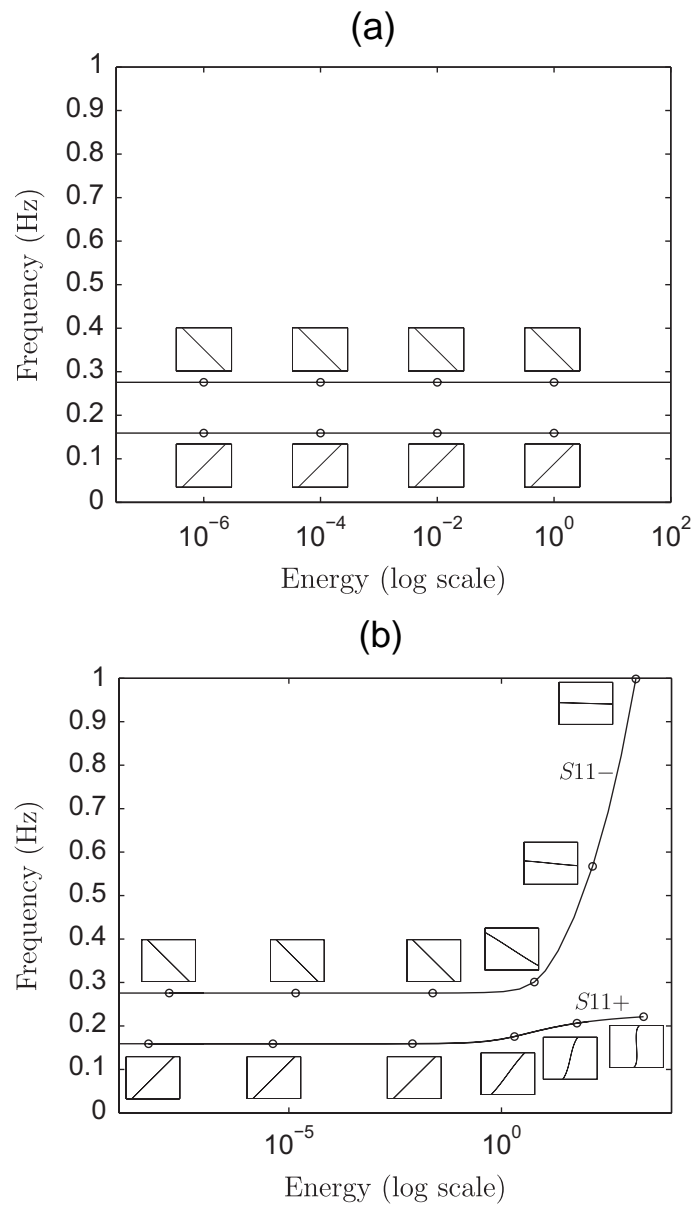


Figure 1.14: Frequency energy plot of (a) linear system and (b) nonlinear system by harmonic balance method [Kerschen et al., 2009].

scale variables for an independent variable, and subsequently treating these variables, fast and slow, as if they are independent [Nayfeh, 2011]. In the solution process, the resulting additional freedom is used to remove (unwanted) secular terms. The latter puts constraints on the approximate solution, which are called solvability conditions. The MMS technique is widely used together with the method of complexification [Manevitch, 2001] in the field of nonlinear dynamics.

Compared to the harmonic balance method, MMS can be applied to the study of transient dynamic behavior and is suitable for understanding nonlinear TET phenomena.

Besides, it can also be used in symbolic manipulation programs, which is essential for application to complex nonlinear systems. Thus, in this thesis, MMS is the preferred alternative to obtain the analytical solution for NES system.

1.4.2 Stability and bifurcation analysis

Based on the perturbation methods, the periodic solutions of the nonlinear system can be obtained. To determine the existence of solutions like fixed points and periodic orbits [Touzé et al., 2002], stability can be analyzed by the following three ways: (1) direct numerical integration of equations of motion; (2) computing their Floquet multipliers; (3) studying the topological structure of numerical Poincaré maps [Lee et al., 2008]. In order to understand transitions that occur in the damped dynamics, or to enhance robustness of instability suppression by means of passive TETs, bifurcation can then be studied.

A bifurcation occurs when a small smooth change made to the parameter values of a system (e.g. control parameters or other induced parameters such as the total energy of the system) causes a sudden 'qualitative' or topological change in its behavior. Many kind of bifurcations have been studied over the past decades, including saddle node bifurcation, Hopf bifurcations, homoclinic bifurcations and so on [Kuznetsov, 2013]. These work will be constructed in our thesis, so as to obtain the optimal response and guide the design of NES system.

1.4.3 Time-frequency analysis

To understand the strongly nonlinear dynamics governing TET, it is essential to analysis the variation of frequency with time. The main techniques of time-frequency analysis include: (1) Wavelet Transforms (WT); (2) Empirical Mode Decomposition (EMD); (3) Hilbert-Transform(HT) [Lee et al., 2008]. WT can be regarded as the 'dynamic' extension of the 'static' Fourier Transform (FT), by means that instead of decomposing a time series in the frequency domain using cosine and sine trigonometric functions, in the WT alternative families of orthogonal functions are employed which are localized in frequency and time. Here, small time intervals are considered for high frequency components, whereas the size of the interval is increased for lower frequency components thereby providing better time and frequency resolutions than the corresponding fast FTs [Vakakis et al., 2008].

EMD is a method for decomposing a signal. With this method, the complex data set can be decomposed into a finite and often small number of components. These components form a complete and nearly orthogonal basis for the original signal, which are described as intrinsic mode functions (IMFs) [Huang et al., 1998]. After applying the EMD analysis

to the time series, the extracted IMFs are Hilbert-transformed in order to compute their approximate transient amplitudes and phases. The technique combining EMD and HT is also called Hilbert Huang Transform (HHT), in which the instantaneous frequency and Hilbert spectrum can be obtained, making it practicable for analyzing the nonstationary and nonlinear time series data [Huang, 2014].

By adopting the above methods, a multi-scale separation of the time series in terms of the oscillating components can be analyzed. The nonlinear resonance interactions can be identified, so as to observe the nonlinear energy exchanges (i.e. TET) between the NES and the primary system.

1.5 Theoretical development of the NES

During the investigation of NES, the energy pumping phenomenon (i.e. TET) is initially studied for the NES with cubic nonlinearity, and then it is generalized to other NES types (with smooth or unsmooth nonlinearity) [Lamarque et al., 2017]. To understand the concept of TET, difficulties and unresolved issues, theoretical development of the NES system is presented. In these works, the topological structure of Slow Invariant Manifold (SIM) is commonly used to predict the response of NES (see Fig. 1.15). Where the vertical and horizontal axis represent the motion amplitude (translational or angular displacement) of primary system and corresponding NES, respectively.

1.5.1 NES with smooth nonlinearity

Substantial theoretical experimental work has been achieved to verify the performance of NES under transient and periodic excitation [Gourc et al., 2014 ; Li et al., 2017d ; Vaurigaud et al., 2011 ; Gendelman and Alloni, 2015 ; Gendelman et al., 2008 ; Lamarque and Savadkoohi, 2015]. Fig. 1.15(a) is the SIM structure of NES with cubic nonlinearity. The interaction between stable and unstable branch corresponds well to the strongly modulated response (SMR), which exhibits more efficient performance than the other steady-state response [Starosvetsky and Gendelman, 2008b]. However, the energy threshold corresponding to SMR is normally narrow, making the NES sensitive to the excitation amplitude and thus restricting its use in engineering applications.

Recent works seeking to improve the robustness of excitation have observed that the bistable NES (with negative linear and cubic nonlinear coupling) shows significant advantages with respect to energy pumping efficiency [Johnson et al., 2013 ; Gourdon and Lamarque, 2005 ; Savadkoohi et al., 2011 ; Harne et al., 2013 ; Mohammad A, 2014 ; Habib and Romeo, 2017 ; Harne and Wang, 2013]. This NES, with negative stiffness and nonlinear stiffness components, has nonzero displacement relative to the linear oscillator (LO)

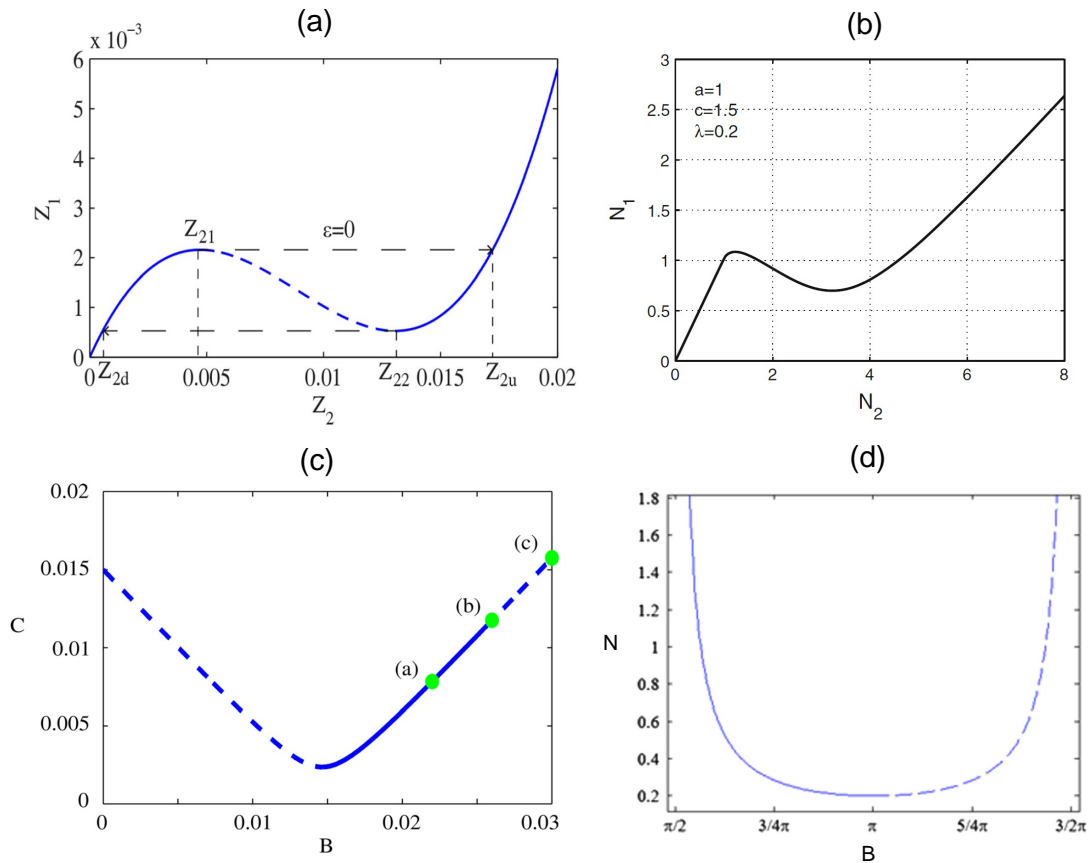


Figure 1.15: Different types of the topological structure of SIM: (a) cubic NES [Gourc et al., 2014]; (b) piecewise NES [Lamarque et al., 2011]; (c) VI NES [Gourc et al., 2015a]; (d) rotational NES [Gendelman and Alloni, 2015].

away from the NES equilibrium positions [Mohammad A, 2014]. This leads to strong suppression of the vibration amplitude of the LO in the first cycle of oscillation for a wide range of initial input energies induced in the linear structure. The analytical and numerical aspects of the transient dynamics of bistable NES are explored in [Manevitch et al., 2014] and [Romeo et al., 2015b], respectively. With the Limiting Phase Trajectories (LPTs) and Poincare section, dynamic mechanisms depending on different types of impulse input are proposed: for high energy levels, strongly modulated oscillation occurs and the dynamics are governed by fundamental (1:1) and superharmonic (1:3) resonances; for low energy levels, chaotic cross-well oscillations of the nonlinear attachment together with subharmonic resonances lead to strong energy exchanges between the two oscillators. In [Romeo et al., 2015a], Lyapunov characteristic exponents and Melnikov analysis are adopted to identify the region where chaotic cross-well oscillations exist as low-intensity impulse applied to the LO. The experimental aspect of a system consisting of a Bernoulli-Euler beam coupled to a continuous bistable NES is developed in [Fang et al., 2017] and

shows that this NES can achieve efficient TET under a wide-range of impacts. In [Mattei et al., 2016], a system of two coupled cantilever beams coupled to a bistable light attachment is tested and proves that this NES has better efficiency in frequency than existing passive devices.

1.5.2 Vibro-impact NES

Vibrating systems with clearance between the moving parts are frequently encountered in engineering fields, such as linkages, gear trains, pinned connections and joints. Impacts occur when the vibration amplitude of some parts are greater than the clearance, leading to high energy being transferred and dissipated in a transient manner. This phenomenon is attractive for vibration control, and a corresponding device termed as impact damper is developed [Lieber and Jensen, 1945]. Over the past decades, impact damper and its dynamics as a typical vibro-impact system have been extensively studied [Ibrahim, 2009 ; Babitsky, 2013 ; Afsharfard, 2016], and it has been demonstrated that in a range of frequencies, impact damper could have a better efficiency than classical damper. With this advantage, various applications of impact damper can be found in turbine blades, machine tools and tall flexible structures [Dimentberg and Iourtchenko, 2004 ; Afsharfard and Farshidianfar, 2013 ; Zhang and Angeles, 2005].

Recently, impact damper has been re-examined from the viewpoint of Targeted Energy Transfer (TET) [Lee et al., 2008 ; Vakakis et al., 2008], and is referred as Vibro-Impact (VI) Nonlinear Energy Sink (NES) [Nucera et al., 2007 ; Karayannis et al., 2008]. The mechanism of TET is revealed from the analytical study of underlying Hamiltonian system [Lee et al., 2009], and it is observed that some special orbits in frequency energy plot are responsible for the irreversible energy transfer from a primary system to an attached VI NES. Inspired by the study of TET, a method of multiple scales originally used for NES with cubic nonlinearity is improved to explain the transient TET process for vibrating system with a VI NES [Gendelman, 2012 ; Gendelman and Alloni, 2015]. A Slow Invariant Manifold (SIM) describing all possible fixed points and possible variation routes is obtained [Gourc et al., 2015b ; Pennisi and Stephan, 2017]. As a consequence, transient response and unsteady response (e.g. chaotic strongly modulated response) are well explained around the position of the fixed points [Gourc et al., 2015a ; Gendelman and Alloni, 2016].

The bifurcation, route to chaos and dynamics of the response regimes are further analyzed around SIM in [Li et al., 2017c], and it shows that the impulse strength is related to TET during the transient resonance capture. In [Li et al., 2017d], efficiency comparison of different response regimes around SIM is performed, and the response with two symmetrical impacts per cycle is proved to be the most efficient. Based on this idea,

a design procedure is proposed, and the essence behind it is similar to the case of NES with cubic nonlinearity [Nguyen and Pernot, 2012]. For periodic excitation, the objective is to tune the response at the boundary between two symmetrical impacts per cycle and Strongly Modulated Response (SMR). For transient excitation, the target is to make the free response start at the regime with two impacts per cycle and ensure that its duration is as long as possible. In [Li et al., 2017a], this optimal mechanism is extended for a linear system coupled with two VI NES in parallel, and the efficiency is demonstrated by the experiments.

1.5.3 Experiments and applications

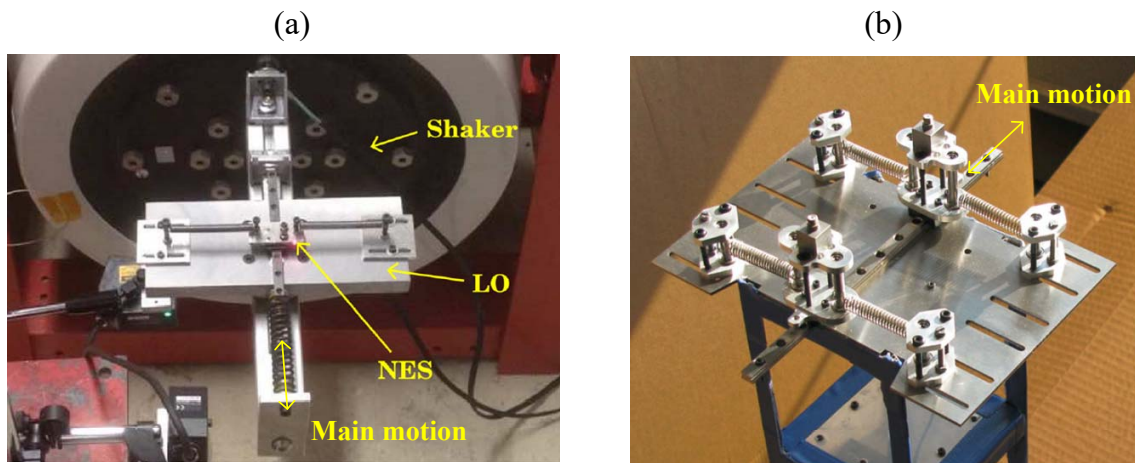


Figure 1.16: Experimental setup for NES with cubic nonlinearity: (a) a single NES [Gourc et al., 2014]; (b) two parallel NESs [Savadkoohi et al., 2012].

Targeted Energy Transfer mechanisms and the feasibility of NES in different experiments have been analyzed in detail by [Gendelman, 2011 ; Ahmadabadi and Khadem, 2013 ; Luo et al., 2014 ; Luo et al., 2013 ; Wang et al., 2015 ; Lamarque and Savadkoohi, 2014]. In these approaches, the essential cubic nonlinearity was mostly achieved by adopting a construction of two linear springs with no pretension (e.g. a beam [Kani et al., 2016], a piano wire [McFarland et al., 2005], a membrane [Mariani et al., 2011] and helical springs [Gourc et al., 2014]). The classical experimental setup for NES with cubic nonlinearity is presented in Fig. 1.16(a), and the second setup of two parallel NESs (see Fig. 1.16(b)) is aimed to improve the robustness for different kinds of excitation. The disadvantage of this type of device is that it cannot effectively profit from spring compression and extension, and the result is a large vertical structure attached to the main system. Addition of a relatively weak nonlinear stiffness existing at the beginning extension, leads to the whole cubic term being approximated to a linear term. Therefore,

implementing a cubic nonlinearity element in practice is still an important issue if the applications of NES are to be broadened.

Various applications of NES with smooth nonlinearity have been developed to control the system under resonance condition, or its instability and limit cycle. For example, cubic NES (membrane type) in the domain of acoustic has been studied and its efficiency has been demonstrated by the experiment [Bellet et al., 2010]. Continuous structures attached to NES system have been studied, such as the supported beam [Georgiades et al., 2007 ; Avramov and Gendelman, 2010], tension-compression bar [Georgiades et al., 2007 ; Tsakirtzis et al., 2007] and plate [Georgiades and Vakakis, 2009]. The applications to the problem of seismic protection of frame structures is also effective [Nucera et al., 2008], and other infrastructural systems such as towers, bridges, and so forth will likely benefit from this technology. Another practical application of NES concerns passive suppression of aero-elastic instabilities in rigid in-flow wings, which has experimentally demonstrated in [Lee et al., 2007].

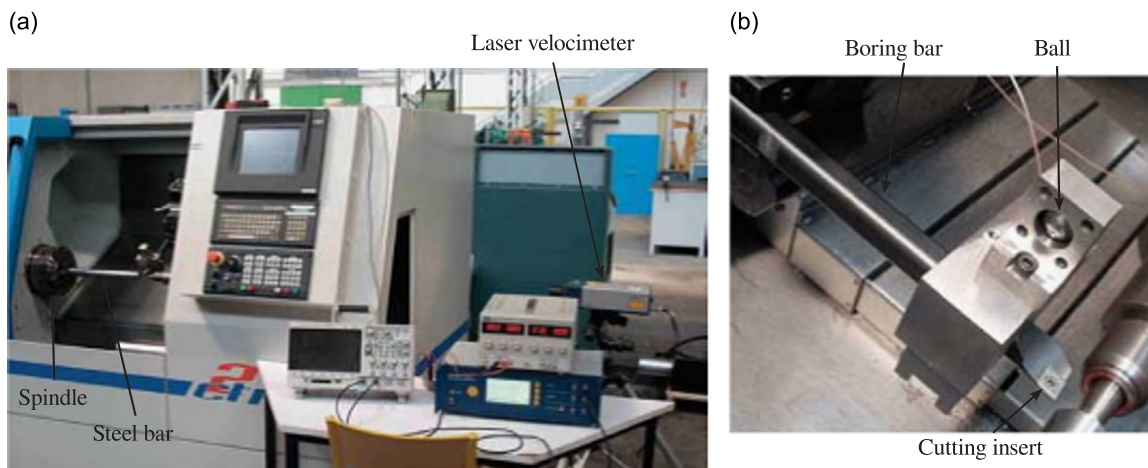


Figure 1.17: Experimental setup for chatter control in turning: (a) global view; (b) detailed view of the VI NES [Gourc et al., 2015b].

About the application of VI NES, the potential benefit of a VI NES to passively control chatter instability in a turning process has been studied in [Gourc et al., 2015b]. The system is composed of a flexible lathe tool on which a NES is embedded, as shown in Fig. 1.17. The results show that with the addition of VI NES, there exists a significant vibration mitigation of the tool (see Fig. 1.18). In [Li et al., 2017b], an activation characteristic generalized from linear systems to nonlinear systems has been studied. It shows that the activation characteristic is independent of frequency, so that the application of a VI NES for a nonlinear system can be simplified to the optimal design of a linear system. In [Viguié and Kerschen, 2009], this kind of design characteristic is explored for a nonlinear vibration absorber, but in a general way. The basic philosophy of this design can

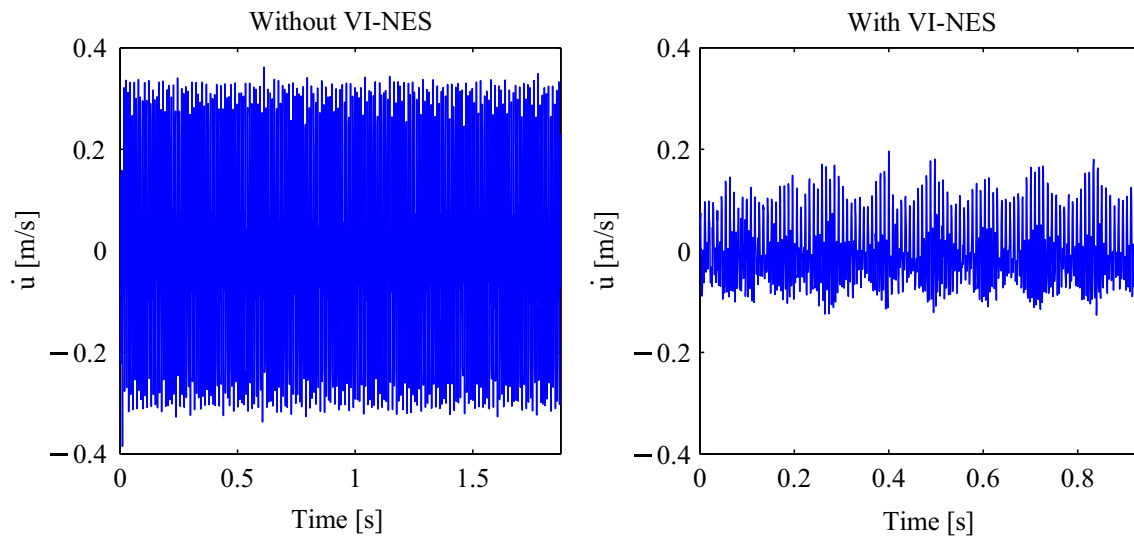


Figure 1.18: Comparison of the behavior during unstable machining operation without and with VI NES [Gourc et al., 2015b].

be reflected by the response regime with two impacts per cycle of systems coupled with VI NES. However, for both the linear and nonlinear system, the activation of VI NES is limited to a range of excitation. This means that a fixed clearance will only be effective in a displacement amplitude range of a primary system. To improve the robustness, using multiple VI NES is an alternative way, and the feasibility is proved in the case of multiple NES with cubic nonlinearity [Borosan et al., 2017 ; Vaurigaud et al., 2011]. In [Li et al., 2017a], two VI NESs with a medium clearance and a small clearance are proposed to be optimal for a given excitation, and experimental result demonstrates the efficiency. However, the detailed analytical calculation for the optimal clearance of VI VINES is still not clear, and the design criterion from a single VI NES to multiple VI NESs needs to be further studied.

1.6 Objective and work of this thesis

From the literature review, it can be found that high Targeted Energy Transfer (TET) efficiency of a Nonlinear Energy Sink (NES) is only achieved in a relatively narrow range of external forcing amplitude. Thus, it is practicable to establish a design criterion to provide the optimally tuned nonlinear stiffness for efficient TET. Besides, implementing cubic nonlinearity elements in practice is still an important issue if the application of NES is to be broadened. Whether it should be possible to combine the advantage of nonlinear springs and variable stiffness mechanisms, so as to obtain strongly cubic nonlinearity without any linear part for the NES system. For this, a generalized methodology for

designing a novel NES with the proposed components will be studied. About the robustness for a range of excitation, it has revealed that an appropriately designed bistable NES can be more efficient than a cubic NES. However, the optimal design criterion of bistable NES is not clear and needs to be further studied, and semi-active control method for this type of NES can also be investigated. As for Vibro-Impact (VI) NES, it is also worth to explore this semi-active control method: by adjusting the clearance, VI NES can be tuned to work robustly with its best performance. With this in mind, design theory and experimental study of a novel NES, efficient TET of bistable NES and design criteria for optimally tuned VI NES will be studied in this thesis. The chapters of this thesis are organized as follows:

In the second chapter, a design criterion intended to find optimal nonlinear stiffness of a NES absorber under a given primary system specification is firstly proposed. Then a novel design of NES system yielding cubic nonlinearity without a linear part is developed. To this end, two kinds of nonlinear springs (i.e. variable pitch spring and conical spring) are specially sized to provide the strong nonlinearity. To eliminate the linear stiffness, the configuration of a negative stiffness mechanism is implemented. Finally, a small-sized NES system is developed.

The third chapter focuses on experimental studies, so as to validate the concept of NES. Firstly, identification of the NES system is performed, including static tests and calculation of effective mass. Then dynamic experiments of the whole system embedded on an electrodynamic shaker are studied. The comparison of frequency response function of primary system with and without NES is explored, and the energy pumping phenomenon is observed. Finally, a sensitivity analysis is performed with respect to the pre-compressed length of springs.

In the fourth chapter, the efficiency of the above device with negative stiffness (termed as bistable NES) is studied. Firstly, a slow invariant manifold (SIM) is obtained and is applied to predict four typical response regimes. Through their efficiency comparison, it is observed that the bistable NES can be efficient and robust in a broad-range of excitation amplitude. With the Hilbert transform and wavelet transform, TET with transient or permanent 1:1 resonance is found to be responsible for the effectiveness of such strongly modulated response and 1:1 resonance. Finally, an optimal design criterion and semi-active control method are proposed to guide the application of this type of NES.

The fifth chapter deals with the design criteria for optimally tuned VI NES. Firstly, the existing analytical and numerical results are briefly introduced. Secondly, detailed analytical calculations of clearance to control the vibration under periodic and transient excitation are proposed, respectively. Thirdly, the procedure extended in case of multiple VI NESs in parallel is studied. Finally, experiments involving the primary system with single VI NES and multiple VI NESs are performed. The results show that the design

criteria can not only predict the efficient TET at resonance frequency, but can also achieve an optimal performance in a range of frequencies. Furthermore, it can be straightforward for the application of multiple VNESs and semi-active control.

Finally, a conclusion is addressed. Then, future researches based on the work of this thesis are presented.

Tuned NES with nonlinear spring: design theory

Abstract

This chapter is devoted to the study of a Nonlinear Energy Sink (NES) intended to attenuate vibration induced in a harmonically forced linear oscillator (LO) and working under the principle of Targeted Energy Transfer (TET). The purpose motivated by practical considerations is to establish a design criterion that first ensures that the NES absorber is activated and second provides the optimally nonlinear stiffness for efficient TET under a given primary system specification. Then a novel NES design yielding cubic nonlinearity without a linear part is exploited. To this end, two kinds of springs (i.e. variable pitch spring and conical spring) are specially sized to provide the nonlinearity. To eliminate the linear stiffness, the concept of a negative stiffness mechanism is implemented by two cylindrical compression springs. A small-sized NES system is finally developed.

Contents

2.1	Design criterion for cubic NES	33
2.1.1	Dynamic modeling	34
2.1.2	Analytical treatment	37
2.1.3	Criterion for efficient energy pumping	41
2.2	Design theory of NES system	43
2.2.1	Generalized methodology of NES	43
2.2.2	Eliminating linear stiffness by negative stiffness mechanism	44
2.2.3	Producing strong nonlinearity by nonlinear springs	47
2.3	Conclusion	55

2.1 Design criterion for cubic NES

To establish a design criterion of cubic NES, dynamic modeling and analytical treatment are studied in this section. The first objective is to ensure that the NES absorber is

activated under a given primary system specification, and the second is to provide the optimally tuned nonlinear stiffness for efficient TET.

2.1.1 Dynamic modeling

The dynamic modeling presented here is based on references [Gendelman et al., 2008 ; Gourc et al., 2014 ; Gourc, 2013]. The system of a harmonically excited linear oscillator (LO) strongly coupled with a cubic NES is illustrated in Fig. 2.1. The objective here is to apply the asymptotic method used in the above papers to obtain a possible design optimization criterion, and thus find the best parameters of the NES. The equations of motion are as follows:

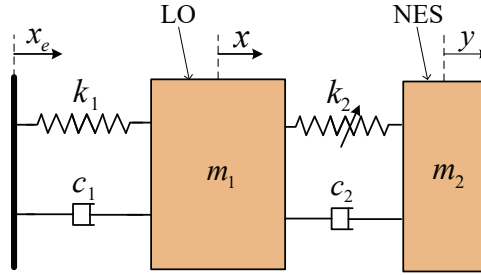


Figure 2.1: Schematic of a harmonically excited LO coupled with a NES

$$\begin{aligned} m_1\ddot{x} + k_1x + c_1\dot{x} + c_2(\dot{x} - \dot{y}) + k_2(x - y)^3 &= k_1x_e + c_1\dot{x}_e \\ m_2\ddot{y} + c_2(\dot{y} - \dot{x}) + k_2(y - x)^3 &= 0 \end{aligned} \quad (2.1)$$

where x , m_1 , c_1 , k_1 and y , m_2 , c_2 , k_2 are the displacement, mass, damping and stiffness of the LO and the cubic NES respectively. The imposed harmonic displacement x_e is expressed as: $x_e = G \cos(\omega t)$.

Substituting $k_1 = m_1\omega_0^2$, $t = \tau/\omega_0$ and $\omega = \Omega\omega_0$ to equations (2.1):

$$\begin{aligned} \ddot{x} + x + \frac{c_1}{m_1\omega_0}\dot{x} + \frac{c_2}{m_1\omega_0}(\dot{x} - \dot{y}) + \frac{k_2}{m_1\omega_0^2}(x - y)^3 &= G\cos(\Omega\tau) - \frac{c_1\Omega}{m_1\omega_0}G\sin(\Omega\tau) \\ \frac{m_2}{m_1}\ddot{y} + \frac{c_2}{m_1\omega_0}(\dot{y} - \dot{x}) + \frac{k_2}{m_1\omega_0^2}(y - x)^3 &= 0 \end{aligned} \quad (2.2)$$

Then introducing $c_1 = \lambda_1 m_2 \omega_0$, $c_2 = \lambda_2 m_2 \omega_0$ and $k_2 = m_2 \omega_0^2 K$ to Eqs. (2.2):

$$\begin{aligned} \ddot{x} + x + \frac{\lambda_1 m_2}{m_1}\dot{x} + \frac{\lambda_2 m_2}{m_1}(\dot{x} - \dot{y}) + \frac{K m_2}{m_1}(x - y)^3 &= G\cos(\Omega\tau) - \frac{\lambda_1 m_2 \Omega}{m_1}G\sin(\Omega\tau) \\ \frac{m_2}{m_1}\ddot{y} + \frac{\lambda_2 m_2}{m_1}(\dot{y} - \dot{x}) + \frac{K m_2}{m_1}(y - x)^3 &= 0 \end{aligned} \quad (2.3)$$

Substituting $m_2/m_1 = \epsilon$ and $G = \epsilon F$ to Eqs. (2.3):

$$\begin{aligned} \ddot{x} + x + \epsilon\lambda_1\dot{x} + \epsilon\lambda_2(\dot{x} - \dot{y}) + \epsilon K(x - y)^3 &= \epsilon F \cos \Omega\tau - \epsilon^2 F \lambda_1 \Omega \sin(\Omega\tau) \\ \epsilon\ddot{y} + \epsilon\lambda_2(\dot{y} - \dot{x}) + \epsilon K(y - x)^3 &= 0 \end{aligned} \quad (2.4)$$

where the term containing ϵ^2 is so small that it can be eliminated. The system of equations (2.1) can be finally reduced to the dimensionless form:

$$\begin{aligned} \ddot{x} + x + \epsilon\lambda_1\dot{x} + \epsilon\lambda_2(\dot{x} - \dot{y}) + \epsilon K(x - y)^3 &= \epsilon F \cos \Omega\tau \\ \epsilon\ddot{y} + \epsilon\lambda_2(\dot{y} - \dot{x}) + \epsilon K(y - x)^3 &= 0 \end{aligned} \quad (2.5)$$

where the term containing ϵ^2 is so small that can be eliminated. The corresponding physical parameters are expressed as follows:

$$\begin{aligned} \epsilon &= \frac{m_2}{m_1}, \quad \omega_0^2 = \frac{k_1}{m_1}, \quad K = \frac{k_2}{m_2\omega_0^2}, \quad \lambda_1 = \frac{c_1}{m_2\omega_0}, \\ \lambda_2 &= \frac{c_2}{m_2\omega_0}, \quad F = \frac{G}{\epsilon}, \quad \Omega = \frac{\omega}{\omega_0}, \quad \tau = \omega_0 t \end{aligned} \quad (2.6)$$

The dots denote differentiation with respect to dimensionless time τ . New variables representing the displacement of the center of mass and the internal displacement of the cubic NES are introduced as follows:

$$v = x + \epsilon y, \quad w = x - y \quad (2.7)$$

Substituting Eqs. (2.7) into Eqs. (2.5):

$$\begin{aligned} \ddot{v} + \epsilon\lambda_1 \frac{\dot{v} + \epsilon\dot{w}}{1 + \epsilon} + \frac{v + \epsilon w}{1 + \epsilon} &= \epsilon F \cos \Omega\tau \\ \ddot{w} + \epsilon\lambda_1 \frac{\dot{v} + \epsilon\dot{w}}{1 + \epsilon} + \frac{v + \epsilon w}{1 + \epsilon} + \lambda_2(1 + \epsilon)\dot{w} + K(1 + \epsilon)w^3 &= \epsilon F \cos \Omega\tau \end{aligned} \quad (2.8)$$

The system is studied in the vicinity of the 1:1 resonance, where both the LO and the NES execute the time-periodic oscillations with identical frequency Ω . To obtain the analytical periodic solution, two new complex variables are introduced:

$$\phi_1 e^{i\Omega\tau} = \dot{v} + i\Omega v, \quad \phi_2 e^{i\Omega\tau} = \dot{w} + i\Omega w \quad (2.9)$$

Substituting Eqs. (2.9) into Eqs. (2.8) and keeping only the secular term containing $e^{i\Omega\tau}$ yields the following slowly modulated system:

$$\begin{aligned}
 \dot{\phi}_1 + \frac{i\Omega}{2}\phi_1 + \frac{\epsilon\lambda_1(\phi_1 + \epsilon\phi_2)}{2(1+\epsilon)} - \frac{i(\phi_1 + \epsilon\phi_2)}{2\Omega(1+\epsilon)} - \frac{\epsilon F}{2} &= 0 \\
 \dot{\phi}_2 + \frac{i\Omega}{2}\phi_2 + \frac{\epsilon\lambda_1(\phi_1 + \epsilon\phi_2)}{2(1+\epsilon)} - \frac{i(\phi_1 + \epsilon\phi_2)}{2\Omega(1+\epsilon)} + \frac{\lambda_2(1+\epsilon)\phi_2}{2} - \frac{3iK(1+\epsilon)\phi_2^2\bar{\phi}_2}{8\Omega^3} - \frac{\epsilon F}{2} &= 0
 \end{aligned} \tag{2.10}$$

In the context of energy pumping, the mass ratio ϵ is taken to be small ($\approx 1\%$). In this case, Eq. (2.10) can be analysed by a perturbation method with respect to this small parameter. For this purpose, the method of multiple scales [Vakakis et al., 2008 ; Nayfeh, 2011] is introduced in the following form:

$$\begin{aligned}
 \phi_i &= \phi_i(\tau_0, \tau_1, + \dots), & \frac{d}{d\tau} &= \frac{\partial}{\partial\tau_0} + \epsilon \frac{\partial}{\partial\tau_1} + \dots \\
 \tau_k &= \epsilon^k \tau, & k &= 0, 1, \dots
 \end{aligned} \tag{2.11}$$

Substituting Eqs. (2.11) into Eqs. (2.10) and equating coefficients of ϵ^0 gives:

$$\begin{aligned}
 \frac{\partial}{\partial\tau_0}\phi_1 &= 0 \\
 \frac{\partial}{\partial\tau_0}\phi_2 + \frac{\lambda_2}{2}\phi_2 + \frac{i}{2}(\phi_2 - \varphi_1) - \frac{3iK}{8}\phi_2^2|\phi_2| &= 0
 \end{aligned} \tag{2.12}$$

Then we introduce the new variables as follows:

$$\phi_1(\tau_1) = N_1 e^{i\theta_1}, \quad \phi_2(\tau_1) = N_2 e^{i\theta_2} \tag{2.13}$$

With this change of variables in Eqs. (2.12), a topological structure of slow invariant manifold (SIM) is obtained in the following form:

$$N_{10}^2 = (1 + \lambda_2^2)N_{20}^2 - \frac{3K}{2}N_{20}^4 + \frac{9K^2}{16}N_{20}^6 \tag{2.14}$$

where N_{10} , N_{20} correspond to the amplitude of LO and NES in slow time scale, respectively. The two extrema of SIM are described as:

$$N_{2,i} = \frac{2}{3}\sqrt{(2 \pm \sqrt{1 - 3\lambda_2^2})/K} \quad i = 1, 2 \tag{2.15}$$

According to [Starosvetsky and Gendelman, 2008b], the SIM structure admits two extrema (N_{21} and N_{22}) and can be divided into two stable branches and one unstable branch (see Fig. 2.2), where the unstable branch of the SIM is mainly responsible for

the possible occurrence of energy pumping and may give rise to the strongly modulated response (SMR).

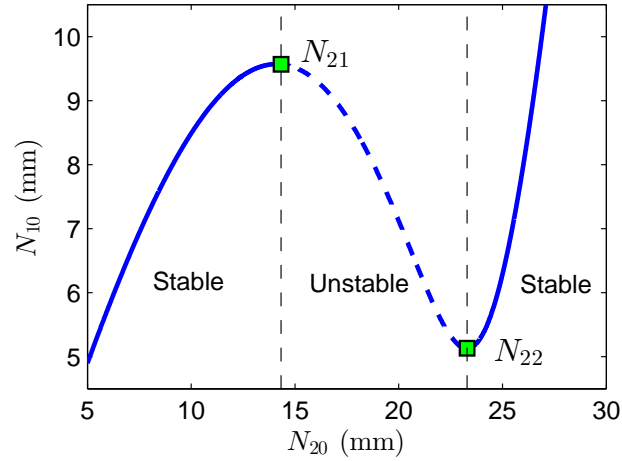


Figure 2.2: SIM structure: two solide blue lines represent the stable branch and a blue dashed line means the unstable branch.

2.1.2 Analytical treatment

To illustrate this mechanism, a strongly modulated response and its corresponding wavelet transform are presented in Fig. 2.3. A quasi-periodic response with slow variation of the amplitudes of both oscillators is observed.

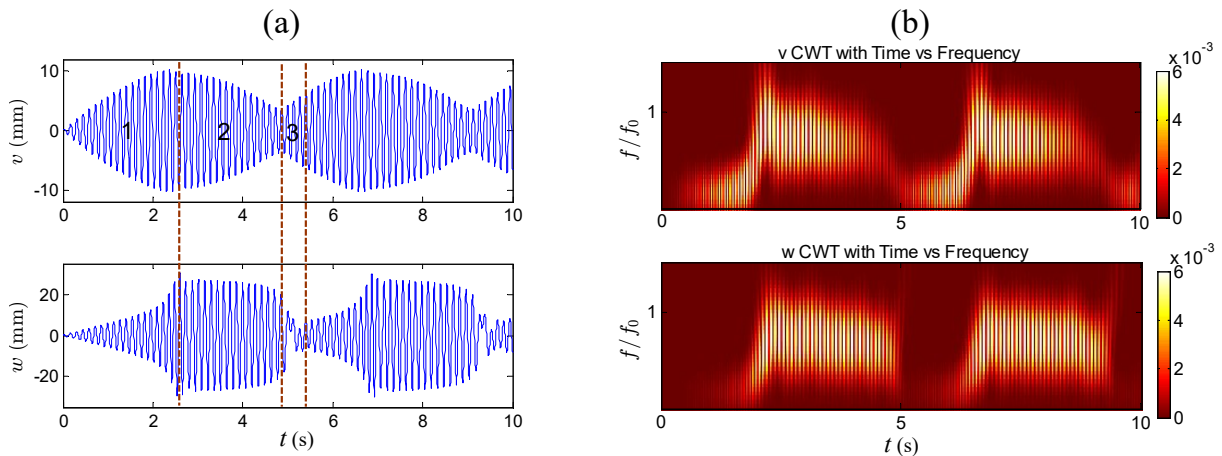


Figure 2.3: Cubic NES under periodic forcing with parameters $K = 2400$, $\lambda_1 = 0.8$, $\lambda_2 = 0.2$, $\epsilon = 0.015$, $G = 0.3 \text{ mm}$ and initial conditions $x_0 = 0$, $\dot{x}_0 = 0$, $y_0 = 0$ and $\dot{y}_0 = 0$. (a) time-displacement of LO and NES; (b) wavelet transform of LO and NES. The states of 1, 2 and 3 represent the regime of nonlinear beating, transient resonance capture and escape from resonance capture, respectively.

In this regime, the procedure of energy pumping can be classified as follows:

- (1) Nonlinear beating, where a small amplitude of NES corresponds to the growth of LO amplitude;
- (2) Transient resonance capture, with the frequency component of 1:1 resonance (see Fig. 2.3(b)), in this case large targeted energy is extracted and dissipated by NES, leading to a fast decrease of the LO amplitude;
- (3) Escape from resonance capture, in which the NES crosses the bifurcation and is quickly attracted to the low branch of SIM (see Fig. 2.4), which leads to a jump down for the energy of the NES.

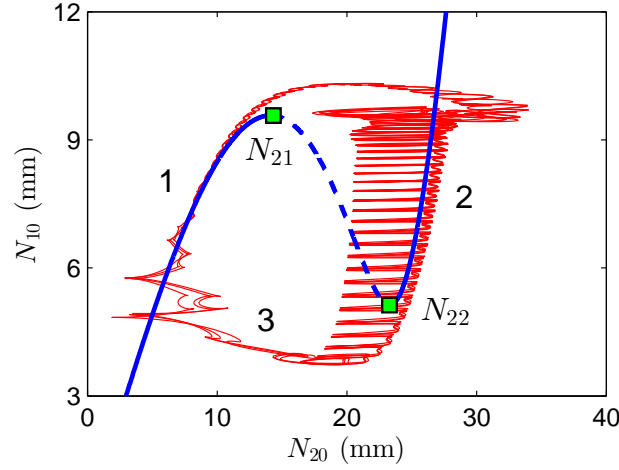


Figure 2.4: SIM structure (blue line) and the transient projection motion of SMR (red line). The states 1, 2 and 3 represent the regime of nonlinear beating, transient resonance capture and escape from resonance capture, respectively.

This SMR regime demonstrates the irreversible targeted energy transfer from LO to NES [Starosvetsky and Gendelman, 2008b], which suppresses energy more efficiently than a steady state response.

With these two extrema of SIM (N_{21} and N_{22}) located at the boundary of SMR and stable periodic response, the excitation threshold of the SMR can be obtained and written as:

$$G_{ic} = \frac{\epsilon N_{2,i}(9\lambda_1 K^2 N_{2,i}^4 - 24\lambda_1 K N_{2,i}^2 + 16(\lambda_1 + \lambda_2 + \lambda_1 \lambda_2^2))}{4\sqrt{9K^2 N_{2,i}^4 - 24K N_{2,i}^2 + 16 + 16\lambda_2^2}} \quad (2.16)$$

The detailed description of Eq. (2.14) and Eq. (2.16) are given in [Gendelman et al., 2008 ; Gourc et al., 2014]. When the excitation amplitude is with the interval $[G_{1c}, G_{2c}]$,

SMR can be produced. Yet this is not sufficient to ensure the activation of SMR regimes; another interacting factor is the excitation frequency. To explain its influence, the stability of the frequency response function (FRF) is analyzed. Here, a detuning parameter σ representing the nearness of the excitation frequency ω to the reduced natural frequency of the LO is introduced:

$$\Omega = 1 + \epsilon\sigma \quad (2.17)$$

The fixed points of the FRF correspond to the periodic solutions of the system. Under the 1:1 resonance hypothesis, the solutions of fixed points can be obtained by equating the derivatives of Eq. (2.10) in the following form:

$$\dot{\phi}_1 = \dot{\phi}_2 = 0 \Rightarrow \phi_1(\tau) = \phi_{10}, \phi_2(\tau) = \phi_{20} \quad (2.18)$$

By introducing Eq. (2.18) into Eq. (2.10), a system of complex algebraic equations is obtained. After several algebraic operations, the system is deduced as:

$$\begin{cases} \alpha_3 Z_{20}^3 + \alpha_2 Z_{20}^2 + \alpha_1 Z_{20} + \alpha_0 = 0, & Z_{20} = |\phi_{20}|^2 \\ \phi_{10} = \frac{\frac{i\epsilon\phi_{20}}{(1+\epsilon)(1+\epsilon\sigma)} - \frac{\epsilon^2\lambda_1\phi_{20}}{1+\epsilon} + \epsilon F + i\epsilon^2\lambda_1 F(1+\epsilon\sigma)}{\frac{\epsilon\lambda_1}{1+\epsilon} - \frac{i}{(1+\epsilon)(1+\epsilon\sigma)}} \end{cases} \quad (2.19)$$

where coefficients α_i depend on the system parameters and excitation parameters. The first equation of Eq. (2.19) is a cubic polynomial that can be resolved analytically, so as to obtain the fixed points. To determine the stability, small perturbations are introduced as follows:

$$\phi_1 = \phi_{10} + \rho_1, \quad \phi_2 = \phi_{20} + \rho_2 \quad (2.20)$$

By substituting Eq. (2.20) into Eq. (2.10), the linearization model with the Jacobian matrix is obtained:

$$\begin{bmatrix} \dot{\rho}_1 \\ \dot{\rho}_2 \\ \bar{\dot{\rho}}_1 \\ \bar{\dot{\rho}}_2 \end{bmatrix} = \begin{bmatrix} M_{11} & \epsilon M_{21} & 0 & 0 \\ M_{22} & M_{22} & 0 & M_{24} \\ 0 & 0 & \bar{M}_{11} & \epsilon \bar{M}_{21} \\ 0 & \bar{M}_{24} & \bar{M}_{21} & \bar{M}_{22} \end{bmatrix} \begin{bmatrix} \rho_1 \\ \rho_2 \\ \bar{\rho}_1 \\ \bar{\rho}_2 \end{bmatrix} \quad (2.21)$$

where

$$\left\{ \begin{array}{l} M_{11} = -\frac{i(1+\epsilon)}{2} - \frac{\epsilon\lambda_1}{2(1+\epsilon)} + \frac{i}{2(1+\epsilon)(1+\epsilon\sigma)} \\ M_{21} = -\frac{\epsilon\lambda_1}{2(1+\epsilon)} + \frac{i}{2(1+\epsilon)(1+\epsilon\sigma)} \\ M_{22} = \frac{3i(1+\epsilon)K\phi_{20}\bar{\phi}_{20}}{4(1+\epsilon\sigma)^3} - \frac{\lambda_2(1+\epsilon)}{2} + \frac{i\epsilon}{2(1+\epsilon)(1+\epsilon\sigma)} \\ M_{24} = \frac{-\frac{i(1+\epsilon\sigma)}{2} - \frac{\epsilon^2\lambda_1}{2(1+\epsilon)}}{8(1+\epsilon\sigma)^3} \end{array} \right. \quad (2.22)$$

By computing the root of the polynomial characteristic equation, the stability of the fixed points is deduced. If a real root crosses the left-half complex plane, the fixed point is unstable. Fig. 2.5 compares the FRF between the system with a cubic NES and without a NES. The maximum amplitude of the axial displacement of the primary system is plotted on the vertical axis as a function of the amplitude G and frequency σ of the excitation.

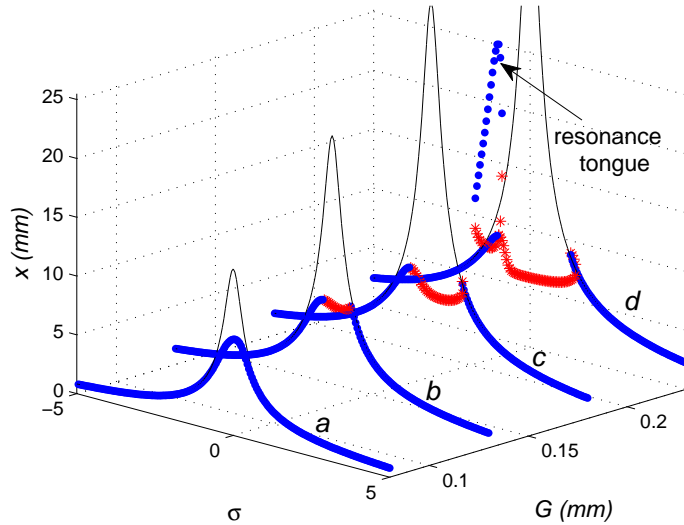


Figure 2.5: Frequency response function (FRF) of LO with cubic NES (points) and without NES (thin line) in different types of excitation: (a) $G = 0.08 \text{ mm}$; (b) $G = 0.13 \text{ mm}$; (c) $G = 0.18 \text{ mm}$; (d) $G = 0.23 \text{ mm}$. The blue points and the red crosses represent stable and unstable fixed points respectively.

With the addition of a NES, the normal model of the LO becomes nonlinear and varies for different types of energy input. When the energy is low and not sufficient to activate the NES, the resonance peak of the LO does not vanish completely (see curve *a*). For a relatively higher excitation, as shown in curves *b* and *c*, the energy pumping of the NES is activated in the unstable area. SMR regimes are possibly produced. As the excitation

amplitude is increased still further to $G = 0.23 \text{ mm}$ (see curve d), the band of frequency for SMR becomes larger. However a high amplitude detached resonance tongue appears on the left of the main backbone branch, which reduces the efficiency of the control and can be dangerous for the system.

2.1.3 Criterion for efficient energy pumping

From the FRF analysis, the aim of a design criterion should be first to ensure that energy pumping of the NES absorber is activated and second to avoid the resonance tongue under a given primary system. For this, the effect of nonlinear stiffness K and excitation G is analyzed. The maximum amplitude of the FRF is calculated and presented in Fig. 2.6(a). As the nonlinear stiffness is larger, the resonance tongue occurs more easily at low excitation. In Fig. 2.6(b), as the excitation is fixed, an optimal nonlinear stiffness located at the critical resonance tongue position can be found, where the amplitude of the LO is minimum. In Fig. 2.6(c), as the nonlinear stiffness is fixed, the maximum amplitude of the LO will not be larger than the value at this critical point. Thus, the critical position for the appearance of the resonance tongue is studied.

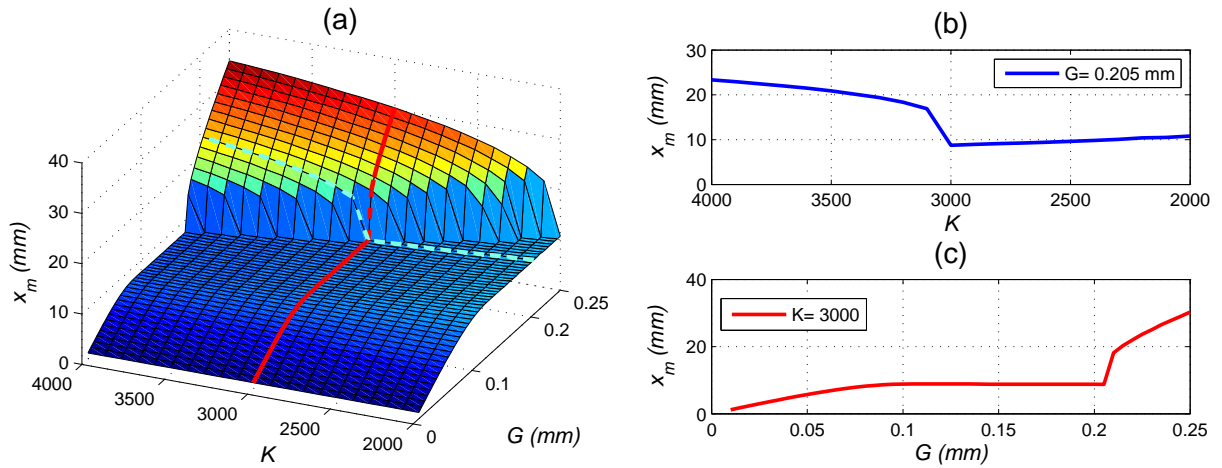


Figure 2.6: Maximum amplitude of LO with the variation of (a) nonlinear stiffness and excitation amplitude; (b) nonlinear stiffness; (c) excitation amplitude. Each point is extracted from the maximum amplitude of FRF.

Fig. 2.7 shows the multiplicity of the periodic solution of the system in Eq. (2.19). Where the boundary separating single and triple solutions corresponds to the saddle-node bifurcation, G_{1c} and G_{2c} represent the threshold of the SMR, G_{sn} represents the boundary where three periodic solutions occur in the left of the main resonance frequency. When the excitation is inside the zone $[G_{1c}, G_{sn}]$, no resonance tongue occurs and the SMR is probably produced. Therefore, once the parameters of the NES are fixed, the value of G_{sn}

can be determined as the maximum amplitude of excitation, so as to avoid the occurrence of a resonance tongue.

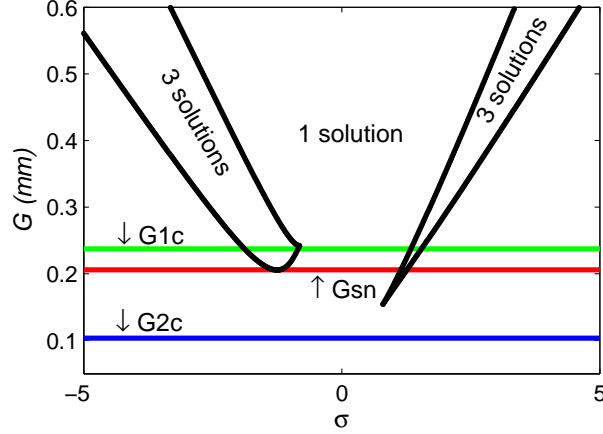


Figure 2.7: Evolution of the multiplicity of periodic solutions for the system with parameters $K = 3000$, $\lambda_1 = 0.6$, $\lambda_2 = 0.3$, $\epsilon = 0.01$.

In Fig. 2.8, the critical excitation amplitudes are presented as a function of the nonlinear stiffness.

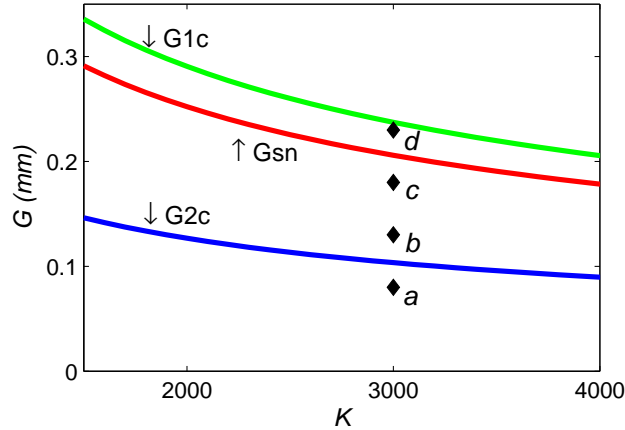


Figure 2.8: Critical excitation amplitude as a function of the nonlinear stiffness, $\lambda_1 = 0.6$, $\lambda_2 = 0.3$, $\epsilon = 0.01$.

As can be seen, the width of the SMR zone decreases as nonlinear stiffness increases. The characteristic points a , b , c and d at $K = 3000$ show good agreement with the behavior of the system in Fig. 2.5, which demonstrates that the critical amplitudes of excitation can predict the response regimes well at different excitations.

Based on the above discussion, for a given primary system, the optimal design for a NES system is dependent on the maximum amplitude of excitation. The design parameter

should be chosen to avoid a detached resonance tongue in the vicinity of the natural frequency and allow strongly modulated response at the same time. An illustration for choosing the tuned parameters of a cubic NES is given in Table 2.1, here the mass ratio, stiffness and damping of the LO, and the damping of the NES are fixed. The corresponding tuned parameters of nonlinear stiffness K are listed for different maximum amplitudes of excitation (using the G_{sn} curve of Fig. 2.8). With this value, the amplitude of the LO is minimum and no resonance tongue exists in a range of frequencies. The next section presents the design of a tuned NES with the proposed design criterion.

Table 2.1: Parameters of the tuned NES

Reduced parameters			
ε	1%	λ_1	0.6
λ_2	0.3	K	K_{sn}
K as a function of G			
G (mm)	K	G (mm)	K
0.291	1500	0.205	3000
0.252	2000	0.191	3500
0.226	2500	0.178	4000

2.2 Design theory of NES system

This section aims to propose a generalized methodology for designing a novel NES with pure cubic nonlinearity. To this end, a generic model of the NES system providing strong nonlinearity is firstly introduced. Then, to eliminate the linear stiffness, the concept of a negative stiffness mechanism is implemented by two cylindrical compression springs. Finally, design parametrizations of two kind of nonlinear springs are implemented.

2.2.1 Generalized methodology of NES

The generic model of the NES system developed in this section is presented in Fig. 2.9(a). It consists of a nonlinear characteristic part and a negative stiffness mechanism. The negative stiffness mechanism is created by two linear springs hinged together at one end with the mass of the NES, while the other ends, subjected to two equivalent preloads P , are allowed to rotate freely in frictionless horizontal channels.

As the two linear springs are subjected only to horizontal forces, their force on the axial spring is zero. From the equilibrium position, an external force (i.e. F) is applied to generate an upward displacement (i.e. u) of the output link. Within an operating

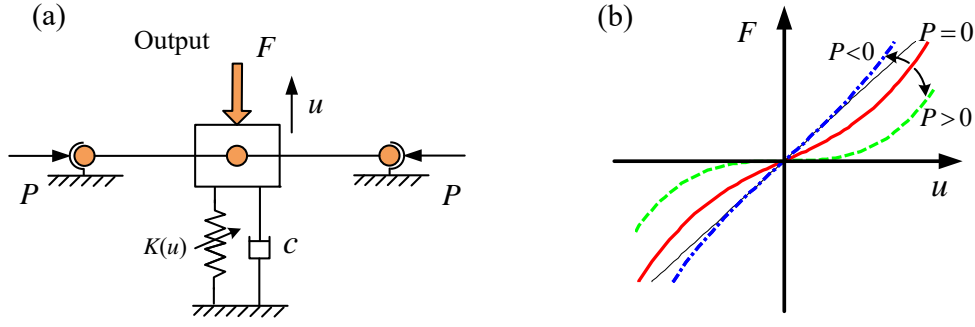


Figure 2.9: (a) Schematic of NES system with negative stiffness mechanism and nonlinear spring; (b) restoring force with respect to the compressing length.

region of the linear spring, the stiffness curve depends on the preload p . The three F - u curves in Fig. 2.9(b) denote the NES system with different lateral preloads. The corresponding force-displacement curves of the two horizontal springs and the vertical spring are presented in Fig. 2.10 (b) and (d), respectively. From the curve with no preload, a positive preload decreases the linear stiffness, whereas a negative preload increases it. As can be seen from Fig. 2.9(b), the force characteristic of case $p < 0$ is almost dominated by its component of linear stiffness (i.e. the thin black line). Thus, to obtain strong (non-linearizable) nonlinearity, the negative stiffness mechanism with $p > 0$ is adopted.

2.2.2 Eliminating linear stiffness by negative stiffness mechanism

A detailed realization of the NES system is presented in Fig. 2.11, where the negative stiffness mechanism is implemented by two cylindrical compression springs having free length l_0 . After pre-compressing to the length l (see Fig. 2.11(a)), the force-displacement relation with the Taylor expansion is expressed as:

$$f_p = 2k \frac{l_p}{l} \cdot u - k \frac{(l + l_p)}{l^3} \cdot u^3 \quad (2.23)$$

For the axial direction, the nonlinear characteristic part is realized by two nonlinear springs (i.g. conical spring or variable pitch spring). Unlike ordinary compression springs, conical springs or variable pitch springs are designed to have a nonlinear spring rate. These springs can have multiple rates or a progressively increasing spring rate as the spring compresses. Since the diameter or pitch is varied, some of the coils close up faster than the rest and become ‘inactive’, meaning that they no longer absorb the compressive energy resulting from applied forces. When the amount of active energy absorbing coils is reduced, the spring becomes stiffer and the rate increases.

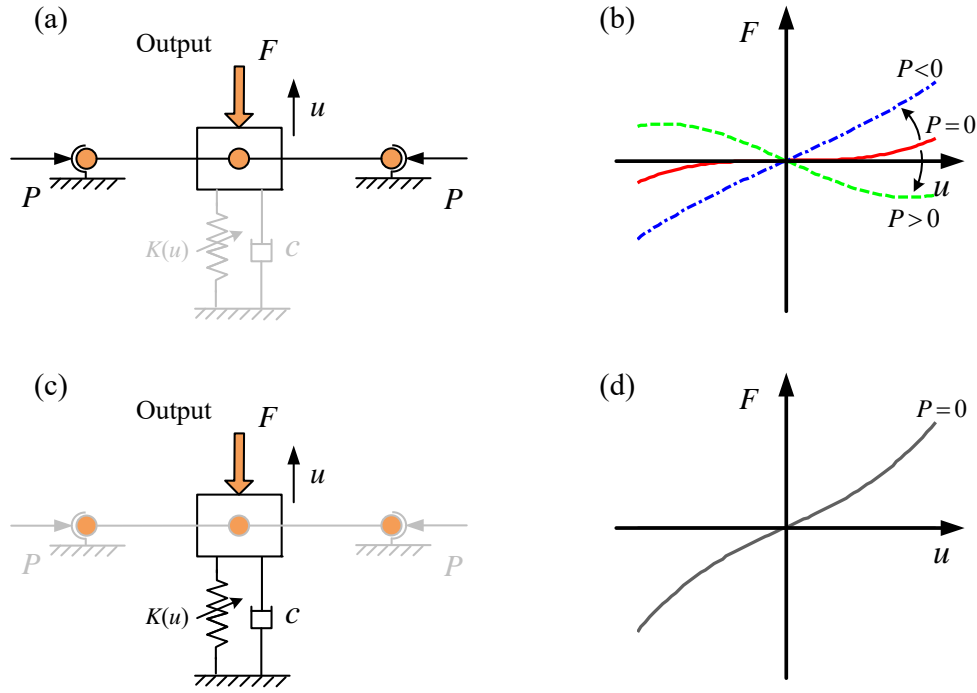


Figure 2.10: Schematic of the sub-system and the corresponding force-displacement curves, with respect to the compressing length: (a)(b) negative stiffness mechanism; (c)(d) nonlinear spring.

To benefit from the nonlinear performance of the nonlinear spring, a symmetrical connecting type of spring is proposed, as shown in Fig. 2.11(b). However, this configuration has a linear stiffness part that is hard to eliminate. To obtain the cubic nonlinearity of the NES system, the objective function of the nonlinear spring is defined as:

$$F = \begin{cases} k_0 \cdot u & (u \leq s_t) \\ a_3(u - s_t)^3 + a_1(u - s_t) + P_t & (u > s_t) \end{cases} \quad (2.24)$$

where k_0 is the stiffness of the linear phase, a_3 is the expected cubic value, a_1 is the spring rate after the group in linear phase is fully compressed to the ground block, P_t and s_t represent the force and displacement of the transition point, respectively.

To skip the linear phase, a method of pre-compressing spring at the transition point is adopted. By changing the initial origin point, the behaviors of two nonlinear springs can belong one to the linear and one to the nonlinear regime simultaneously.

By combining the two spring curves, a composed stiffness curve is obtained and the force relation is:

$$f_K = (a_1 + k_0) \cdot u + a_3 \cdot u^3 \quad (2.25)$$

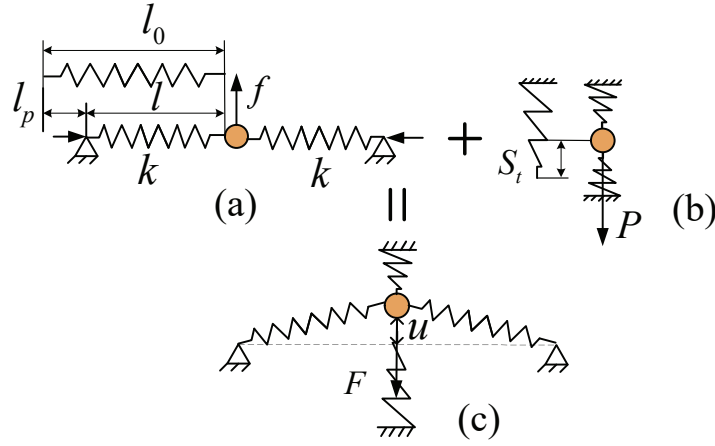


Figure 2.11: Detailed realization of NES system: (a) negative stiffness mechanism; (b) conical spring; (c) the composed system.

Obviously, the new curve is smooth and no longer piecewise (see Fig. 2.12). By adding the force of two nonlinear springs (i.e. f_K) to the force of the negative stiffness mechanism (i.e. f_p), the composed force of the NES system is obtained:

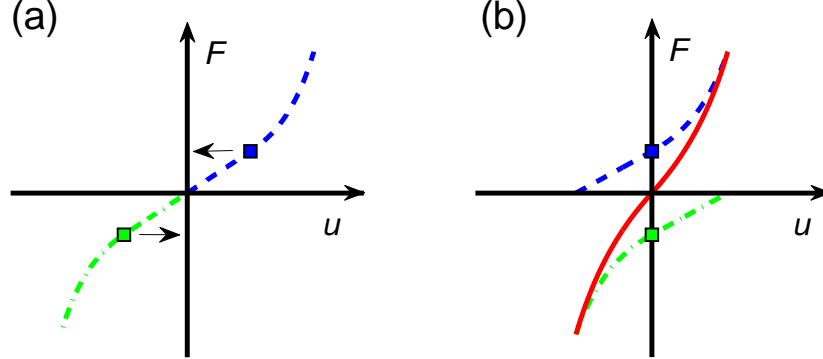


Figure 2.12: Force characteristics of two nonlinear springs (green and blue): (a) at original length; (b) pre-compressed at the transition point. The red curve represents the composed force.

$$F = (a_1 + k_0 - 2k \frac{l_p}{l}) \cdot u + (a_3 + k \frac{(l + l_p)}{l^3}) \cdot u^3 \quad (2.26)$$

As can be seen from Eq. (2.26), if $a_1 + k_0 = 2kl_p/l$, the linear component can be counterbalanced by the negative stiffness mechanism. In this case, only the pure cubic term of the equation will be left, and its coefficient will be larger with the addition of two linear springs.

2.2.3 Producing strong nonlinearity by nonlinear springs

To obtain strong nonlinearity, the design theory of nonlinear springs is proposed in this subsection. The objective here is to generate the force characteristics curve of Eq. (2.24). To this end, design parametrization of two kinds of nonlinear springs is studied. The first one is a conical spring with a constant pitch, and the second one is a cylindrical spring with variable pitch (termed as variable pitch spring).

2.2.3.1 Conical spring

Due to its self-nonlinearity, a conical spring has the advantage of providing variable spring rates and varying natural frequencies. For this work, two conical springs with a constant pitch and a constant coil diameter were adopted. The detailed design of the conical springs has been achieved in [Rodriguez et al., 2006 ; Paredes, 2013a] so that the springs do not buckle at large deflections [Patil et al., 2014]. Considering the strong nonlinearity and lower installation height, the shape of conical spring with large cone angle was used [Qiu et al., 2017].

The force characteristic of a conical spring with a constant pitch can be separated into a linear and a nonlinear part. To distinguish the two phases, three particular points are introduced, as shown in Fig. 2.13: point O corresponds to the spring free state, point T is the transition point where the nonlinear behavior starts, and point C represents the state of maximum compression.

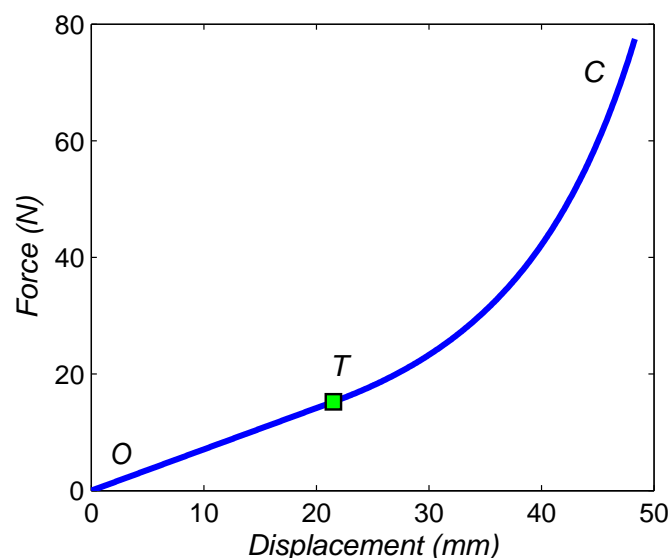


Figure 2.13: Force characteristic of conical spring , T represents the transition point between linear and nonlinear phase.

In the linear phase (from point O to point T), the largest coil is free to deflect like the

other coils, so the force-displacement relation is linear and the stiffness is expressed as:

$$R = \frac{Gd^4}{2n_a(D_1^2 + D_2^2)(D_1 + D_2)} \quad (2.27)$$

In the nonlinear regime (from point T to point C), the first elementary part of the largest coil has reached its maximum physical deflection. It starts to be a non-active element of the spring. During the second compression regime, the number of active coils decreases continuously, leading to a gradual increase of the spring stiffness. The force-displacement (F - u) relation can be described by:

$$u(F) = \frac{2FD_1^4n_a}{Gd^4(D_2 - D_1)} \left[\left(1 + \left(\frac{D_2}{D_1} - 1\right) \cdot \frac{n_f}{n_a}\right)^4 - 1 \right] + (L_a - L_s) \left(1 - \frac{n_f}{n_a}\right) \quad (2.28)$$

where d , n_a , n_f , L_a , L_s , G represent the wire diameter, number of active coils, number of free coils, initial active length, solid length of active coils and shear modulus of elasticity, respectively, and D_1 and D_2 represent the mean diameter of the smallest and largest coils. A detailed description of Eq. (2.27) and Eq. (2.28) can be found in [Rodriguez et al., 2006].

To benefit from the nonlinear performance of the conical spring, a symmetrical connecting type of spring is proposed, as shown in Fig. 2.14(a). However, this configuration has the piecewise stiffness of a linear and a nonlinear part. To skip the linear phase, a method of pre-compressing the spring at the transition point is proposed, as shown in Fig. 2.14(b).

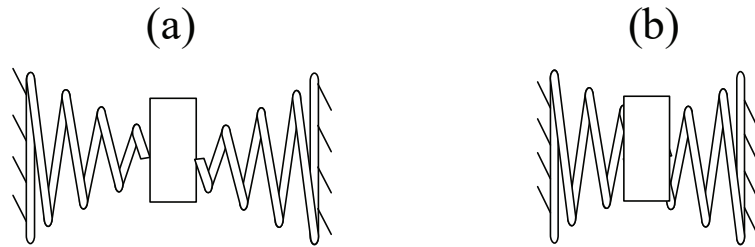


Figure 2.14: State of two conical springs: (a) at original length; (b)) pre-compressed at the transition point.

To analyze the internal polynomial components of composed force (see Fig. 2.12), the method of polynomial fitting is used, and the new force-displacement relation is written as:

$$F = b_1u + b_2u^2 + b_3u^3 + O(u^4) \quad (2.29)$$

Because of the superposition of linear and nonlinear parts, the linear term of Eq. (2.29) is hard to eliminate, yet it is possible to make the value of the square term b_2u^2 small. For this, optimization of conical spring is introduced, and the optimization model can be expressed as follows:

• **Minimize:**

the absolute values of square coefficient $|b_2|$

• **Variable:**

the mean diameter of smallest coil D_1

the mean diameter of largest coil D_2

the free length of conical spring L

the wire diameter of spring d

the number of active coils n_a

• **Constraints:**

the cubic coefficient $b_{3min} < b_3 < b_{3max}$

the linear stiffness $b_{1min} < b_1 < b_{1max}$

the transition point $s_{min} < s_t < s_{max}$

the buckling condition $0 < L_f/D < 2.6$

the spring index $5 < D_i/d < 25, i = 1, 2$

After optimizing the parameters of the conical spring (where the mean diameters D_1 and D_2 are the main factors to determine the nonlinearity), two groups of conical spring are obtained and the designed parameters are presented in Table 2.2.

Table 2.2: Designed parameters of two groups of conical spring

Designed parameters						
	d (mm)	D_1 (mm)	D_2 (mm)	n_a	L_f (mm)	\bar{G}
spring #1	2.2	12	50	8	70	7.929×10^{10}
spring #2	1.7	12	40	16	105	7×10^{10}
Force characteristics						
	$F = \begin{cases} k_0 \cdot u & (u \leq s_t) \\ a_3(u - s_t)^3 + a_2(u - s_t)^2 + a_1(u - s_t) + P_t & (u > s_t) \end{cases}$					
	k_0 (N/m)	a_1 (N/m)	a_2 (N/m ²)	a_3 (N/m ³)	s_t (mm)	
spring #1	708	836	-1.94×10^3	1.95×10^6	21.5	
spring #2	201	300	-6.67×10^3	5.01×10^5	28	

The polynomial components of springs #1 are presented in Fig. 2.15. It can be observed that the curve of the cubic and linear terms is close to the original curve $F(u)$, which

means that the contribution of the square term was small enough to be almost neglected.

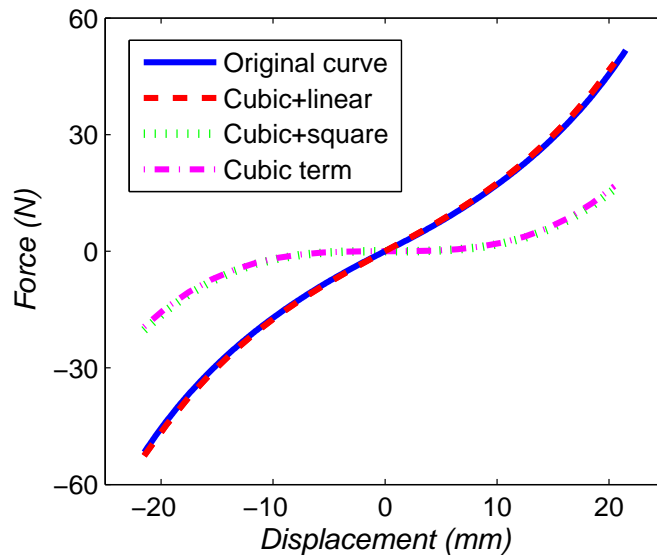


Figure 2.15: Polynomial components of the two optimized conical springs

2.2.3.2 Variable pitch spring

Since the stiffness of a variable pitch spring is piecewise, producing a smooth and nonlinear curve like that of a conical spring is hard. Here, a method using special coordinate points to fit the required stiffness curve is adopted. Depending on the method of curve fitting, two types of shape providing the polynomial components with only linear and cubic terms are proposed: (1) each coil having a different pitch; (2) each group of coils having a different pitch (see Fig. 2.16).

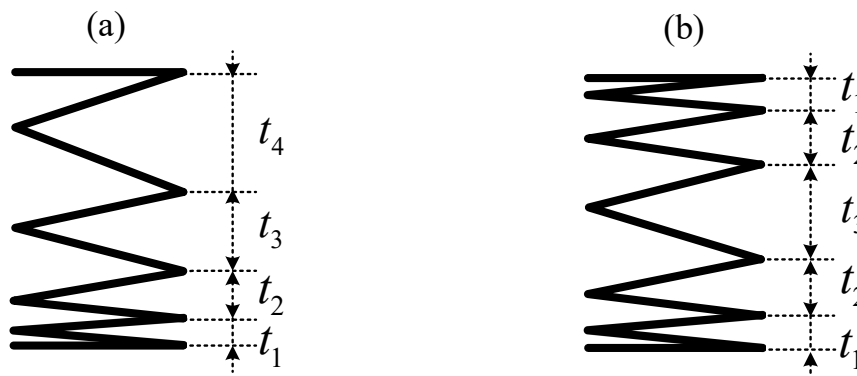


Figure 2.16: Two types of shape for variable pitch spring: (a) each coil with a different pitch; (b) each group of coils with a different pitch.

The detailed force characteristics of the two types are presented in Fig. 2.17. For the first type, each coil is set with a different pitch. As one coil is fully compressed and becomes “inactive”, a transition point occurs and the spring rate increases considerably. By fitting the transition points on the objective function curve, the pitch of each coil can be calculated. However, the positions of these transition points cannot be selected, which leads to the last pitch being exceptionally large. As can be seen from Fig. 2.17(a), the last part is hard to fit on the objective function.

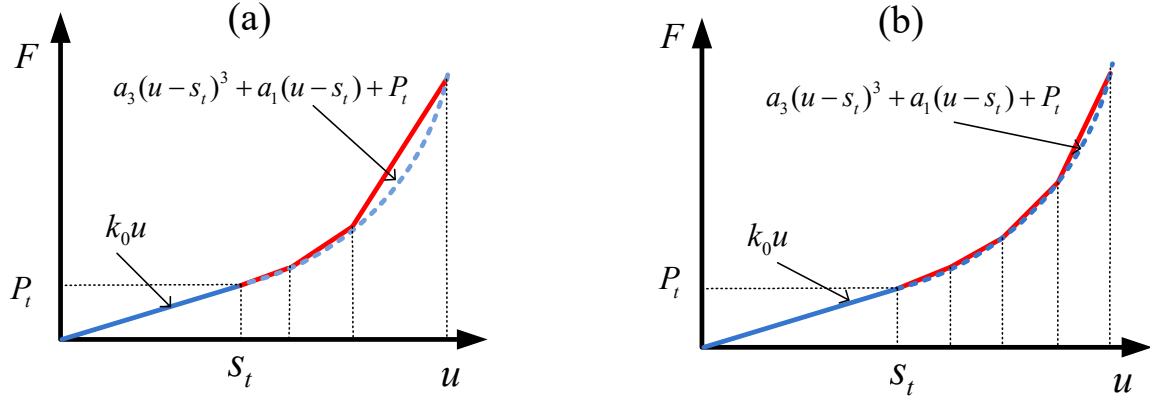


Figure 2.17: Force characteristics of variable pitch spring: (a) each coil with a different pitch; (b) each group of coils with a different pitch.

To overcome this limitation, the second type is adopted. Here, we allow some coils (usually the number is not an integer) to have the same pitch, which leads to several groups of ordinal linear springs being generated. By defining the transition points of the piecewise curve averagely on the nonlinear part, the stiffness in each piece will correspond well to the required value (see Fig. 2.17(b)). In this method, the number of transition points determines the number of groups possessing the same pitch. Then the number of active coils can be expressed by using the common formula:

$$n_a = \frac{\bar{G}d^4}{8D^3 \cdot k_0} \quad (2.30)$$

where D , d and \bar{G} represent the mean diameter of the coils, the wire diameter and shear modulus of elasticity, respectively. k_0 is the initial stiffness when all coils are active, as proposed in Eq. (2.24). Defining the total deflection length of the spring as l_f ($l_f > 2s_t$), and the number of spring groups in nonlinear regime as n , the interval of each part in the nonlinear phase is obtained:

$$\Delta = \frac{l_f - s_t}{n} \quad (2.31)$$

Within the interval of each part of the curve, the displacement and the force of each

transition point are given by:

$$\begin{aligned} u_i &= s_t + i \cdot \Delta, \quad i = 1..n \\ F_i &= a_3 i^3 \cdot \Delta^3 + a_1 i \cdot \Delta + P_t \end{aligned} \quad (2.32)$$

Then the detailed expression of each stiffness $k_1 \dots k_n$ yields:

$$k_i = \frac{F_i - F_{i-1}}{u_i - u_{i-1}} = a_3(3i^2 - 3i + 1) \cdot \Delta^2 + a_1 \quad (2.33)$$

As the stiffness is held at k_i , the remaining active coils n_i and the number of coils in each spring group \bar{n}_i can be obtained:

$$n_i = \frac{\bar{G}d^4}{8D^3 \cdot k_i}, \quad \bar{n}_i = n_{i-1} - n_i \quad (2.34)$$

Once the number of coils in each group has been obtained, the corresponding pitch can be calculated. When the force reaches the transition point between the linear and nonlinear parts, the first group of coils is fully compressed and its corresponding pitch is:

$$t_0 = \frac{s_t}{n} + d \quad (2.35)$$

When the force reaches the i_{th} transition point of the nonlinear regime, the i_{th} group of coils is fully compressed and its corresponding pitch is given by:

$$t_i = \frac{u_i - u_{i-1}}{\bar{n}_i} + t_{i-1} = \frac{\Delta}{\bar{n}_i} + t_{i-1}, \quad i = 1..n \quad (2.36)$$

By adding the length of each spring group to that of the closed ends, the free length of the variable pitch spring is obtained:

$$L_f = \sum_{i=1}^{n_a} n_i t_i + 1.5 \cdot d \quad (2.37)$$

Here, it is important to highlight that the free length should satisfy the condition: $\lambda = L_f/D \leq 2.6$, so that the variable pitch spring will not buckle as the NES mass moves in a large displacement.

To illustrate the detailed realization of a NES system, an example of the design of a variable pitch spring is presented in Table 2.3. The objective parameters are given, and the force-displacement equation of the variable pitch spring corresponds to Eq. (2.24), of which the force at the transition point is given by $P_t = k_0 s_t$. We can note that the displacement of the transition point (i.e. s_t) determines the maximum amplitude of the NES mass. The number of spring groups in the nonlinear regime (i.e. n) controls the accuracy of the curve fitting. The variable pitch characteristics are detailed in a dedicated

Table 2.3: Parameters of the variable pitch spring

Objective parameters				
k_0	160 N/m	a_1	165 N/m	
a_3	2.3×10^5 N/m ³	s_t	35 mm	
Designed parameters				
D	40 mm	d	2 mm	
G	7×10^4 Mpa	n	7	
L_f	105.6 mm	n_a	13.7	
Pitch parameters				
\bar{n}_i	t_i (mm)	α_i ($^\circ$)	k_i (N/m)	u_i (mm)
1	4.56	2.08	160	35
2.65	5.01	2.28	173	40.75
2.96	5.59	2.55	218	46.5
2.17	6.40	2.92	309	52.25
1.42	7.57	3.45	446	58
0.93	9.23	4.20	629	63.75
0.62	11.48	5.22	857	69.5
1.93	14.45	6.56	1131	75.25

table as follows. The columns from left to right show the number of coils, the pitch, the helix angle, the stiffness and the displacement of the corresponding transition point.

As can be seen, the pitch and helix angle of each spring group increase monotonously, meaning that the pitch distribution has an ascending order. To facilitate the manufacturing process, the final pitch distribution is split to symmetrical shape, as shown in Fig. 2.18.

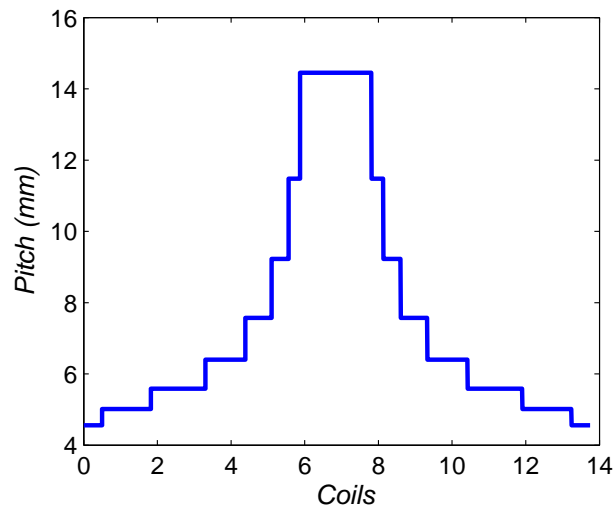


Figure 2.18: Symmetrical type of pitch distribution for the spring

With this distribution, the number of spring groups is increased but the stiffness curve keeps the same shape.

2.2.3.3 Linear spring and designed NES system

According to the design theory of two kinds of nonlinear springs, it can be observed that the design parameters of conical spring are mainly obtained by optimization, while the design parameters of variable pitch spring are directly obtained by analytical calculation. For the linear spring, the design theory is relatively well known so that only the main procedures will be presented in this subsection.

According to Eq. (2.26), the stiffness of linear spring can be obtained once the nonlinear spring is determined:

$$k = (a_1 + k_0) \frac{l}{l_p} \quad (2.38)$$

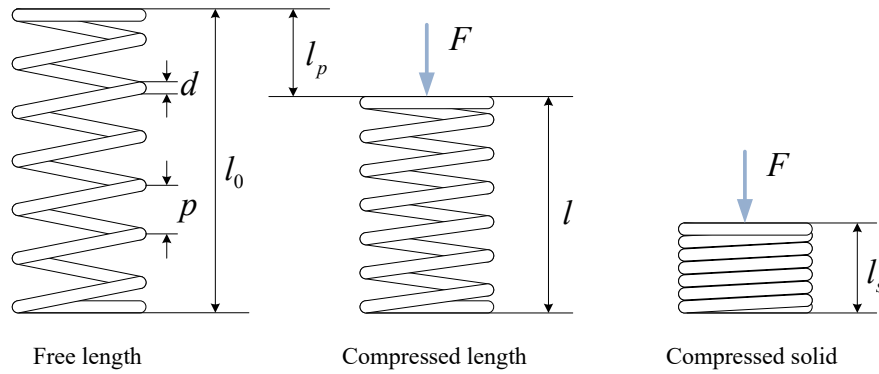


Figure 2.19: Compression spring for negative stiffness mechanism

Where l_p is the pre-compressed length, and l is the spring length after compressing, as shown in Fig. 2.19. The free length l_0 is the length of spring in the free or unloaded condition, which can be expressed as

$$l_0 = n_a \cdot p + 1.5 \cdot d \quad (2.39)$$

Depending on the requirement of the size of negative stiffness mechanism, the compressed length l_0 can be determined. Then, the pre-compressed l_p can be obtained, with the ratio of two spring set as $l_p/l_0 \approx 0.5$. With with two lengths, the stiffness of linear spring can be calculated with Eq. (2.38), and the free length can be obtained with $l_0 = l + l_p$. Considering the buckling condition and spring index, the constraints are given as:

the buckling condition $l_0/D < 2.6$
the spring index $5 < D/d < 20$
the pre-compressed length $l_p \leq l_0 - l_s = l_0 - (n_a + 1.5)d$

With the above constraints, the active coils n_a and mean diameter D can be obtained with the following formula:

$$n_a = \frac{Gd^4}{8kD^3} \quad (2.40)$$

To summarize, the process of linear spring can be generalized as $l \rightarrow l_p \rightarrow l_0 \rightarrow k \rightarrow D \rightarrow d \rightarrow n_a$. More detailed verification of the designed spring (e.g. stress and buckling) can be referred from the software of Advanced Spring Design.

Based on the proposed methods, a small-sized NES system providing strongly non-linear stiffness was designed and the assembly drawing is presented in Fig. 2.20. The component parts are spherical plain bearings, a linear guide, two nonlinear springs, two linear springs and a NES mass. It is important to highlight that the distance between each spring and the NES mass is adjustable so that a suitable force shape can be reached.

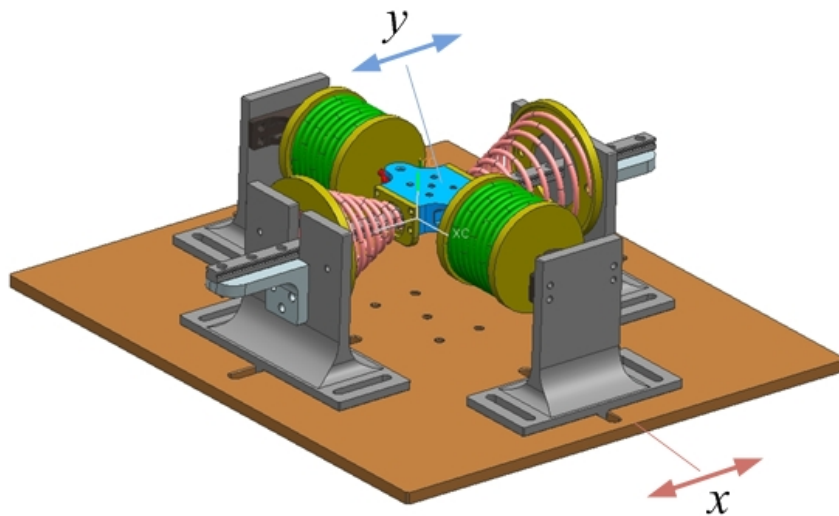


Figure 2.20: Assembly of NES system. x and y correspond to the displacement of LO and NES respectively.

2.3 Conclusion

In this chapter, the design theory of a tuned NES attached to a harmonically forced linear oscillator is investigated. Firstly, a design criterion intended to find the tuned

parameter of nonlinear stiffness for a given primary system specification is proposed. The aim of this criterion is to avoid the detached resonance tongue in the vicinity of the resonance frequency and allow SMR at the same time. To this end, a combined method with slow invariant manifold (SIM), threshold of SMR and stability of the fixed points is studied theoretically. Frequency response functions (FRF) are calculated when the different parameters (i.e. amplitude and frequency of excitation, nonlinear stiffness) are varied and explain the behavior of the NES well. As a result, an optimal nonlinear stiffness is obtained, so as to tune the NES be activated and produce the efficient TET.

Secondly, a physical configuration of the NES system for obtaining strongly cubic non-linearity is introduced. Key features of the structure include: (i) specifically sizing two nonlinear springs to provide the force polynomial components with only linear and cubic terms; (ii) pre-compressing the two springs at the transition point to produce smooth nonlinear force characteristics; (iii) adding a negative stiffness mechanism to counterbalance the linear term. To generate the nonlinear springs (i.e. variable pitch springs and conical springs), design parametrization and optimization are implemented, respectively. Finally, a special sized NES system is developed, in which the distance between each spring and the NES mass is adjustable so that a suitable force shape can be reached. In the next chapter, experimental validation of the designed NES system will be studied.

Tuned NES with nonlinear spring: experimental study

Abstract

This chapter is devoted to the experiment study of tuned nonlinear energy sink. Firstly, to validate the concept, identification of the NES system is performed, which contains the part static test of force characteristics, and detailed calculation of effective NES mass. Then experiments on the whole system embedded on an electrodynamic shaker are studied. The results show that this type of NES can not only output the expected nonlinear characteristics, but can also be tuned to work robustly over a range of excitation, thus making it practical for the application of passive vibration control. Finally, to avoid the generation of resonance tongue, a sensitivity analysis is performed with respect to the pre-compressed length of the springs.

Contents

3.1 Identification of the NES system	57
3.1.1 Static test	58
3.1.2 Effective mass	62
3.2 Dynamic test under periodic excitation	64
3.2.1 NES system with conical spring	64
3.2.2 NES system with variable pitch spring	65
3.3 Sensitivity analysis	69
3.4 Conclusion	72

3.1 Identification of the NES system

To validate the concept, identification of the NES system is studied in this section. For this, static test for two kinds of nonlinear springs and corresponding NES system is implemented, and the results are compared to that of theoretical model. Then detailed calculation of effective NES mass is explored.

3.1.1 Static test

3.1.1.1 Conical spring

Based on the design parameters of Table 2.2, two groups of conical spring were manufactured, and its force characteristics test were executed by a Spring Test 1 test bench from Andilog, Vitrolles, France (see Fig. 3.1). The force gauge had a 500 N capacity with 0.1% accuracy and 0.04 N resolution. The handle enabled a stroke of 2mm per revolution. The displacement transducer with digital display had a resolution of 0.01 mm. The axial stiffness of the test bench was taken into account to correct the lengths and reach a precision of 0.02 mm [Paredes, 2016]. The test results of two groups of conical springs are presented in Fig. 3.2 and Fig. 3.3, respectively. As expected, correspondence is good between the experimental results and the theoretical curve.

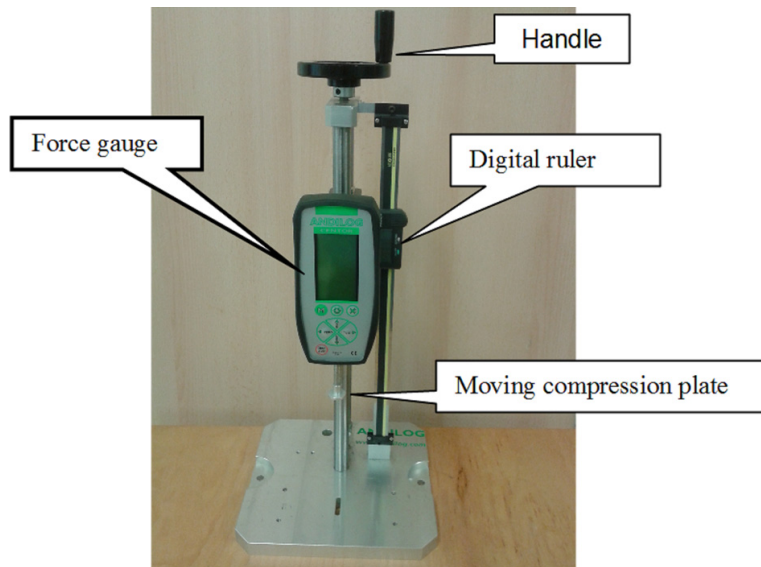


Figure 3.1: Details of the experimental setup and measuring system

In Fig. 3.4, an installed NES system with linear springs of small mean diameter and first group of conical spring is illustrated. It can be found, the linear spring has a tendency to buckle when the deflection reaches the anticipated length.

According to [Wahl, 1944], the behaviour of buckling can be characterized by using two dimensionless parameters, critical length and critical deflection. Where critical deflection is defined as the ratio of deflection l_p to the free length l_0 , the critical length is the ratio of free length l_0 to mean coil diameter D . The critical deflection is a function of critical length and has to be below a certain limit. As the connection of the spring is hinged-hinged adjustment, the corresponding critical deflection is smaller than that of fixed-fixed type. To increase critical deflection, decreasing the critical length is a feasible way. By decreasing the free length and increasing the mean coil diameter, the ratio of l_0/D can

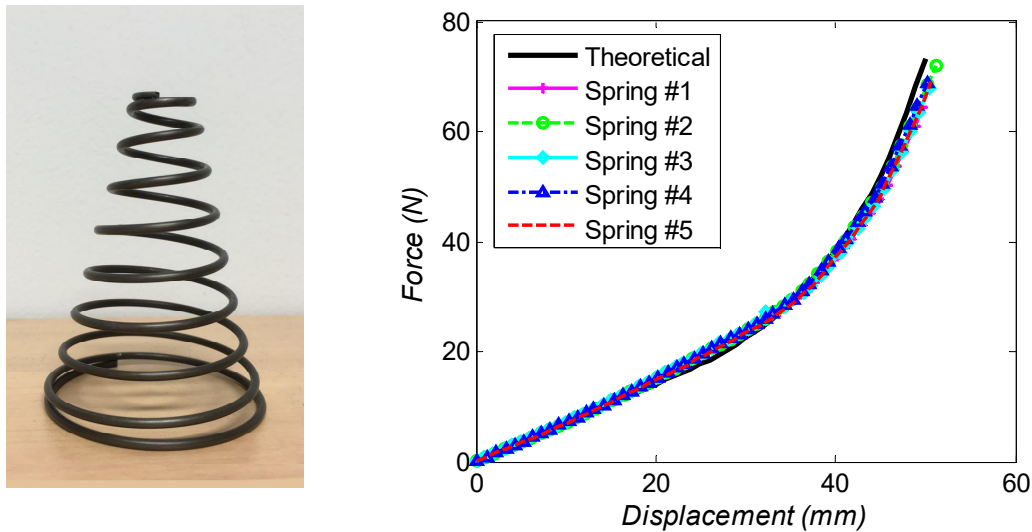


Figure 3.2: First group of conical spring and the corresponding force characteristics

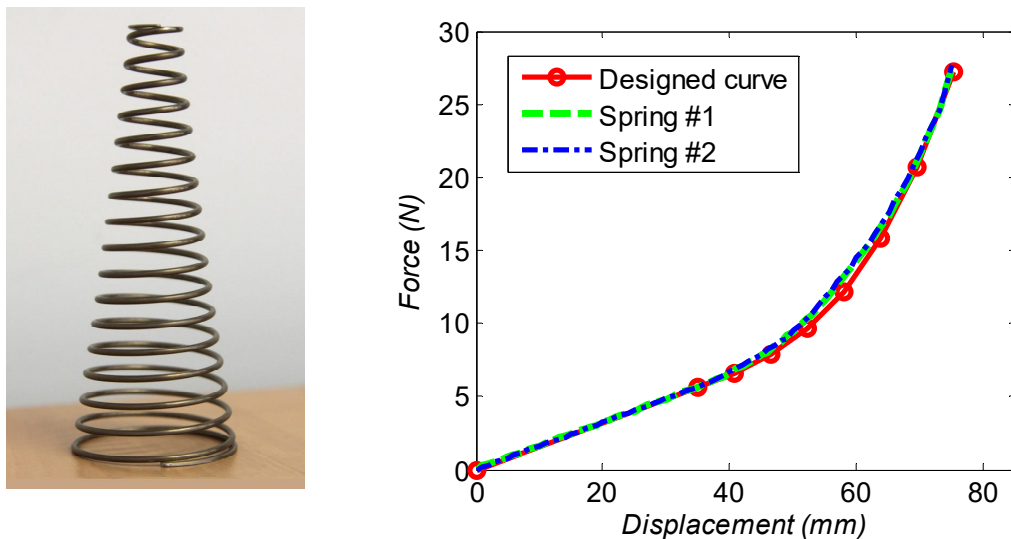


Figure 3.3: Second group of conical spring and the corresponding force characteristics

be decreased. A new system with large mean diameter of linear spring is presented in Fig. 3.5, where the buckling of spring is eliminated.

Fig. 3.6 shows the force-displacement relation of the NES with first group of conical springs. Detailed information of experimental setup is introduced in the following section. As can be seen, the experimental curve and the theoretical cubic curve corresponded well. Thus it can be concluded that combining conical springs and a negative stiffness mechanism is a feasible way to produce pure cubic nonlinearity. To enable the anticipated nonlinearity to be obtained, enough pre-compressed length should be reserved in both the variable pitch and the linear springs. Moreover, buckling of the negative stiffness

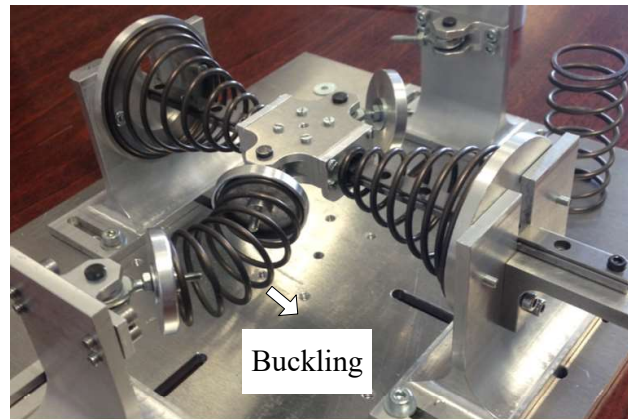


Figure 3.4: NES system with linear springs of small mean diameter

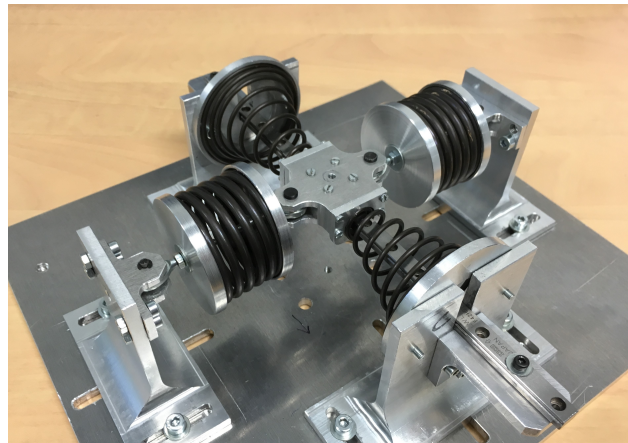


Figure 3.5: NES system with linear springs of large mean diameter

mechanism should not be neglected during the design procedure.

3.1.1.2 Variable pitch spring

Based on the design parameters of Table 2.3, the variable pitch spring was manufactured, and its force characteristics test were executed, as shown in Fig. 3.7.

With this spring, a NES system providing strongly nonlinear stiffness was designed, the components of which were spherical plain bearings, a linear guide, two variable pitch springs, two linear springs and a NES mass. It is important to highlight that the distance between each spring and the NES mass was adjustable so that a suitable force shape could be reached.

Details of the NES experimental setup and the measuring equipment are presented in Fig. 3.8. The NES mass was held by a ring so that it could be connected to the internal load cell of the force gauge. With this experimental setup, the force could be measured

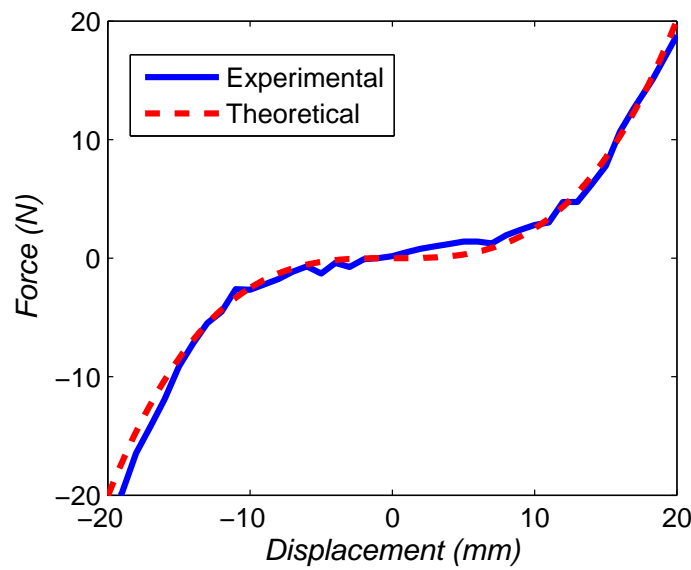


Figure 3.6: Force-displacement relation of the designed NES



Figure 3.7: Manufactured variable pitch spring and measuring equipment

by turning the handle to control the deflection of spring.

Fig. 3.9 (a) and (b) show the force characteristics of the designed spring and the NES system. Detailed comparison of parameters between the design and test is presented in Table 3.1. As can be seen, the manufactured spring curves and designed piecewise curve correspond to the objective curve well. The experimental curve of the NES system is close to the objective cubic curve.

Thus it can be concluded that the design theory of variable pitch spring is efficient to produce the anticipated nonlinearity for the NES system. Combining variable pitch springs and a negative stiffness mechanism is a feasible way to generate pure cubic non-

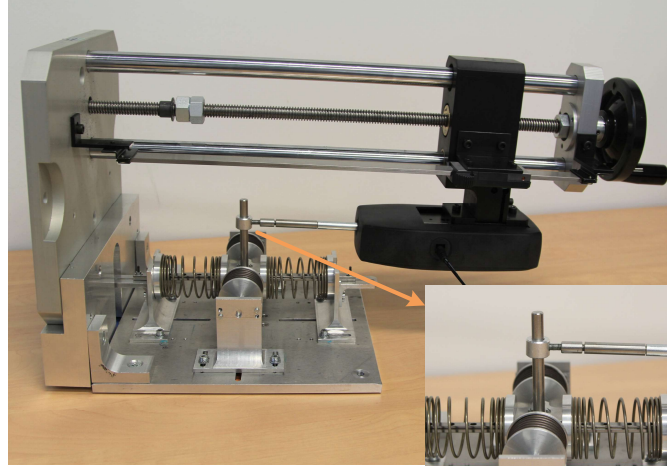


Figure 3.8: Details of the NES experimental setup and measuring system

Table 3.1: Comparison of parameters between design and test

Variable pitch spring				
$F = \begin{cases} k_0 \cdot u & (u \leq s_t) \\ a_3(u - s_t)^3 + a_1(u - s_t) + P_t & (u > s_t) \end{cases}$				
	k_0 (N/m)	a_1 (N/m)	a_3 (N/m ³)	s_t (mm)
design	160	165	2.3×10^5	35
test	160	218	1.9×10^5	35
NES system				
$F = b_0 + b_1 u + b_2 u^2 + b_3 u^3$				
	b_0 (N/m)	b_1 (N/m)	b_2 (N/m ²)	b_3 (N/m ³)
design	0	0	0	4×10^5
test	0	62	161	3.7×10^5

linearity.

3.1.2 Effective mass

The NES system can be divided in several parts: a part attached to the primary system, a NES part and the springs. The NES part includes the mass of the sliding part, the spherical plain bearing, and the support base of the linear and conical springs. For dynamic calculations, as the NES mass (m_a) is very small, the inertia of the springs is not negligible and has to be considered.

To a rough approximation, considering the spring as a beam and neglecting axial inertia, the kinetic energy of the NES mass and the linear spring is written as follows:

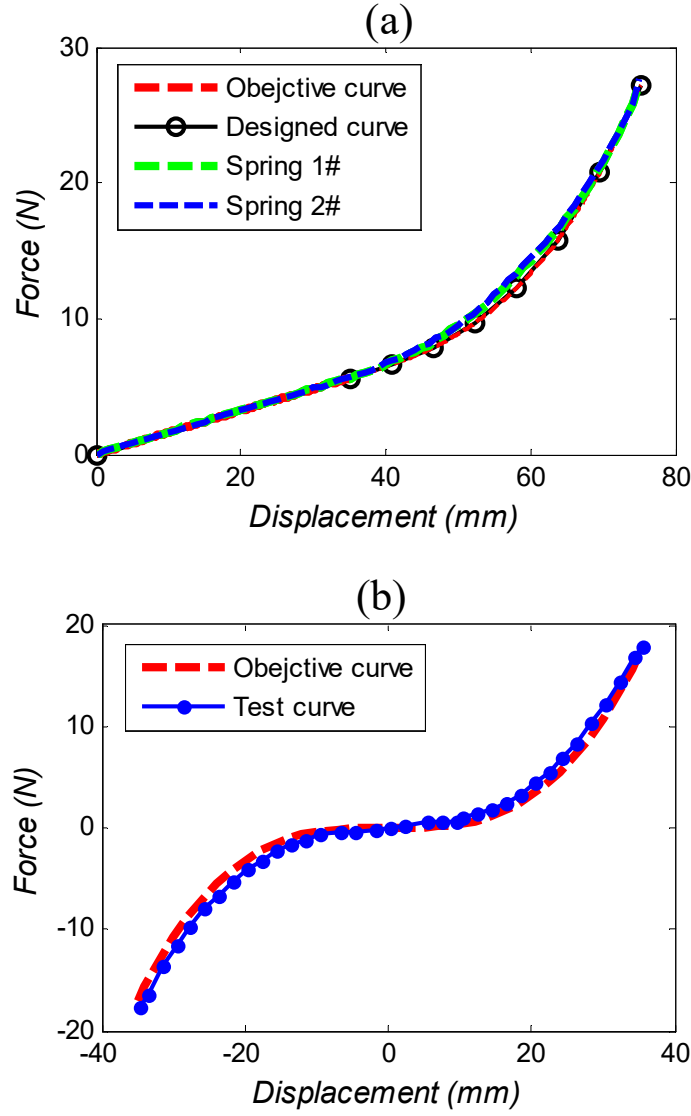


Figure 3.9: Force-displacement relation of the designed spring (a) and NES system (b)

$$T_{NES} = \int_0^{l_0} \rho_s \left(\frac{x}{l_0} \dot{y}\right)^2 dx + \frac{1}{2} m_2 \dot{y}^2 \quad (3.1)$$

where $\rho_s = m_s/l_0$ is the mass density of the spring. Thus the effective mass of a linear spring is calculated:

$$\hat{m}_s = m_s/3 \quad (3.2)$$

For the conical spring, the effective mass of \hat{m}_c can be expressed as [Yamamoto, 1999]:

$$\hat{m}_c = 2m_c \frac{\frac{1}{10}(1 - \beta^{10}) - \frac{1}{3}\beta^4(1 - \beta^6) + \frac{1}{2}\beta^8(1 - \beta^2)}{(1 - \beta^4)^2(1 - \beta^2)}, \quad \beta = \frac{D_2}{D_1} \quad (3.3)$$

Thus, the total effective mass of the NES for dynamic equations is obtained:

$$m_2 = m_a + 2\hat{m}_s + 2\hat{m}_c \quad (3.4)$$

3.2 Dynamic test under periodic excitation

The aim of dynamic test under periodic excitation is to obtain the nonlinear frequency response function of the system around the 1:1 resonance, so as to verify the energy pumping phenomenon and the efficiency of the designed NES. Here, two kinds of primary system under excitation around $G = 0.25$ mm are adopted for the experiments. The stiffness of first device is provided by two leaf springs (see Fig. 3.10), which is much stronger than the second one generated from four tension springs. According to Table 2.1, as the system is excited at $G = 0.25$ mm, the reduced parameter of nonlinear stiffness should be set around the value of 2000. For this, the #1 conical spring is adopted for the first primary system (with leaf springs), and the variable pitch spring is used for the second primary system (with tension springs).

3.2.1 NES system with conical spring

The experimental setup for NES with #1 conical springs is presented in Fig. 3.10, which consists of an LO with an embedded NES. For the LO, a weakly nonlinear behavior exists but does not affect the purpose of the tests.

The frequency response function of LO obtained with the sweeping frequency test is presented in Fig. 3.11, where the thick blue and the thin red lines represent the response of the LO with and without NES, respectively. It can be seen that the original peak of the FRF has vanished and the detached resonance tongue no longer exists. The RMS value of LO amplitude is obviously decreased with the vibration mitigation of the NES.

In the response of the LO, the dynamical flow for different values of the frequency might be attracted either to a smooth zone, or alternatively, to a number of discontinuities (range of non-monotonicity). The former corresponds to the steady state response; the latter corresponds to the unstable fixed points, where a Strongly Modulated Response (SMR) occurs. A detailed view of the SMR is presented in Fig. 3.12. Where the displacements of the LO increase and decrease alternately with the cyclical activation and deactivation of the NES. In this process, targeted energy transfer (TET) occurs and the energy is irreversibly dissipated from the LO to the NES. Thus it can be concluded that this NES with conical springs can also produce energy pumping and is efficient to protect the primary system in a large band of resonance frequencies.

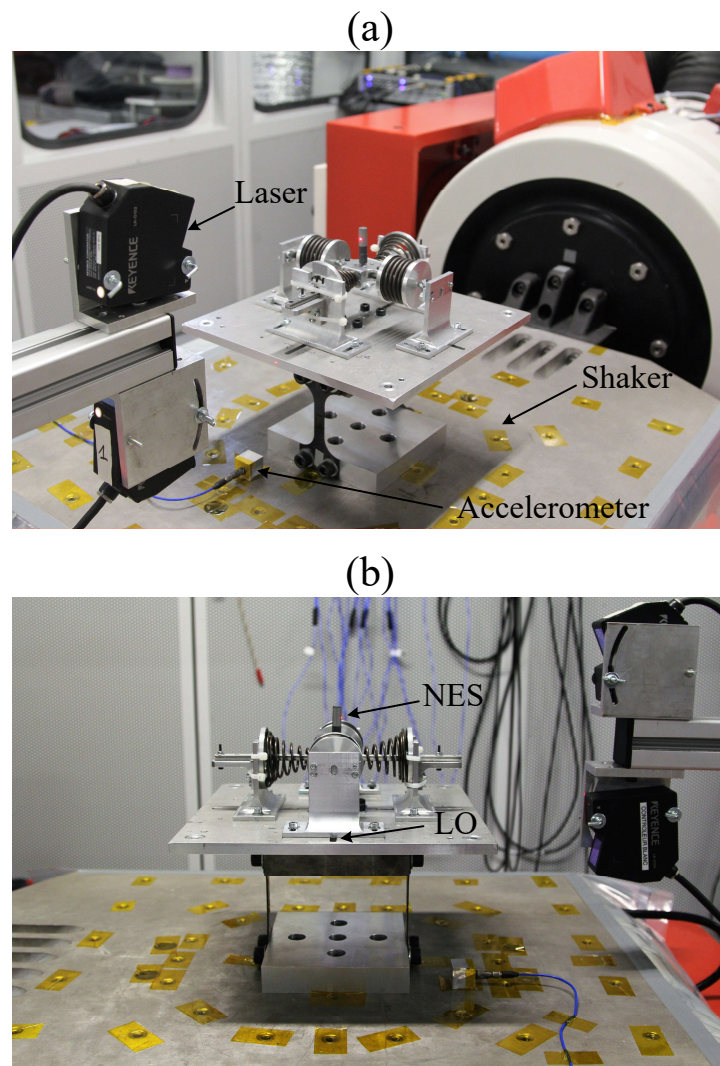


Figure 3.10: Experimental setup: (a) global view of the system and (b) detailed view of LO and NES

3.2.2 NES system with variable pitch spring

To verify the efficiency of the designed NES with variable pitch springs, an experimental study to obtain the nonlinear frequency response function of the system around the 1:1 resonance was also performed. The experimental setup is presented in Fig. 3.13.

This setup consisted of a linear oscillator (LO), with an embedded NES. The whole system was fixed on a 10 kN electrodynamic shaker. The displacement of the LO and NES, and the acceleration of the shaker were measured by two contactless laser displacement sensors and an accelerometer, respectively. The raw signals were recorded using a digital oscilloscope and a bandpass filter was applied to correct biases and suppress high frequency noise. The parameters of the experimental setup are given in Table 3.2.

The frequency response functions (FRF) under excitation with $G = 0.25$ mm and

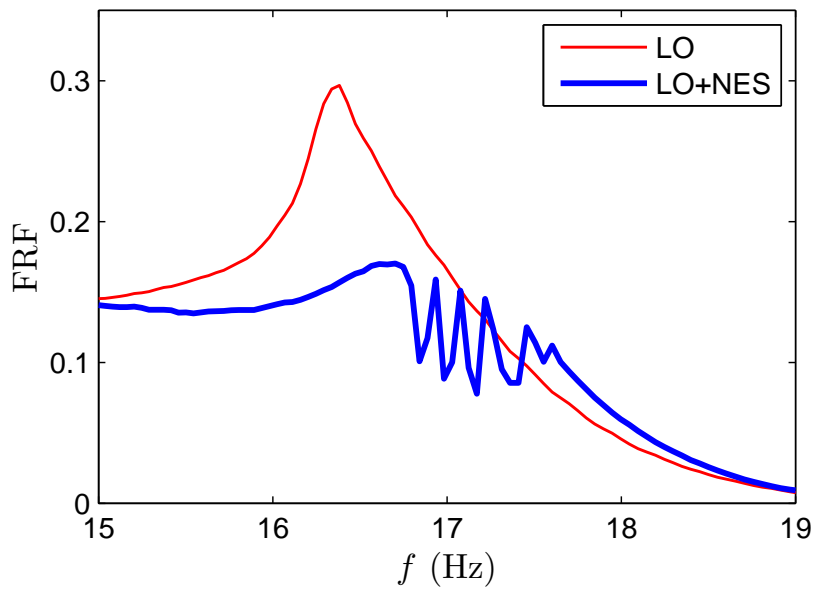


Figure 3.11: Frequency response curve of LO with (blue) and without (red) the designed NES

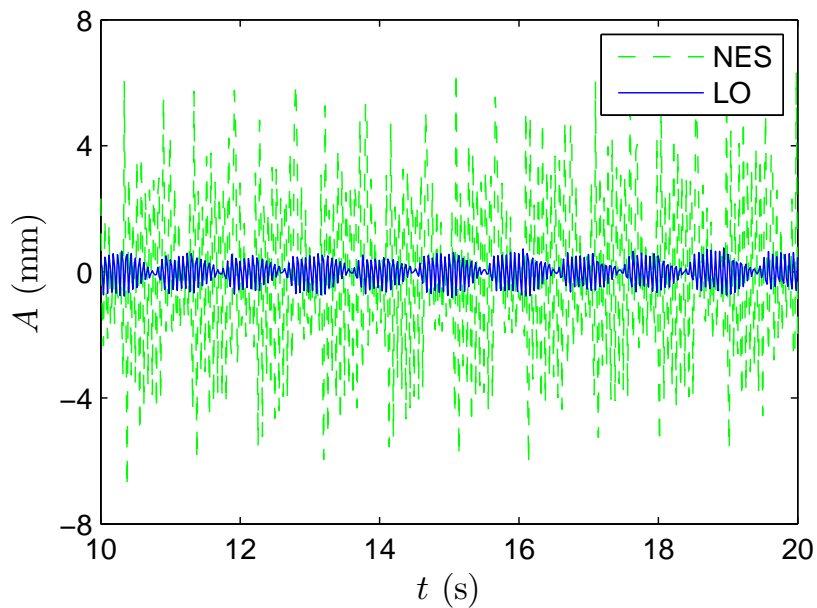


Figure 3.12: Strongly Modulated Response of LO (blue) and NES (green)

$G = 0.40$ mm are illustrated in Fig. 3.14 (a) and (b), respectively, where the thick blue and the thin red lines represent the response of the LO with and without the NES, x is the amplitude of LO, and A is the displacement of response under time history. It can be seen that the original peak of FRF has vanished, and the RMS value of LO amplitude is obviously decreased with vibration mitigation by the NES. As the excitation increases further, the maximum amplitude of the LO remains at the same value (5.3 mm). This

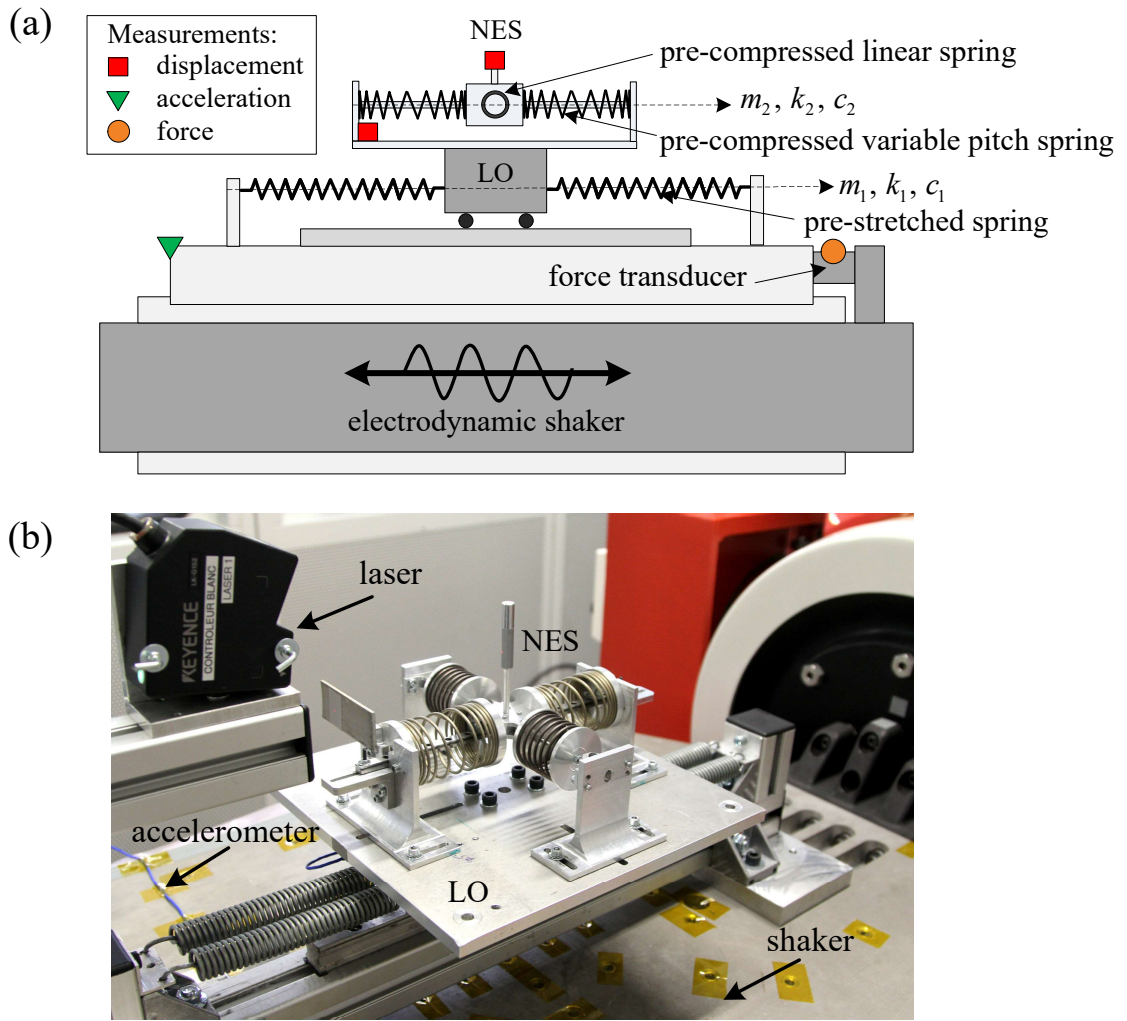


Figure 3.13: Experimental setup: (a) global scheme of the system and (b) detailed view of LO and NES.

Table 3.2: Parameters of the experiment

Physical Parameters			
m_1	5.5 kg	m_2	0.1 kg
k_1	1.15×10^4 N/m	k_2	4×10^5 N/m ³
c_1	3 Ns/m	c_2	0.4 Ns/m
Reduced Parameters			
ε	1.8%	λ_2	0.088
λ_1	0.66	K	1913

result is contrary to that for the traditional linear absorber, the tuned mass damper (TMD), where the maximum amplitude of the LO is proportional to the amplitude of excitation. Beside, an interesting phenomenon is observed: as the excitation amplitude

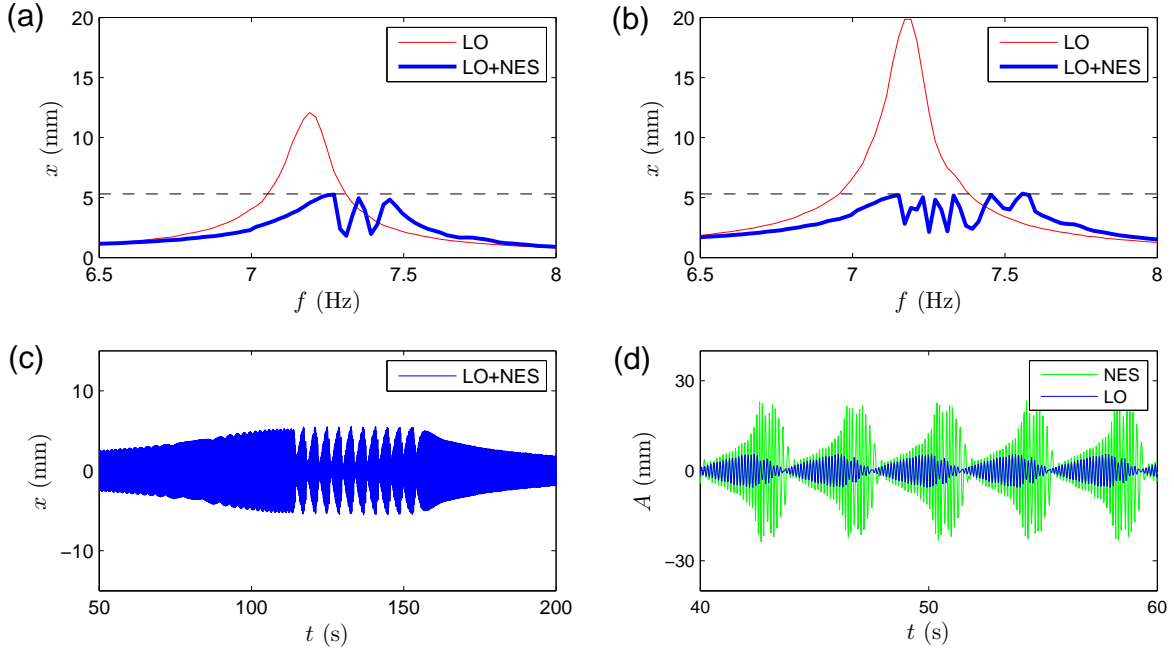


Figure 3.14: Experimental results: (a) frequency response curve of LO with (blue) and without (red) designed NES, $G = 0.25$ mm; (b) frequency response curve of LO with (blue) and without (red) designed NES, $G = 0.40$ mm; (c) detailed view of response of LO under frequency sweep test with $G = 0.25$ mm; (d) Strongly Modulated Response of LO (blue) and NES (green) with $G = 0.25$ mm, $\sigma = 0$.

becomes higher, the impact of variable pitch spring is produced when the spring is at the solid length, and the efficiency of TET is enhanced. Thus, a further study of NES with combined nonlinearity (i.e. impact and cubic nonlinearity) may be useful here.

The time-displacement response of a frequency sweep test under $G = 0.25$ mm is presented in Fig. 3.14(c). It shows that the unsmooth blue curve in Fig. 3.14(a) corresponds to the unstable fixed points, where a strongly modulated response (SMR) occurs. A detailed view of the SMR is presented in Fig. 3.14(d), where the displacements of the LO increase and decrease alternately with the cyclical activation and deactivation of the NES. In this process, targeted energy transfer (TET) occurs and the energy is irreversibly dissipated from the LO to the NES. Thus it can be concluded that this type of NES can produce energy pumping and is efficient to protect the primary system in a large band of frequencies. Moreover, it performs well in terms of controlling the maximum amplitude of the LO for different types of excitation.

3.3 Sensitivity analysis

From the static test, it is found that adjusting the pre-compressed length is easy to change the force characteristics of designed NES system, and correspondingly the results of dynamic test are also influenced. Thus, a sensitivity analysis of NES system is addressed in this section, considering the precision of the installation and quantifying the uncertainty [Opgenoord et al., 2016].

The performance of the NES relies on the given primary system specification, which is presented in Table 3.3. Here, the stiffness of primary system is larger than the previous two systems for dynamic test, so that a much larger cubic nonlinearity is adopted for the NES system.

Table 3.3: Parameters of the designed NES

Tuned parameters			
G	0.205 mm	K	3000
System parameters			
m_1	5 kg	m_2	50 g
k_1	$1 \times 10^5 N/m$	k_2	$3 \times 10^6 N/m^3$
c_1	4 Ns/m	c_2	2 Ns/m
Anticipated parameters			
\bar{S}_t	24.8 mm	\bar{l}_p	11.9 mm
b_0	0 N	b_1	0 N/m
b_2	$-4.4 N/m^2$	b_3	$2.97 \times 10^6 N/m^3$

Here, the maximum excitation amplitude is fixed as $G = 0.205 mm$, and the system parameters are related to the reduced parameters of Table 2.1. Thus the tuned parameter of nonlinear stiffness can be determined as $K = 3000$, with the physical value of $k_2 = 3 \times 10^6 N/m^3$. To obtain this value, both the conical springs and the cylindrical compression springs need to be pre-compressed to the anticipated lengths, with $\bar{S}_t = 24.8 mm$ and $\bar{l}_p = 11.9 mm$. However, it is hard to control the coefficients a_0, a_1, a_2 and a_3 at the anticipated value since differences exist in practice. To analyze their influence, differences of the adjustment length for conical and linear springs were selected as the variables, defined as γ_i and η_i , respectively (see Fig. 3.15). Then the real adjustment lengths are:

$$S_{t,i} = \bar{S}_{t,i} + \gamma_i, \quad l_{p,i} = \bar{l}_{p,i} + \eta_i, \quad i = 1, 2 \quad (3.5)$$

Thus, the system of equations (2.5) can be written in the following form:

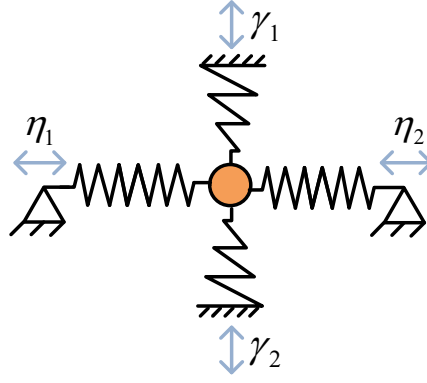


Figure 3.15: Differences of the adjustment length for conical springs (γ_i) and linear springs (η_i)

$$\begin{aligned} \ddot{x} + x + \epsilon\lambda_1\dot{x} + \epsilon\lambda_2(\dot{x} - \dot{y}) + \epsilon\zeta \cdot f(x - y) &= \epsilon F \cos \Omega\tau \\ \epsilon\ddot{y} + \epsilon\lambda_2(\dot{y} - \dot{x}) - \epsilon\zeta \cdot f(x - y) &= 0 \end{aligned} \quad (3.6)$$

where the corresponding parameters are expressed as:

$$\begin{aligned} f(x - y) &= a_0 + a_1(x - y) + a_2(x - y)^2 + a_3(x - y)^3 \\ \zeta &= 1/(m_2\omega_0^2) \end{aligned} \quad (3.7)$$

Based on Eq. (3.6), a sensitivity analysis for the stiffness of the NES is summarized in Table 3.4, where the variables γ_i and η_i are selected in the interval $[-1, 1] mm$, the objective x_m is extracted from the maximum amplitude of the LO in the numerical FRF. As can be seen, in the vicinity of the frequency of the resonance, no resonance tongue occurs, and all the maximum amplitudes of the LO are smaller than $12 mm$. In comparison with the maximum amplitude of the LO without NES ($36.2 mm$), the amplitude of the LO is decreased by more than 67% with the help of NES.

Another factor that needs to be considered is the damping of the NES. With the variation of the adjustment lengths, this value could also be changed. A sensitivity analysis for the NES damping is presented in Table 3.5, where the stiffness of the NES is fixed and the damping c_2 is selected in the variation interval $[-15, 15]\%$. The maximum amplitudes of LO are close to each other, which means that the NES is not sensitive to small differences of damping.

Three particular examples of Table 3.4 were extracted and the corresponding nonlinear force versus the response of LO and NES were calculated. The results are presented in Fig. 3.16, where positive stiffness, negative stiffness and unsymmetrical stiffness are observed, according to the example. In Fig. 3.16 (a) and (d), as the pre-compressed lengths η_i are smaller than the anticipated value, the stiffness curve is no longer pure

Table 3.4: Sensitivity analysis for the stiffness of NES

Adjustment parameters (mm)									
γ_1	γ_2	η_1	η_2	x_m	γ_1	γ_2	η_1	η_2	x_m
0	0	0	0	9.7	1	1	0	0	9.1
0	0	1	0	10.5	1	1	1	0	9.8
0	0	-1	0	9.0	1	1	-1	0	8.4
0	0	1	1	11.2	1	1	1	1	10.5
0	0	-1	-1	8.3	1	1	-1	-1	7.7
1	0	0	0	9.2	-1	-1	0	0	10.3
1	0	1	0	10.0	-1	-1	1	0	11.0
1	0	-1	0	8.5	-1	-1	-1	0	9.5
1	0	1	1	10.7	-1	-1	1	1	11.9
1	0	-1	-1	7.9	-1	-1	-1	-1	8.8
-1	0	0	0	9.8	1	-1	0	0	9.1
-1	0	1	0	10.6	1	-1	1	0	9.9
-1	0	-1	0	9.1	1	-1	-1	0	8.5
-1	0	1	1	11.4	1	-1	1	1	10.6
-1	0	-1	-1	8.4	1	-1	-1	-1	7.9

Table 3.5: Sensitivity analysis for the damping of NES

Adjustment parameters							
$c_2 (Ns/m)$	1.7	1.8	1.9	2.0	2.1	2.2	2.3
$x_m (mm)$	9.5	9.6	9.7	9.7	9.8	9.8	9.9

cubic and a positive linear stiffness is produced. It is interesting to observe that the amplitude of the LO is lower here than in the other cases, which indicates that adding a small positive stiffness may help with vibration mitigation under a certain excitation.

In Fig. 3.16 (b) and (e), the force curve has two stable equilibria and one unstable equilibrium. Between the two stable equilibria, the stiffness is negative and a bistable NES is obtained. In this case, the amplitude of the LO is increased, and the range of excitation amplitude for efficient TET is broader [Romeo et al., 2015b]. This suggests that, as the springs of this prototype are fixed for engineering applications, adjusting the pre-compressed length would provide an alternative way to increase the band in which excitation amplitude is robust. In Fig. 3.16 (c) and (f), the equilibrium of the force curve is no longer located at the center but shifts to the left. Although the stiffness curve is unsymmetrical, the energy pumping between NES and LO is still activated, leading to a significant decrease of the amplitude of the LO. Therefore, this type of NES can work robustly with differences in the adjustment lengths.

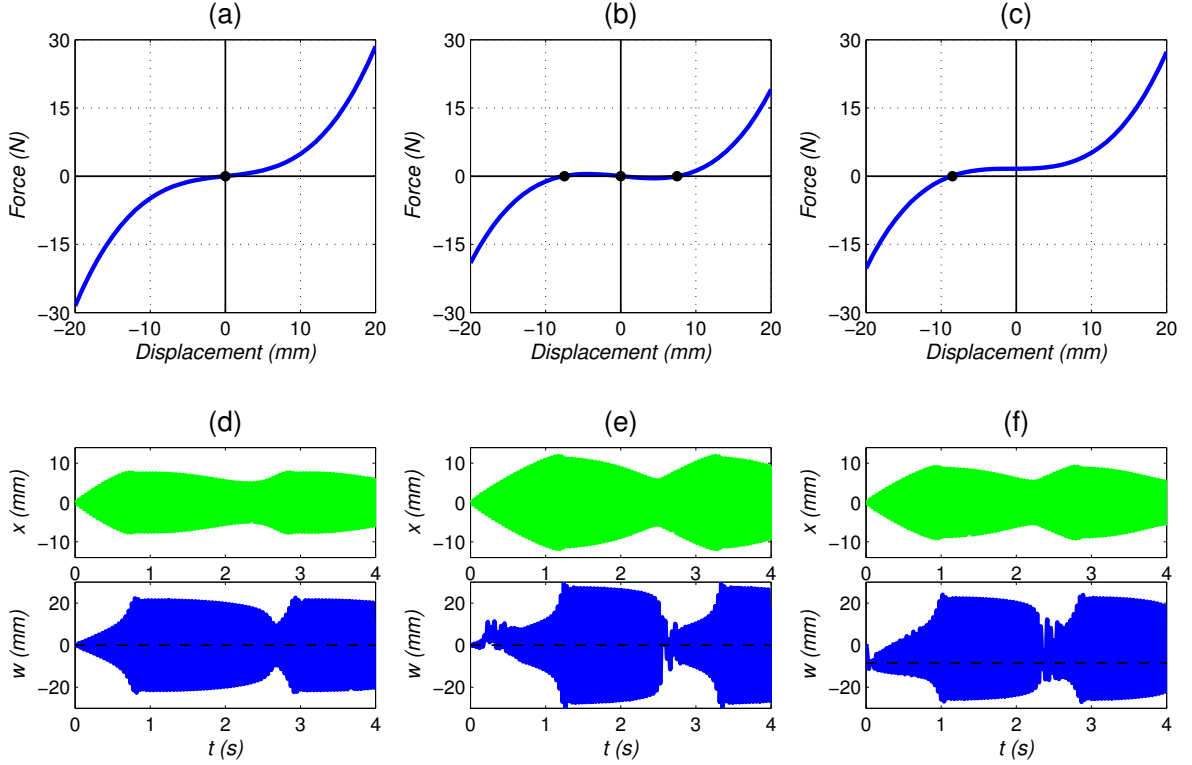


Figure 3.16: The nonlinear NES force versus the response of LO and NES with $G = 0.205 \text{ mm}$, $\sigma = -0.2$: (a)(d) positive linear stiffness, $\gamma_1 = \gamma_2 = 1$, $\eta_1 = \eta_2 = -1$; (b)(e) negative linear stiffness, $\gamma_1 = \gamma_2 = -1$, $\eta_1 = \eta_2 = 1$; (c)(f) unsymmetrical stiffness, $\gamma_1 = 1$, $\gamma_2 = -1$, $\eta_1 = \eta_2 = 0$.

3.4 Conclusion

In this chapter, experiment study of tuned nonlinear energy sink is preformed, so as to validate the concept. Firstly, identification of the NES system and calculation of effective mass are implemented. The results of force characteristics show that both the variable pitch spring and conical spring can produce strong nonlinearity, and a good correlation between the theoretical and the experimental results are observed. Thus it can be concluded that combining nonlinear springs and a negative stiffness mechanism is a feasible way to produce pure cubic nonlinearity. To enable the anticipated nonlinearity to be obtained, enough pre-compressed length should be reserved in both the nonlinear and the linear springs.

Secondly, experiments for the whole system embedded on an electrodynamic shaker are studied. The results show that the designed NESs are efficient to protect the primary system in a large band of frequencies. Moreover, it performs well in terms of controlling the maximum amplitude of the LO for different types of excitation, thus making it practical for the application of passive vibration control. For the NES with variable pitch spring,

an interesting phenomenon is observed: as the excitation amplitude becomes higher, the impact of variable pitch spring is produced, and the efficiency of TET is enhanced. To understand the efficiency of NES with impact nonlinearity, detailed theoretical study will be presented in the fifth chapter.

Finally, a sensitivity analysis is performed with respect to the adjustment differences of the springs. With the variation of adjustment length, NES with positive stiffness, negative stiffness and unsymmetrical stiffness are generated, which lays the foundation that: as the springs of this prototype are fixed for engineering applications, adjusting the pre-compressed length could provide an alternative way to increase the band in which excitation amplitude is robust. In the next chapter, detailed analysis of bistable NES (with negative stiffness) and semi-active control of this device will be studied.

Efficient targeted energy transfer of bistable NES

Abstract

This chapter is dedicated to the optimal design of a bistable NES for the vibration control of a periodically excited linear oscillator. This system with negative linear and cubic nonlinear coupling is analytically studied with the method of multiple scales. As a result, a slow invariant manifold is obtained and is applied to predict four typical response regimes at different energy levels. Moreover, asymptotic analysis and Melnikov analysis are respectively used to obtain the thresholds of these typical responses. Through their efficiency comparison, it is observed that the bistable NES can be efficient and robust in a broad-range of excitation amplitude. With the Hilbert transform and wavelet transform, Targeted energy transfer with transient or permanent 1:1 resonance is found to be responsible for the effectiveness of such responses as strongly modulated response and 1:1 resonance. Finally, an optimal design criterion and a corresponding parameter configuration are proposed to guide the semi-active control and application of this type of NES.

Contents

4.1	Theoretical Development	76
4.1.1	Modelling and analytical treatment	76
4.1.2	Response regimes	79
4.2	Study of threshold at different levels of energy	83
4.2.1	Asymptotic analysis for high energy level	83
4.2.2	Melnikov analysis for low energy level	85
4.3	Dynamical efficiency and design criterion	89
4.3.1	Efficiency of bistable NES and cubic NES	89
4.3.2	Detailed analysis of each regime	92
4.3.3	Optimal design criterion	98
4.4	Semi-active control of NES	100
4.5	Conclusion	105

4.1 Theoretical Development

From the literature review, it reveals that an appropriately designed bistable NES may be more efficient than the NES with cubic nonlinearity [Johnson et al., 2013 ; Harne et al., 2013 ; Mohammad A, 2014 ; Habib and Romeo, 2017]. However, recent studies have mainly focused on the transient dynamics between a conservative system with impulsively excited LO and a NES. The efficiency of each response regime and its corresponding threshold under periodic excitation are uncertain, so the optimal design criterion of bistable NES needs to be further studied. With this in mind, the main objective of this chapter is first to study the efficiency of different response regimes and then to establish the relation of optimization for different excitation conditions. To this end, theoretical development a 2 DOF system comprising a harmonically excited LO strongly coupled to a bistable NES is investigated in the first section.

4.1.1 Modelling and analytical treatment

The system of a harmonically excited linear oscillator (LO) with a bistable NES is illustrated in Fig. 4.1, and the equations of motion are as follows:

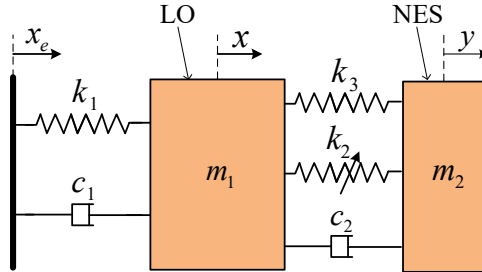


Figure 4.1: Schematic of the 2 DOF system comprising a LO and a bistable NES

$$\begin{aligned} m_1 \ddot{x} + k_1 x + c_1 \dot{x} + c_2 (\dot{x} - \dot{y}) + k_2 (x - y)^3 + k_3 (x - y) &= k_1 x_e + c_1 \dot{x}_e \\ m_2 \ddot{y} + c_2 (\dot{y} - \dot{x}) + k_2 (y - x)^3 + k_3 (y - x) &= 0 \end{aligned} \quad (4.1)$$

where x , m_1 , c_1 , k_1 and y , m_2 , c_2 , k_2 , k_3 are the displacement, mass, damping and stiffness of the LO and the bistable NES respectively. The imposed harmonic displacement x_e is expressed as: $x_e = G \cos(\omega t)$.

After rescaling, the system of equation (4.1) can be reduced to the dimensionless form:

$$\begin{aligned} \ddot{x} + x + \epsilon \lambda_1 \dot{x} + \epsilon \lambda_2 (\dot{x} - \dot{y}) + \epsilon K (x - y)^3 + \epsilon \delta (x - y) &= \epsilon F \cos \Omega \tau \\ \epsilon \ddot{y} + \epsilon \lambda_2 (\dot{y} - \dot{x}) + \epsilon K (y - x)^3 + \epsilon \delta (y - x) &= 0 \end{aligned} \quad (4.2)$$

where the term containing ϵ^2 is small and can be neglected. The corresponding physical parameters are expressed as follows:

$$\begin{aligned} \epsilon &= \frac{m_2}{m_1}, & \omega_0^2 &= \frac{k_1}{m_1}, & K &= \frac{k_2}{m_2\omega_0^2}, & \delta &= \frac{k_3}{m_2\omega_0^2}, \\ \lambda_1 &= \frac{c_1}{m_2\omega_0}, & \lambda_2 &= \frac{c_2}{m_2\omega_0}, & F &= \frac{G}{\epsilon}, & \Omega &= \frac{\omega}{\omega_0}, & \tau &= \omega_0 t \end{aligned} \quad (4.3)$$

The dots denote differentiation with respect to dimensionless time τ . New variables representing the displacement of the centre of mass and the internal displacement of the bistable NES are introduced:

$$v = x + \epsilon y, \quad w = x - y \quad (4.4)$$

Substituting Eqs. (4.4) into Eqs. (4.2):

$$\begin{aligned} \ddot{v} + \epsilon\lambda_1 \frac{\dot{v} + \epsilon\dot{w}}{1 + \epsilon} + \frac{v + \epsilon w}{1 + \epsilon} &= \epsilon F \cos \Omega\tau \\ \ddot{w} + \epsilon\lambda_1 \frac{\dot{v} + \epsilon\dot{w}}{1 + \epsilon} + \frac{v + \epsilon w}{1 + \epsilon} + \lambda_2(1 + \epsilon)\dot{w} + K(1 + \epsilon)w^3 + \delta(1 + \epsilon)w &= \epsilon F \cos \Omega\tau \end{aligned} \quad (4.5)$$

The system is studied in the vicinity of the 1:1 resonance, where both the LO and the NES execute time-periodic oscillations with identical frequency Ω . To obtain the analytical periodic solution, two new complex variables are introduced:

$$\phi_1 e^{i\Omega\tau} = \dot{v} + i\Omega v, \quad \phi_2 e^{i\Omega\tau} = \dot{w} + i\Omega w \quad (4.6)$$

Substituting Eqs. (4.6) into Eqs. (4.5) and keeping only the secular term containing $e^{i\Omega\tau}$ yields the following slowly modulated system:

$$\begin{aligned} \dot{\phi}_1 + \frac{i\Omega}{2}\phi_1 + \frac{\epsilon\lambda_1(\phi_1 + \epsilon\phi_2)}{2(1 + \epsilon)} - \frac{i(\phi_1 + \epsilon\phi_2)}{2\Omega(1 + \epsilon)} - \frac{\epsilon F}{2} &= 0 \\ \dot{\phi}_2 + \frac{i\Omega}{2}\phi_2 + \frac{\epsilon\lambda_1(\phi_1 + \epsilon\phi_2)}{2(1 + \epsilon)} - \frac{i(\phi_1 + \epsilon\phi_2)}{2\Omega(1 + \epsilon)} + \frac{\lambda_2(1 + \epsilon)\phi_2}{2} \\ - \frac{3iK(1 + \epsilon)\phi_2^2\bar{\phi}_2}{8\Omega^3} - \frac{\epsilon F}{2} - \frac{i\phi_2\delta(1 + \epsilon)}{2\Omega} &= 0 \end{aligned} \quad (4.7)$$

Substituting Eq. (2.17) and Eqs. (2.11) into Eqs. (4.7) and equating coefficients of ϵ^0 and ϵ^1 gives:

Order ϵ^0 :

$$\begin{aligned}\frac{d}{d\tau_0}\phi_1 &= 0 \\ \frac{d}{d\tau_0}\phi_2 + \frac{1}{2}i(\phi_2 - \phi_1) + \frac{1}{2}\phi_2\lambda_2 - \frac{3}{8}iK\phi_2^2\bar{\phi}_2 - \frac{1}{2}i\delta\phi_2 &= 0\end{aligned}\quad (4.8)$$

Order ϵ^1 :

$$\begin{aligned}\frac{d}{d\tau_1}\phi_1 + \frac{1}{2}\lambda_1\phi_1 + \frac{1}{2}i(\phi_1 - \phi_2) + i\sigma\phi_1 - \frac{1}{2}F &= 0 \\ \frac{d}{d\tau_1}\phi_2 + \frac{1}{2}\lambda_1\phi_1 + \frac{1}{2}\phi_2\lambda_2 + \frac{1}{2}i\sigma(\phi_1 + \phi_2) + \frac{1}{2}i(\phi_1 - \phi_2) \\ - \frac{3}{8}iK(1 - 3\sigma)\phi_2^2\bar{\phi}_2 - \frac{1}{2}F + \frac{1}{2}i\delta(\sigma - 1)\phi_2 &= 0\end{aligned}\quad (4.9)$$

By changing of variables of Eqs. (2.13) in Eqs. (4.8), the expression for a slow invariant manifold (SIM) is obtained:

$$\begin{aligned}Z_1 &= \lambda_2^2 Z_2 + (\delta - 1)^2 Z_2 + \frac{3K}{2}(\delta - 1)Z_2^2 + \frac{9K^2}{16}Z_2^3 \\ Z_1 &= N_1^2, \quad Z_2 = N_2^2\end{aligned}\quad (4.10)$$

By taking the derivative of the right-hand side with respect to Z_2 , the multiplicity of solutions can be studied. After resolution, the singular values of Z_2 are calculated:

$$Z_{2i} = \frac{4\left(2(1 - \delta) \pm \sqrt{(1 - \delta)^2 - 3\lambda_2^2}\right)}{9K}\quad (4.11)$$

In Eq. (4.11), the existence of two roots and a pair of saddle-node bifurcations needs to satisfy the condition:

$$\delta < 1 - \sqrt{3}\lambda_2\quad (4.12)$$

If δ is greater than this critical value, the SIM is monotonous. Otherwise, the SIM admits extrema and can be divided into two stable branches and one unstable branch.

An illustration of a SIM with different values of δ is given in Fig. 4.2. When the value of δ decreases, the topological shape of the SIM becomes larger and the unstable branch is shifted towards the right up direction. For a cubic NES as $\delta = 0$, the unstable branch of SIM is mainly responsible for the possible occurrence of energy pumping and it may give rise to the strongly modulated response (SMR) [Gendelman et al., 2008]. For a bistable NES as $\delta < 0$, the relation between the unstable branch and the SMR is uncertain. So in the next section, the response regimes and the corresponding SIM positions will be discussed.

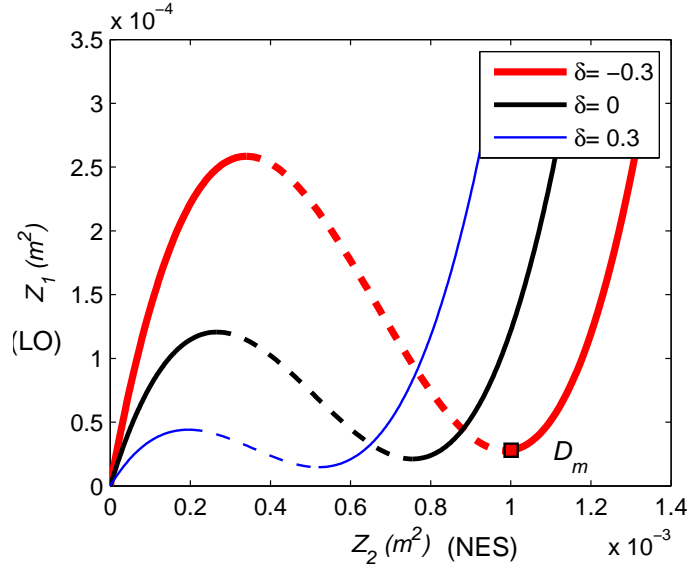


Figure 4.2: The SIM structure with different value of δ . The solid line represents the stable branch, and the dotted line the unstable branch.

4.1.2 Response regimes

The parameters identified on the simulation setup and used for the calculations are given in Tab. 4.1. The corresponding force-displacement relation of a bistable NES is presented in Fig. 4.3, where the curve has two stable equilibria and an unstable equilibrium. The region of negative stiffness is located between the two stable equilibrium points. In this area, the dynamic transition is rapid and sweeps out a large stroke, thus including viscous damping that can provide high levels of energy dissipation. If these parameters are transferred to the double-well restoring force potential, four different response regimes are obtained, as shown in Fig. 4.4, which illustrates that, with different levels of input energy, the dynamic response of a bistable NES can be classified as (a) intra-well oscillation, (b) chaotic inter-well oscillation, (c) strongly modulated response and (d) stable periodic response.

To demonstrate these regimes, the time-displacement response of the LO and NES, and the projection of motion of the system into SIM are presented in Fig. 4.5, in the first and second column, respectively. Where the simulation model is described by Fig. 2.1 under periodic excitation, the transient modulus of the LO and NES are calculated by $Z_1 = \left| (\dot{v} + i\Omega v)e^{-i\Omega\tau} \right|^2$ and $Z_2 = \left| (\dot{w} + i\Omega w)e^{-i\Omega\tau} \right|^2$. As a result, the following response regimes will occur consecutively with increasing excitation amplitude:

(a) Intra-well oscillation with $G = 0.06 \text{ mm}$. In this case, the NES exhibits a small amplitude response of oscillation about one of the stable equilibria (the dashed line). Owing to the asymmetric of amplitude of the NES, the projection in the SIM structure is a cyclic motion around the stable equilibrium, and the location is far away from the first

Table 4.1: Parameters of bistable NES

Physical Parameters			
m_1	5 kg	k_1	$11.4 \times 10^3 \text{ N/m}$
m_2	50 g	k_2	$2 \times 10^5 \text{ N/m}^3$
c_1	4 Ns/m	k_3	-50 N/m
c_2	0.4 Ns/m		
Reduced Parameters			
ϵ	1%	λ_1	1.67
K	1742	λ_2	0.167
δ	-0.44		

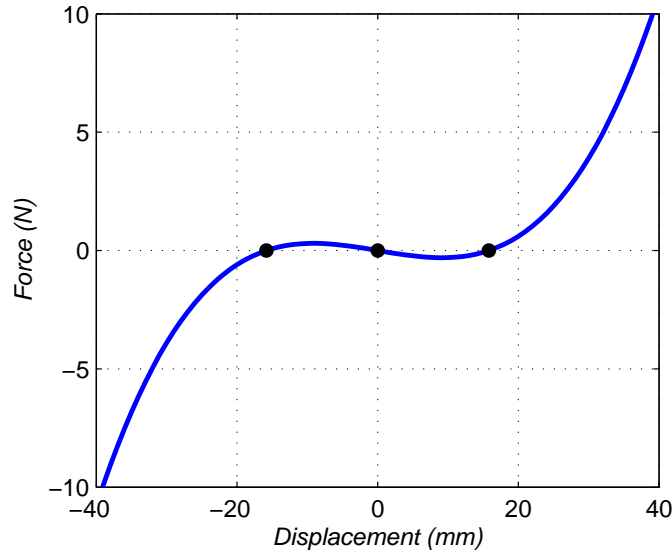


Figure 4.3: The force displacement relation of a bistable NES: the two side points represent the two stable equilibria, and the middle point represents the unstable equilibrium

stable branch of the SIM;

(b) As the excitation amplitude G increases to 0.1 mm, chaotic alternating in-well and cross-well oscillations are observed, the two stable equilibria of which are indicated by two horizontal dashed lines in the time response plots and by the vertical dashed line in the SIM plots. Taking the dashed line as a reference, it illustrates that the amplitude of cross-well oscillations is close to the value of stable equilibrium. With the characteristics of irregular in both duration and occurrence, the transient trajectory in SIM is chaotic and not repeatable;

(c) For a relatively higher level of excitation amplitude $G = 0.42 \text{ mm}$, a quasi-periodic regime with slow variation of the amplitudes of both oscillators is observed. For the LO,

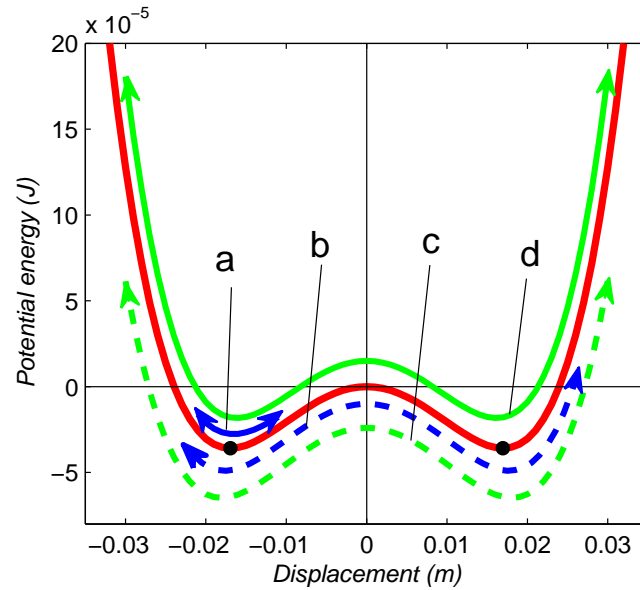


Figure 4.4: Responses at different levels of energy: **a** intra-well oscillation; **b** chaotic inter-well oscillation; **c** strongly modulated response; **d** stable periodic response

the amplitude increases and decreases repeatedly in a regular fashion. The amplitude of the bistable NES can be roughly classified into two regimes: a small region (chaotic and growing envelope) corresponding to the increase of the LO amplitude, and a large region (relatively stable envelope) corresponding to the decrease of the LO amplitude. This alternating regime of strongly modulated response (SMR) produces the jump phenomenon in SIM. However, unlike the cubic NES, the hypothetical “jump” of bistable NES does not start from the first singular point, which means that the first stable branch of SIM can not predict the threshold of targeted energy transfer;

(d) As the excitation amplitude is increased still further to $G = 0.55 \text{ mm}$, both the LO and NES show a stable periodic response, the amplitudes of which are symmetrical. This means that 1:1 resonance of LO and NES is produced. The corresponding right sub-figure shows that the steady projected motion focuses on the second stable branch of the SIM, and it has been demonstrated in [Starosvetsky and Gendelman, 2008b] that this projection can be represented by a fixed point of the SIM.

Knowing the variation mechanism of the response regimes, it would be interesting to investigate the efficiency of each regime and the corresponding threshold for periodic excitation so as to guide the design of a bistable NES. When the input energy is high, as shown in Fig. 4.4, there is a threshold that fixes whether SMR (c) or the stable periodic response (d) is obtained. By comparing the two SIM projections of Fig. 4.5, a critical fixed point located at the lowest point of the second stable branch can be found, and its position can be used to evaluate the type of response regime. For the low level of

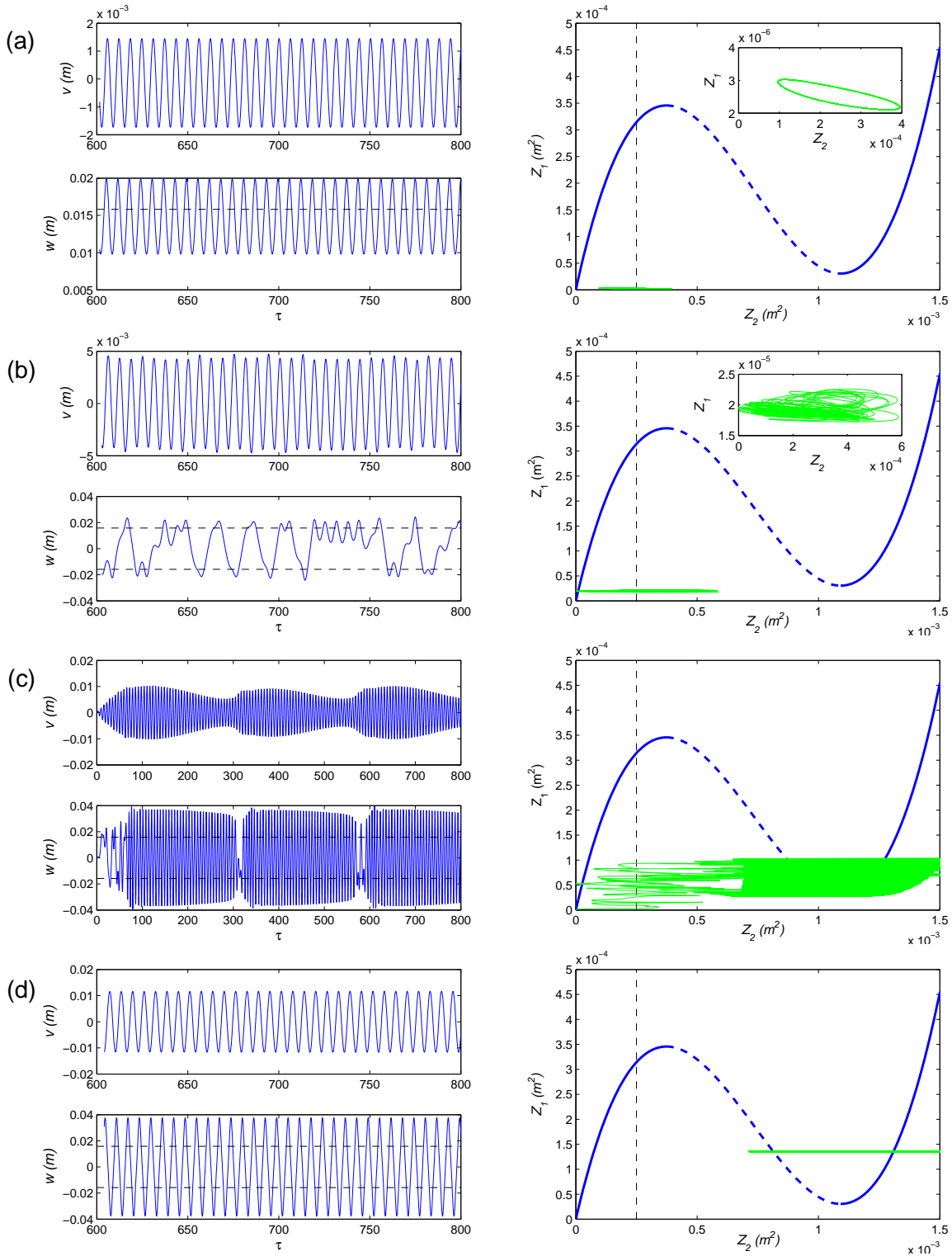


Figure 4.5: Time-displacement response of LO and bistable NES, and the motion of the system projected into SIM (a) intra-well oscillation with $G = 0.06$ mm (b) chaotic inter-well oscillation with $G = 0.1$ mm (c) strongly modulated response with $G = 0.42$ mm (d) stable periodic response with $G = 0.55$ mm

energy, the state of the bistable NES can be imagined as a ball moving in the 'double-well' structure, the dynamic response of which is restricted to oscillations confined to one stable state corresponding to response (a). When sufficient energy is input to elevate the state beyond the hilltop, the second response (b) alternating in-well and cross-well oscillation is produced. In physical terms, this hilltop analogy can be defined as a force threshold or critical load. Based on the above analysis, the threshold and the efficiency of each regime will be studied further in the following sections.

4.2 Study of threshold at different levels of energy

To predict the occurrence of intra-well oscillation or chaotic inter-well oscillation, and the transition between SMR and stable periodic response, asymptotic analysis and Melnikov analysis are respectively studied in this section.

4.2.1 Asymptotic analysis for high energy level

To obtain the threshold at high energy level, asymptotic analysis will continue to be used so as to analyse the bifurcations of the SMR regime. The fixed point corresponding to periodic responses is described in Eqs. (4.8), and we assume the solution on the stable branch to be $\Phi(\tau_1) = \lim_{\tau_0 \rightarrow \infty} \phi_2(\tau_0, \tau_1)$. By introducing this expression and Eqs. (4.8) into the first equation of Eqs. (4.9), the asymptotic stability of the points of the stable branch with respect to time scale τ_1 is studied in the following form:

$$\begin{aligned} & \frac{d}{d\tau_1} \Phi(1 - i\lambda_2 - \delta - \frac{3}{2}K\Phi\bar{\Phi}) - \frac{d}{d\tau_1} \bar{\Phi} \frac{3}{4}K\Phi^2 - \frac{3}{8}iK\Phi^2\bar{\Phi}(1 - i\lambda_1 + 2\sigma) \\ & + \frac{1}{2}\Phi(2i\sigma + \lambda_1 + \lambda_2 - \sigma\lambda_1 - i\delta + 2\sigma\lambda_2 - 2i\sigma\delta - i\lambda_1\lambda_2) - \frac{1}{2}F = 0 \end{aligned} \quad (4.13)$$

By transferring $\Phi(\tau_1)$ into polar coordinates, the expression governing the evolution of amplitude N_2 and the phase angle θ_2 are obtained:

$$\frac{\partial N_2}{\partial \tau_1} = \frac{f_2(N_2, \theta_2)}{g(N_2)}, \quad \frac{\partial \theta_2}{\partial \tau_1} = \frac{f_1(N_2, \theta_2)}{g(N_2)} \quad (4.14)$$

where

$$\left\{ \begin{array}{l} f_1 = -54 K^2 N_2^4 \sigma - 27 K^2 N_2^4 - 96 K N_2^2 \delta \sigma - 24 K N_2^2 \lambda_1 \lambda_2 + 36 F K N_2 \sin \theta_2 \\ \quad - 48 K N_2^2 \delta + 96 \sigma K N_2^2 + 12 K N_2^2 - 32 \delta^2 \sigma - 32 \lambda_2^2 \sigma - 16 \delta^2 + 64 \sigma \delta \\ \quad - 16 \lambda_2^2 + 16 \delta - 32 \sigma + \frac{1}{N_2} (16 F \delta \sin \theta_2 + 16 F \cos \theta_2 \lambda_2 - 16 F \sin \theta_2) \\ f_2 = -9 K^2 N_2^5 \lambda_1 - 24 K N_2^3 \delta \lambda_1 + 24 \lambda_1 K N_2^3 - 12 F K N_2^2 \cos \theta_2 - 16 N_2 \delta^2 \lambda_1 \\ \quad - 16 N_2 \lambda_1 \lambda_2^2 + 16 F \sin \theta_2 \lambda_2 - 16 F \delta \cos \theta_2 + 32 \lambda_1 \delta N_2 + 16 F \cos \theta_2 \\ \quad - 16 \lambda_1 N_2 - 16 N_2 \lambda_2 \\ g = 54 K^2 N_2^4 + 96 K N_2^2 \delta - 96 K N_2^2 + 32 \lambda_2^2 + 32(\delta - 1)^2 \end{array} \right. \quad (4.15)$$

In [Starosvetsky and Gendelman, 2008b], it is shown that Eq. (4.14) has two kinds of fixed point. The first is referred to as an ordinary fixed point. It is located at the branch of SIM and satisfies the condition $f_1 = f_2 = 0$ and $g \neq 0$. The others correspond to the folded singularities. In this case the derivative of Eq. (4.10) is related to the third equation of Eqs. (4.15), so it can be found that $g = 0$. Based on this, the system $f_1 = f_2 = 0$ will be discussed and is rewritten in the following matrix form:

$$\begin{bmatrix} \alpha_1 & \alpha_2 \\ \beta_1 & \beta_2 \end{bmatrix} \begin{bmatrix} \sin \theta_2 \\ \cos \theta_2 \end{bmatrix} = \begin{bmatrix} \eta_1 \\ \eta_2 \end{bmatrix} \quad (4.16)$$

where

$$\left\{ \begin{array}{l} \alpha_1 = \frac{1}{N_2} (36 F K N_2^2 - 16 F + 16 F \delta), \quad \alpha_2 = \frac{16 F \lambda_2}{N_2} \\ \beta_1 = 16 \lambda_2 F, \quad \beta_2 = -12 F K N_2^2 + 16 F - 16 F \delta \\ \eta_1 = 54 K^2 N_2^4 \sigma + 27 K^2 N_2^4 + 96 K N_2^2 \delta \sigma + 24 K N_2^2 \lambda_1 \lambda_2 \\ \quad + 48 K N_2^2 \delta - 96 \sigma K N_2^2 - 12 K N_2^2 + 32 \delta^2 \sigma + 32 \lambda_2^2 \sigma \\ \quad + 16 \delta^2 - 64 \sigma \delta + 16 \lambda_2^2 - 16 \delta + 32 \sigma \\ \eta_2 = 9 K^2 N_2^5 \lambda_1 + 24 K N_2^3 \delta \lambda_1 - 24 \lambda_1 K N_2^3 + 16 N_2 \delta^2 \lambda_1 \\ \quad + 16 N_2 \lambda_1 \lambda_2^2 - 32 \lambda_1 \delta N_2 + 16 \lambda_1 N_2 + 16 N_2 \lambda_2 \end{array} \right. \quad (4.17)$$

By solving Eq. (4.16), the phase angle of ordinary points θ_2 can be obtained as the determinant does not vanish. For the folded singularities $Z_i c$, it is observed that $\det(A) = 8F^2g/N = 0$, which means that, when $f_2 = 0$ is eliminated, the condition $f_1 = 0$ can be automatically satisfied by Eq. (4.16). Thus we can study the expression of f_2 only:

$$\sqrt{\beta_1^2 + \beta_2^2} \cos(\theta_2 - \gamma) = \eta_2, \quad \gamma = \arctan\left(\frac{\beta_1}{\beta_2}\right) \quad (4.18)$$

Then θ_2 can be deduced as:

$$\theta_2 = \arctan\left(\frac{\beta_1}{\beta_2}\right) + \arccos\left(\frac{\eta_2}{\sqrt{\beta_1^2 + \beta_2^2}}\right) \quad (4.19)$$

Based on this, the critical condition of the excitation amplitude for the existence of the folded singularities is:

$$\left| \frac{\eta_2}{\sqrt{\beta_1^2 + \beta_2^2}} \right| = 1 \quad (4.20)$$

Thus the threshold of SMR is calculated as:

$$G_{ic} = \epsilon \frac{N_{2i} F_1}{4 F_2} \quad (4.21)$$

where

$$\begin{aligned} F_1 &= 9 K^2 N_{2i}^4 \lambda_1 + 24 K N_{2i}^2 \delta \lambda_1 - 24 K N_{2i}^2 \lambda_1 + 16 \delta^2 \lambda_1 \\ &\quad + 16 \lambda_1 \lambda_2^2 - 32 \delta \lambda_1 + 16 \lambda_1 + 16 \lambda_2 \\ F_2 &= (9 K^2 N_{2i}^4 + 24 K N_{2i}^2 \delta - 24 K N_{2i}^2 + 16 \lambda_2^2 + 16(\delta^2 - 1)^2)^{\frac{1}{2}} \end{aligned} \quad (4.22)$$

4.2.2 Melnikov analysis for low energy level

The criterion of excitation amplitude to produce SMR at high level of energy having been detected, the next objective is to predict the ignition area of chaotic response at low level of energy. For this, Melnikov analysis is introduced. It is a function that can measure the distance between the stable and unstable manifolds for a saddle of the perturbed system [Wiggins, 2003 ; Guckenheimer and Holmes, 2013]. The dynamical system is written as:

$$\dot{z} = f(z) + \epsilon g(z, t); \quad z = \begin{Bmatrix} u_1 \\ u_2 \end{Bmatrix} \in \mathbb{R}^2 \quad (4.23)$$

where $f(z)$ is a Hamiltonian vector field on \mathbb{R}^2 and $\epsilon g(z, t)$ is a small perturbation which does not need to be Hamiltonian itself. To fit this function, the second equation of the system of equations (4.2) is equivalent to:

$$\ddot{w} + \lambda_2 \dot{w} + Kw^3 + \delta w = \ddot{x} \quad (4.24)$$

Then we define that

$$\lambda_2 = \epsilon \hat{\lambda}_2, \quad \ddot{x} = \epsilon \hat{x} \quad (4.25)$$

Substituting Eq. (4.25) into Eq. (4.24) and transferring it into the form of Eq. (4.23), the expression can be written as:

$$\begin{aligned} \dot{u}_1 &= u_2 \\ \dot{u}_2 &= -\delta u_1 - Ku_1^3 + \epsilon(\hat{x} - \hat{\lambda}_2 u_2) \end{aligned} \quad (4.26)$$

For $\epsilon = 0$, Eq. (4.26) has two centres at $(u_1, u_2) = (\pm\sqrt{-\delta/K}, 0)$ and a hyperbolic saddle at $(u_1, u_2) = (0, 0)$, the Hamiltonian of the system is:

$$H(u_1, u_2) = \frac{u_2^2}{2} + \delta \frac{u_1^2}{2} + K \frac{u_1^4}{4} \quad (4.27)$$

where the potential function can be written as:

$$U(u_1) = \delta \frac{u_1^2}{2} + K \frac{u_1^4}{4} \quad (4.28)$$

The corresponding curve is presented in Fig. 4.6(a). It shows that, when the energy has the local maximum at $u_1 = 0$, a global homoclinic bifurcation will be produced, which implies a transition from intra-well oscillation to inter-well oscillation.

The unperturbed homoclinic orbits that connect the saddle point of the potential energy curve are given by:

$$\begin{aligned} q_+^0(\tau) &= (R \cdot \operatorname{sech}(S\tau), -RS \cdot \operatorname{sech}(S\tau) \tanh(S\tau)) \\ q_-^0(\tau) &= -q_+^0(\tau) \end{aligned} \quad (4.29)$$

where $S = \pm\sqrt{-\delta}$ and $R = \sqrt{-2\delta/K}$. Additionally, two homoclinic orbits based at $q_{\pm}^0 = (\pm R, 0)$ are presented in Fig. 4.6(b). Its function as the pseudo-separatrix for the occurrence of chaotic motion will be discussed later.

According to the Melnikov function, the distance between stable and unstable manifolds is given by $M(\tau_0)$:

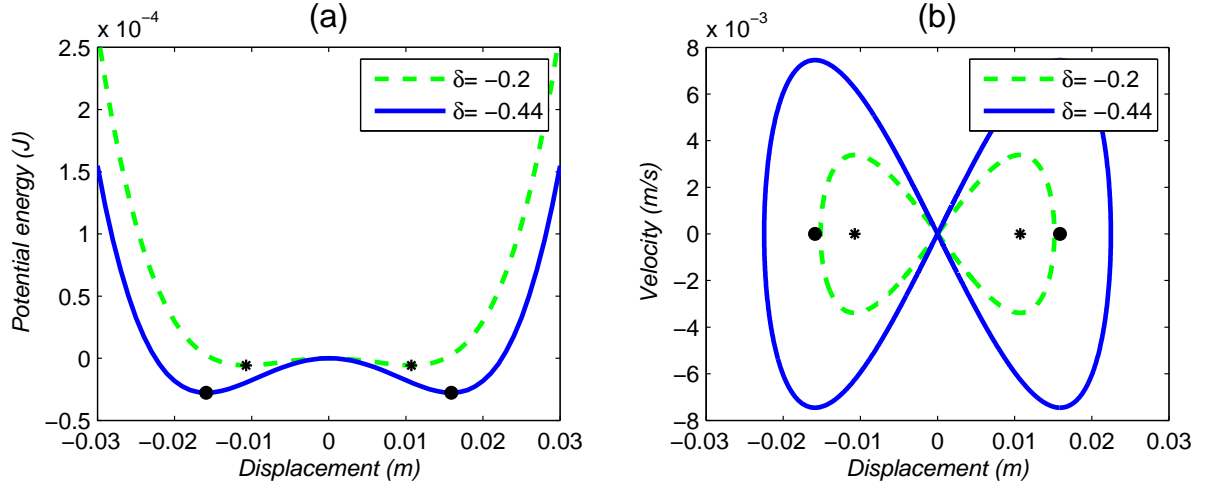


Figure 4.6: (a) Potential energy and (b) Hamilton phase plane: pseudo-separatrix

$$M(\tau_0) = \int_{-\infty}^{\infty} f(q^0(\tau)) \wedge g(q^0(\tau), \tau + \tau_0) d\tau \quad (4.30)$$

The \wedge operator is the wedge product of $f(q^0(\tau))$ and $g(q^0(\tau), \tau + \tau_0)$. To present the computation of $M(\tau_0)$ for $q_+^0(\tau)$, f and g are written as:

$$f(q^0(\tau)) = \begin{pmatrix} -RS \cdot \operatorname{sech}(S\tau) \tanh(S\tau) \\ -\delta R \cdot \operatorname{sech}(S\tau) - KR^3 \cdot \operatorname{sech}^3(\tau) \end{pmatrix} \quad (4.31)$$

$$g(q^0(\tau, \tau + \tau_0)) = \begin{pmatrix} 0 \\ \hat{x} - \hat{\lambda}_2 RS \cdot \operatorname{sech}(S\tau) \tanh(S\tau) \end{pmatrix} \quad (4.32)$$

Thus,

$$M(\tau_0) = -RS \int_{-\infty}^{\infty} \operatorname{sech}(S\tau) \tanh(S\tau) \hat{x}(\tau + \tau_0) d\tau - R^2 S \hat{\lambda}_2 \underbrace{\int_{-\infty}^{\infty} S \cdot \operatorname{sech}^2(S\tau) \tanh^2(S\tau) d\tau}_{= [\frac{\tanh^2}{3}]_{-\infty}^{+\infty} = 2/3} \quad (4.33)$$

Yielding

$$M(\tau_0) = -RS \int_{-\infty}^{\infty} \operatorname{sech}(S\tau) \tanh(S\tau) \hat{x}(\tau + \tau_0) d\tau - \frac{2R^2 S \hat{\lambda}_2}{3} \quad (4.34)$$

As the energy of excitation decreases, the response of the NES will change from aperiodic alternating cross-well and intra-well oscillation to intra-well oscillation. During this

process, the phase trajectory will pass the pseudo-separatrix, the amplitude of LO will tend to be stable, and pass through the critical maximum value N_0c . To obtain this value, we suppose that the periodic response of \hat{x} is written as:

$$\hat{x} = \hat{A}\cos(\Omega\tau + \phi) \quad (4.35)$$

Substituting Eq. (4.35) into Eq. (4.34), and using the theorem that trigonometric functions are even or odd since $\cos(\Omega(\tau + \tau_0) + \phi) = \cos(\Omega\tau_0 + \phi)\cos(\Omega\tau) - \sin(\Omega\tau_0 + \phi)\sin(\Omega\tau)$, $M(\tau_0)$ can be expressed as:

$$M(\tau_0) = - \int_{-\infty}^{\infty} \text{sech}(S\tau)\tanh(S\tau)\sin\left(\frac{\Omega}{S}S\tau\right)dS\tau \times R\hat{A}\sin(\Omega\tau_0 + \phi) - \frac{2R^2S\hat{\lambda}_2}{3} \quad (4.36)$$

With the method of residues, the integral term can be calculated as:

$$M(\tau_0) = -R\hat{A}\frac{\pi\Omega}{S}\sin(\Omega\tau_0 + \phi)\text{sech}\left(\frac{\pi\Omega}{2S}\right) - \frac{2R^2S\hat{\lambda}_2}{3} \quad (4.37)$$

According to Eq. (4.25), $\hat{A} = -N_1\Omega^2/\epsilon$. By substituting this equation to Eq. (4.37), $M(\tau_0)$ finally becomes:

$$M(\tau_0) = \sqrt{\frac{2}{K}} \frac{N_1\pi\Omega^3}{\epsilon}\sin(\Omega\tau_0 + \phi)\text{sech}\left(\frac{\pi\Omega}{2\sqrt{-\delta}}\right) \pm \frac{4\delta\sqrt{-\delta}}{3K} \frac{\lambda_2}{\epsilon} \quad (4.38)$$

From Melnikov theory, the fact that $M(\tau_0)$ has a zero solution means that the transverse interaction between stable and unstable manifolds exists in the system, which leads to the appearance of chaos. Then we can obtain the necessary condition for this chaos interaction as:

$$N_{0c} = \frac{2\sqrt{2}(-\delta)^{\frac{3}{2}}\cosh\left(\frac{\pi\Omega}{2\sqrt{-\delta}}\right)}{3\sqrt{K}\pi\Omega^3}\lambda_2 \quad (4.39)$$

When $N_1 < N_0c$, the movement of the NES will enter one of the two wells. When the excitation exceeds this value, inter-well motion will occur as a consequence of the homoclinic bifurcation. So there is an analytical border that indicates whether the response is likely to chaos or not.

The effects of negative stiffness δ and cubic nonlinearity K on the Melnikov threshold for homoclinic bifurcation are illustrated in Fig. 4.7, where the excitation frequency is given by $f = \omega/2\pi$. The curves shown represent a boundary with the upper domain

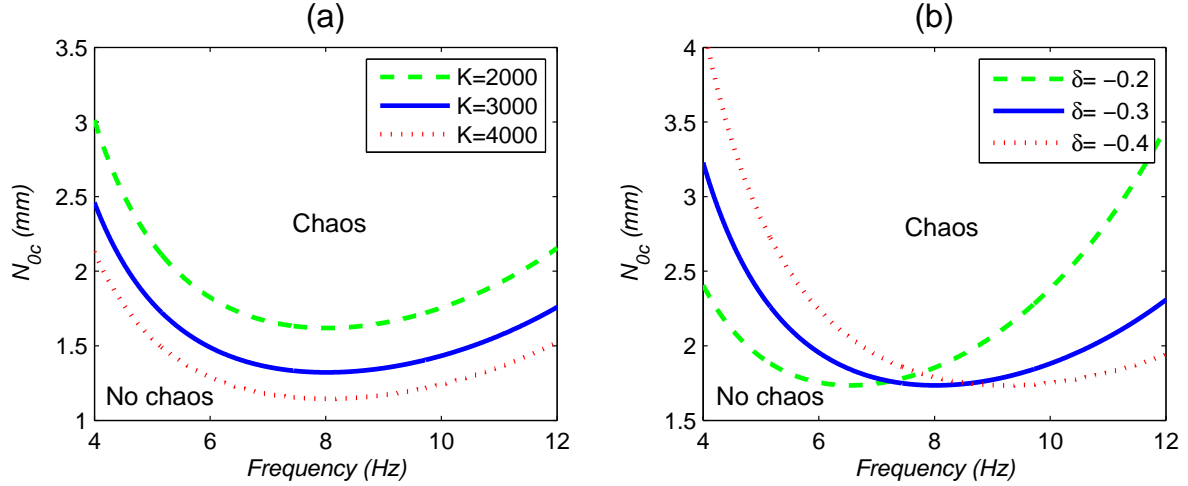


Figure 4.7: The critical amplitude for the appearance of intra-well and chaotic oscillations as a function of the excitation frequency, with the various values of (a) cubic nonlinearity and (b) negative stiffness.

indicating the area for corresponding chaotic inter-well oscillation. From the perspective of the LO amplitude in Fig. 4.7(a), we can find that increasing the value of cubic nonlinearity will result in a decreased amplitude threshold for homoclinic bifurcation. In Fig. 4.7(b), an increase in the negative stiffness δ leads to a shift of the stationary point ($\partial N_{0c}/\partial f = 0$) toward a higher frequency, which means that, if a system has resonance in the high frequency range, using higher negative stiffness is an easier way to obtain a low amplitude threshold.

4.3 Dynamical efficiency and design criterion

To guide the application of bistable NES under harmonic excitation, the efficiency of different response regimes is compared and their underlying TET is firstly studied in this section. Then, an optimal design criterion of bistable NES and a corresponding parameter configuration are proposed.

4.3.1 Efficiency of bistable NES and cubic NES

Since the thresholds have been deduced for each level of energy, the corresponding dynamical efficiency will be discussed in this section. For a better understanding of the performance of a bistable NES, Fig. 4.8 and Fig. 4.9 provide a comparison between a cubic NES and a bistable NES for the energy dissipation ratio and the amplitude of the LO. The energy dissipated by the LO and the NES in the time interval (τ_0, τ) is:

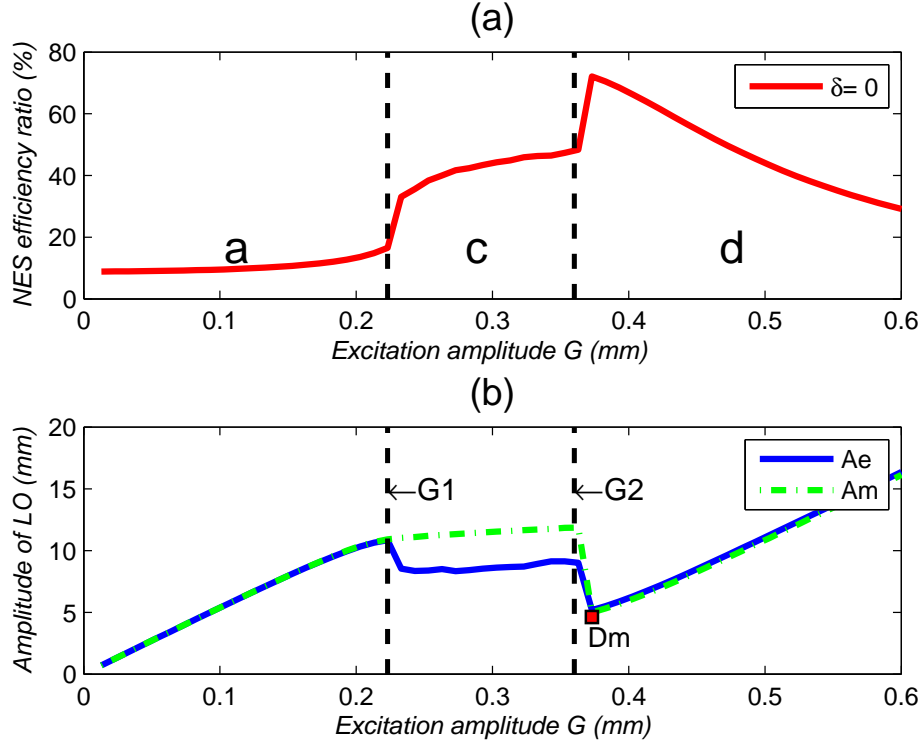


Figure 4.8: Efficiency of cubic NES (a) energy dissipation ratio of NES and (b) amplitude of the LO. A_e represents the mean amplitude, and A_m the maximum amplitude

$$\begin{aligned}
 E_{LO}(\tau) &= \int_{\tau_0}^{\tau} \epsilon \lambda_1 \dot{x}^2 d\tau \\
 E_{NES}(\tau) &= \int_{\tau_0}^{\tau} \epsilon \lambda_2 (\dot{x} - \dot{y})^2 d\tau
 \end{aligned} \tag{4.40}$$

Therefore, the energy dissipation ratio of the NES (i.e. the efficiency) can be defined as:

$$r_{NES} = \frac{E_{NES}}{E_{LO} + E_{NES}} \times 100\% \tag{4.41}$$

For the cubic NES in Fig. 4.8, the areas a , c and d respectively represent the fixed point, SMR and fixed point in the SIM structure. Where A_e is the mean amplitude (i.e. average value of the slowly varying envelopes), A_m is the maximum amplitude (i.e. maximum value of the slowly varying envelopes). When the input energy is too low to activate the energy pumping of the cubic NES, the efficiency is poor, and the amplitude of LO increases linearly with the excitation amplitude. As the input increases to the range $[G_1, G_2]$, the difference between the mean amplitude and the maximum amplitude is distinguished for SMR, in which the amplitude of NES is no longer stable. When the excitation amplitude passes the threshold G_2 and makes the NES work in area d , an

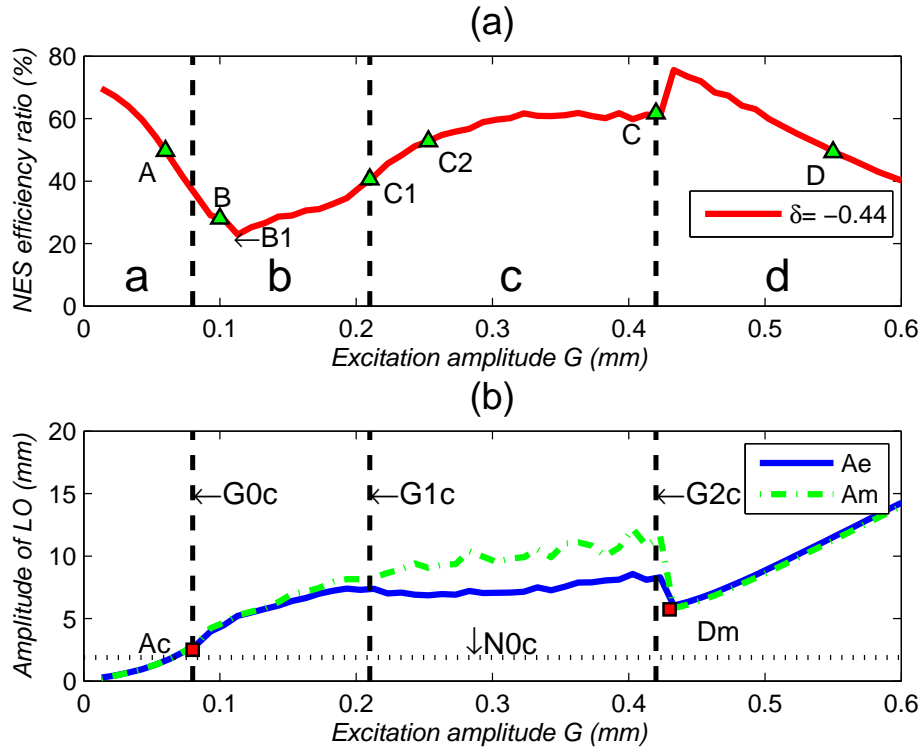


Figure 4.9: Efficiency of bistable NES (a) energy dissipation ratio of NES and (b) amplitude of the LO. A_e represents the mean amplitude, and A_m the maximum amplitude

optimal point D_m is observed where A_e and A_m are the same at the minimum value, and the efficiency ratio of the NES is maximum, almost 74% of the targeted energy is dissipated by the cubic NES.

For bistable NES in Fig. 4.9, the areas *a*, *b*, *c* and *d* represent four different regimes: intra-well oscillation, chaotic inter-well oscillation, SMR and stable periodic response, respectively, where the points *A*, *B*, *C* and *D* correspond to the excitations $G = 0.06$ mm, $G = 0.1$ mm, $G = 0.42$ mm and $G = 0.55$ mm that we observed previously. Unlike the cubic NES, as the input energy is low, the bistable NES shows high efficiency, even it works in the intra-well oscillation area with small displacement, it can produce a higher dynamical performance. For relatively higher levels of excitation in area *b*, this regime of chaotic response is observed to have low efficiency of energy dissipation. Comparing the excitation threshold of SMR to that of the cubic NES, as given in Tab. 4.2, shows that the amplitude band $[G_{1c}, G_{2c}]$ is broader once the contribution of negative stiffness is added. Moreover, owing to the higher speed and larger stroke swept in the dynamic transition of negative stiffness area, the efficiency of the bistable NES will be higher than that of the cubic NES. An interesting point is that the threshold of G_{1c} is close to the corresponding value G_1 of cubic NES. A further study of the theoretical aspects may be useful here. For

area d , there is a minimum amplitude D_m , where the LO amplitude starts to increase and the efficiency of NES decreases with the growth of excitation amplitude. By comparing the threshold of $G_2c = 0.42 \text{ mm}$ to the calculation result of Eq. (4.21) that equals 0.422 mm , it can be demonstrated that these two solutions correspond with each other well. So in the following section, the analytical solution of G_2c can be used to predict the location of D_m .

Table 4.2: Excitation threshold

bistable NES			cubic NES	
G_1c	G_2c	G_0c	G_1	G_2
0.21 mm	0.42 mm	0.08 mm	0.22 mm	0.36 mm

Here, it is important to emphasize that at the condition of “monochromatic” external excitation ($\omega/\omega_0 \approx 1$), the TMD performs better than the cubic NES or bistable NES. The configuration of the primary system coupled either to the TMD or the NES can be obtained by setting k_2 to zero or non-zero value in Eqs. (4.1), respectively. The main expected advantage of the NES were observed when it was applied to linear multi-dof systems (with remote frequencies), as demonstrated in [Starosvetsky and Gendelman, 2008a]. Owing to its self-tuning property, energy pumping may be excited in the vicinity of each natural frequency (under periodic excitation), thus providing a substantial reduction of energy for the main structure as compared to the TMD case (which may be tuned to a single frequency only). Additionally, the NES can be effective over a much broader range of frequencies than the TMD and does not suffer from the problem of amplification just outside the target bandwidth [Gourdon et al., 2007], thus making it preferable for various engineering applications when the primary system is subject to harmonic forcing in a wide range of excitation frequencies.

4.3.2 Detailed analysis of each regime

To further explain the efficiency and verify the thresholds proposed in previous methods, the pseudo-separatrix mentioned above, the Hilbert transform and wavelet transform are introduced to discuss the detailed dynamics in the following subsection.

4.3.2.1 Intra-well oscillation

In Fig. 4.9, the threshold G_0c exists between areas a and b , when the LO excited at this value, the corresponding oscillation amplitude A_c obtained is close to the dashed line N_0c calculated by Eq. (4.39), so it proves that the numerical result coincides with the

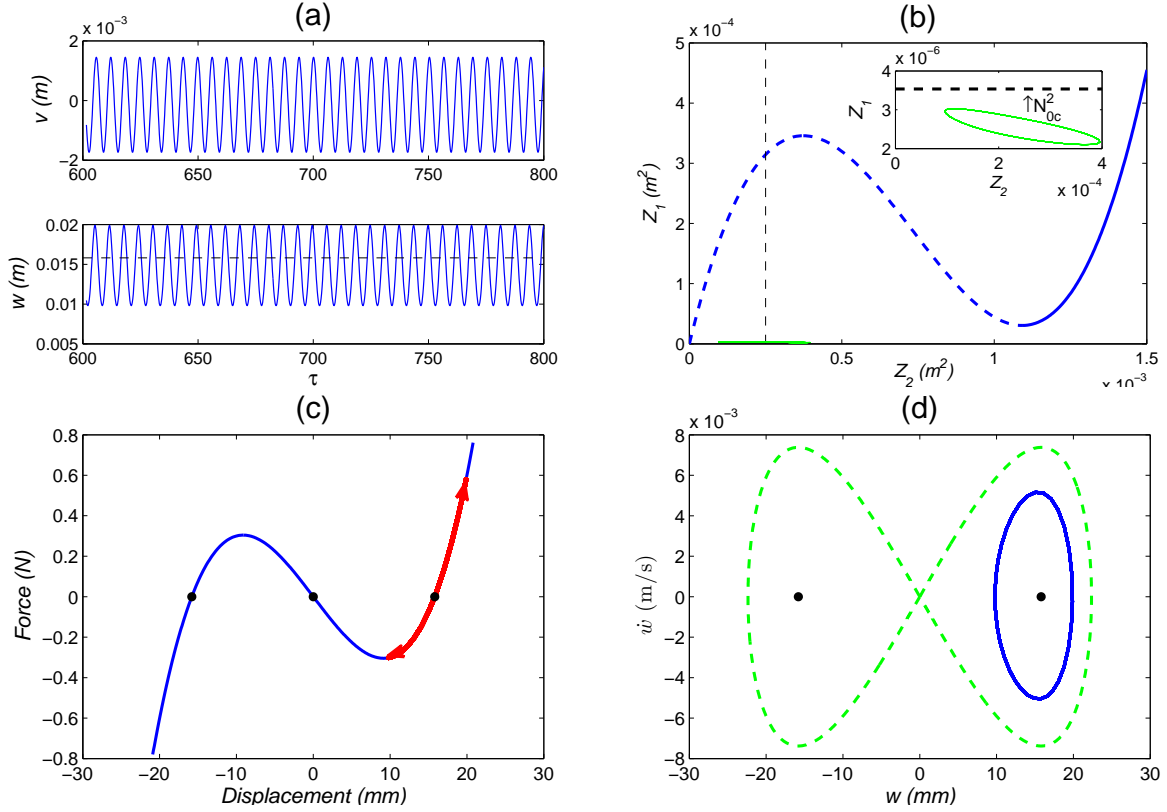


Figure 4.10: Response corresponding to point A (a) time-displacement response (b) projection in SIM structure (c) working range in the force-displacement relation (d) phase trajectory of NES

analytical prediction. When the energy is lower than G_{0c} , as shown in Fig. 4.10(b), the cyclic projection in the SIM structure is under the dashed line N_{0c} , which corresponds to Fig. 4.10(d) where the phase trajectory is inner the pseudo-separatrix. The red curve in Fig. 4.10(c) shows that the bistable NES works around the stable equilibrium on the force-displacement curve.

Due to the asymmetricity of the force-displacement curve, the two sides of the amplitude of NES presented in Fig. 4.10(a) are also asymmetric. Since the initial nonlinear stiffness around the stable equilibrium is far larger than that of cubic NES, which is close to zero, the bistable NES can produce nonlinear beating even under a small excitation. Therefore, the bistable NES can have a high efficiency ratio with low energy input.

4.3.2.2 Chaotic inter-well oscillation

As the excitation amplitude increases to the range of response b , the working force-displacement range of the NES becomes large and starts to pass the two stable equilibria. It is observed that the dynamic trajectory escapes from one potential well to the other, achieving a global snap-through motion. The chaotic behaviour in this regime is identified

in [Romeo et al., 2015a], where the Lyapunov characteristic exponents are calculated and the values of exponents are found to be positive. In Fig. 4.11(b), the chaotic projection in the SIM structure is above the dashed line N_{0c} , which means that enough energy is supplied so to overcome the potential barrier: the hilltop of Fig. 4.4. With reference of the pseudo-separatrix, the outer, inner and crossing transient trajectories on the phase diagram are observed consecutively in Fig. 4.11(d). These three regimes correspond respectively to the steady transition motion between two stable equilibria, the transition motion captured by a stable equilibrium and the subharmonic nonlinear beating.

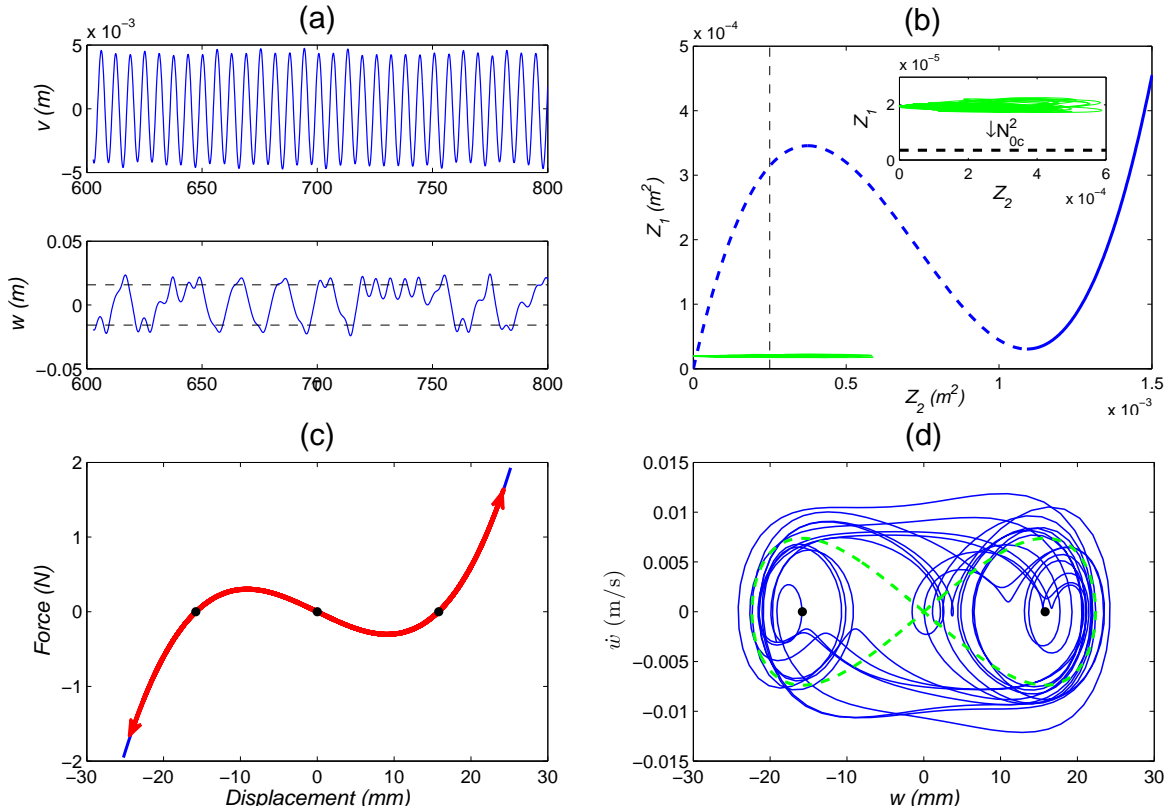


Figure 4.11: Response corresponding to point B (a) time-displacement response (b) projection in SIM structure (c) working range in the force-displacement relation (d) phase trajectory of NES

In Fig. 4.9, it is interesting to note the existence of a particular response at point B_1 , where the energy dissipation ratio is the lowest. Fig. 4.12 shows the corresponding time-displacement response and the phase trajectory. It can be seen that this response is no longer chaotic and shows periodic performance. By introducing the wavelet transform method, the frequency components of the LO and bistable NES are obtained, which illustrates that the transition point represents a resonance capture with the frequency of 1:3 subharmonic. With the increase of input energy, the periodic performance will disappear while the component of 1:3 subharmonic response will hold for the following

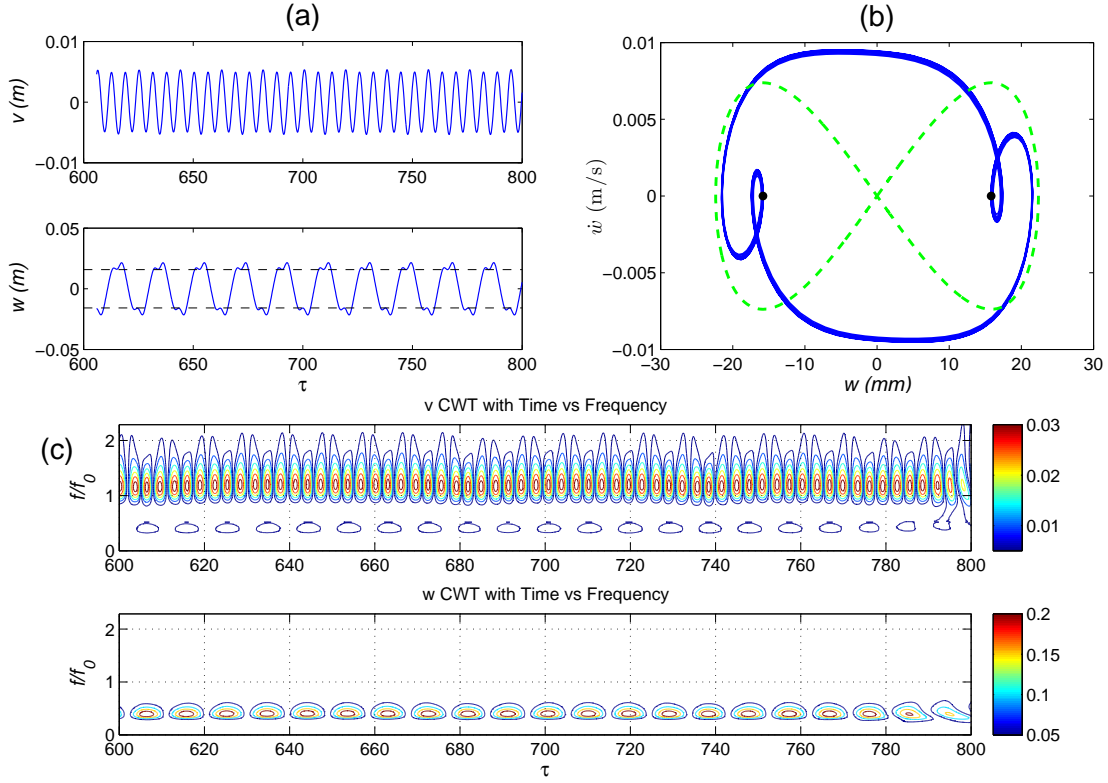


Figure 4.12: Response corresponding to point B_1 (a) time-displacement response (b) phase trajectory of NES (c) wavelet transform: 1:3 subharmonic resonance. Where the natural frequency of LO (f_0) is given by $f_0 = 2\pi/\omega_0$.

response.

4.3.2.3 Strongly modulated response

To illustrate the global performance of the SMR, three specified responses with the excitation amplitude of 0.21 mm , 0.25 mm and 0.42 mm are calculated and presented in Fig. 4.13, where the first and the last corresponding points are located at the two thresholds of SMR. In these responses, three different TET mechanisms of bistable NES are observed and classified as:

1. Fundamental TET (1:1 resonance capture);
2. Subharmonic resonance capture TET;
3. TET initiated by nonlinear beating.

The first column of Fig. 4.13 shows the time displacement response of the LO and bistable NES, the second column shows the corresponding instantaneous amplitude and frequency. To illustrate the basic underlying dynamic mechanism of bistable NES, the

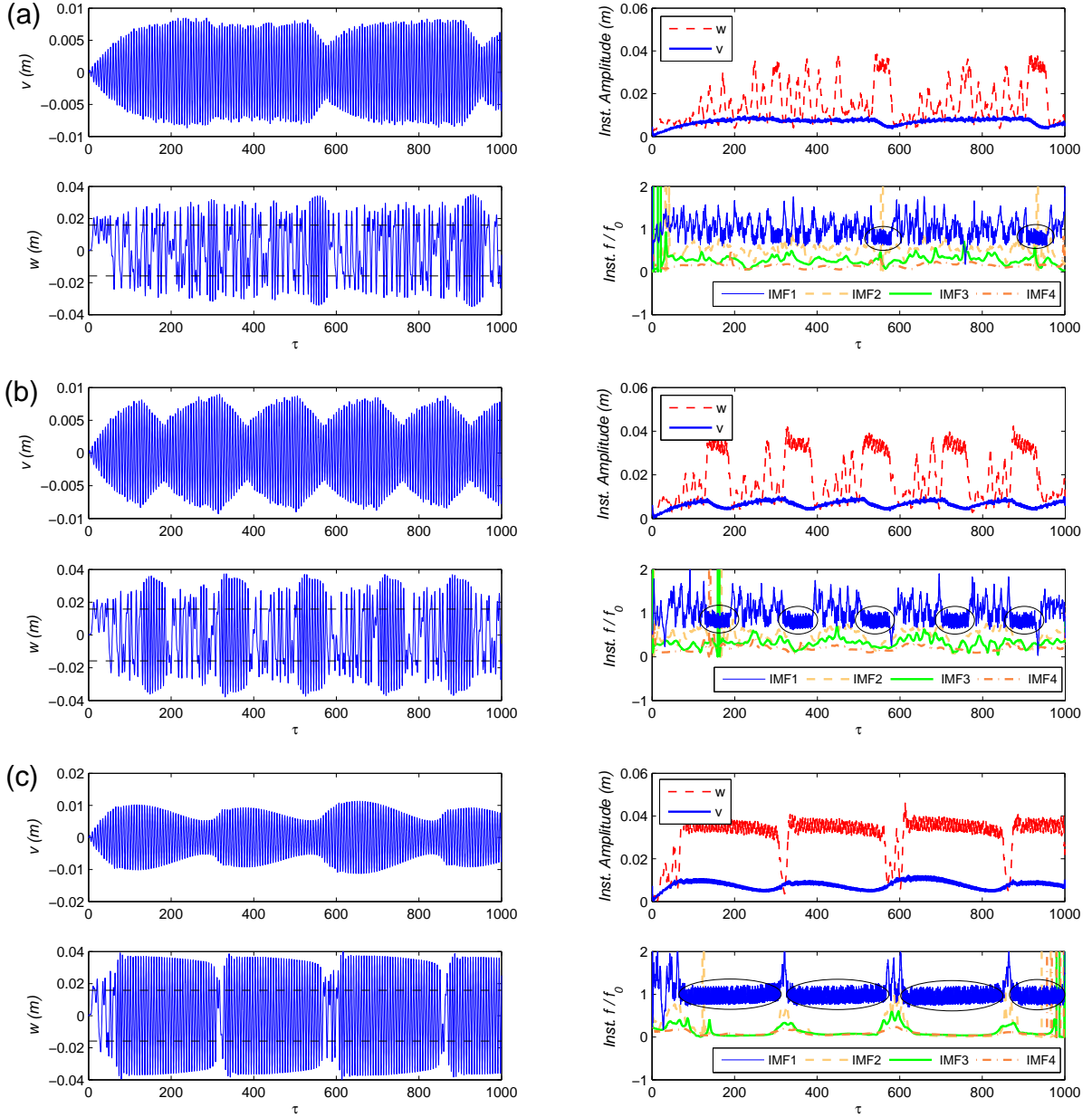


Figure 4.13: SMR response in the first column, and the corresponding instantaneous amplitude and frequency in the second column, for different types of energy: (a) input $G = 0.21 \text{ mm}$, corresponding to point C_1 ; (b) input $G = 0.25 \text{ mm}$, corresponding to point C_2 ; (c) input $G = 0.42 \text{ mm}$, corresponding to point C . Where the instantaneous amplitude of w is inferred from the leading (first) IMF, the instantaneous frequency of bistable NES is defined as f , and the natural frequency of LO is defined as f_0 .

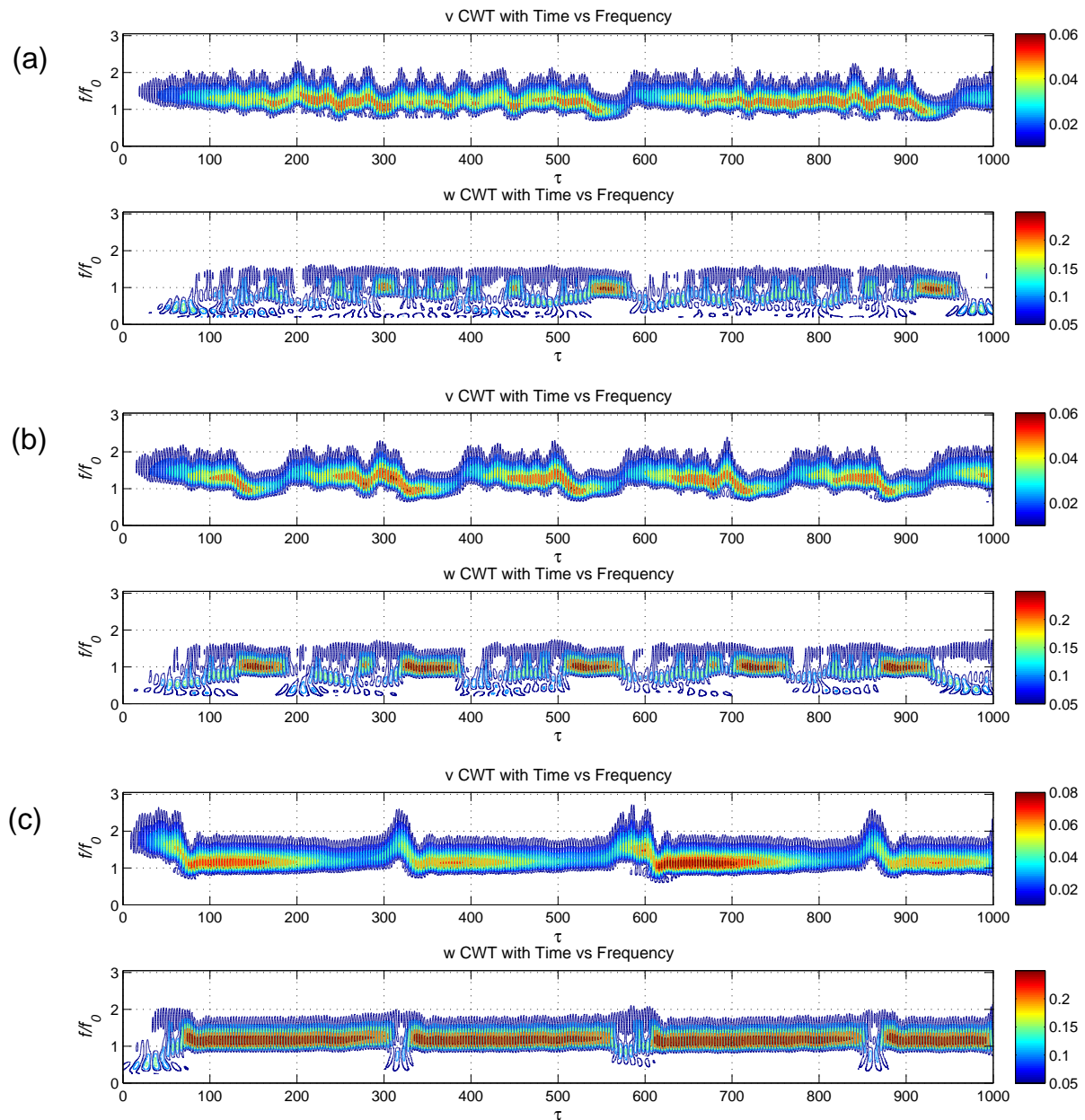


Figure 4.14: Wavelet transform for different type of energy: (a) input $G = 0.21mm$ corresponding to point C_1 ; (b) input $G = 0.25mm$ corresponding to point C_2 ; (c) input $G = 0.42mm$ corresponding to point C

empirical mode decomposition (EMD) applied to decomposition of nonlinear and nonstationary signals is adopted [Huang et al., 1998]. With this method, a collection of intrinsic mode functions (IMFs) is obtained. Then Hilbert Transform is used to calculate the instantaneous frequency and amplitude. Fig. 4.14 illustrates the frequency components of the LO and bistable NES with the wavelet transform method. By combining these two figures, it can be found that: as the instantaneous frequency of leading (first) IMF of the bistable NES is concentrated on the natural frequency of the LO (i.e. the area of ellipses), the fundamental TET takes place and the dynamics is captured in the domain of attraction of 1:1 resonant manifold. This area is additionally demonstrated by the red zone of bistable NES in Fig. 4.14. It is also represented the in phase NNM manifold S_{11+} in the Frequency Energy Plot (FEP) [Kerschen et al., 2007]. At this regime, large targeted energy is extracted and dissipated by bistable NES, leading to a fast decrease of the LO amplitude.

When the LO amplitude decreases to a certain value, the dynamics transfers to the subharmonic resonance capture TET, where the contribution of 1:3 subharmonic resonance response is observed. Owing to its low energy dissipation ratio and the continuous energy input, the LO amplitude starts to increase, and the duration of this transition is small, resulting in a fast resonance escape to the last regime: TET initiated by nonlinear beating. In this regime, three different response components are observed: a) Fundamental nonlinear beating, occurs in the motion that captured by a stable equilibrium, b) Subharmonic nonlinear beating, c) Nonlinear beating that occurs in the steady transition motions between two stable equilibria.

From Fig. 4.14, it can be found that the contribution of each regime is related to the input of excitation energy. When the input G is 0.21 mm , the interval of fundamental TET is small and the nonlinear beating regime plays a large prolonged part in the process. When $G = 0.25 \text{ mm}$, the duration of the fundamental TET regime starts to increase with the decrease of TET initiated by nonlinear beating. As the input reaches the maximum of 0.42 mm , the fundamental TET makes the largest contribution to the process while the transition of subharmonic TET and TET initiated by nonlinear beating are decreased to a narrow zone. In this case, the chaotic aspect almost disappears, and the 1:1 resonance is the strongest, making the NES transfer a relatively high amount of energy in a finite time interval.

4.3.3 Optimal design criterion

As shown in Fig. 4.9, the optimal working point (D_m) is located at the lowest value of the second stable branch of the SIM, in which the efficiency reaches its maximal value. In this case, there exist 1:1 resonance between bistable NES and LO. The comparison of

SIM structure between cubic NES and bistable NES can be found in Fig. 4.2, which shows that, after the addition of the negative stiffness part, the location of optimal point D_m shifts to right, and the corresponding excitation amplitude becomes higher. For this, it is suggested that, if the primary system is excited at a fixed periodic loading, the objective of the optimal design should be to adjust the parameters of NES so as to make it work at the location D_m . By introducing Eq. (4.21), the excitation amplitude at this point is calculated with the nonlinear stiffness K and negative stiffness δ , as shown in Fig. 4.15. Here, it can be observed that, adjusting these two variables K and δ is feasible to control the value of G_{2c} in a certain range, so as to ensure the response of NES located at its optimal point.

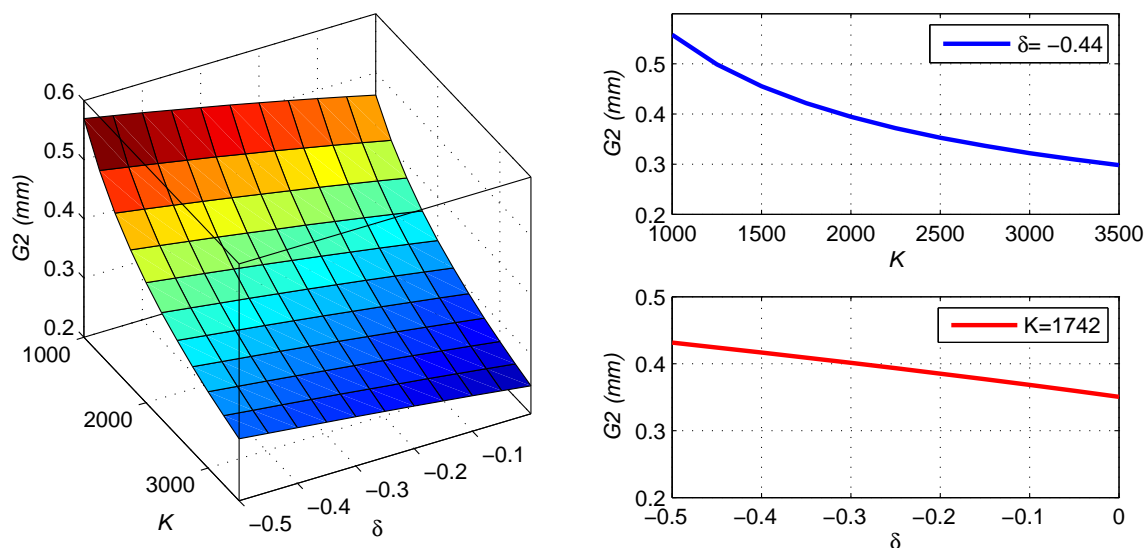


Figure 4.15: Controlling the optimal working point of NES by adjusting the nonlinear stiffness K and negative stiffness δ

For this, a configuration to achieve the negative stiffness and the cubic nonlinearity is proposed. Where the pure cubic nonlinearity is obtained by means of two transverse linear springs with no pretension in their vertical direction [Gourdon et al., 2007], the essentially negative stiffness component is produced by adopting the method of pre-compressing two springs at initial position [Mohammad A, 2014], so as to achieve the bistable geometry. In this structure, an amount of potential energy is pre-stored and the two stable equilibria are obtained when both springs are in the unstretched state. The corresponding force displacement relationship based on Taylor expansion is given by:

$$f(w) = -2k \frac{l_p}{l_0} w + k \frac{l_p + l_0}{l_0^3} w^3 \quad (4.42)$$

In this equation, the value of cubic nonlinearity K is related to the stiffness of spring k and the free length l_0 , where the influence of pre-compressed length l_p is so small that it can be neglected. For the negative nonlinearity δ , it mainly depends on the value of the pre-compressed length l_p since the two springs are installed. As the two springs of a cubic NES are fixed for engineering applications, adjusting the pre-compressed length l_p would provide an alternative way to increase the band in which excitation amplitude is robust. By obtaining the anticipated negative stiffness, the NES can be adjusted to work at the optimal point with its best performance.

4.4 Semi-active control of NES

According to the results of optimal design criterion, semi-active control of the NES is studied in this section. A scheme to realize NES with different kinds of linear stiffness is presented in Fig. 4.16. By controlling initial state (compression or extension) of springs, NES with positive stiffness, pure cubic nonlinearity and negative stiffness can be generated, respectively.

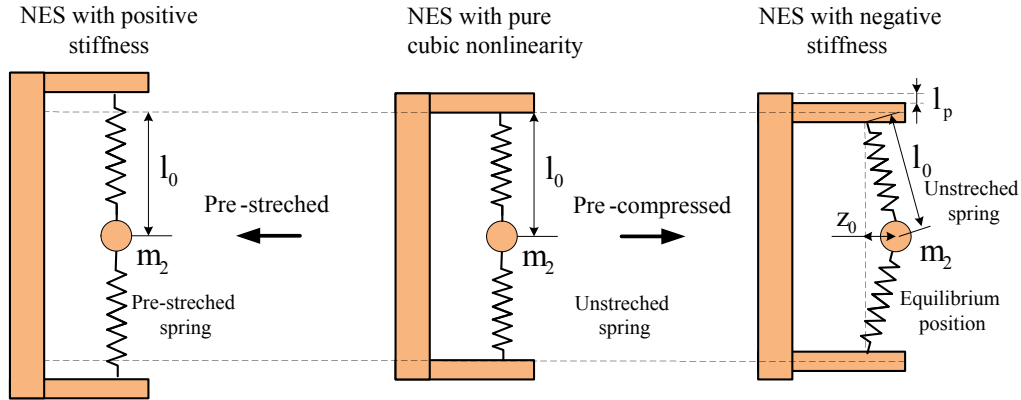


Figure 4.16: NES with different kinds of linear stiffness, with respect to the state (compression or extension) of springs.

Based on this idea, NES system with second group of conical springs is adopted for the experiment of semi-active control. Unlike the scheme of Fig. 4.16, this NES system has two conical springs in translational direction and two linear springs in lateral direction, and all these four springs are pre-compressed at the initial state. The experimental setup is presented in Fig. 4.17, and detailed information of measurement can be referred from chapter 3.2. Based on the idea of Fig. 4.16, differences (i.e. η_1 and η_2) of adjustment length of negative stiffness mechanism is set as the variables for semi-active control (see Fig. 3.15).

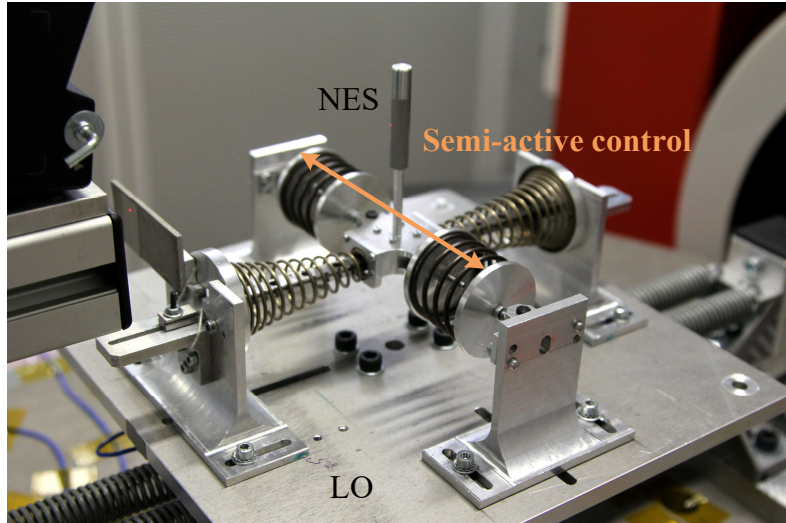


Figure 4.17: NES system with second group of conical springs: experiment for semi-active control

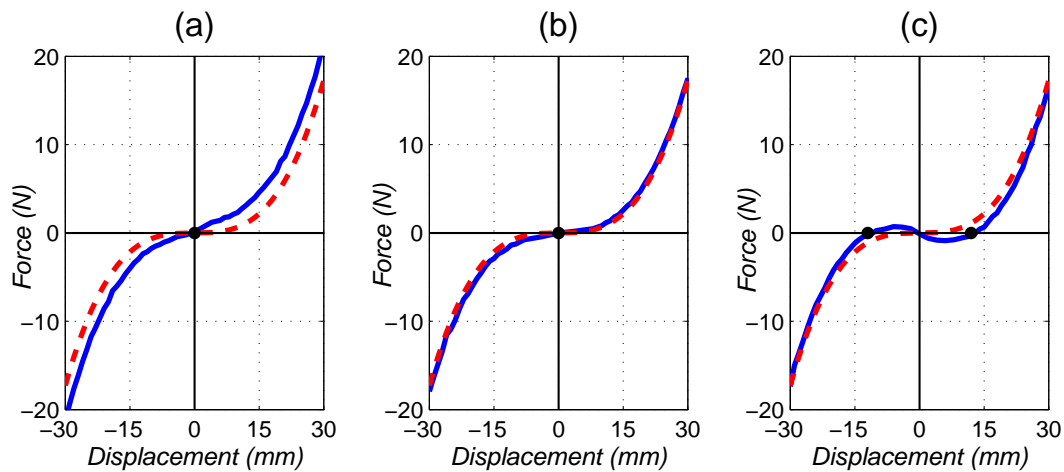


Figure 4.18: Force characteristics of NES system with respect to compressing length: (a) NES with positive stiffness, $\eta_1 = \eta_2 = -1.5$ mm; (b) NES with pure cubic nonlinearity $\eta_1 = \eta_2 = 0$ mm; (c) NES with negative stiffness $\eta_1 = \eta_2 = 3$ mm. The red dashed line is the objective curve of pure cubic nonlinearity, the blue solid line is the measured curve.

The static force applied on the NES mass is measured with variation of η_1 and η_2 , as shown in Fig. 4.18. Three particular examples of NES with positive stiffness, pure cubic nonlinearity and negative stiffness are observed, respectively. Where the red dashed line is the objective curve of pure cubic nonlinearity, the blue solid line is the measured curve. Owing to the elastic hysteresis of NES with negative stiffness, the unloading process is adopted for the measurement. As can be seen, the force characteristics of designed NES system corresponds to the objective curve of pure cubic nonlinearity, and a slight adjustment of pre-compressed may cause NES with different kind of nonlinearity. For

the three configurations, the coefficients of linear and cubic nonlinearity are identified in Table 4.3. It can be observed that the type of NES with negative stiffness has the largest cubic term.

Table 4.3: Experimental stiffness coefficients

$F = k_3x + k_2x^3$			
Param	Fig. 4.18(a)	Fig. 4.18(b)	Fig. 4.18(c)
k_3 (N/m)	139	43	-106
k_2 (N/m ³)	6.35×10^5	6.09×10^5	7.51×10^5

Fig. 4.19 shows the time history of displacement of LO at a fixed frequency excitation around natural frequency. Three different types of response are obtained. At the excitation amplitude $G = 0.5$ mm, NES with pure cubic nonlinearity performs optimally, since its fixed point is located at lowest point of SIM (i.e. D_m). For the NES with positive stiffness, its fixed point is located at a higher position of second stable branch of SIM, and the amplitude is also larger than that of NES with pure cubic nonlinearity. While for the NES with negative stiffness (bistable NES), the fixed point is unstable and the system still works at the excitation range of strongly modulated response, which indirectly reflect that bistable NES has a shift towards higher excitation amplitude of the optimal working point.

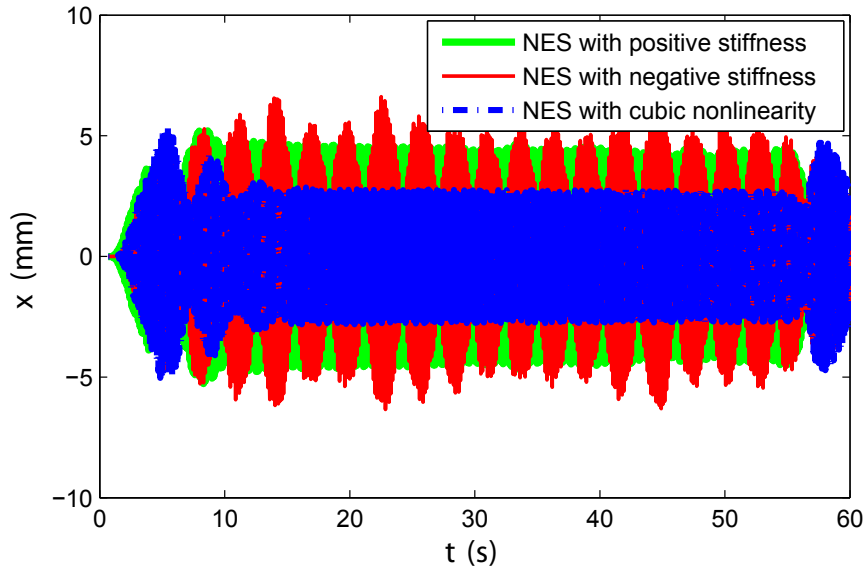


Figure 4.19: Time history of displacement of the LO with different kinds of NES, $G = 0.5$ mm.

Then the band of excitation frequency is enlarged around the natural frequency of LO. The objective here is to study the influence of adjustment length (η_1 and η_2) on the response regimes and their efficiency. Three groups of frequency response function (FRF) with different excitation amplitude (G) are tested, and detailed view of time displacement of LO under frequency sweep test is also presented, as shown in Fig. 4.20-4.22.

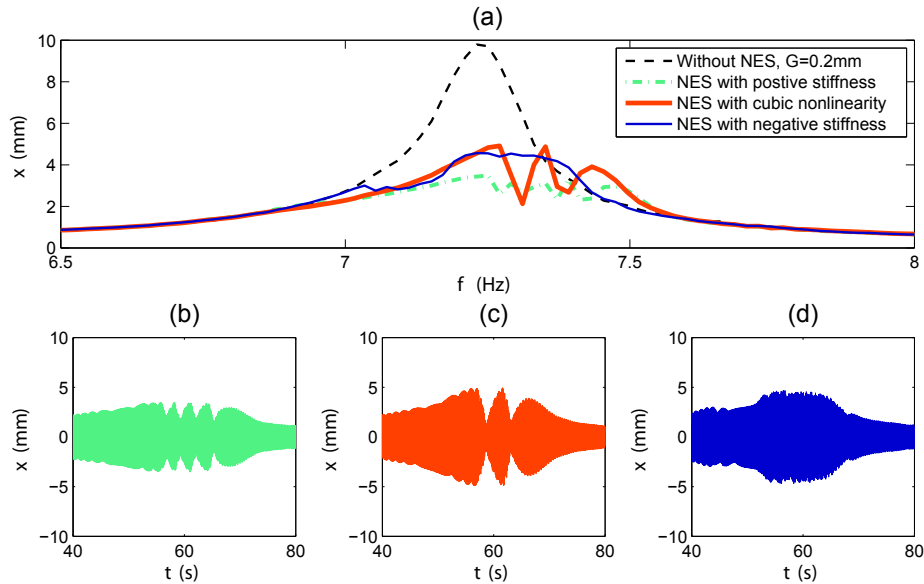


Figure 4.20: (a) Frequency response curve of LO with semi-active control of the NES, at low energy excitation $G = 0.20$ mm, and detailed view of time displacement of LO under frequency sweep test for NES with positive stiffness (b), pure cubic nonlinearity (c) and negative stiffness (d).

As the LO is excited at low energy level $G = 0.20$ mm, the amplitude of NES with positive stiffness is lower than the other two NESs (see Fig. 4.20). As the excitation is increased to a moderate energy $G = 0.35$ mm, all the three NESs perform strongly modulated response at the frequency band around natural frequency, while the amplitude of LO attached to NES with pure cubic nonlinearity is lower than the other two NESs (see Fig. 4.21). For a relatively high level of excitation amplitude $G = 0.45$ mm (see Fig. 4.22), both the responses of LO attached to NES with positive stiffness and pure cubic nonlinearity have the resonance tongue at the left side of natural frequency (more detailed information of resonance tongue can be found in Fig. 2.5). While for NES with negative stiffness, the high amplitude detached resonance is significantly attenuated, and its average amplitude of LO is lower than other two NESs. Thus it can be concluded that adjusting the pre-compressed length of negative stiffness mechanism is feasibly to make NES work robustly and efficiently for different types of excitations. Particularly, at higher energy excitation, adding an extra negative stiffness to produce a bistable NES is helpful

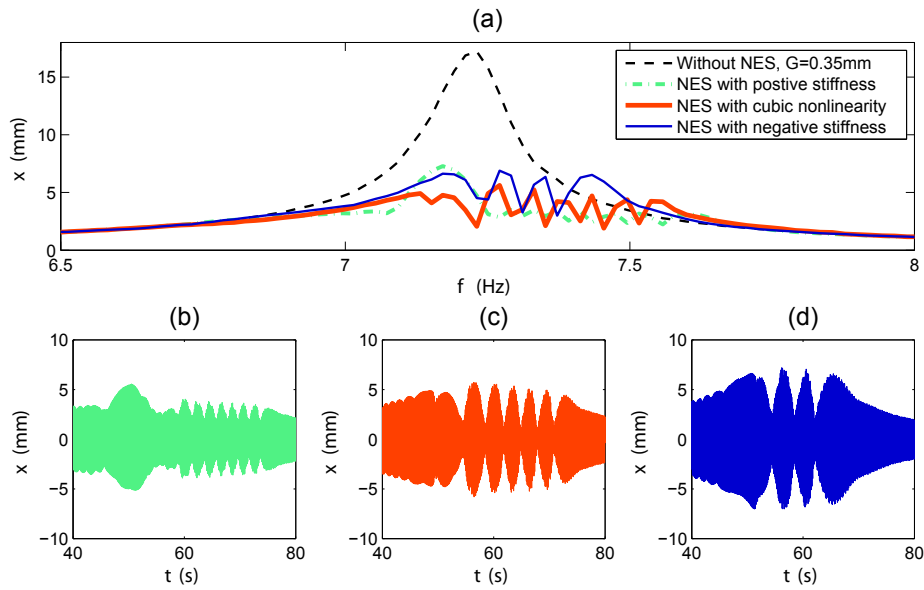


Figure 4.21: (a) Frequency response curve of LO with semi-active control of the NES, at moderate energy excitation $G = 0.35$ mm, and detailed view of time displacement of LO under frequency sweep test for NES with positive stiffness (b), pure cubic nonlinearity (c) and negative stiffness (d).

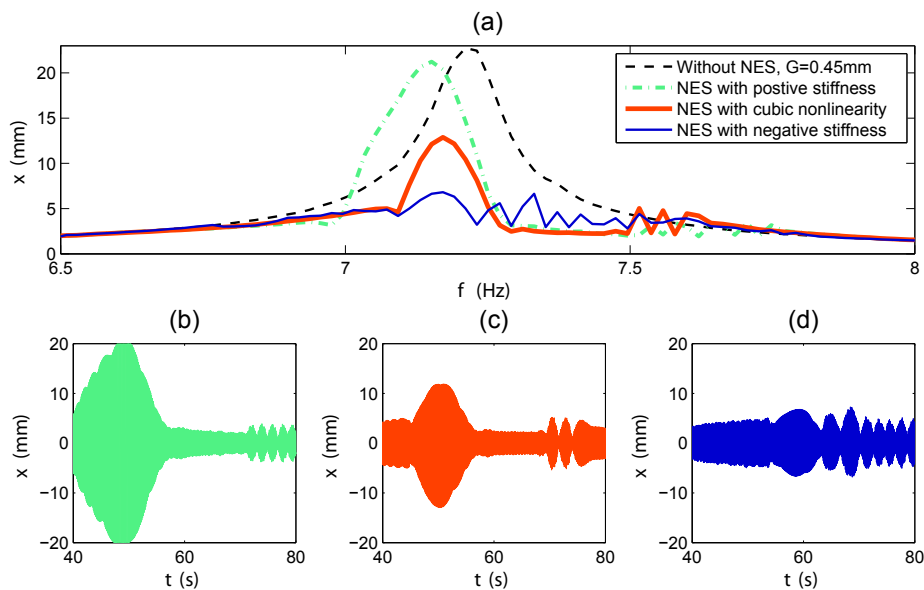


Figure 4.22: (a) Frequency response curve of LO with semi-active control of the NES, at high energy excitation $G = 0.45$ mm, and detailed view of time displacement of LO under frequency sweep test for NES with positive stiffness (b), pure cubic nonlinearity (c) and negative stiffness (d).

to avoid a high dangerous amplitude detached resonance curves being generated.

Consequently, semi-active control of the NES is capable of attenuating the structural

response significantly and robustly with the additional benefit over the pure cubic NES of not producing resonance tongue at high level of excitation amplitude, which make it suitable for various engineering applications when the primary system is subject to harmonic forcing in a broad range of excitation.

4.5 Conclusion

In this chapter, the dynamic response of a 2 degrees of freedom system comprising a harmonically excited Linear Oscillator (LO) strongly coupled to a bistable NES is investigated. An analytically obtained Slow Invariant Manifold (SIM) is used to explain the different response regimes. Unlike cubic NES, bistable NES only follows the second stable branch of the SIM. Asymptotic analysis and Melnikov analysis are respectively used to obtain the thresholds of different response regimes at different energy levels. These analytical solutions are verified in numerical simulation, which correctly predicts the occurrence of intra-well oscillation or chaotic inter-well oscillation, and the transition between Strongly Modulated Response (SMR) and stable periodic response.

The efficiency of different response regimes is studied and demonstrates that a bistable NES working in the first regime with intra-well oscillation can transfer the targeted energy with a relatively high efficiency, but the chaotic inter-well response dissipates energy with low efficiency. For this regime, a point with 1:3 subharmonic resonance captures exists where its efficiency is the lowest. This result is contrary to the traditional idea that 1:3 subharmonic resonance may result in a strong energy exchange and dissipation under periodic excitation. About the band of excitation amplitude with the occurrence of SMR, it becomes broader with the addition of negative stiffness, and the efficiency of bistable NES in this band is larger than that of cubic NES. With the Hilbert transform and wavelet transform, three different Targeted Energy Transfer (TET) mechanisms are observed and it shows that 1:1 resonance is mainly responsible for the efficient TET.

Finally, an optimal point located at the boundary between the SMR and stable periodic response is found, at which the efficiency of NES is largest and the amplitude of LO is smallest. Based on this, an optimal design criterion and the corresponding configuration are proposed, and experiments for semi-active control of NES are also explored. By adjusting the pre-compressed length of spring, the NES can be tuned to robustly work at its best performance for a range of excitation. Furthermore, it is worth to explore that this tuned method may also be applied to vibro-impact NES: by adjusting its clearance, the TET efficiency may be tuned at an optimal value. In the next chapter, detailed design criteria for optimally tuned vibro-impact NES will be discussed.

Design criteria for optimally tuned vibro-impact NES

Abstract

This chapter is devoted to propose the design criteria for optimally tuned Vibro-Impact (VI) NES to control the vibration under periodic and transient excitation. To this end, a generalized dimensionless model of a 2 degrees of freedom system comprising a harmonically excited linear oscillator strongly coupled to a VI NES is investigated. Bifurcation analysis and efficiency of Targeted Energy Transfer (TET) around the Slow Invariant Manifold (SIM) are studied with the variation of clearance. As a result, the optimal clearances for periodic and transient excitation are calculated from two transition points of the SIM, respectively. Then the procedure is extended in case of multiple VI NESs in parallel to the Linear Oscillator (LO). Two principles of additivity and separate activities of VI NESs are verified theoretically. Finally, experiments involving the whole system for periodic and transient excitation are performed.

Contents

5.1	Asymptotic analysis of a single VI-NES	108
5.1.1	Dynamical modeling	108
5.1.2	Analytical treatment of Slow Invariant Manifold (SIM)	111
5.1.3	Bifurcation analysis	112
5.2	Criteria for efficient targeted energy transfer	114
5.2.1	Optimal design criterion for periodic excitation	114
5.2.2	Optimal design criterion for transient excitation	116
5.3	Optimal design of multiple VI-NESs	119
5.4	Experimental validation	121
5.4.1	Periodic excitation	122
5.4.2	Transient excitation	125
5.5	Conclusion	129

5.1 Asymptotic analysis of a single VI-NES

This chapter presented here is referred from Ref. [Li, 2016], in which efficiency comparison of response regimes, activation mechanism of VI NES and dynamics of two VI NESs in parallel have been studied in detail. However, the optimal values of clearance in Ref. [Li, 2016] is obtained by trial and errors. If the primary system and the excitation are changed, the clearance will no longer be optimal. For two VI NESs in parallel, it is proposed that VI NES with a medium clearance and a small clearance can be optimal for a given excitation. Yet, the design criterion from a single VI NES to multiple VI NESs and its corresponding calculation are still not clear. Thus, to obtain the optimal performance for a VI NES or multiple VI NESs and lay the foundation for semi-active control, analytical calculation for the clearance needs to be further studied. To this end, asymptotic analysis of a single VI NES is firstly studied in this section.

5.1.1 Dynamical modeling

The dynamic modeling presented here is based on Refs. [Li, 2016 ; Gourc, 2013]. The system of a harmonically excited linear oscillator (LO) attached with a VI NES is illustrated in Fig. 5.1. The objective here is to apply the asymptotic method used in the above papers to deduce the generalized dimensionless model, so as to obtain the optimal design criteria of VI NES for any targeted primary system.

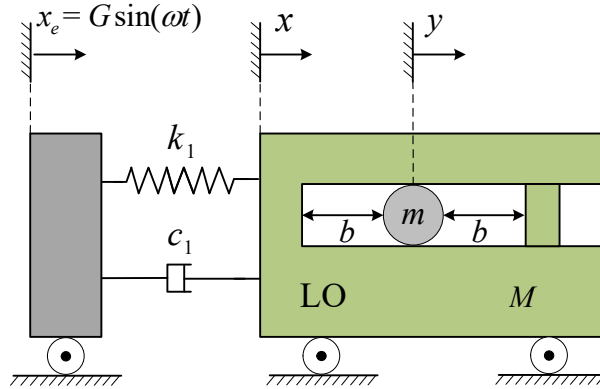


Figure 5.1: Schematic of the dynamic system: a harmonically excited LO coupled with a VI NES

The system is excited by the base, and the equations of motion between impacts are described as follows:

$$\begin{aligned} M\ddot{x} + c_1\dot{x} + k_1x &= k_1x_e + c_1\dot{x}_e \\ m\ddot{y} &= 0, \quad \forall |x - y| < b \end{aligned} \quad (5.1)$$

where x , M , c_1 and k_1 are the displacement, mass, damping and stiffness of the LO respectively. y and m are the displacement and mass of VI NES. b represents the clearance that can be adjusted by the length of cavity. The imposed harmonic displacement x_e is expressed as:

$$x_e = G \cos(\omega t) \quad (5.2)$$

After rescaling, the system of equation (5.1) can be reduced to the dimensionless form:

$$\begin{aligned} \ddot{X} + \epsilon \lambda \dot{X} + X &= \epsilon F \sin \Omega \tau + \epsilon^2 \lambda F \Omega \cos \Omega \tau \\ \epsilon \ddot{Y} &= 0, \quad \forall |X - Y| < 1 \end{aligned} \quad (5.3)$$

where the variables of the displacements are dimensioned by:

$$x = Xb, \quad y = Yb \quad (5.4)$$

The corresponding physical parameters are expressed as follows:

$$\epsilon = \frac{m}{M}, \quad \omega_0^2 = \frac{k_1}{M}, \quad \tau = \omega_0 t, \quad \lambda = \frac{c_1}{m\omega_0}, \quad \Omega = \frac{\omega}{\omega_0}, \quad F = \frac{G}{\epsilon b} \quad (5.5)$$

When $|X - Y| = 1$, an impact occurs. The state of the system after impact is obtained using the simplified shock theory and the condition of total momentum conservation:

$$\begin{aligned} X^+ &= X^-, \quad Y^+ = Y^- \\ \dot{X}^+ + \epsilon \dot{Y}^+ &= \dot{X}^- + \epsilon \dot{Y}^- \\ \dot{X}^+ - \dot{Y}^+ &= -r (\dot{X}^- - \dot{Y}^-), \quad \text{for } |X - Y| = 1 \end{aligned} \quad (5.6)$$

where r is the restitution coefficient and the superscripts $+$ and $-$ denote time immediately after and before impact. Two new variables representing the displacement of the center of mass and the internal displacement of the VI NES are introduced (both of them are dimensionless):

$$V = X + \epsilon Y, \quad W = X - Y \quad (5.7)$$

Substituting Eq. (5.7) into Eqs. (5.6) and (5.3), the equation between impacts in barycentric coordinate is given as:

$$\begin{aligned} \ddot{V} + \epsilon \lambda \frac{\dot{V} + \epsilon \dot{W}}{1 + \epsilon} + \frac{V + \epsilon W}{1 + \epsilon} &= \epsilon F \sin \Omega \tau \\ \ddot{W} + \epsilon \lambda \frac{\dot{V} + \epsilon \dot{W}}{1 + \epsilon} + \frac{V + \epsilon W}{1 + \epsilon} &= \epsilon F \sin \Omega \tau, \quad \forall |W| < 1 \end{aligned} \quad (5.8)$$

where the term containing ϵ^2 is very small, and can be neglected. The impact condition

(5.6) can be rewritten as:

$$\begin{aligned} V^+ &= V^-, & W^+ &= W^-, \\ \dot{V}^+ &= \dot{V}^-, & \dot{W}^+ &= -r\dot{W}^-, \quad \text{for } |W| = 1 \end{aligned} \quad (5.9)$$

Then multiple scales are introduced in the following form:

$$\begin{aligned} V(\tau; \epsilon) &= V_0(\tau_0, \tau_1, \dots) + \epsilon V_1(\tau_0, \tau_1, \dots) + \dots \\ W(\tau; \epsilon) &= W_0(\tau_0, \tau_1, \dots) + \epsilon W_1(\tau_0, \tau_1, \dots) + \dots \\ \tau_k &= \epsilon^k \tau, \quad k = 0, 1, \dots \end{aligned} \quad (5.10)$$

The system is studied in the vicinity of the 1:1 resonance, where both the LO and the VI NES execute time periodic oscillations with identical frequency. Thus, a detuning parameter σ representing the nearness of the forcing frequency Ω to the reduced natural frequency of the LO is introduced:

$$\Omega = 1 + \epsilon\sigma \quad (5.11)$$

Substituting Eqs. (5.10) and (5.11) into Eqs. (5.8) and (5.9), then equating coefficients of like power of ϵ gives:

Order ϵ^0 :

$$\begin{aligned} D_0^2 V_0 + V_0 &= 0 \\ D_0^2 W_0 + V_0 &= 0, \quad \forall |W_0| < 1 \end{aligned} \quad (5.12)$$

$$\begin{aligned} V_0^+ &= V_0^-, & W_0^+ &= W_0^-, \quad \text{for } |W_0| = 1 \\ D_0 V_0^+ &= D_0 V_0^-, & D_0 W_0^+ &= -r D_0 W_0^- \end{aligned} \quad (5.13)$$

Order ϵ^1 :

$$\begin{aligned} D_0^2 V_1 + V_1 &= -2D_0 D_1 V_0 - \lambda D_0 V_0 - W_0 + V_0 + F \sin(\tau_0 + \sigma\tau_1) \\ D_0^2 W_1 + V_1 &= -2D_0 D_1 V_0 - \lambda D_0 V_0 - W_0 + V_0 + F \sin(\tau_0 + \sigma\tau_1) \\ \forall |W_0| &< 1 \end{aligned} \quad (5.14)$$

where D_0 represents partial derivative with respect to time τ_0 . From the first equation of system (5.12), the solution of V_0 (in slow time scale) can be deduced as follows:

$$V_0 = A(\tau_1) \sin(\tau_0 + \theta(\tau_1)) \quad (5.15)$$

where $A(\tau_1)$ and $\theta(\tau_1)$ represent the amplitude and phase of the LO, respectively. For W_0 (in slow time scale), Eq. (5.12) and (5.13) represent a harmonically forced impact oscillator with symmetric barrier. Under the assumption of 1 : 1 resonance, its solution

can be searched in the following form:

$$W_0 = A(\tau_1) \sin(\tau_0 + \theta(\tau_1)) + \frac{2}{\pi} C(\tau_1) \Pi(\tau_0 + \eta(\tau_1)) \quad (5.16)$$

where $C(\tau_1)$ and $\eta(\tau_1)$ represent the amplitude and phase of VI NES, respectively. $\Pi(z)$ is a non-smooth saw tooth function [Pilipchuk, 2015], its folded function is expressed as follows:

$$\Pi(z) = \arcsin(\sin z), \quad M(z) = \frac{d\Pi}{dz} = \text{sgn}(\cos z) \quad (5.17)$$

As can be observed from Eq. (5.16) and (5.17), impact occurs at $\tau_0 = \pi/2 - \eta + j\pi$ with $j = 0, 1, 2, \dots$. Substituting the above equations to the impact condition Eq. (5.13), it yields:

$$\cos(\eta - \theta) = \frac{1 - C}{A}, \quad \sin(\eta - \theta) = \frac{2C\Gamma}{\pi A} \quad (5.18)$$

where $\Gamma = (1 - r)/(1 + r)$. By combining the above two equations with trigonometric identity, the expression for a Slow Invariant Manifold (SIM) is obtained:

$$A^2 = (1 - C)^2 + \frac{4C^2\Gamma^2}{\pi^2} \quad (5.19)$$

5.1.2 Analytical treatment of Slow Invariant Manifold (SIM)

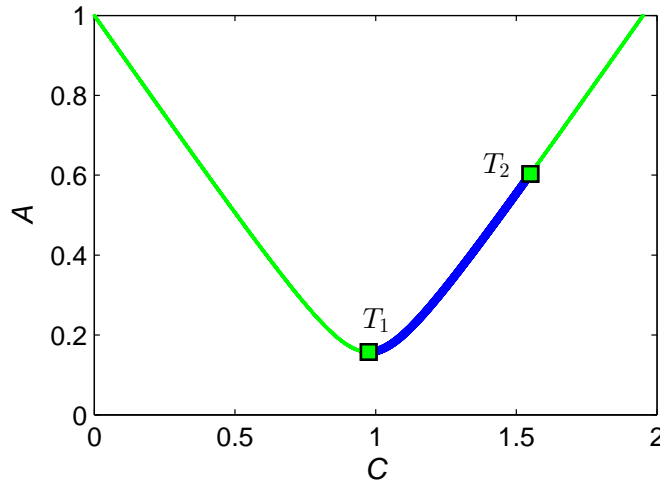


Figure 5.2: SIM of VI NES: on the stable branch in blue line and two unstable branches in green line with two transition point T_1 and T_2 . $\epsilon = 0.68\%$, $\lambda = 1.91$

An illustration of the SIM is presented in Fig. 5.2. Unlike cubic NES, the topological structure of SIM is composed of two branches. It can be observed that the left side of

branch is unstable, only a part of the right side is stable (between the point T_1 and T_2). The stability of the SIM can be evaluated by direct numerical integration of Eq. (5.12) and (5.13).

Depending on the different positions of the fixed point in SIM [Li et al., 2017c], five types of response regimes are obtained: (1) chaos with no duration of two impacts per cycle, where no fixed point occurs and the energy is low and not sufficient to activate the energy pumping; (2) chaos by intermittency, i.e., Strongly Modulated Response (SMR), with the fixed point located at the left unstable branch of the SIM; (3) two symmetric impacts per cycle, while the fixed point is located at the stable branch; (4) two asymmetric impacts per cycle, the fixed point starts to pass the transition point T_2 and stays on the right unstable branch; (5) chaos with infinite number of impact per cycle, i.e., the regime with more than two impacts per cycle, where the fixed point stays higher than the above cases.

Knowing the variation mechanism of the response regimes, it would be interesting to investigate the efficiency of each regime and the corresponding threshold for periodic excitation so as to guide the design of VI NES. In [Li et al., 2017d], it is demonstrated that the boundary between response with permanent two impacts per cycle and that with intermittent two impact cycle (SMR) is optimal, and the critical point is located at the extreme T_1 of the SIM. By vanishing the derivative of the right hand side of Eq. (5.19) to zero, its expression can be obtained as follows:

$$C_1 = \frac{\pi^2}{\pi^2 + 4\Gamma^2}, \quad A_1^2 = \frac{4\Gamma^2}{\pi^2 + 4\Gamma^2} \quad (5.20)$$

Here the values C_1 corresponds to the minimum amplitude of the LO, where 1:1 Targeted Energy Transfer (TET) is allowed. However, the precise analytical calculation of the cavity length (i.e., b) to ensure response at the critical point is still not clear. For this, bifurcations of the system at the next order of approximation is analyzed.

5.1.3 Bifurcation analysis

By introducing Eq. (5.15) and (5.16) into the first equation of system (5.14) and eliminating the secular term, the asymptotic stability of the fixed points at the stable branch with respect to time scale τ_1 is studied in the following form:

$$\begin{aligned} D_1 A &= \frac{F}{2} \sin(\sigma\tau_1 - \theta) - \frac{4C}{\pi^2} \sin(\eta - \theta) - \frac{\lambda C}{2} \\ D_1 \theta &= -\frac{F}{2A} \cos(\sigma\tau_1 - \theta) + \frac{4}{\pi^2 A} B \cos(\eta - \theta) \end{aligned} \quad (5.21)$$

Substituting Eqs. (5.18) into Eq. (5.21) and introducing $\rho = \sigma\tau_1 - \theta$, the expressions governing the evolution of the amplitude A and the phase ρ are obtained:

$$\frac{\partial A}{\partial \tau_1} = \frac{f_1(A, \rho)}{g(A)}, \quad \frac{\partial \rho}{\partial \tau_1} = \frac{f_2(A, \rho)}{g(A)} \quad (5.22)$$

where

$$f_1 = F\pi^3(1 - A) \sin(\rho) + 2FA\Gamma\pi^2 \cos(\rho) - 4\Gamma^2\pi A^2\lambda - 16A^2\Gamma - \pi^3\lambda(A - 1)^2 \quad (5.23)$$

$$f_2 = -2F\Gamma\pi \sin(\rho) - F\pi^2 \cos(\rho) + 8\Gamma^2A\sigma + 2\pi^2A\sigma + 2\Gamma\pi\lambda - 2\pi^2\sigma + 8A \quad (5.24)$$

$$g = 8\Gamma^2A + 2\pi^2A - 2\pi^2 \quad (5.25)$$

By equating the derivative of the right-hand side of Eq. (5.22) to zero, two kinds of fixed point are calculated. The first is referred to as an ordinary fixed point located at the stable branch of SIM, and it also satisfies the condition $f_1 = f_2 = 0$ and $g \neq 0$. The other corresponds to the folded singularity (i.e., T_1). In this case the derivative of Eq. (5.19) is related to Eq. (5.25), so it can be found that $g = 0$. Based on this, the system $f_1 = f_2 = 0$ will be discussed and is rewritten in the following matrix form:

$$\begin{bmatrix} \alpha_{11} & \alpha_{12} \\ \alpha_{21} & \alpha_{22} \end{bmatrix} \begin{bmatrix} \sin \rho \\ \cos \rho \end{bmatrix} = \begin{bmatrix} \beta_1 \\ \beta_2 \end{bmatrix} \quad (5.26)$$

where

$$\begin{cases} \alpha_{11} = F\pi^3(1 - A), & \alpha_{12} = 2FA\pi^2\Gamma, \\ \alpha_{21} = -2F\pi\Gamma, & \alpha_{22} = -F\pi^2 \\ \beta_1 = 4\Gamma^2\pi A^2\lambda + 16A^2\Gamma + \pi^3\lambda(A - 1)^2 \\ \beta_2 = -8\Gamma^2A\sigma - 2\pi^2A\sigma - 2\Gamma\pi\lambda + 2\pi^2\sigma - 8A \end{cases} \quad (5.27)$$

By solving Eq. (5.26) for $\sin \rho$ and $\cos \rho$, ordinary fixed points can be obtained by assuming that the determinant does not vanish. For the folded singularity, it is observed that $\det(\alpha) = F^2\pi^3g/2 = 0$, which means that, when eliminating f_2 and g , the condition $f_1 = 0$ can be automatically satisfied by Eq. (5.26). Thus the expression of $f_2 = 0$ can be studied in the following form:

$$\sqrt{\alpha_{21}^2 + \alpha_{22}^2} \cdot \cos(\rho - \delta) = \beta_2, \quad \delta = \arctan\left(\frac{\alpha_{21}}{\alpha_{22}}\right) \quad (5.28)$$

Then the phase ρ can be deduced as:

$$\rho = \arctan\left(\frac{\alpha_{21}}{\alpha_{22}}\right) + \arccos\left(\frac{\beta_2}{\sqrt{\alpha_{21}^2 + \alpha_{22}^2}}\right) \quad (5.29)$$

According to Eq. (5.29), the critical condition of the excitation amplitude for the existence of the folded singularity is obtained:

$$\left| \frac{\beta_2}{\sqrt{\alpha_{21}^2 + \alpha_{22}^2}} \right| = 1 \quad (5.30)$$

Thus the threshold of the SMR is calculated as:

$$F_c = \frac{2(4 A_I \Gamma^2 \sigma + A_I \pi^2 \sigma + \Gamma \pi \lambda - \pi^2 \sigma + 4 A_I)}{\pi \sqrt{4 \Gamma^2 + \pi^2}} \quad (5.31)$$

Substituting Eq. (5.20) to Eq. (5.31), the threshold can be expressed in a convenient form:

$$F_c = \frac{2(4 \Gamma^3 \lambda + \Gamma \pi^2 \lambda + 4 \pi)}{(4 \Gamma^2 + \pi^2)^{3/2}} \quad (5.32)$$

Here, it is noted that the variable F_c is a dimensionless variable of excitation, which is only dependent on the intrinsic properties of the LO and NES (i.e., the damping of the LO and the restitution coefficient).

5.2 Criteria for efficient targeted energy transfer

This section aims to propose the analytical calculation of optimal clearance for a single VI NES. To this end, the obtained results in above section are used to provide the design criteria for periodic excitation and transient excitation, respectively.

5.2.1 Optimal design criterion for periodic excitation

Based on the above analysis, the optimal design of VI NES is to make the target displacement amplitude of the LO locate at T_1 of the corresponding SIM under periodic excitation. For this, the cavity length b is chosen as the design parameter, and the objective is to obtain its optimal value so as to produce the efficient TET for different types of excitation. According to Eq. (5.5), the relation between the cavity length and the amplitude of excitation can be written as:

$$b = \frac{G}{\epsilon F} \quad (5.33)$$

By introducing Eq. (5.32) into Eq. (5.33), the critical value of the cavity length is obtained as:

$$b_c = \frac{G(4\Gamma^2 + \pi^2)^{3/2}}{2\epsilon(4\Gamma^3\lambda + \Gamma\pi^2\lambda + 4\pi)} \quad (5.34)$$

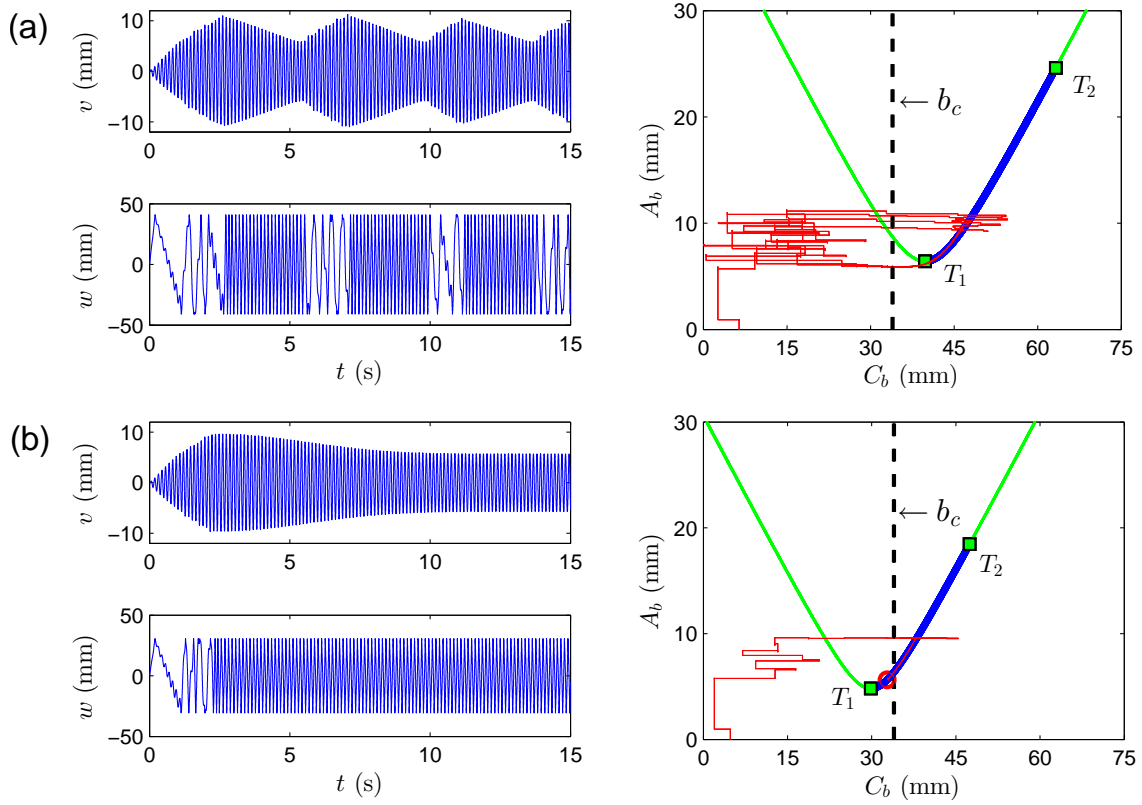


Figure 5.3: Time-displacement response of LO and VI NES, and the motion of the system projected into the SIM: (a) SMR with $b > b_c$; (b) steady state response with $b < b_c$.

To demonstrate the critical function of b_c , two response regimes with different cavity length are illustrated in Fig. 5.3. The time-displacement response of the LO and VI NES, and the projection of motion of the system into the SIM are presented in the first and second column, respectively. As the cavity length is set as $b > b_c$, a strongly modulated response and its flow jump on the SIM are observed. In this case, the response acts through successive synchronization between the LO and the VI NES. When the VI NES is not synchronized, the amplitude of the LO grows. Under a certain circumstance, the VI NES enters into the 1:1 resonance capture with the LO, making the amplitude of the LO decrease fast by successive impacts until it decays at the transition point T_1 . As the cavity length is set as $b < b_c$, a steady state response with two symmetric impacts per cycle is observed. As can be seen, after a short transient, the flow is rapidly attracted to the red fixed point.

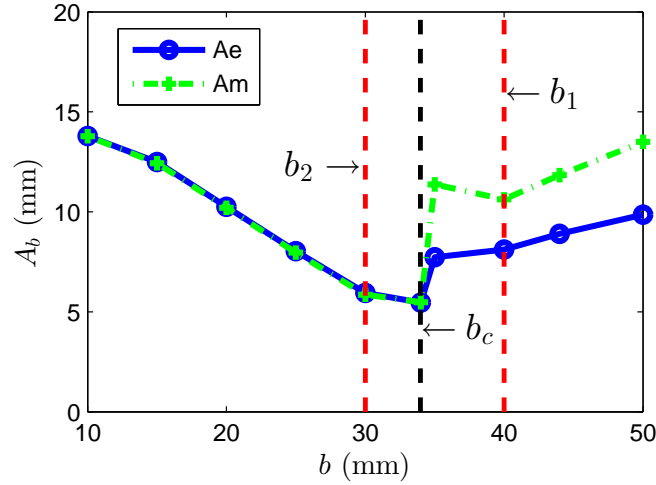


Figure 5.4: TET efficiency explained by the amplitude of LO with the variation of clearance b : A_e represents the mean amplitude, and A_m the maximum amplitude.

The variation law of TET efficiency with different lengths of cavity b under a fixed periodic excitation is presented in Fig. 5.4, where A_e and A_m represent the mean and the maximum amplitude of the LO, respectively. The above two examples are illustrated by b_1 and b_2 . As can be seen, when the clearance equals b_c , the amplitude of the LO is minimum. Thus the calculation of b_c can be used to provide the highest TET efficiency for the NES system.

5.2.2 Optimal design criterion for transient excitation

For the transient excitation, there does not exist SMR, the response regime transits continuously from one type to another type with the decrease of the master energy. If the initial master energy is still set around the transition point T_1 , the NES system will rapidly pass the 1:1 resonance capture and enter the chaos with no duration of two impacts per cycle. In this case, the VI NES is only activated in a very short time, resulting in a low energy dissipation ratio being produced. In [Li et al., 2017d], it demonstrates that the efficiency of TET should not only be high at the beginning but also last as long as possible. So in this paper, the transition point T_2 between the response with two symmetric and two asymmetric impacts per cycle is proposed to be the position of the initial master energy. The analytical value of T_2 can be obtained from Fig. 5.2, with $A_2 = 0.6$. Based on this idea, the tuned parameter of the clearance b can be calculated in the following form:

$$b_t = \frac{x_m}{A_2}, \quad x_m = \sqrt{(x_0^2 + \frac{\dot{x}_0^2}{\omega_0^2})} \quad (5.35)$$

Where the x_m represents the initial master energy, x_0 and \dot{x}_0 represents the initial position

and velocity of the LO, respectively.

To demonstrate the criterion, three cases with different clearances are calculated under the condition: $G = 0$, $\dot{x}_0 = 0$ and $x_0 = 30$ mm. The tuned parameters are given in Table 5.1 and the optimal value b_t is obtained by Eq. (5.35). Where x_1 and x_2 represent the amplitude of the LO at the transition point T_1 and T_2 , $t_{x=15}$ and $t_{x=5}$ represent the time duration when the amplitude of the LO decreases to 15mm and 5mm, respectively.

Table 5.1: Three cases with different clearance under transient excitation

Tuned parameters					
<i>case</i>	b (mm)	x_1 (mm)	x_2 (mm)	$t_{x=15}$ (s)	$t_{x=5}$ (s)
$< b_t$	20	3.1	12	1.8	3.7
$= b_t$	50	7.8	30	1.3	2.6
$> b_t$	80	11.8	48.2	1	3.3

Transient responses of the first and second case with $b < b_t$ and $b = b_t$ are respectively presented in Fig. 5.5 (a) and (b). For the first case, four response regimes during the whole process are observed. Detailed view of these regimes can be found in Fig. 5.6. Firstly, the regime with three impacts per cycles is excited as shown in area *a*. Then the response of two asymmetric impacts per cycles appears consecutively as demonstrated in area *b*. When the amplitude of the system decreases to the transition point T_2 , the flow starts to follow the fixed points on the stable branch, which means that the response of two symmetric impacts per cycles with the 1:1 resonance capture is activated in area *c*. When the amplitude of the system decays until reaching the transition point T_1 , the system escapes from resonance capture, and the VI NES performs the chaotic motion, as shown in area *d*.

For the second case, as the cavity length is set as $b = b_t$, the master energy is directly decreased from T_2 . Under a fast nonlinear beating, the system enters the 1:1 resonance capture and the amplitude of the LO undergoes a higher decay ratio than the first case. Meanwhile, with the increase of the clearance b , the SIM structure shifts to the upper right side, and the band of the stable branch largely increases. For the third case, the cavity length increases to $b > b_t$, making the initial master energy escape T_2 and approach T_1 more closely. As a result, its TET efficiency is large at the beginning period, as can be seen from the comparison of $t_{x=15}$ in Table 5.1. However, as the the amplitude of the LO decreases to 5 mm, the TET efficiency of this case becomes low and the second case performs the best in terms of energy dissipation for the whole process.

Thus it can be concluded that tuning the cavity length of VI NES at b_t is a feasible way to achieve a high TET efficiency under transient excitation. However, optimal efficiency

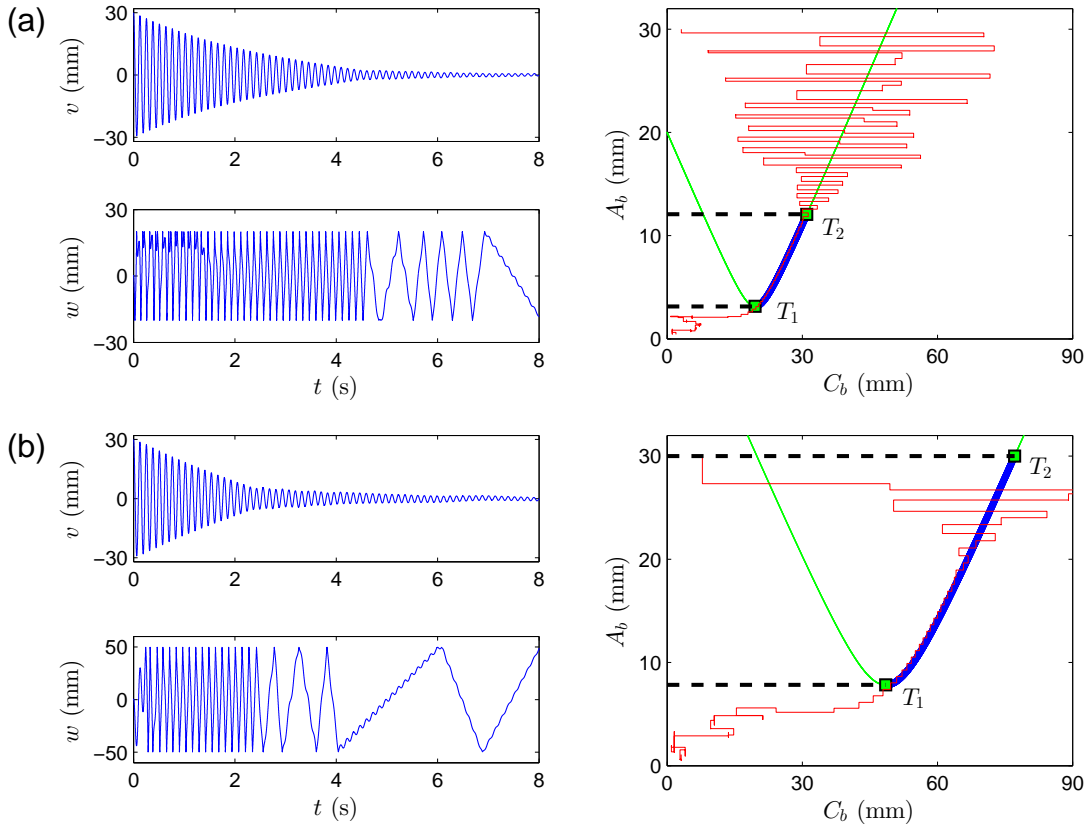


Figure 5.5: Time-displacement response of LO and VI NES, and the motion of the system projected into the SIM: (a) four response regimes with $b < b_t$; (b) two response regimes with $b = b_t$.

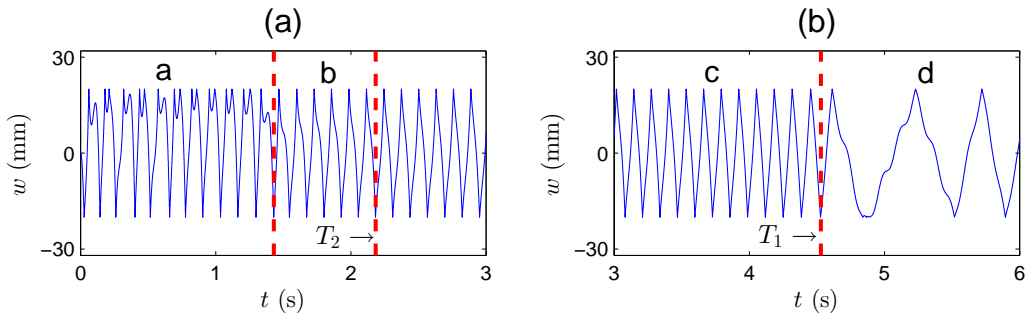


Figure 5.6: Four response regimes of VI NES: (a) three impacts per cycle; (b) two asymmetric impacts per cycle; (c) two symmetric impacts per cycle; (d) chaos with no duration of two impacts per cycle.

of TET is achieved only in the stable branch of the SIM (between T_1 and T_2), which means that the VI NES is only effective in a certain range of the external forcing amplitude. For the engineering application, the cavity length of VI NES is usually fixed. To improve the robustness of VI NES for different types of excitation, tuning the clearances of multiple

degree of freedom VI NESs in parallel is an alternative way. For this, the optimal design of multiple VI-NESs is discussed in the next section.

5.3 Optimal design of multiple VI-NESs

In this section, academic model is updated by replacing single VI NES attachments with a parallel configuration of n VI NESs, and a schematic of the dynamic system with $n = 2$ is illustrated in Fig. 5.7. Dynamic motion is consequently related to a set of $n + 1$ ordinary differential equations given by:

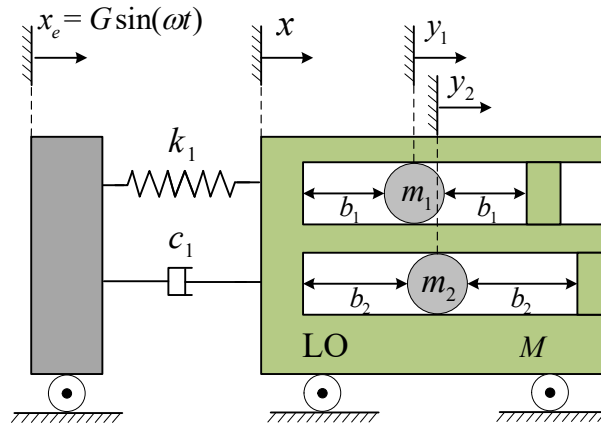


Figure 5.7: Schematic of the dynamic system: a harmonically excited LO coupled with two VI NESs in parallel

$$\begin{aligned}
 M\ddot{x} + c_1\dot{x} + k_1x &= k_1x_e + c_1\dot{x}_e \\
 m\ddot{y}_1 &= 0, \quad \forall |x - y_1| < b_1 \\
 m\ddot{y}_i &= 0, \quad \forall |x - y_i| < b_i, \quad i = 2..n
 \end{aligned} \tag{5.36}$$

System of (5.36) then can be rewritten as the dimensionless form:

$$\begin{aligned}
 \ddot{X} + \epsilon\lambda\dot{X} + X &= \epsilon F \sin \Omega\tau + \epsilon^2\lambda F\Omega \cos \Omega\tau \\
 \epsilon\ddot{Y}_1 &= 0, \quad \forall |X - Y| < 1 \\
 \epsilon\ddot{Y}_i &= 0, \quad \forall |X - Y| < \Delta_i, \quad i = 2..n
 \end{aligned} \tag{5.37}$$

where the variables of the displacements are dimensioned by $x = Xb_1$ and $y_i = Y_ib_1$. The new physical parameters are expressed as follows:

$$\begin{aligned}
 \epsilon &= \frac{m_1 + m_2 + ..m_n}{M}, \quad \alpha_i = \frac{m_i}{\epsilon M}, \quad \omega_0^2 = \frac{k_1}{M}, \quad \tau = \omega_0 t, \\
 \lambda &= \frac{c_1}{\epsilon M \omega_0}, \quad \Omega = \frac{\omega}{\omega_0}, \quad F = \frac{G}{\epsilon b_1}, \quad \Delta_i = \frac{b_i}{b_1}
 \end{aligned} \tag{5.38}$$

In the same way, when $|X - Y_i| = \Delta_i$, an impact occurs, it yields:

$$\begin{aligned} X^+ &= X^-, \quad Y_i^+ = Y_i^- \\ \dot{X}^+ + \epsilon \sum_{i=1}^n \alpha_i \dot{Y}_i^+ &= \dot{X}^- + \epsilon \sum_{i=1}^n \alpha_i \dot{Y}_i^- \\ \dot{X}^+ - \dot{Y}_i^+ &= -r (\dot{X}^- - \dot{Y}_i^-), \quad \dot{Y}_j^+ = \dot{Y}_j^-, \quad (j \neq i) \end{aligned} \quad (5.39)$$

Motions of the center of mass and internal displacement are introduced in the following way:

$$V = X + \epsilon \sum_{i=1}^n \alpha_i Y_i, \quad W_i = X - Y_i \quad (5.40)$$

Then substituting Eq. (5.40) in Eqs. (5.39) and (5.38), it gives

$$\begin{aligned} \ddot{V} + \epsilon \lambda \frac{\dot{V} + \epsilon \sum_{i=1}^n \dot{W}_i}{1 + \epsilon} + \frac{V + \epsilon \sum_{i=1}^n W_i}{1 + \epsilon} &= \epsilon F \sin \Omega \tau \\ \ddot{W}_i + \epsilon \lambda \frac{\dot{W}_i + \epsilon \sum_{i=1}^n \dot{W}_i}{1 + \epsilon} + \frac{W_i + \epsilon \sum_{i=1}^n W_i}{1 + \epsilon} &= \epsilon F \sin \Omega \tau \\ \forall |W_i| &< \Delta_i \end{aligned} \quad (5.41)$$

For this system, the impact condition (5.39) can be rewritten as:

$$\begin{aligned} V^+ &= V^-, \quad W_i^+ = W_i^-, \quad \dot{V}^+ = \dot{V}^- \\ \text{if } |W_1| = 1 : \dot{W}_1^+ &= -r \dot{W}_1^-, \quad \dot{W}_i^+ = \dot{W}_i^- - \frac{\epsilon \alpha_1 (1+r)}{1 + \epsilon \alpha_1} \dot{W}_1^-, \quad (i \neq 1) \\ \text{if } |W_i| = \Delta_i : \dot{W}_i^+ &= -r \dot{W}_i^-, \quad \dot{W}_j^+ = \dot{W}_j^- - \frac{\epsilon \alpha_i (1+r)}{1 + \epsilon \alpha_i} \dot{W}_i^-, \quad (j \neq i) \end{aligned} \quad (5.42)$$

Then multiple scales Eq. (5.10) and Eq. (5.11) are introduced in Eq. (5.42), system approximated at order ϵ^0 and order ϵ^1 is obtained:

Order ϵ^0 :

$$\begin{aligned} D_0^2 V_0 + V_0 &= 0 \\ D_0^2 W_{i0} + V_0 &= 0, \quad \forall |W_{i0}| < \Delta_i \end{aligned} \quad (5.43)$$

$$\begin{aligned} V_0^+ &= V_0^-, \quad W_0^+ = W_0^-, \quad \text{for } |W_{i0}| = \Delta_i \\ D_0 V_0^+ &= D_0 V_0^-, \quad D_0 W_{i0}^+ = -r D_0 W_{i0}^- \end{aligned} \quad (5.44)$$

Order ϵ^1 :

$$\begin{aligned}
 D_0^2 V_1 + V_1 &= -2D_0 D_1 V_0 - \lambda D_0 V_0 - \sum_{i=1}^n \alpha_i W_{i0} + V_0 + F \sin(\tau_0 + \sigma \tau_1) \\
 D_0^2 W_i + V_1 &= -2D_0 D_1 V_0 - \lambda D_0 V_0 - \sum_{i=1}^n \alpha_i W_{i0} + V_0 + F \sin(\tau_0 + \sigma \tau_1) \\
 \forall |W_{i0}| &< 1, \quad i = 2..n
 \end{aligned} \tag{5.45}$$

With the same method used in Eq. (5.19), the SIM expression for multi VI NESs is finally deduced as:

$$\begin{aligned}
 A^2 &= (1 - C_1)^2 + \frac{4C_1^2 \Gamma^2}{\pi^2} \\
 A^2 &= (\Delta_i - C_i)^2 + \frac{4C_i^2 \Gamma^2}{\pi^2}, \quad i = 2..n
 \end{aligned} \tag{5.46}$$

Here it can be observed that each VI NES is dependent on the initial energy stored in the primary system and their performance is decoupled. With the principle of additivity and activities of VI NESs, the NESs efficiency is solely driven by intrinsic properties of LO and their own individual characteristics. Referring to the issue of optimal design for a single VI NES studied in section 5.2, it can be straightforward to extend optimal criteria in the case of n -parallel VI NES by adjusting the two dimensionless variables Δ_i and α_i , so as to ensure VI NESs be activated in a large band of excitation.

The transition point T_{i1} , which corresponds to the optimal activation energy of each VI NES that allows 1:1 TET, is given by:

$$C_{i1} = \frac{\pi^2 \Delta_i}{\pi^2 + 4\Gamma^2}, \quad A_{i1}^2 = \frac{4\Gamma^2 \Delta_i^2}{\pi^2 + 4\Gamma^2}, \quad i = 2..n \tag{5.47}$$

Thus the multiple VI NES can be designed as the following rule: $A_{11}^2 < A_{21}^2 < \dots < A_{n1}^2$. In this case, the activation energy of each VI NES is monotonously increased, making VI-NESs work robustly in different types of energy.

5.4 Experimental validation

The objective of this section is to experimentally verify the optimal design criteria proposed in the above sections. For periodic excitation, the focus is initially to verify the periodic case at the resonance frequency and then to validate the results under a range of frequency. As for transient excitation, tuned method for optimal efficiency is verified, and two VI NESs in parallel are tested with the purpose of robustness improvement. The detailed procedures are as follows.

5.4.1 Periodic excitation

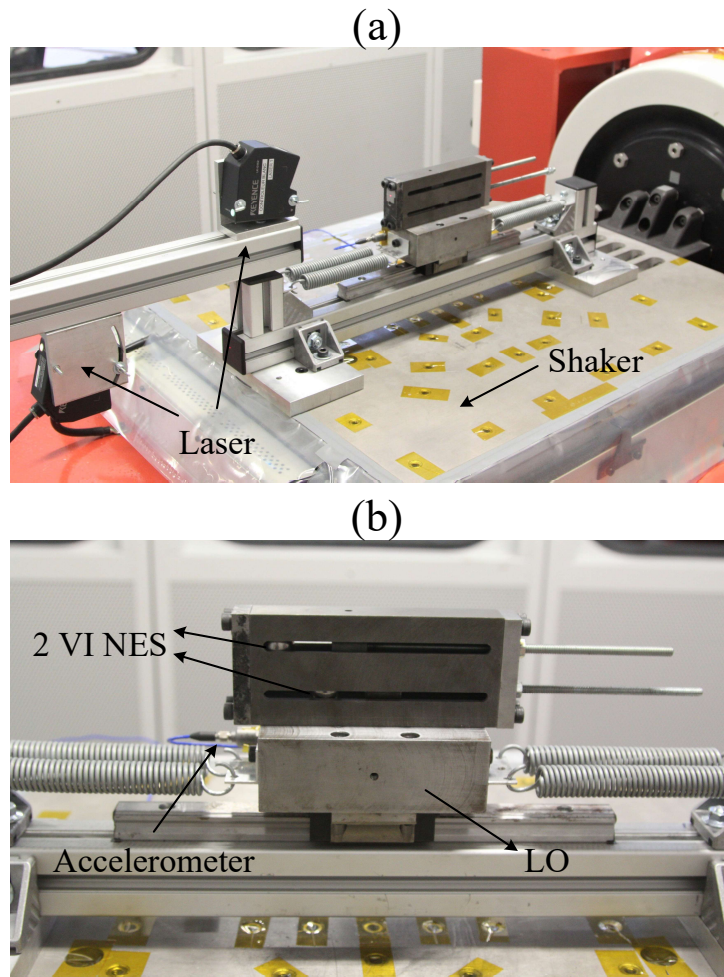


Figure 5.8: Experimental setup for periodic excitation:(a) global view of the configuration; (b) detailed view of the VI NES

The experimental setup of periodic excitation is same as that in [Li, 2016] (see Fig. 5.8). Where two clearances in parallel are used to decide whether a VI NES or two VI NESs are attached to the LO. The whole system is embedded on a 10 kN electrodynamic shaker. The raw signals are recorded using a digital oscilloscope and a bandpass filter is applied to correct biases and suppress high frequency noise. The displacement of the LO as well as the imposed displacement of the shaker are measured by two contactless laser displacement sensors. The acceleration is measured by a accelerometer and the impacts between LO and VI NES can be judged from sudden changes of the acceleration of the LO. The parameters identified on the experimental setup and used for the calculation are given in Table. 5.2.

With the variation of the clearance, three different responses of the LO under periodic excitation $G = 0.25$ mm are obtained, as shown in Fig. 5.9(a-c). Where the excitation

Table 5.2: Experimental parameters

Physical Parameters			
M	4.7 kg	c_1	3.02 Ns/m
k_1	1.147×10^4 N/m	m	32 g
Reduced Parameters			
ϵ	0.68 %	λ	1.91
f_0	7.86 Hz	r	0.6

frequency is fixed at the resonance frequency. As can be seen, the amplitude of the LO with $b = b_c$ is smaller than the other two cases (i.e., steady state response with $b < b_c$ and chaotic SMR with $b > b_c$), since its fixed point is targeted at the transition point T_1 . The optimal length of the cavity b_c under different types of excitation is calculated by Eq. (5.34) and presented in Fig. 5.9(d). It can be observed that the experimental points are close to the theoretical values and almost locate in a line. The differences between the theoretical and experimental values are mainly caused by the weakly nonlinear damping of the LO. Thus it can be demonstrated that the analytical calculation b_c is feasible to predict the efficient TET at resonance frequency for different types of excitation.

For the system under a range of frequencies, if the optimal clearance is still chosen by the value for resonance frequency, the responses of the other frequency points will not be optimal and may result in SMR or irregular response without any duration of two impacts per cycle. Therefore, there does not exist an optimal value of b for all frequencies. In [Li et al., 2017d], it is suggested that the objective to control the amplitude of the LO for a range of frequency can be simplified to that of resonance frequency. Thus the clearance b_c is continually used as the optimal value.

Based on the sweep frequency test, frequency response functions (FRF) with $b < b_c$, $b = b_c$ and $b > b_c$ are obtained and illustrated in Fig. 5.10(a). The detailed time-displacement responses are presented in Fig. 5.10(b-c). As $b < b_c$, the amplitude of LO is decreased with the addition of VI NES, and a small resonance peak still exists in this case. As $b > b_c$, the resonance peak is vanished and a large band of SMR can be found. However, the average amplitude of LO is still large in a range around the resonance frequency. As $b = b_c$, there exists a narrow range of frequency where SMR occurs. Although the VI NES can not work at its optimal state for other frequency except resonance frequency, the average amplitude of LO is smaller than the above two cases. Thus, the optimal design for a range of frequency can directly use the analytical calculation of b_c , so as to make VI NES achieve a high TET efficiency for vibration mitigation.

For the above experimental configuration, the single VI NES case with the clearance

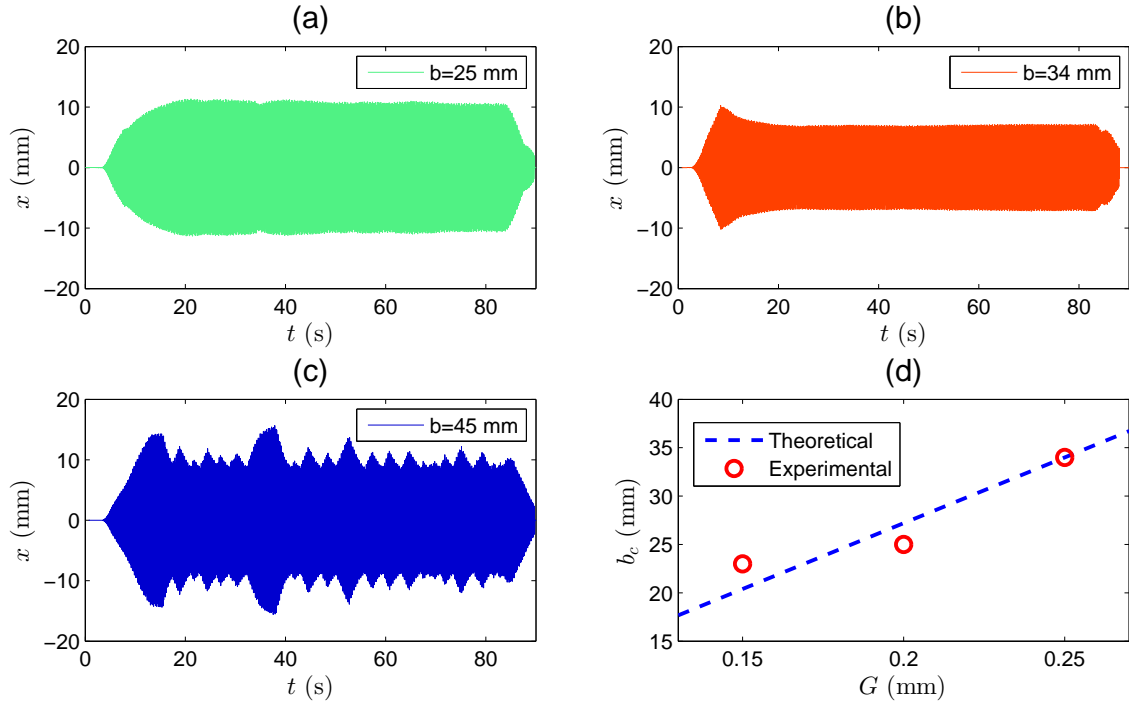


Figure 5.9: Experimental results of single VI NES: response of the LO under periodic excitation $G = 0.25$ mm with (a) $b = 25$ mm ($< b_c$); (b) $b = 34$ mm ($= b_c$); (c) $b = 45$ mm ($> b_c$) and (d) optimal length of the cavity b_c under different types of excitation.

$b = 34$ and 23 mm has been observed optimal for the excitation with $G = 0.25$ mm and 0.15 mm, respectively. Consequently, the clearances of two VI NESs in parallel are selected by these two values. The frequency response curves under $G = 0.25$ mm are recorded for different combinations of b_1 and b_2 and are showed in Fig. 5.11(a). The detailed time-displacement responses are presented in Fig. 5.11(b-c). As $b_1 = b_2 = 34$ mm, the amplitude of the LO around the resonance frequency is decreased. However, its maximum amplitude shifts to the left side and still perform the same value (7.9 mm) with that of single VI NES with $b = 34$ mm. As $b_1 = b_2 = 23$ mm, the amplitudes of the LO in the other frequencies are decreased. Yet there exists a small resonance peak at the resonance frequency, since the clearance is not optimal for this excitation. As $b_1 = 23$ mm and $b_2 = 34$ mm, the small resonance peak is vanished and the frequency range for response with two impacts per cycle is increased. Although there still exist a narrow range of frequency where SMR occurs, its maximum amplitude of the LO is decreased to 4.9 mm. This value is far lower than the above two cases, which means that adding two VI NESs with different clearance can perform a better TET efficiency and improve the robustness in a range of resonance frequency.

Therefore, the design criteria for optimally tuned VI NES are summarized. If single

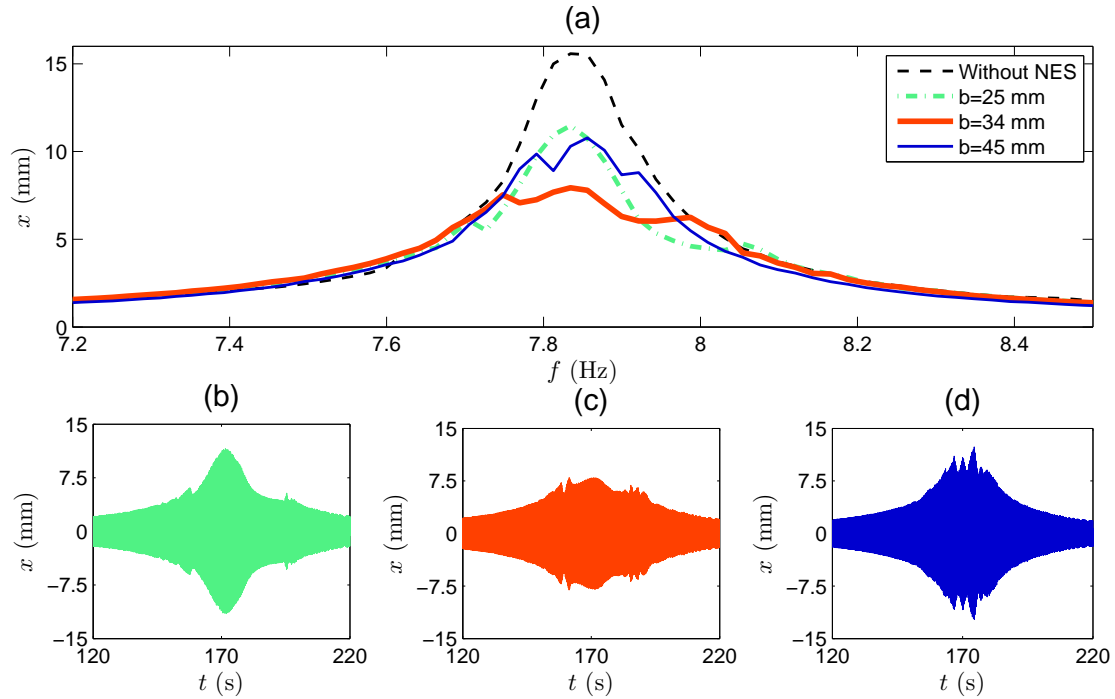


Figure 5.10: Experimental results of single VI NES: (a) frequency response curve of the LO with $G = 0.25$ mm and detailed view of response of the LO under sweep frequency test with (b) $b = 25$ mm ($< b_c$); (c) $b = 34$ mm ($= b_c$); (d) $b = 45$ mm ($> b_c$).

VI NES is applied, it is recommended that the clearance of VI NES should be optimized at the point of resonance frequency. By using the calculation of Eq. (5.34), the maximum amplitude of the LO can be controlled well at resonance condition (i.e., a single resonance frequency or a range of frequency). In this case, semi-active control method can also be realized: by adjusting the clearance, VI NES can be tuned to work robustly with its best performance. If multiple VI NESs are adopted to improve the robustness, the objective should be first to calculate the optimized clearance for the maximum excitation and then to choose a smaller length of clearance for a lower level of energy. By making VI NESs activated at different types of energy, a high TET efficiency can be obtained in a large band of excitation.

5.4.2 Transient excitation

The experimental setup for transient excitation is presented in Fig. 5.12, and corresponding parameters can be referred from Table. 5.2. Here, the initial displacement of LO is obtained by stretching the string to a fixed position ($x_0 = 20$ mm). Once the string is cut, both the LO and the VI NES start to vibrate, and the movement is recorded. The displacement and acceleration of the LO are measured by a laser and an accelerometer,

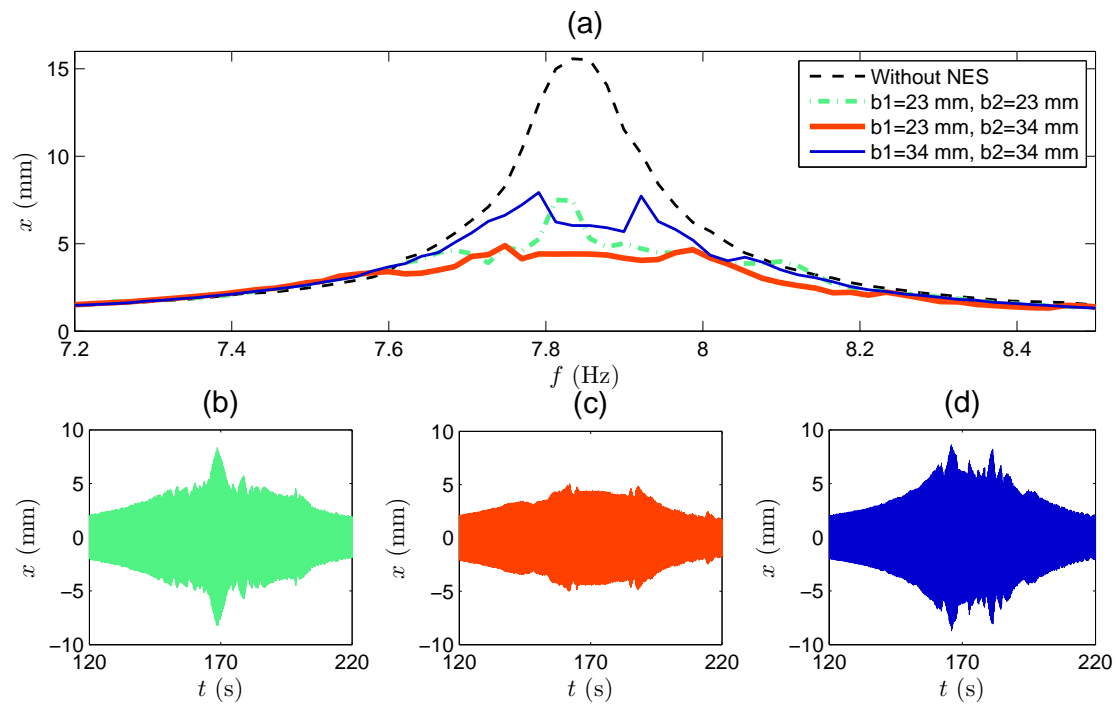


Figure 5.11: Experimental results of two VI NESs: (a) frequency response curve of the LO with $G = 0.25$ mm and detailed view of response of the LO under sweep frequency test with (b) $b_1 = 23$ mm, $b_2 = 23$ mm; (c) $b_1 = 23$ mm, $b_2 = 34$ mm; (d) $b_1 = 34$ mm, $b_2 = 34$ mm.

respectively. By varying the length of cavity, the transition of response regimes is observed and the comparison of efficiency for different cavity lengths can be further studied.

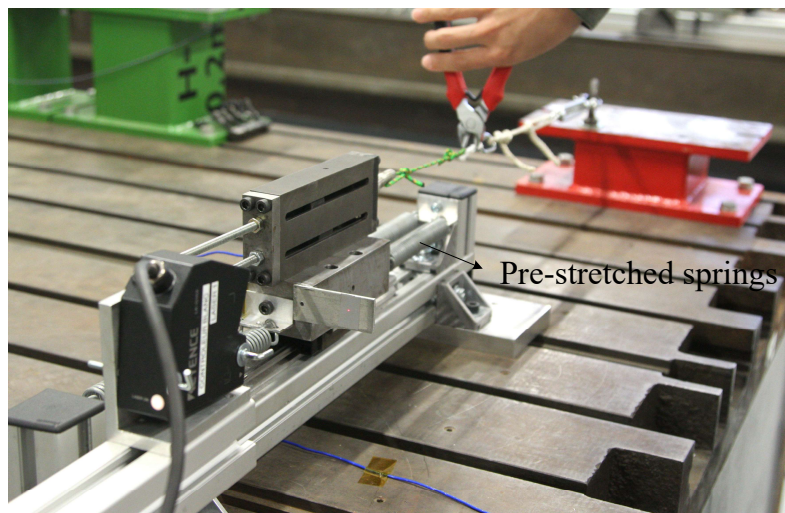


Figure 5.12: Experimental setup for transient excitation

The experimental results of single VI NES are presented in Fig. 5.13. As can be

seen from Fig. 5.13(a), without VI NES, the vibration extinction of LO follows a natural exponential decrease; while with VI NES, it follows two phases of quasi-linear decrement, much faster than the exponential one, during which the displacement of LO decreases fastly until it reaches a transition point (T_1) and the decay rate after this point is obviously lower than the previous one. An enlarged view of acceleration around this transition point is showed in Fig. 5.13(b). As the sudden pulse of acceleration denotes an impact moment, the transition between response regime of two symmetric impacts per cycle and chaos with infinite number of impact per cycle can be clearly identified.

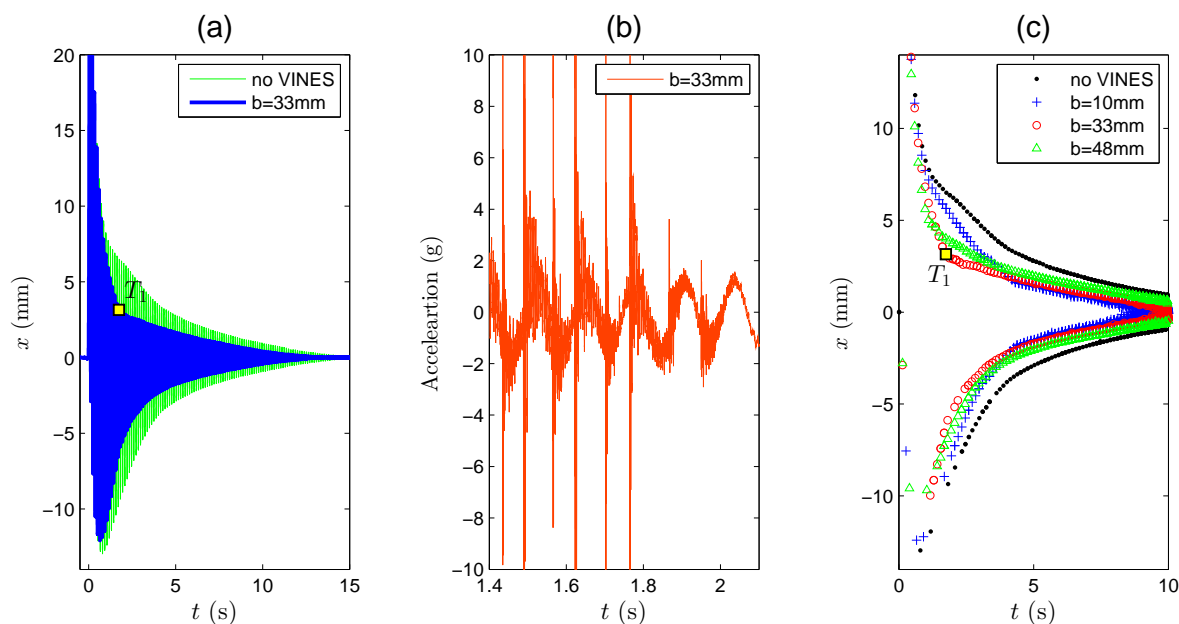


Figure 5.13: Experimental results of single VI NES: (a) time history of the displacement; (b) time history of the acceleration; (c) comparison of the displacement envelope with different b .

Fig. 5.13(c) shows the comparison of the displacement envelope of LO attached to single VI NES with different cavity lengths. As $b = 10 \text{ mm} < b_t$, the master energy is higher than that of transition point T_2 (see Fig. 5.5), resulting in the decay rate being relatively low. As $b = 33 \text{ mm} = b_t$ and $b = 48 \text{ mm} > b_t$, both their responses start from regime with two symmetric impacts per cycle, making the vibration extinction of LO directly follow a quasi-linear decrease. In addition, it can be observed that the transition point T_1 with $b = b_t$ is lower than that with $b > b_t$. Thus, tuning the cavity length at b_t is a feasible way to obtain an optimal TET efficiency during the whole vibration process.

The experimental results of two VI NESs are presented in Fig. 5.14. As the cavity lengths of two VI NESs are set as two different values with $b_1 = 33 \text{ mm}$ and $b_2 = 10 \text{ mm}$, the vibration extinction of LO follows three quasi-linear decreases (see Fig. 5.14(a)). If

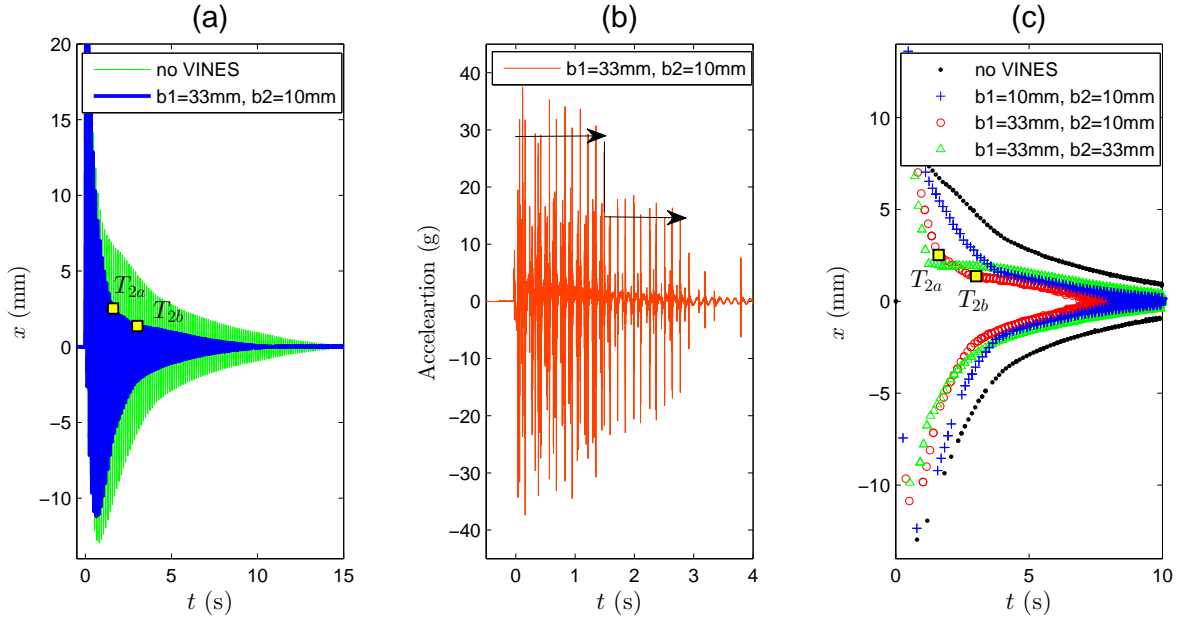


Figure 5.14: Experimental results of two VI NESs: (a) time history of the displacement; (b) time history of the acceleration; (c) comparison of the displacement envelope with different b .

the amplitude of LO is higher than the transition point T_{1a} , the first VI NES with a large cavity length is activated with two impacts per cycle. If the amplitude of LO is located in the range between T_{1a} and T_{1b} , the first VI NES escapes from the activation and the second VI NES with a small clearance is activated with 1:1 resonance capture. The principle of separate activation can also be found from the time history of acceleration (see Fig. 5.14(b)). As can be seen, the impact strength of VI NES is related to the cavity length. The horizontal arrows show the two activations of two VI NESs with different cavity lengths, and the vertical line illustrates the sudden change between them.

Fig. 5.14(c) shows the comparison of the displacement envelope of LO attached to two VI NESs with different cavity lengths. With the addition of another ball, the three groups of two VI NESs perform better than the case of single VI NES. As $b_1 = b_2 = 10$ mm, the decay rate of first decrease phase is slightly improved, while the displacement of the transition point is almost the same as that of single VI NES with $b = 10$ mm. As $b_1 = b_2 = 33$ mm, the decay rate of first decrease phase is optimal. However, the efficiency at low energy level is not improved, and the decay rate is far lower than the other two cases. As $b_1 = 33$ mm and $b_2 = 10$ mm, the decay rate of first decrease phase is close to that of VI NESs with $b_1 = b_2 = 33$ mm. At low energy level (the amplitude of LO is lower than T_{1a}), the decay rate performs optimal than the other two cases. Thus this groups of VI NES can work robustly and efficiently for different kinds of transient excitation.

In summary, tuned method for transient excitation is verified. The analytical calcu-

lation of Eq. (5.35) is demonstrated to predict the optimal clearance well. Moreover, the principles of additivity and separate activities of multiple VI NESs are observed, and the robustness of vibration control can be improved for a large band of transient excitation.

5.5 Conclusion

The ultimate goal of this chapter is to propose the design criteria for optimally tuned Vibor-Impact (VI) NES to control the vibration under periodic and transient excitation. To this end, a generalized dimensionless model of a 2 degrees of freedom system comprising a harmonically excited LO strongly coupled to a VI NES is studied. An analytically obtained Slow Invariant Manifold (SIM) is used to explain the different response regimes. Where the transition point (i.e., T_1) between the regime with two symmetrical impacts per cycles and that of Strongly Modulated Response (SMR) is demonstrated to be optimal for periodic excitation. Thereafter, a bifurcation analysis is carried out. Activation energy threshold for targeted energy transfer is obtained and used to design an optimal criterion for a single NES.

For transient excitation, the critical point (i.e., T_2) between the regime with two symmetrical impacts per cycles and two asymmetrical impacts per cycles is adopted to calculate the optimal clearance, and it proves that tuning the initial master energy at this point can achieve a high TET efficiency during the whole vibration process. Thirdly, the procedure is extended in case of multiple VI NESs in parallel. Two principles of additivity and separate activities of VI NESs are verified theoretically and experimentally.

Finally, experiments involving the whole system for periodic and transient excitation are performed. The results show that the analytical calculation of the clearance can not only predict the efficient TET at resonance frequency, but can also achieve an optimal performance to protect the primary system in a range of frequency. Furthermore, the design criteria for single VI NES can be straightforward for the application of multiple VI NESs and semi-active control, so as to make VI NES work robustly under different types of excitation.

Conclusion and Perspectives

The work of this thesis is dedicated to the passive control of dynamics systems subjected to harmonic and transient excitations using a Nonlinear Energy Sink (NES). All studies, no matter analytical, numerical or experimental, are tightly around the four questions raised in the introduction. The response are almost positive as follows:

- The optimal nonlinear stiffness proposed for NES system is efficient to avoid the detached resonance tongue and allows energy pumping at the same time.
- The designed NES can not only output the expected nonlinear characteristics, but can also be tuned to work robustly over a range of excitation.
- Bistable NES can be efficient and robust in a broad-range of excitations, and its optimal design criterion is practicable to guide the semi-active control method.
- The optimal clearance calculated for a Vibro-Impact (VI) NES can be straightforward for multiple VI NESs and semi-active control, so as to improve the robustness.

Developed around them, the work of this thesis is organized in five chapters. In the first chapter, a general background and the state of art is introduced. The latter is developed around two axes: NES with smooth nonlinearity and VI NES. The general study results are presented for cubic NES. More importantly, its unresolved issues are exposed, e.g., how to optimize the NES under a given primary system specification, and how to implement a cubic nonlinearity element in practice without any linear part. As for VI NES, its former study show the possibility of semi-active control of this NES but the limitation results from the analytical calculation. With this in mind, design theory and experimental study of a novel NES, efficient Targeted Energy Transfer (TET) of bistable NES and design criteria for optimally tuned VI NES are studied in this thesis.

The second chapter is devoted to the design criterion and design theory of a novel NES. To this end, a combined method with slow invariant manifold (SIM) and stability of the fixed points is studied theoretically. Frequency response functions (FRF) are calculated when the different parameters are varied and explain the behavior of the NES

well. As a result, an optimal nonlinear stiffness is obtained, so as to tune the NES be activated and produce the efficient TET. Then a novel design of NES system yielding cubic nonlinearity without a linear part is developed. Key features of the system include: (i) specifically sizing two nonlinear springs to provide the force polynomial components with only linear and cubic terms; (ii) pre-compressing the two springs at the transition point to produce smooth nonlinear force characteristics; (iii) adding a negative stiffness mechanism to counterbalance the linear term. Finally, a special sized NES system is developed, in which the distance between each spring and the NES mass is adjustable so that a suitable force shape can be reached.

In the third chapter, experimental study to validate the concept of NES is performed. Firstly, identification and calculation of effective mass are implemented. The results of force characteristics show that both the variable pitch spring and conical spring can produce strong nonlinearity. Furthermore, combining nonlinear springs and a negative stiffness mechanism is a feasible way to produce pure cubic nonlinearity. Then, dynamic tests are carried out. The results show that the designed NESs are efficient to protect the primary system in a large band of frequencies. Moreover, it performs well in terms of controlling the maximum amplitude of the LO for different types of excitation. Finally, a sensitivity analysis is performed with respect to the pre-compressed length. Different kinds of NES (with positive stiffness, negative stiffness and unsymmetrical stiffness) are generated, which lays the foundation that: as the springs of this device are fixed for engineering applications, semi-active control of this NES may provide an alternative way to increase the band in which excitation amplitude is efficient.

In the fourth chapter, efficient TET of bistable NES (with cubic and negative stiffness) is investigated. An analytically obtained SIM is used to explain the different response regimes. Asymptotic analysis and Melnikov analysis are respectively used to obtain the thresholds of different response regimes. Then efficiency of different response regimes is studied and demonstrates that with the addition of negative stiffness, the efficiency of bistable NES in the band of Strongly Modulated Response (SMR), is larger than that of cubic NES. Finally, an optimal point located at the boundary between the SMR and stable periodic response is found, at which the efficiency of NES is largest and the amplitude of LO is smallest. Based on this, an optimal design criterion and the corresponding configuration are proposed, and experiments for semi-active control of NES are also explored. By adjusting the pre-compressed length of spring, the NES can be tuned to robustly work at its best performance for a range of excitation.

The fifth chapter aims to propose the design criteria for optimally tuned VI NES to control the vibration under periodic and transient excitation. Firstly, bifurcation analysis and efficiency of TET around the SIM are studied with the variation of clearance. As a result, the optimal clearances for periodic and transient excitation are calculated from

two transition points of the SIM, respectively. Then the procedure is extended in case of multiple VI NESs in parallel to the LO. Two principles of additivity and separate activities of VI NESs are verified theoretically. Finally, experiments involving the primary system with single VI NES and multiple VI NESs are performed. The results show that the design criteria can not only predict the efficient TET at resonance frequency, but can also achieve an optimal performance in a range of frequencies. Furthermore, it can be straightforward for the application of multiple VI NESs and semi-active control, so as to make VI NES work robustly under different types of excitation.

Following this work, several points of research can be envisaged:

- One NES
 - The design parameters of conical spring are mainly obtained by optimization, detailed analytical calculation for this spring (or even with variable pitch) can be further studied.
 - Negative stiffness mechanism with linear springs requires extra space in lateral direction, using the magnetic components to replace such springs may be an alternative way.
 - Chaotic characteristic of bistable NES and VI NES should be further studied. Especially, Lyapunov exponent can be calculated, so as guide the threshold of each response regimes.
- Multiple NESs
 - Using multiple NESs is feasible to enhance the TET efficiency, but additional external degrees of freedom requires additional spaces for the NES. A generalized design theory considering this problem should be further studied.
 - Since the activation of VI NES depends on its clearance, mass and restitution coefficient, it is desirable to further study the combination of different VI NES with these different parameters.
- Other NES
 - The NES with combined nonlinearity (i.e. impact and cubic nonlinearity) seems perform better than pure cubic NES, more theoretical development and experimental validation can be further studied.
 - The non-smooth NES (with piecewise stiffness springs) only needs the space of translational direction, it is interesting to realize the mechanical design of such springs and make the experimental comparison with other NES.

- The optimal design criteria of bistable NES and VI NES is obtained under the context of TET, it is reasonable to generalize the results to other NES or even other absorbers.
- Application
 - With the designed NES, other excitation such as random excitation to simulate the seismic activity can be further studied .
 - Application of the designed NES to the control of chatter, e.g., experimental validations can be further studied.
 - Using the designed NES or VI NES to semi-active control (with linear actuator) the vibration of linear and nonlinear systems can be further studied.

Bibliography

- [Afsharfard, 2016] Afsharfard, A. (2016). Suppressing forced vibrations of structures using smart vibro-impact systems. *Nonlinear Dynamics*, 83(3):1643–1652. Cited page 26
- [Afsharfard and Farshidianfar, 2013] Afsharfard, A. and Farshidianfar, A. (2013). Free vibration analysis of nonlinear resilient impact dampers. *Nonlinear Dynamics*, 73(1-2):155–166. Cited page 26
- [Ahmadabadi and Khadem, 2013] Ahmadabadi, Z. N. and Khadem, S. (2013). Self-excited oscillations attenuation of drill-string system using nonlinear energy sink. *Proc IMechE, Part C: J Mechanical Engineering Science*, 227(2):230–245. Cited page 27
- [Alabuzhev and Rivin, 1989] Alabuzhev, P. and Rivin, E. I. (1989). *Vibration protection and measuring systems with quasi-zero stiffness*. CRC Press. Cited page 19
- [Alexander and Schilder, 2009] Alexander, N. A. and Schilder, F. (2009). Exploring the performance of a nonlinear tuned mass damper. *Journal of Sound and Vibration*, 319(1):445–462. Cited page 7
- [Avramov and Gendelman, 2010] Avramov, K. and Gendelman, O. (2010). On interaction of vibrating beam with essentially nonlinear absorber. *Meccanica*, 45(3):355–365. Cited page 28
- [Babitsky, 2013] Babitsky, V. I. (2013). *Theory of vibro-impact systems and applications*. Springer Science & Business Media, Berlin. Cited page 26
- [Bellet et al., 2010] Bellet, R., Cochelin, B., Herzog, P., and Mattei, P.-O. (2010). Experimental study of targeted energy transfer from an acoustic system to a nonlinear membrane absorber. *Journal of Sound and Vibration*, 329(14):2768–2791. Cited page 28
- [Bentley et al., 2015] Bentley, A., Hodges, T., Jiang, J., Krueger, J., Nannapaneni, S., Qiu, T., Massad, J., and Webb, S. (2015). A flexible methodology for optimal helical compression spring design. Cited page 12
- [Borosan et al., 2017] Borosan, E., SamyMissoum, Mattei, P.-O., and Vergez, C. (2017). Optimization under uncertainty of parallel nonlinear energy sinks. *Journal of Sound and Vibration*, 394:451–464. Cited page 29
- [Carrella et al., 2007] Carrella, A., Brennan, M., and Waters, T. (2007). Static analysis of a passive vibration isolator with quasi-zero-stiffness characteristic. *Journal of Sound and Vibration*, 301(3):678–689. Cited page 19

- [Casado et al., 2007] Casado, C. M., Poncela, A. V., and Lorenzana, A. (2007). Adaptive tuned mass damper for the construction of concrete piers. *Structural engineering international*, 17(3):252–255. *Cited page 9*
- [Chang and Soong, 1980] Chang, J. C. and Soong, T. T. (1980). Structural control using active tuned mass dampers. *Journal of the Engineering Mechanics Division*, 106(6):1091–1098. *Cited page 9*
- [Chen and Lan, 2012] Chen, Y.-H. and Lan, C.-C. (2012). An adjustable constant-force mechanism for adaptive end-effector operations. *Journal of Mechanical Design*, 134(3):031005. *Cited page 20*
- [Chicurel-Uziel, 2001] Chicurel-Uziel, E. (2001). Exact, single equation, closed-form solution of vibrating systems with piecewise linear springs. *Journal of Sound and Vibration*, 245(2):285–301. *Cited page 16*
- [Choi and Kim, 2000] Choi, S.-B. and Kim, W.-K. (2000). Vibration control of a semi-active suspension featuring electrorheological fluid dampers. *Journal of Sound and Vibration*, 234(3):537–546. *Cited page 7*
- [Den boer, 2009] Den boer, L. (2009). *Nonlinear dynamic behaviour of a conical spring with top mass*. PhD thesis, Master Dissertation, Eindhoven University of Technology, Eindhoven, Netherlands. *Cited page 17*
- [Dimentberg and Iourtchenko, 2004] Dimentberg, M. and Iourtchenko, D. (2004). Random vibrations with impacts: a review. *Nonlinear Dynamics*, 36(2):229–254. *Cited page 26*
- [Dowdell and Cherry, 1994] Dowdell, D. and Cherry, S. (1994). Semi-active friction dampers for seismic response control of structures. In *Proc. 5th US Nat. Conf. on Earthquake Engrg*, volume 1, pages 819–828. *Cited page 7*
- [Dyke et al., 1996a] Dyke, S., Spencer Jr, B., Sain, M., and Carlson, J. (1996a). Modeling and control of magnetorheological dampers for seismic response reduction. *Smart materials and structures*, 5(5):565. *Cited page 7*
- [Dyke et al., 1996b] Dyke, S., Spencer Jr, B., Sain, M., and Carlson, J. (1996b). Seismic response reduction using magnetorheological dampers. *IFAC Proceedings Volumes*, 29(1):5530–5535. *Cited page 7*
- [Dyke et al., 1998] Dyke, S., Spencer Jr, B., Sain, M., and Carlson, J. (1998). An experimental study of mr dampers for seismic protection. *Smart materials and structures*, 7(5):693. *Cited page 7*
- [Fang et al., 2017] Fang, X., Wen, J., Yin, J., and Yu, D. (2017). Highly efficient continuous bistable nonlinear energy sink composed of a cantilever beam with partial constrained layer damping. *Nonlinear Dynamics*, 87(4):2677–2695. *Cited page 25*
- [Feng et al., 1993] Feng, M. Q., Shinozuka, M., and Fujii, S. (1993). Friction-controllable sliding isolation system. *Journal of Engineering Mechanics*, 119(9):1845–1864. *Cited page 7*

- [Feng and Shinozuka, 1990] Feng, Q. and Shinozuka, M. (1990). Use of a variable damper for hybrid control of bridge response under earthquake. In *Proceedings of the US national workshop on structural control research*, pages 107–112. Cited page 7
- [Fisco and Adeli, 2011] Fisco, N. and Adeli, H. (2011). Smart structures: part i—active and semi-active control. *Scientia Iranica*, 18(3):275–284. Cited page 6
- [Franchek et al., 1996] Franchek, M., Ryan, M., and Bernhard, R. (1996). Adaptive passive vibration control. *Journal of Sound and Vibration*, 189(5):565–585. Cited page 6
- [Fuller et al., 1996] Fuller, C. C., Elliott, S., and Nelson, P. A. (1996). *Active control of vibration*. Academic Press. Cited page 6
- [Gendelman, 2011] Gendelman, O. (2011). Targeted energy transfer in systems with external and self-excitation. *Proc IMechE, Part C: J Mechanical Engineering Science*, 225(9):2007–2043. Cited page 27
- [Gendelman, 2012] Gendelman, O. (2012). Analytic treatment of a system with a vibro-impact nonlinear energy sink. *Journal of Sound and Vibration*, 331:4599–4608. Cited page 26
- [Gendelman and Alloni, 2015] Gendelman, O. and Alloni, A. (2015). Dynamics of forced system with vibro-impact energy sink. *Journal of Sound and Vibration*, 358:301–314. 4 citations pages [xiii](#), [24](#), [25](#), et [26](#)
- [Gendelman and Alloni, 2016] Gendelman, O. and Alloni, A. (2016). Forced system with vibro-impact energy sink: Chaotic strongly modulated responses. *Procedia IUTAM*, 19:53 – 64. IUTAM Symposium Analytical Methods in Nonlinear Dynamics. Cited page 26
- [Gendelman et al., 2008] Gendelman, O., Starosvetsky, Y., and Feldman, M. (2008). Attractors of harmonically forced linear oscillator with attached nonlinear energy sink i: Description of response regimes. *Nonlinear Dynamics*, 51(1):31–46. 4 citations pages [24](#), [34](#), [38](#), et [78](#)
- [Georgiades and Vakakis, 2009] Georgiades, F. and Vakakis, A. F. (2009). Passive targeted energy transfers and strong modal interactions in the dynamics of a thin plate with strongly nonlinear attachments. *International Journal of Solids and Structures*, 46(11):2330–2353. Cited page 28
- [Georgiades et al., 2007] Georgiades, F., Vakakis, A. F., and Kerschen, G. (2007). Broad-band passive targeted energy pumping from a linear dispersive rod to a lightweight essentially non-linear end attachment. *International Journal of Non-Linear Mechanics*, 42(5):773–788. Cited page 28
- [Gopinath and Mayuram, 2006] Gopinath, K. and Mayuram, M. (2006). Machine design ii. *Indian Institute of Technology, Madras*. Cited page 12
- [Gourc, 2013] Gourc, E. (2013). *Etude du contrôle passif par pompage énergétique sous sollicitation harmonique: Analyses théoriques et expérimentales*. PhD thesis, Toulouse, INSA. 2 citations pages [34](#) et [108](#)

- [Gourc et al., 2014] Gourc, E., Michon, G., Seguy, S., and Berlioz, A. (2014). Experimental investigation and design optimization of targeted energy transfer under periodic forcing. *Journal of Vibration and Acoustics*, 136(2):021021. *7 citations pages [xiii](#), [10](#), [24](#), [25](#), [27](#), [34](#), et [38](#)*
- [Gourc et al., 2015a] Gourc, E., Michon, G., Seguy, S., and Berlioz, A. (2015a). Targeted energy transfer under harmonic forcing with a vibro-impact nonlinear energy sink: Analytical and experimental developments. *Journal of Vibration and Acoustics*, 137(3):031–008. *4 citations pages [xiii](#), [10](#), [25](#), et [26](#)*
- [Gourc et al., 2015b] Gourc, E., Seguy, S., Michon, G., Berlioz, A., and Mann, B. (2015b). Quenching chatter instability in turning process with a vibro-impact nonlinear energy sink. *Journal of Sound and Vibration*, 355:392–406. *4 citations pages [xiii](#), [26](#), [28](#), et [29](#)*
- [Gourdon et al., 2007] Gourdon, E., Alexander, N. A., Taylor, C. A., Lamarque, C.-H., and Pernot, S. (2007). Nonlinear energy pumping under transient forcing with strongly nonlinear coupling: Theoretical and experimental results. *Journal of Sound and Vibration*, 300(3):522–551. *5 citations pages [xiii](#), [9](#), [10](#), [92](#), et [99](#)*
- [Gourdon and Lamarque, 2005] Gourdon, E. and Lamarque, C.-H. (2005). Energy pumping with various nonlinear structures: numerical evidences. *Nonlinear Dynamics*, 40(3):281–307. *Cited page [24](#)*
- [Guckenheimer and Holmes, 2013] Guckenheimer, J. and Holmes, P. J. (2013). *Nonlinear oscillations, dynamical systems, and bifurcations of vector fields*, volume 42. Springer Science & Business Media. *Cited page [85](#)*
- [Habib and Romeo, 2017] Habib, G. and Romeo, F. (2017). The tuned bistable nonlinear energy sink. *Nonlinear Dynamics*, 89(1):179–196. *2 citations pages [24](#) et [76](#)*
- [Harne et al., 2013] Harne, R., Thota, M., and Wang, K. (2013). Bistable energy harvesting enhancement with an auxiliary linear oscillator. *Smart Materials and Structures*, 22(12):125028. *2 citations pages [24](#) et [76](#)*
- [Harne and Wang, 2013] Harne, R. and Wang, K. (2013). A review of the recent research on vibration energy harvesting via bistable systems. *Smart Materials and Structures*, 22(2):023001. *Cited page [24](#)*
- [Hartog, 1956] Hartog, D. J. (1956). *Mechanical vibrations*. McGraw-Hill Book Company. *Cited page [8](#)*
- [Hazra et al., 2010] Hazra, B., Sadhu, A., Lourenco, R., and Narasimhan, S. (2010). Re-tuning tuned mass dampers using ambient vibration measurements. *Smart Materials and Structures*, 19(11):115002. *Cited page [9](#)*
- [Hoff, 1954] Hoff, N. J. (1954). Forty-first wilbur wright memorial lecture: Buckling and stability. *The Aeronautical Journal*, 58(517):3–52. *Cited page [16](#)*
- [Hrovat et al., 1983] Hrovat, D., Barak, P., and Rabins, M. (1983). Semi-active versus passive or active tuned mass dampers for structural control. *Journal of Engineering Mechanics*, 109(3):691–705. *Cited page [9](#)*

- [Huang, 2014] Huang, N. E. (2014). *Hilbert-Huang transform and its applications*, volume 16. World Scientific. *Cited page 24*
- [Huang et al., 1998] Huang, N. E., Shen, Z., Long, S. R., Wu, M. C., Shih, H. H., Zheng, Q., Yen, N.-C., Tung, C. C., and Liu, H. H. (1998). The empirical mode decomposition and the hilbert spectrum for nonlinear and non-stationary time series analysis. *Proceedings of the Royal Society of London A: mathematical, physical and engineering sciences*, 454(1971):903–995. *2 citations pages 23 et 98*
- [Huang et al., 2014] Huang, X., Liu, X., Sun, J., Zhang, Z., and Hua, H. (2014). Vibration isolation characteristics of a nonlinear isolator using euler buckled beam as negative stiffness corrector: A theoretical and experimental study. *Journal of Sound and Vibration*, 333(4):1132–1148. *Cited page 19*
- [Ibrahim, 2009] Ibrahim, R. A. (2009). *Vibro-impact dynamics: modeling, mapping and applications*, volume 43. Springer Science & Business Media, Berlin. *Cited page 26*
- [Jansen and Dyke, 2000] Jansen, L. M. and Dyke, S. J. (2000). Semiactive control strategies for mr dampers: comparative study. *Journal of Engineering Mechanics*, 126(8):795–803. *Cited page 7*
- [Johnson et al., 2013] Johnson, D. R., Thota, M., Semperlotti, F., and Wang, K. (2013). On achieving high and adaptable damping via a bistable oscillator. *Smart Materials and Structures*, 22(11):115027. *2 citations pages 24 et 76*
- [Jutte and Kota, 2008] Jutte, C. V. and Kota, S. (2008). Design of nonlinear springs for prescribed load-displacement functions. *Journal of Mechanical Design*, 130(8):081403. *Cited page 16*
- [Kamath et al., 1996] Kamath, G. M., Hurt, M. K., and Wereley, N. M. (1996). Analysis and testing of bingham plastic behavior in semi-active electrorheological fluid dampers. *Smart Materials and Structures*, 5(5):576. *Cited page 7*
- [Kani et al., 2016] Kani, M., Khadem, S. E., Pashaei, M. H., and Dardel, M. (2016). Design and performance analysis of a nonlinear energy sink attached to a beam with different support conditions. *Proc IMechE, Part C: J Mechanical Engineering Science*, 230(4):527–542. *Cited page 27*
- [Karayannis et al., 2008] Karayannis, I., Vakakis, A., and Georgiades, F. (2008). Vibro-impact attachments as shock absorbers. *Proc IMechE, Part C: Journal of Mechanical Engineering Science*, 222(10):1899–1908. *Cited page 26*
- [Kerschen et al., 2007] Kerschen, G., Kowtko, J. J., McFarland, D. M., Bergman, L. A., and Vakakis, A. F. (2007). Theoretical and experimental study of multimodal targeted energy transfer in a system of coupled oscillators. *Nonlinear Dynamics*, 47(1):285–309. *Cited page 98*
- [Kerschen et al., 2009] Kerschen, G., Peeters, M., Golinval, J.-C., and Vakakis, A. F. (2009). Nonlinear normal modes, part i: A useful framework for the structural dynamicist. *Mechanical Systems and Signal Processing*, 23(1):170–194. *3 citations pages xiii, 21, et 22*

- [Kobori et al., 1993] Kobori, T., Takahashi, M., Nasu, T., Niwa, N., and Ogasawara, K. (1993). Seismic response controlled structure with active variable stiffness system. *Earthquake engineering & structural dynamics*, 22(11):925–941. *Cited page 7*
- [Kovacic et al., 2008] Kovacic, I., Brennan, M. J., and Waters, T. P. (2008). A study of a nonlinear vibration isolator with a quasi-zero stiffness characteristic. *Journal of Sound and Vibration*, 315(3):700–711. *Cited page 19*
- [Kuznetsov, 2013] Kuznetsov, Y. A. (2013). *Elements of applied bifurcation theory*, volume 112. Springer Science & Business Media. *Cited page 23*
- [Lamarque et al., 2011] Lamarque, C.-H., Gendelman, O. V., Savadkoohi, A. T., and Etcheverria, E. (2011). Targeted energy transfer in mechanical systems by means of non-smooth nonlinear energy sink. *Acta mechanica*, 221(1-2):175–200. *3 citations pages xiii, 10, et 25*
- [Lamarque and Savadkoohi, 2014] Lamarque, C.-H. and Savadkoohi, A. T. (2014). Dynamical behavior of a bouc-wen type oscillator coupled to a nonlinear energy sink. *Meccanica*, 49(8):1917–1928. *Cited page 27*
- [Lamarque and Savadkoohi, 2015] Lamarque, C.-H. and Savadkoohi, A. T. (2015). Targeted energy transfer between a system with a set of saint-venant elements and a nonlinear energy sink. *Continuum Mechanics and Thermodynamics*, 27(4-5):819–833. *Cited page 24*
- [Lamarque et al., 2017] Lamarque, C.-H., Savadkoohi, A. T., Charlemagne, S., and Abdoulhadi, P. (2017). Nonlinear vibratory interactions between a linear and a non-smooth forced oscillator in the gravitational field. *Mechanical Systems and Signal Processing*, 89:131–148. *Cited page 24*
- [Lan et al., 2014] Lan, C.-C., Yang, S.-A., and Wu, Y.-S. (2014). Design and experiment of a compact quasi-zero-stiffness isolator capable of a wide range of loads. *Journal of Sound and Vibration*, 333(20):4843–4858. *Cited page 19*
- [Le and Ahn, 2011] Le, T. D. and Ahn, K. K. (2011). A vibration isolation system in low frequency excitation region using negative stiffness structure for vehicle seat. *Journal of Sound and Vibration*, 330(26):6311–6335. *Cited page 19*
- [Lee et al., 2009] Lee, Y., Nucera, F., Vakakis, A., McFarland, D., and Bergman, L. (2009). Periodic orbits, damped transitions and targeted energy transfers in oscillators with vibro-impact attachments. *Physica D: Nonlinear Phenomena*, 238(18):1868–1896. *Cited page 26*
- [Lee et al., 2007] Lee, Y., Vakakis, A., Bergman, L., McFarland, D. M., and Kerschen, G. (2007). Suppression aeroelastic instability using broadband passive targeted energy transfers, part 1: Theory. *AIAA Journal*, 45(3):693–711. *Cited page 28*
- [Lee et al., 2008] Lee, Y., Vakakis, A. F., Bergman, L., McFarland, D., Kerschen, G., Nucera, F., Tsakirtzis, S., and Panagopoulos, P. (2008). Passive non-linear targeted energy transfer and its applications to vibration absorption: a review. *Proc IMechE, Part K: Journal of Multi-body Dynamics*, 222(2):77–134. *4 citations pages 9, 21, 23, et 26*

- [Li, 2000] Li, C. (2000). Performance of multiple tuned mass dampers for attenuating undesirable oscillations of structures under the ground acceleration. *Earthquake Engineering & Structural Dynamics*, 29(9):1405–1421. *Cited page 9*
- [Li, 2016] Li, T. (2016). *Study of nonlinear targeted energy transfer by vibro-impact*. PhD thesis, INSA de Toulouse. *2 citations pages 108 et 122*
- [Li et al., 2017a] Li, T., Gourc, E., Seguy, S., and Berlioz, A. (2017a). Dynamics of two vibro-impact nonlinear energy sinks in parallel under periodic and transient excitations. *International Journal of Non-Linear Mechanics*, 90:100 – 110. *2 citations pages 27 et 29*
- [Li et al., 2017b] Li, T., Qiu, D., Seguy, S., and Berlioz, A. (2017b). Activation characteristic of a vibro-impact energy sink and its application to chatter control in turning. *Journal of Sound and Vibration*, 405:1 – 18. *Cited page 28*
- [Li et al., 2017c] Li, T., Seguy, S., and Berlioz, A. (2017c). On the dynamics around targeted energy transfer for vibro-impact nonlinear energy sink. *Nonlinear Dynamics*, 87(3):1453–1466. *2 citations pages 26 et 112*
- [Li et al., 2017d] Li, T., Seguy, S., and Berlioz, A. (2017d). Optimization mechanism of targeted energy transfer with vibro-impact energy sink under periodic and transient excitation. *Nonlinear Dynamics*, 87(4):2415–2433. *5 citations pages 24, 26, 112, 116, et 123*
- [Lieber and Jensen, 1945] Lieber, P. and Jensen, D. (1945). An acceleration damper: development, design and some applications. *Trans. ASME*, 67(10):523–530. *Cited page 26*
- [Liu and Liu, 2006] Liu, J. and Liu, K. (2006). A tunable electromagnetic vibration absorber: characterization and application. *Journal of Sound and Vibration*, 295(3):708–724. *Cited page 19*
- [Liu et al., 2008] Liu, Y., Matsuhisa, H., and Utsuno, H. (2008). Semi-active vibration isolation system with variable stiffness and damping control. *Journal of sound and vibration*, 313(1):16–28. *Cited page 7*
- [Luo et al., 2013] Luo, J., Wierschem, N. E., Fahnestock, L. A., Bergman, L. A., Spencer Jr, B. F., AL-Shudeifat, M., McFarland, D. M., Quinn, D. D., and Vakakis, A. F. (2013). Realization of a strongly nonlinear vibration-mitigation device using elastomeric bumpers. *Journal of Engineering Mechanics*, 140(5):04014009. *Cited page 27*
- [Luo et al., 2014] Luo, J., Wierschem, N. E., Hubbard, S. A., Fahnestock, L. A., Quinn, D. D., McFarland, D. M., Spencer, B. F., Vakakis, A. F., and Bergman, L. A. (2014). Large-scale experimental evaluation and numerical simulation of a system of nonlinear energy sinks for seismic mitigation. *Engineering Structures*, 77:34–48. *Cited page 27*
- [Malher et al., 2017] Malher, A., Touzé, C., Doaré, O., Habib, G., and Kerschen, G. (2017). Flutter control of a two-degrees-of-freedom airfoil using a nonlinear tuned vibration absorber. *Journal of Computational and Nonlinear Dynamics*, 12(5):051016. *Cited page 16*

- [Manevitch, 2001] Manevitch, L. (2001). The description of localized normal modes in a chain of nonlinear coupled oscillators using complex variables. In *Normal Modes and Localization in Nonlinear Systems*, pages 95–109. Springer. *Cited page 22*
- [Manevitch et al., 2014] Manevitch, L., Sigalov, G., Romeo, F., Bergman, L., and Vakakis, A. (2014). Dynamics of a linear oscillator coupled to a bistable light attachment: analytical study. *Journal of Applied Mechanics*, 81(4):041011. *Cited page 25*
- [Mariani et al., 2011] Mariani, R., Bellizzi, S., Cochelin, B., Herzog, P., and Mattei, P.-O. (2011). Toward an adjustable nonlinear low frequency acoustic absorber. *Journal of Sound and Vibration*, 330(22):5245–5258. *Cited page 27*
- [Matta, 2011] Matta, E. (2011). Performance of tuned mass dampers against near-field earthquakes. *Structural Engineering and Mechanics*, 39(5):621–642. *Cited page 8*
- [Mattei et al., 2016] Mattei, P.-O., Ponçot, R., Pachebat, M., and Côte, R. (2016). Non-linear targeted energy transfer of two coupled cantilever beams coupled to a bistable light attachment. *Journal of Sound and Vibration*, 373:29–51. *Cited page 26*
- [McFarland et al., 2005] McFarland, D. M., Bergman, L. A., and Vakakis, A. F. (2005). Experimental study of non-linear energy pumping occurring at a single fast frequency. *International Journal of Non-linear Mechanics*, 40(6):891–899. *Cited page 27*
- [Mead, 1999] Mead, D. J. (1999). *Passive vibration control*. John Wiley & Sons Inc. *2 citations pages 6 et 7*
- [Mohammad A, 2014] Mohammad A, A.-S. (2014). Highly efficient nonlinear energy sink. *Nonlinear Dynamics*, 76(4):1905–1920. *4 citations pages 24, 25, 76, et 99*
- [Nagarajaiah and Varadarajan, 2005] Nagarajaiah, S. and Varadarajan, N. (2005). Short time fourier transform algorithm for wind response control of buildings with variable stiffness tmd. *Engineering Structures*, 27(3):431–441. *2 citations pages xiii et 20*
- [Nayfeh, 2011] Nayfeh, A. H. (2011). *Introduction to perturbation techniques*. John Wiley & Sons. *2 citations pages 22 et 36*
- [Nayfeh and Mook, 2008] Nayfeh, A. H. and Mook, D. T. (2008). *Nonlinear oscillations*. John Wiley & Sons. *Cited page 21*
- [Nguyen and Pernot, 2012] Nguyen, T. A. and Pernot, S. (2012). Design criteria for optimally tuned nonlinear energy sinks—part 1: transient regime. *Nonlinear Dynamics*, 69(1):1–19. *Cited page 27*
- [Nucera et al., 2008] Nucera, F., Lo Iacono, F., McFarland, D., Bergman, L., and Vakakis, A. (2008). Application of broadband nonlinear targeted energy transfers for seismic mitigation of a shear frame: Experimental results. *Journal of Sound and Vibration*, 313(1):57–76. *Cited page 28*
- [Nucera et al., 2007] Nucera, F., Vakakis, A., McFarland, D., Bergman, L., and Kerschen, G. (2007). Targeted energy transfers in vibro-impact oscillators for seismic mitigation. *Nonlinear Dynamics*, 50(3):651–677. *Cited page 26*

- [Occhiuzzi et al., 2008] Occhiuzzi, A., Spizzuoco, M., and Ricciardelli, F. (2008). Loading models and response control of footbridges excited by running pedestrians. *Structural control and health monitoring*, 15(3):349–368. Cited page 9
- [Opgenoord et al., 2016] Opgenoord, M. M., Allaire, D. L., and Willcox, K. E. (2016). Variance-based sensitivity analysis to support simulation-based design under uncertainty. *Journal of Mechanical Design*, 138(11):111410. Cited page 69
- [Paredes, 2000] Paredes, M. (2000). *Développement d’outils d’assistance à la conception optimale des liaisons élastiques par ressorts*. PhD thesis, INSA de Toulouse. Cited page 14
- [Paredes, 2013a] Paredes, M. (2013a). Analytical and experimental study of conical telescoping springs with nonconstant pitch. *Journal of Mechanical Design*, 135(9):094502. 2 citations pages 17 et 47
- [Paredes, 2013b] Paredes, M. (2013b). <http://www.meca.insa-toulouse.fr/paredes/Springs2K/index.php?men=com&ide=Cnomenclature>. Cited page 11
- [Paredes, 2016] Paredes, M. (2016). Enhanced formulae for determining both free length and rate of cylindrical compression springs. *Journal of Mechanical Design*, 138(2):021404. Cited page 58
- [Paredes and Rodriguez, 2009] Paredes, M. and Rodriguez, E. (2009). Optimal design of conical springs. *Engineering with computers*, 25(2):147. Cited page 16
- [Pati et al., 2015] Pati, R. V., Reddy, P. R., and Laxminarayana, P. (2015). Development of buckling equation for conical spring and its experimental verification. *American Journal of Engineering and Technology Research Vol*, 15(1). Cited page 17
- [Patil et al., 2014] Patil, R. V., Reddy, P. R., and Laxminarayana, P. (2014). Comparison of cylindrical and conical helical springs for their buckling load and deflection. *Int. J. Adv. Sci. Technol*, 73:33–50. 2 citations pages 17 et 47
- [Pennisi and Stephan, 2017] Pennisi, G. and Stephan, Cyrille and Gourc, E. a. G. (2017). Experimental investigation and analytical description of a vibro-impact nes coupled to a single-degree-of-freedom linear oscillator harmonically forced. *Nonlinear Dynamics*, 88(3):1769–1784. Cited page 26
- [Pilipchuk, 2015] Pilipchuk, V. (2015). Closed-form solutions for oscillators with inelastic impacts. *Journal of Sound and Vibration*, 359:154–167. Cited page 111
- [Pinkaw and Fujino, 2001] Pinkaw, T. and Fujino, Y. (2001). Effectiveness of semi-active tuned mass dampers under harmonic excitation. *Engineering Structures*, 23(7):850–856. Cited page 9
- [Preumont, 2011] Preumont, A. (2011). *Vibration control of active structures: an introduction*, volume 179. Springer Science & Business Media. Cited page 8
- [Pullbarspring, 2017] Pullbarspring (2017). <https://www.hypercoils.com/pull-barsprings/>. Cited page 18

- [QIN et al., 2009] QIN, L., YAN, W., and LI, Y. (2009). Design of frictional pendulum tmd and its wind control effectiveness. *Journal of Earthquake Engineering and Engineering Vibration*, 5:020. *Cited page 8*
- [Qiu et al., 2017] Qiu, D., Seguy, S., and Paredes, M. (2017). A novel design of cubic stiffness for a nonlinear energy sink (nes) based on conical spring. In *Advances on Mechanics, Design Engineering and Manufacturing*, pages 565–573. Springer. *Cited page 47*
- [Rodriguez, 2006] Rodriguez, E. (2006). *Etude du comportement des ressorts coniques et ressorts de torsion en vue du développement d'outils de synthèse associés*. PhD thesis, INSA de Toulouse. *Cited page 17*
- [Rodriguez et al., 2006] Rodriguez, E., Paredes, M., and Sartor, M. (2006). Analytical behavior law for a constant pitch conical compression spring. *Journal of Mechanical Design*, 128(6):1352–1356. *5 citations pages xiii, 17, 18, 47, et 48*
- [Romeo et al., 2015a] Romeo, F., Manevitch, L., Bergman, L., and Vakakis, A. (2015a). Transient and chaotic low-energy transfers in a system with bistable nonlinearity. *Chaos: An Interdisciplinary Journal of Nonlinear Science*, 25(5):053109. *2 citations pages 25 et 94*
- [Romeo et al., 2015b] Romeo, F., Sigalov, G., Bergman, L. A., and Vakakis, A. F. (2015b). Dynamics of a linear oscillator coupled to a bistable light attachment: Numerical study. *Journal of Computational and Nonlinear Dynamics*, 10(1):011007. *2 citations pages 25 et 71*
- [Sack et al., 1994] Sack, R., Kuo, C., Wu, H., Liu, L., and Patten, W. (1994). Seismic motion control via semiactive hydraulic actuators. In *Proc., US 5th Nat. Conf. on Earthquake Engrg*, volume 2, pages 311–320. *Cited page 7*
- [Savadkoohi et al., 2011] Savadkoohi, A. T., Manevitch, L. I., and Lamarque, C.-H. (2011). Analysis of the transient behavior in a two dof nonlinear system. *Chaos, Solitons & Fractals*, 44(6):450–463. *Cited page 24*
- [Savadkoohi et al., 2012] Savadkoohi, A. T., Vaurigaud, B., Lamarque, C.-H., and Pernot, S. (2012). Targeted energy transfer with parallel nonlinear energy sinks, part ii: theory and experiments. *Nonlinear Dynamics*, 67(1):37–46. *2 citations pages xiii et 27*
- [Sigalov et al., 2012] Sigalov, G., Gendelman, O., Al-Shudeifat, M., Manevitch, L., Vakakis, A., and Bergman, L. (2012). Resonance captures and targeted energy transfers in an inertially-coupled rotational nonlinear energy sink. *Nonlinear Dynamics*, 69(4):1693–1704. *Cited page 10*
- [Simcoespring, 2010] Simcoespring (2010). <http://www.simcoespring.com/catalogue/>. *Cited page 18*
- [Sönmez and Tutum, 2008] Sönmez, Ü. and Tutum, C. C. (2008). A compliant bistable mechanism design incorporating elastica buckling beam theory and pseudo-rigid-body model. *Journal of Mechanical Design*, 130(4):042304. *Cited page 20*

- [Soong and Costantinou, 2014] Soong, T. T. and Costantinou, M. C. (2014). *Passive and active structural vibration control in civil engineering*, volume 345. Springer. Cited page 6
- [Stanleyspring, 2011] Stanleyspring (2011). <http://www.stanleyspring.com/variable-pitch-springs/>. Cited page 18
- [Stanton et al., 2010] Stanton, S. C., McGehee, C. C., and Mann, B. P. (2010). Nonlinear dynamics for broadband energy harvesting: Investigation of a bistable piezoelectric inertial generator. *Physica D: Nonlinear Phenomena*, 239(10):640–653. Cited page 20
- [Starosvetsky and Gendelman, 2008a] Starosvetsky, Y. and Gendelman, O. (2008a). Dynamics of a strongly nonlinear vibration absorber coupled to a harmonically excited two-degree-of-freedom system. *Journal of Sound and Vibration*, 312(1):234–256. Cited page 92
- [Starosvetsky and Gendelman, 2008b] Starosvetsky, Y. and Gendelman, O. (2008b). Strongly modulated response in forced 2dof oscillatory system with essential mass and potential asymmetry. *Physica D: Nonlinear Phenomena*, 237(13):1719–1733. 5 citations pages 24, 36, 38, 81, et 84
- [Touzé and Thomas, 2006] Touzé, C. and Thomas, O. (2006). Non-linear behaviour of free-edge shallow spherical shells: effect of the geometry. *International Journal of non-linear Mechanics*, 41(5):678–692. Cited page 16
- [Touzé et al., 2002] Touzé, C., Thomas, O., and Chaigne, A. (2002). Asymmetric non-linear forced vibrations of free-edge circular plates. part 1: Theory. *Journal of Sound and Vibration*, 258(4):649–676. Cited page 23
- [Trabelsi, 2014] Trabelsi, H. (2014). *Contribution à la prise en compte d'exigences dynamiques en conception préliminaire de systèmes complexes*. PhD thesis, Châtenay-Malabry, Ecole centrale de Paris. Cited page 14
- [Trabelsi et al., 2015] Trabelsi, H., Yvars, P.-A., Louati, J., and Haddar, M. (2015). Interval computation and constraint propagation for the optimal design of a compression spring for a linear vehicle suspension system. *Mechanism and Machine Theory*, 84:67–89. Cited page 12
- [Tsakirtzis et al., 2007] Tsakirtzis, S., Panagopoulos, P. N., Kerschen, G., Gendelman, O., Vakakis, A. F., and Bergman, L. A. (2007). Complex dynamics and targeted energy transfer in linear oscillators coupled to multi-degree-of-freedom essentially nonlinear attachments. *Nonlinear Dynamics*, 48(3):285–318. Cited page 28
- [Vakakis et al., 2008] Vakakis, A. F., Gendelman, O., Bergman, L., McFarland, D., Kerschen, G., and Lee, Y. (2008). *Nonlinear targeted energy transfer in mechanical and structural systems*, volume 156. Springer Science & Business Media, Berlin. 4 citations pages 10, 23, 26, et 36
- [Vakakis and Gendelman, 2001] Vakakis, A. F. and Gendelman, O. V. (2001). Energy pumping in nonlinear mechanical oscillators: part ii: resonance capture. *Journal of Applied Mechanics*, 68(1):42–48. Cited page 9

- [Van Ham et al., 2009] Van Ham, R., Sugar, T. G., Vanderborght, B., Hollander, K. W., and Lefeber, D. (2009). Compliant actuator designs. *IEEE Robotics & Automation Magazine*, 16(3). *Cited page 18*
- [Vasques and Rodrigues, 2006] Vasques, C. and Rodrigues, J. D. (2006). Active vibration control of smart piezoelectric beams: Comparison of classical and optimal feedback control strategies. *Computers & structures*, 84(22):1402–1414. *Cited page 8*
- [Vaurigaud et al., 2011] Vaurigaud, B., Savadkoobi, A. T., and Lamarque, C.-H. (2011). Targeted energy transfer with parallel nonlinear energy sinks. part i: Design theory and numerical results. *Nonlinear Dynamics*, 66(4):763–780. *2 citations pages 24 et 29*
- [Viguié and Kerschen, 2009] Viguié, R. and Kerschen, G. (2009). Nonlinear vibration absorber coupled to a nonlinear primary system: a tuning methodology. *Journal of Sound and Vibration*, 326(3):780–793. *Cited page 28*
- [Wahl, 1944] Wahl, A. M. (1944). *Mechanical springs*. Penton Publishing Company. *2 citations pages 11 et 58*
- [Wang et al., 2017] Wang, H., He, P., Pang, B., and Gao, X. (2017). A new computational model of large three-row roller slewing bearings using nonlinear springs. *Proc IMechE, Part C: Journal of Mechanical Engineering Science*, 231(20):3831–3839. *Cited page 16*
- [Wang et al., 2015] Wang, J., Wierschem, N. E., Spencer Jr, B. F., and Lu, X. (2015). Track nonlinear energy sink for rapid response reduction in building structures. *Journal of Engineering Mechanics*, 141(1):04014104. *Cited page 27*
- [Weber, 2014] Weber, F. (2014). Semi-active vibration absorber based on real-time controlled mr damper. *Mechanical Systems and Signal Processing*, 46(2):272–288. *Cited page 8*
- [Weber and Maślanka, 2012] Weber, F. and Maślanka, M. (2012). Frequency and damping adaptation of a tmd with controlled mr damper. *Smart Materials and Structures*, 21(5):055011. *Cited page 8*
- [Wiggins, 2003] Wiggins, S. (2003). *Introduction to applied nonlinear dynamical systems and chaos*, volume 2. Springer Science & Business Media. *Cited page 85*
- [Wu and Lan, 2014] Wu, Y.-S. and Lan, C.-C. (2014). Linear variable-stiffness mechanisms based on preloaded curved beams. *Journal of Mechanical Design*, 136(12):122302. *2 citations pages 18 et 19*
- [Xu et al., 2013] Xu, D., Yu, Q., Zhou, J., and Bishop, S. (2013). Theoretical and experimental analyses of a nonlinear magnetic vibration isolator with quasi-zero-stiffness characteristic. *Journal of Sound and Vibration*, 332(14):3377–3389. *Cited page 19*
- [Xu et al., 2001] Xu, Y., Qu, W., and Chen, Z. (2001). Control of wind-excited truss tower using semiactive friction damper. *Journal of structural engineering*, 127(8):861–868. *Cited page 7*

- [Yamaguchi and Harnpornchai, 1993] Yamaguchi, H. and Harnpornchai, N. (1993). Fundamental characteristics of multiple tuned mass dampers for suppressing harmonically forced oscillations. *Earthquake engineering & structural dynamics*, 22(1):51–62. Cited page [9](#)
- [Yamamoto, 1999] Yamamoto, Y. (1999). Spring’s effective mass in spring mass system free vibration. *Journal of Sound and Vibration*, 220(3):564–570. Cited page [63](#)
- [Yao et al., 2002] Yao, G., Yap, F., Chen, G., Li, W., and Yeo, S. (2002). Mr damper and its application for semi-active control of vehicle suspension system. *Mechatronics*, 12(7):963–973. Cited page [7](#)
- [Zhang and Angeles, 2005] Zhang, D.-G. and Angeles, J. (2005). Impact dynamics of flexible-joint robots. *Computers & structures*, 83(1):25–33. Cited page [26](#)

Publications

This work of thesis has produced the following publications:

Journal papers:

- D. Qiu, M. Paredes and S. Seguy. (2019). Variable pitch spring for nonlinear energy sink: application to passive vibration control. *Proceedings of the Institution of Mechanical Engineers, Part C: Journal of Mechanical Engineering Science*. 233, 611-622.
- D. Qiu, S. Seguy and M. Paredes. (2019). Design criteria for optimally tuned vibro-impact nonlinear energy sink. *Journal of Sound and Vibration*. 442, 497-513.
- D. Qiu, T. Li, S. Seguy and M. Paredes. (2018). Efficient targeted energy transfer of a bistable nonlinear energy sink: application to optimal design. *Nonlinear Dynamics*. 92, 443-461.
- D. Qiu, S. Seguy and M. Paredes. (2018). Tuned nonlinear energy sink with conical spring: design theory and sensitivity analysis. *Journal of Mechanical Design*, 140, 01104-10.
- T. Li , D. Qiu, S. Seguy and A. Berlioz. (2017). Activation characteristic of a vibro-impact energy sink and its application to chatter control in turning. *Journal of Sound and Vibration*, 405, 1-18.

Conference papers:

- D. Qiu, S. Seguy and M. Paredes. A novel design of cubic stiffness for a Nonlinear Energy Sink (NES) based on conical spring. *Proceedings of International Joint Conference on Mechanics, Design Engineering & Advanced Manufacturing*, 14-26 septembre 2016, Catane, Italie, p.565-573, 2016
- D. Qiu, S. Seguy and M. Paredes. Design of cubic stiffness for the absorber of Nonlinear Energy Sink (NES). *Proceedings of 13th Symposium Vibrations, Shocks and Noise VISHNO*, 11-15 avril 2016, Le Mans, France p.2295-2300, 2016

